ULTRASONIC IMAGING AND TACTILE SENSING FOR ROBOTIC SYSTEMS

A Dissertation
Presented to
The Academic Faculty

By

Aravind Baradhwaj Balasubramanian

In Partial Fulfillment
of the Requirements for the Degree
Doctor of Philosophy in the
School of Electrical and Computer Engineering
College of Engineering

Georgia Institute of Technology

August 2022

ULTRASONIC IMAGING AND TACTILE SENSING FOR ROBOTIC SYSTEMS

Thesis committee:

Dr. David G. Taylor, Advisor
Electrical and Computer Engineering
Georgia Institute of Technology

Dr. Ying Zhang
Electrical and Computer Engineering
Georgia Institute of Technology

Dr. Gregory D. Durgin
Electrical and Computer Engineering
Georgia Institute of Technology

Dr. Aldo A. Ferri
Mechanical Engineering
Georgia Institute of Technology

Dr. Yorai Wardi
Electrical and Computer Engineering
Georgia Institute of Technology

Date approved: July 6, 2022

To my family for making this possible

ACKNOWLEDGMENTS

This dissertation has been possible only because of the guidance and support from multiple individuals.

First and foremost, I want to express my deepest appreciation to my advisor, Dr. David Taylor, for giving me the opportunity to work with him. Prof. Taylor has helped and supported me throughout the research. I am very grateful for his invaluable advice, encouragement, and insight throughout the multi-year research project.

I am grateful to Prof. Durgin and Prof. Wardi for serving on the reading committee and providing valuable feedback during the proposal and the dissertation phases. I also want to sincerely thank Prof. Ferri and Prof. Zhang for their time in serving on the dissertation committee.

Sponsorship for this research from Texas Instruments is gratefully acknowledged. Many thanks to Dr. David Magee from Texas Instruments for his helpful feedback through monthly meetings. I want to thank the school of Electrical and Computer Engineering for support as a Teaching Assistant during the initial and final phases of the research.

I also want to recognize my lab mate Kartik Sastry for his input during the middle phase of the project.

I want to thank James Steinberg and Kevin Ferri for their practical suggestions during hardware development.

Lastly, I want to thank my family, my father Balasubramanian, my mother Radha, and my brother Vishwanath without whom I would not have seen the light of this day. They have been a constant source of strength and motivation, patiently supporting me in my higher education pursuits.

TABLE OF CONTENTS

LIST OF TABLES

LIST OF FIGURES

LIST OF ACRONYMS

ADC Analog to Digital Converter

BASE Baseline Excitation Signal

BVD Butterworth Van Dyke

DAS Delay and Sum Beamformer

FUT Flexural Ultrasonic Transducer

LSTM Long Short Term Memory

MCU Microcontroller Unit

MUSIC MUltiple SIgnal Classification Beamformer

MVDR Minimum Variance Distortionless Response Beamformer

NLP Nonlinear Programming Problem

NN Neural Network

NRMSE Normalized Root Mean Square Error

OCP Optimal Control Problem

PWM Pulse Width Modulation

RMS Root Mean Square

RXOPT Time Optimal Receive Excitation Signal

SNR Signal to Noise Ratio

SPL Sound Pressure Level

SVM Support Vector Machine

ToF Time of Flight

TXOPT Time Optimal Transmit Excitation Signal

SUMMARY

This research develops several novel algorithms that enhance the operation of ultrasonic and tactile sensors for robotic applications. The emphasis is on reducing the overall cost, system complexity, and enabling operation on resource-constrained embedded devices with the main focus on ultrasonics. The research improves key performance characteristics of pulse-echo sensor systems – the minimum range, range resolution, and multi-object localization. The former two aspects are improved through the application of model-based and model-free techniques. Time optimal principles precisely control the oscillations of transmitting and receiving ultrasonic transducers, influencing the shape of the pressure waves. The model-free approach develops simple learning procedures to manipulate transducer oscillations, resulting in algorithms that are insensitive to parameter variations. Multi-object localization is achieved through phased array techniques that determine the positions of reflectors in 3-D space using a receiver array consisting of a small number of elements. The array design and the processing algorithm allow simultaneous determination of the reflector positions, achieving high sensor throughputs. Tactile sensing is a minor focus of this research that leverages machine learning in combination with an exploratory procedure to estimate the unknown stiffness of a grasped object. Gripper mechanisms with full-actuation and under-actuation are studied, and the object stiffness is estimated using regression. Sensor measurements use actuator position and current as the inputs. Regressor design, dataset generation, and the estimation performance under nonlinear effects, such as dry friction, parameter variations, and under-actuated transmission mechanisms are addressed.

CHAPTER 1
INTRODUCTION AND BACKGROUND

Ultrasonic sensing is a rapidly growing technology. Example applications include navigation in vehicles (blind spot detection, lane assisting), mapping for robotics, and fluid flow rate estimation. The measurement process involves a pulse-echo trial, where a short duration pressure wave is emitted by a transmitting device and the collection of pressure waves occurs at a receiving device. Transmission and reception may occur on the same device, or two separate devices may be used. The time elapsed between the transmission of a pressure wave and the reception of echoes determines the Time of Flight (ToF). Scaling the ToF by the speed of sound in the transmission medium provides the travel distance of the pressure wave. Air ultrasonic applications are the focus of this research, and employ a frequency between 25 – 80 kHz (wavelength of 4 – 14 mm).

Ultrasonic sensing offers several advantages over other modalities, such as optical or electromagnetic. Ultrasonic sensors have lower complexity and cost – computation requirements, analog signal chain, and power budget. The low volume of data reduces the redundancy and requires a fewer number of transducer elements. The analog signal provides details about the operating conditions, leveraged by applications such as flow metering. Ultrasonic sensors are immune to illumination conditions, which can vary significantly in different environments, an important advantage over optical sensing technologies. Ultrasonic sensor operation is also possible in harsh settings with high temperature, humidity, or in dirt and dust-prone areas, with comparatively limited performance degradation.

Air ultrasonic applications also have a set of challenges. The lower propagation speed of sound reduces the rate of pulse-echo trials. As an ultrasonic wave is a pressure wave, typically launched through the vibration of a mechanical membrane, substantial conversion losses can occur due to the lower transfer of energy between the electrical and acoustic

domains requiring care during the design of transmitter hardware. A related issue is the reduced sensitivity of received pressure waves, which requires amplification and filtering of the signal content. Multi-path propagations, like other wave-based sensing techniques, degrade the overall performance. Hence applications must be designed to overcome the alterations imposed due to multi-path phenomena. The received pressure waves from a reflector depend on the shape of the reflector degrading the Signal to Noise Ratio (SNR) for ToF estimation applications. Other applications may use this degradation aspect to classify targets of different shapes.

A minor focus of this research is on tactile sensing, another important measurement quantity in robotic automation and haptic feedback devices. Tactile sensors detect contacts between two surfaces and the respective contacting forces. Traditionally, the sensors utilize piezo-resistive or piezo-capacitive modalities to monitor a change in the resistance or the capacitance in response to an applied force. Several tactile sensor elements are employed in an array to detect the contact location. The cost of high precision tactile sensing array with associated electronics is high, which also substantially drives up the overall cost of integration into a robotic system. Also, contact sensor arrays require routine maintenance and care during operation. Obtaining reliable and repeatable measurements from a contact force sensor needs a suitable actuation mechanism. In this research, a low-cost alternative utilizing the measurements made with an electric motor (actuator position and actuator current) is pursued instead of traditional approaches to tactile sensing, suitable for low complexity mechanisms. However, nonlinear effects in the system and unmodeled dynamics appear in the sensor measurements requiring data processing and extraction of relevant metrics.

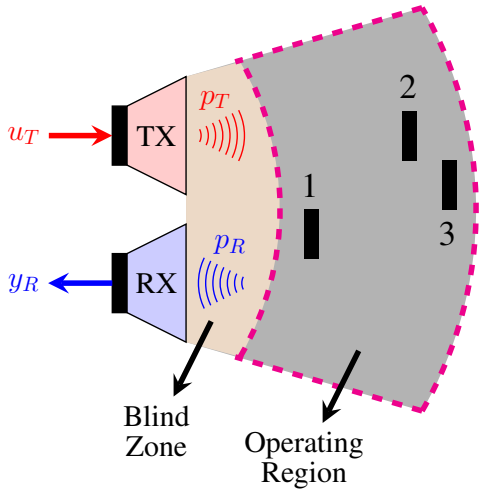

Figure 1.1: Ultrasonic sensing system in the pulse-echo mode of operation. The reflecting objects in the scene are labeled $(1,\ 2,\ 3)$ and are located within the operating range shown in [- -].

1.1 Background

1.1.1 Ultrasonic Sensing

The ultrasonic sensor system of interest is illustrated in Figure 1.1. It consists of a transmitter (TX), a receiver (RX), and several reflectors $(1,\ 2,\ 3)$. Although a TX-RX pair is shown for generality, the sensor system may utilize a single transducer for both TX and RX operations. The objective of the setup is to determine the location of multiple reflectors in the scene using the pulse-echo mode of operation. Application of a time-gated electrical voltage u_T at the transmitter launches a pressure wave burst p_T. The incoming pressure wave at the receiver after propagating through the medium is p_R, and y_R is the voltage generated at the receiver due to the pressure input signal p_R. The echo bursts corresponding to each reflector are separated in time. Determination of the time delay between the transmission and the reception of echo bursts provides the round-trip Time of Flight (ToF). The range is computed by scaling the ToF by the speed of sound as

$$\text{Range} = \frac{\text{ToF} \times v_{sound}}{2} \tag{1.1}$$

where $v_{sound} = 340$ m/s as air is the propagation medium. Additionally, the echo bursts at y_R also experience attenuation due to propagation through the medium, the reflector properties, and the electric $\leftrightarrow$ acoustic conversion losses of the devices.

This research addresses improvements in important performance metrics of an ultrasonic sensor system – the minimum range, range resolution, and multi-object localization. Figure 1.1 clarifies the metrics in more detail. During transmission events, the signal y_R at RX is influenced by the transmission bursts u_T applied at TX. This aspect results in an initial region where the sensor cannot detect echoes called the blind zone. The length of the blind zone translates to the minimum range at which the sensing system can begin detecting echoes from reflectors. As the pulse-echo process experiences amplitude losses, the magnitude of y_R imposes limits on the maximum range of the sensor system. A single reflector (object 1) induces a voltage response y_R at RX only when it is located within the operating region of the sensor. Range resolution is the smallest separation between two reflectors (objects 2 and 3) for which both objects are detectable and their distances measured. In the sensor's scene shown by Figure 1.1, the objects are located at an off-centered position about the sensor's center; they all have a coordinate in the 3-D space. Determination of the reflector locations for each object from y_R is another important performance metric of an ultrasonic sensing system, useful in several robotics applications.

This work considers piezoelectric and electrostatic ultrasonic transducers; both exchange energy across multiple domains. Piezoelectric transducers have a thin slab of piezoelectric material bonded to a metallic plate. During the transmission of a pressure wave, the application of u_T to the piezoelectric material results in the mechanical deformations of the material, which in turn causes the bending or flexing of the metal plate. During the reception, incoming pressure waves result in the flexing of a metal plate generating y_R at the electrical terminals. Such a transducer may be referred to as the Flexural Ultrasonic Transducer (FUT). The transducer construction results in a narrowband operation, with a bandwidth of about 3 – 4 kHz around the resonant frequency of the transducer.

The electrostatic transducer is similar to the FUT, where a thin foil is mounted between two electrodes. The application of large oscillatory voltages creates deflections in the foil, allowing pressure waves to be launched. Such a transducer requires large voltages (few kVs) to launch pressure waves of sufficient magnitude compared to much smaller voltages (few 10s of volts) for a FUT. An advantage of the electrostatic transducer is the increased sensitivity to incoming pressure waves compared to a FUT. Micromachined electrostatic receivers are available at a low cost (a few cents), have wideband operating characteristics, and are in a small form factor suitable for sensor array design.

In this work, the FUT is used for transmitting pressure waves and also as a receiver in the vibration control work; electrostatic transducers are used in the receiver array design for multi-object detection.

1.1.2 Tactile Sensing

The problem of applying tactile sensing to determine the unknown stiffness of an object under a grasp by a gripper is studied. It is an essential distinguishing feature, and one candidate application is to determine if a fruit is ripe. Figure 1.2 illustrates a parallel jaw gripper grasping an object, commonly found in several industrial applications. The mechanism consists of one actuated jaw and one fixed jaw. A position encoder measures the jaw position, and a current sensor measures the applied force onto the object. Grasp is achieved by operating the gripper either in the position control mode or force (current) control mode. The objective is to determine the unknown stiffness k_o of the grasped object using only actuator position and current measurements; the literature utilizes dedicated tactile sensor arrays mounted on the gripper's jaws. Drawing inspiration from how humans perceive stiffness, an exploratory procedure is employed, wherein the object's stiffness is estimated by squeezing it. Applying an increasing position command is equivalent to the squeezing effect; the actuator current increases proportionally to the object's stiffness. Determining the object's stiffness with the elementary approach of computing the stiffness

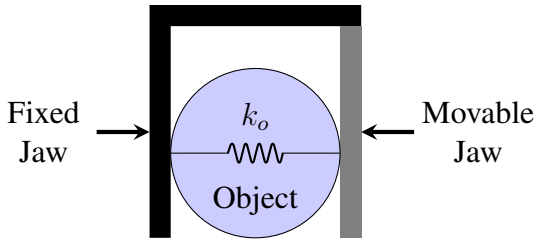

Figure 1.2: Gripper grasping an object with unknown stiffness k_o.

as a ratio of a change in force (current) to the change in displacement yields inaccurate results due to system nonlinearities, such as friction or transmission mechanism. Machine learning-based regression is leveraged as an alternative to estimate object stiffness and overcome the system nonlinearities with the tactile sensorless approach presented in this work.

1.2 Research Overview

The main focus of this research is to enhance the operation of ultrasonic transducers and tactile sensors through algorithm development and validation on experimental hardware. The research contributions are organized into three areas –

1. Vibration control of transducers: A time-gated u_T launches a pressure wave but results in sustained residual vibrations of $p_T,\ p_R$, and y_R long after the excitation ends. Due to the slow decaying tail, the minimum range and the range resolution are affected. The research addresses the decaying tail issue by developing model-based techniques to accelerate the decay process of p_T and y_R. Additionally, model-free algorithms in this work rely on simple learning procedures resulting in methods insensitive to parameter or component variations.

2. 3-D ultrasonic imaging: Array-based sensing hardware consisting of a small number of receiver elements is designed to perform 3-D imaging of a robot's workspace. The sensor data processing scheme based on beamforming is developed and allows the detection of multiple objects with a single pulse-echo trial. An embedded imple-

mentation provides computing requirements and achieves high detection throughputs suitable for object tracking.

3. Stiffness estimation: The stiffness of an object is estimated through a bio-inspired approach using machine learning regression methods. Nonlinearities due to dry friction are effectively overcome through regression. The stiffness estimation approach is extended to an underactuated human-like finger mechanism consisting of a complex tendon-pulley transmission.

CHAPTER 2
LITERATURE SURVEY

The literature survey is also organized into the three focus areas of the research – vibration control of transducers, 3-D ultrasonic imaging, and stiffness estimation.

2.1 Vibration Control of Transducers

Figure 2.1 shows an example of the signal $\tilde{y}_R$ acquired in the pulse-echo process after passing the signal y_R at the FUT through the analog signal chain consisting of a high gain bandpass filter. By the pressure $\leftrightarrow$ voltage analogy, the pressure signals p_T and p_R are proportional to their electrical counterparts – the voltage signals v_T and u_R, respectively. Since a single FUT is used to both transmit pressure waves and receive echoes, the signal y_R contains two components expressed as $y_R = v_T + u_R$. The first component is the response v_T due to the time-gated voltage excitation component u_T, and the second component is the echo-induced component u_R. Note that $\tilde{y}_R$ also inherits the decomposition: $\tilde{y}_R = \tilde{v}_T + \tilde{u}_R$ because $\tilde{y}_R$ represents y_R after passing through the high-gain bandpass filter ($\tilde{v}_T =$ excitation component and $\tilde{u}_R =$ echo-induced component). As the FUT is a resonant device, u_T is a 5 cycle rectangular pulse voltage excitation at the FUT's resonant frequency of 58.5 kHz. The voltage excitation ends at about 0.1 ms, after which the terminal voltage of the FUT (the pulse-imposed component) decays slowly to equilibrium conditions, reaching noise floor levels at about 1.2 ms. The slow decay is due to the high quality factor that enhances the transmission characteristics and the echo sensitivity during reception. An effect is a blind zone (the first 20 cm from the transducer), where no ToF or range estimate can be obtained as the amplified signal y_R remains saturated. Any echoes from reflectors located near the FUT in the blind zone have a considerably lower amplitude compared to the high-amplitude decay voltage appearing across the transmitter. The slow decay affects both single transducer and

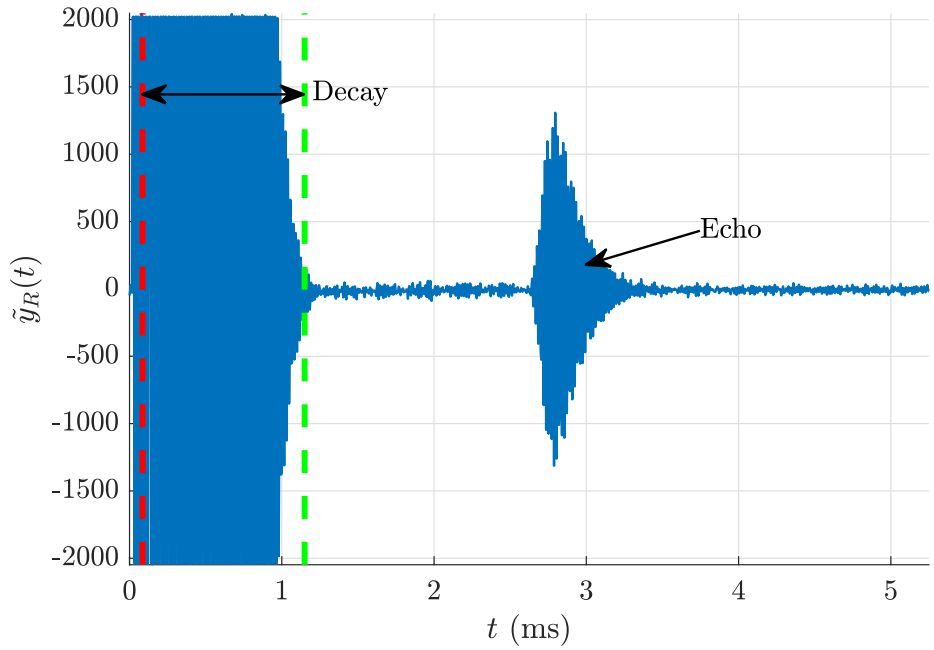

Figure 2.1: Pulse-echo measurement with a single reflector for a 58.5 kHz FUT after amplification. End of excitation [- -], end of natural decay [- -]. The signal $\tilde{y}_R$ is obtained after filtering and amplifying the signal y_R.

multiple transducers systems, and the boundary of the blind-zone in Figure 1.1 is determined by the end of the decay period as shown in Figure 2.1.

The Figure 2.1 also shows an echo from a single reflector at about 2.8 ms (47 cm). As the pulse-echo process is linear, the echoes u_R at the receiver's input are scaled and time-shifted copies of the transmitted pressure wave p_T. Due to the extended decaying tail of p_T, the ability to resolve closely separated targets is reduced as copies of p_T superimpose, degrading the ability to detect two distinct objects. Sensor operation is enhanced by reducing the decaying envelope of p_T; the blind zone in y_R reduces, and the echo shape characteristics improve, enhancing the range resolution.

Prior work on transducer vibration control and enhancing sensor operation can be classified into two broad approaches – hardware-based [1–5], and the addition of damping pulses [6–9]. Hardware-based approaches achieve passive damping by adding external components [2, 3, 5]. The added passive circuits require system models during the design phase. Otherwise, the inserted components need manual tuning. This method is ineffective,

especially when part-to-part component variations can degrade the amplitude of the emitted pressure wave. Active damping has been studied for linear-mode transmitter drives [1] and switched-mode transmitter drives [4]. In both cases, an open-loop operation proved sufficient to achieve desired results if the excitation and damping pulses are applied with precise timing.

In [6], model-based command shaping is utilized to achieve damping. The resulting design produced a non-oscillatory unipolar excitation signal that significantly limits the amplitude of the generated pressure wave. Recent techniques append phase-shifted damping pulses to u_T after the application of excitation pulses [7–9]. These studies impose highly specialized pulses onto the transducer using laboratory instrumentation (i.e. waveform generators feeding power amplifiers for transmitter realization and conditioning amplifiers feeding digital oscilloscopes for receiver realization), adjusted to demonstrate reduced burst duration. Pulse train design parameters include: the shape, amplitude, and the number of pulses in each pulse group; the number of pulse groups; and the time delay between pulse groups. Procedures for selecting pulse train parameters are not discussed in these references. The damping mechanism is analyzed in [7] using second-order models, but the relevant case of transducer + drive circuits with higher-order dynamics studied in this research is not considered. Phase-shifted damping pulses have two distinct applications as clarified by [8]. The voltage excitation applied to a transducer can be designed to emit a temporally short burst of output pressure p_T; the excitation applied to the transducer can generate an input pressure to produce a temporally-short burst of output voltage at the receiver y_R.

The article [10] studies the intentional application of excess phase-shifted pulses resulting in the creation of a second pressure burst with a detectable null. The double pressure burst method improves the detection accuracy but degrades the FUT's performance metrics. The experimental systems studied in these references differ. The systems in [8] and [11] consider separate transmitting and receiving transducers with no reflectors; [7] focuses on the behavior of a transmitting transducer with no reflectors; [9] focuses on a transceiving

transducer used to detect echoes from one reflector, and [12] considers the measurement of airflow using separate transmitting and receiving transducers.

Note that the vibration control algorithms developed for ultrasonic sensors also apply to vibrotactile actuators. The linear resonant actuator is a commonly used vibrotactile actuator that provides tactile feedback to a user [13]. The actuators are present in smartphones and vehicles and produce a short duration vibration to alert the user; an example is the vibrations produced by a smartphone in response to the touch of a screen. Vibrotactile applications have resonant frequencies in the range of 100s of Hz, unlike ultrasonic sensing, where the resonant frequency is above 20 kHz. The generation of short-duration vibrations with sufficient amplitude for human perception is a feature of interest for several vibrotactile applications, an aspect addressed by the algorithms developed in this research.

2.2 3-D Ultrasonic Imaging

The emission of a pressure wave results in the dispersion about the transducer's normal and is called the main lobe. The operating region in Figure 1.1 illustrates this aspect. For the pulse-echo operation mode, the reflected power is received from objects within the main lobe of the transducer. When the system only has a single transmitter and a single receiver, y_R contains echoes produced by objects $(1,\ 2,\ 3)$ of Figure 1.1, but details characterizing the angular position of the reflector are not available in the signal y_R. Consequently, only the radial position of the echo can be extracted and corresponds to the ToF estimate for each reflector. This aspect is clarified in the example of Figure 2.1, where the angular position of the reflectors is unknown. Utilizing several closely-spaced transducers allows the determination of the radial distance and the bearing angles – azimuth and elevation of the reflectors.

Algorithms for determining the 3-D positions of reflectors can broadly be divided into – multilateration [14–19] and phased-array techniques [20–26]. Multilateration methods utilize transducers in a special arrangement – ring in [15–17, 19] and triangular in [14,

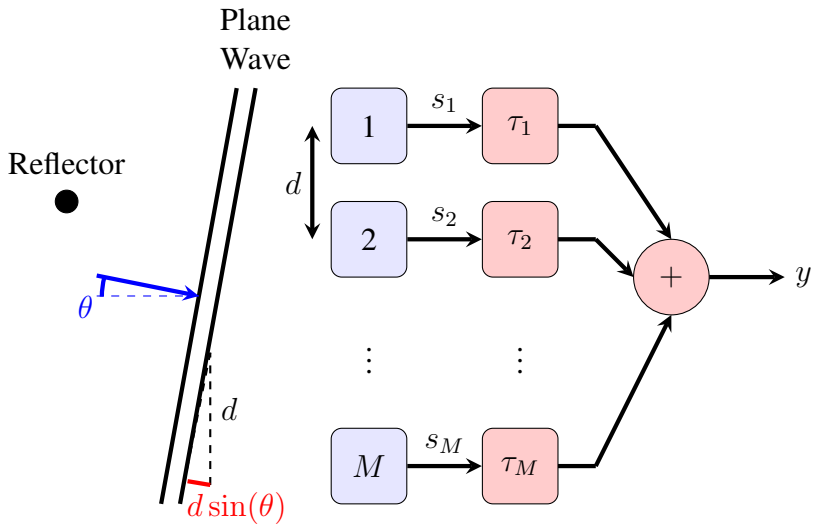

Figure 2.2: Schematic representation of an array of $1, \ldots,$ M elements receiving echoes from a reflector in the scene. The delay blocks $\tau_1, \ldots,$ τ_M and the summing junction producing the output signal y illustrate the phased array mode of operation. d is the inter-element separation for a linear array of reflectors, and θ is the arrival direction of pressure waves.

18]. Echo processing at each receiver element in the array results in a round-trip distance estimate traveled by the pressure waves between the transmitter and each receiver element after reflecting off from the objects in the scene. For objects located away from the array's normal, the distance estimate is different at each reflector. Figure 2.2 clarifies this aspect for a uniform linear array of receiver elements with an inter-element separation of d. The scene consists of a reflector located at an angle of θ with respect to the array's normal axis and generates plane waves. The sensor array consists of M elements, which simultaneously capture the incoming waves. As the reflector is located at an offset, the plane waves arrive at different instants. In the example, sensor element 1 is the first to receive waves. The plane waves travel an extra distance of $d\sin(\theta)$ to reach sensor element 2, resulting in the delayed arrival of pressure waves at the element. Sensor element M will be the last to receive waves as the pressure waves travel an extra distance of $(M-1)d\sin(\theta)$.

The objective of multilateration techniques is to combine the plurality of range estimates to determine the range and bearing of the reflector's position, which results in a tight

dependence on the transducer array's geometry as explicit round-trip formulas need to be derived. Since multiple range measurements need to be processed simultaneously, a range association step needs to occur. This step is the issue of associating which echoes on different receivers correspond to one another and ultimately to the same physical reflector. An incorrect association of echoes between reflectors can yield significant errors and is discussed in [14]. The research suggests radial and angular separation distances between reflectors to overcome correspondence ambiguity problems. Mechanical motion is used in [15, 19] to obtain pulse-echo measurements from different vantage points. Although detection improves and the correspondence ambiguity problem is resolved, the hardware cost and complexity increase. But any motion of the reflectors in the scene can result in estimation errors. Also, the sensor throughput reduces as the sensor has to move to a new mechanical configuration to acquire a snapshot of the scene.

On the other hand, phased array techniques (beamforming) improve the detection robustness but at an increased computation cost. Figure 2.2 also illustrates the array processing scheme. The sensor elements simultaneously receive the plane wave represented by the signals $s_1, \ldots, s_M$. The output y in the phased array mode of operation is given by

$$y = \sum_{m=1}^{M} s_m(t - \tau_m) \tag{2.1}$$

where $\tau_1, \ldots, \tau_M$ are the delays applied to the signals $s_1, \ldots, s_M$, and for a uniform linear array of elements

$$\tau_m = \frac{(m-1)d\sin(\theta)}{v_{sound}} \tag{2.2}$$

The signal y has maximum power when the time delays correspond to the arrival direction of the echoes, which is also the bearing angle of the reflectors. Although the delays are applied digitally, phased array processing has the effect of steering the sensor array mechanically to be sensitive to signals from a look direction. A search in the region of interest by

varying the angle θ (time delays τ_m) in Equation 2.2 determines the directions in which the maxima occur. Several search-free techniques exist but are limited to specific receiver array geometries [27].

Phased array techniques for air ultrasonic sensing applications have been explored only recently due to the availability of small-sized micromachined electrostatic microphones [20, 22, 24–26]. Transducer array design requires care, as spurious artifacts called grating lobes can occur during processing. This phenomenon arises due to the spatial separation between the transducer elements and is avoided with a small inter-transducer separation, typically, $< \lambda/2$, where λ is the wavelength of the pressure wave [28–30]. In air-based ultrasonic applications, as the wavelength is between 4–14 mm, the development has been limited mainly because of the transducer size.

Two possible phased-array implementations exist – a single transmitter with multiple receivers [23–25], and multiple transmitters with multiple receivers [20, 22, 31]. In [20] two dedicated linear FUT arrays are used, one for transmission and one for reception, each with a different inter-transducer separation. Grating lobe artifacts are canceled in the transmit-receive radiation pattern due to the array design. However, the usable field of view reduces. The sensor array presented in [31] utilizes a 64 element FUT array. A 3-D printed waveguide routes pressure waves between the transducer's aperture that is large to smaller outlets of a rectangular grid to satisfy the inter-element separation distance of $< \lambda/2$. As the waveguides are reverberant, substantial loss in signal amplitude occurs due to internal reflections and wave propagation through the printed part. Additionally, the noise floor level of the beamformer output is higher, reducing the overall sensitivity of the sensor array. Moreover, 3-D printing requires extensive post-processing due to the debris in the waveguide and the non-uniform surface of the printed part.

Several recent publications explore the use of a receiver array consisting of low-cost micromachined microphones [24–26]. To break the spatial periodicity, a random inter-element separation between the microphones is utilized. Designs with 32 elements [24],

and 36 elements [25, 26] are proposed. Although the grating lobe artifacts are suppressed, [28] suggests an increase in the noise floor level of the beamformer's output. Moreover, a large size array increases the overall cost of the analog signal chain as data from each element requires a dedicated path. The digital processing costs also increase as phased array techniques require complex math matrix computations. The articles employ graphic processing units to perform computations, increasing the overall sensor system cost and power budget. Also, the articles employ a wideband transmitter to emit pressure waves and focus on the array design aspects.

2.3 Stiffness Estimation

Stiffness estimation in prior research work utilizes a combination of position measurements along with tactile sensor arrays installed on the jaws of grippers [32–35]. A multi-degree of freedom gripper mechanism is used in [32, 33, 36], where the gripper jaws resemble a human finger. The finger-like mechanisms have multiple links and are actuated by a tendon-pulley transmission. Position measurements are obtained through encoders on the gripper or through a camera in the workspace in [33, 34]. Tactile sensor arrays significantly increase the overall system cost and complexity due to additional signal processing. As noted in [37–40], tactile sensor arrays have actuation zones, and obtaining reliable and repeatable measurements is challenging. They are also susceptible to hysteresis and have a slow response time. The use of overhead cameras increases complexity due to image processing software and results in low accuracy of stiffness estimation. A special feature of [32, 33, 36] is the underactuation due to the transmission mechanism, which results in a coupled motion of the finger links. Underactuated systems are increasing in popularity due to the shape adaptation feature during grasping events and is also explored in this dissertation.

Prior articles employing machine learning use experiments to generate datasets to perform classification of objects [33, 35]. In [33], a measure representative of the stiffness

is used to classify objects into four categories ranging from low to high linear stiffness (150 – 2000 N/m). The study also allows a change in the object shape in addition to a change in stiffness during data collection. It is possible for the classifier to exploit shape-related features during the prediction process, resulting in high classification accuracy. In [35], the objects are classified into two categories – as hard or soft. In both studies, the classifiers are trained on datasets containing a small number of items (about 50 items) which increases the tendency to overfit during the training step [41, 42].

Datasets using experimental measurements have several advantages. They do not require a knowledge of the system's physics, which can be challenging to develop for systems with multiple degrees of freedom operating under friction with complex transmission mechanisms. However, an experimental approach must limit the amount of data collected from the hardware, as it is a time-consuming and expensive exercise requiring human intervention [43]. Moreover, it is possible to overuse the experimental hardware during data collection. Additionally, manufactured items have a tolerance associated with each component present in the system. A regressor trained via experiments on one hardware may not achieve a similar level of performance on another hardware. A simulation approach to dataset generation for training the regressor can overcome many of the shortcomings of experimental data collection [41–43].

2.4 Unique Contributions of This Research

The algorithms developed in this research emphasize reducing the overall cost, system complexity, and operation on resource-constrained embedded devices. The research contributes to the body of knowledge in the following ways:

Vibration Control of Transducers:

1. Develops a generalized time-optimal control framework to enhance the operation of transmitting Flexural Ultrasonic Transducer (FUTs) fed by driver circuits. Extends the time-optimal framework to enhance the operation of receiving FUTs.

2. Develops model-free algorithms to address residual vibrations – transmitter enhancement that accelerates damping and a receiver enhancement through a subtractive masking process.

3. Demonstrates enhancements to the minimum range and range resolution through accelerated damping of FUTs. Provides a detailed comparison of the schemes in item 1.

4. Develops a Pulse Width Modulation (PWM) synthesis algorithm based on superposition principles for bench realization using an off-the-shelf Microcontroller Unit (MCU).

5. Develops Nonlinear Programming Problem (NLP) based numerical methods to generate solutions for high order time-optimal control problems.

3-D Ultrasonic Imaging:

6. Designs a low-cost ultrasonic sensor consisting of a small number of elements for the detection of reflectors in 3-D space.

7. Identifies system design requirements – for the sensor, analog signal chain, and digital processing.

8. Develops a high throughput processing algorithm. Fully embedded operation on a low-cost MCU achieves high update rates comparable to vision systems.

9. Develops a 2-D peak interpolation algorithm.

10. Compares sensor array performance with different beamformers.

Stiffness Estimation:

11. Develops a bio-inspired approach using a squeeze test to estimate the stiffness of objects for a single degree of freedom gripper using regression. Extends the stiffness

estimation approach to an underactuated finger mechanism driven by a tendon-pulley transmission.

12. Leverages machine learning to determine the stiffness of objects under grasp with a sparse sensor suite (uses only position and current sensor measurements instead of expensive tactile sensor arrays). Exposes the ability of regressors to overcome nonlinear effects due to dry friction, gripper actuation commands, and tendon-pulley underactuated transmissions.

13. Training for machine learning occurs on datasets generated through simulations. Trained regressors are evaluated on a representative single degree of freedom experimental hardware. Dataset generation simulation program models dry friction in the mechanism.

14. Designs a stiffness apparatus to systematize the generation of linear stiffness for experimental data collection. Achieves linear stiffness regression for an underactuated finger system using an experimentally generated dataset.

2.5 Dissertation Outline

The remainder of this dissertation is organized as follows. Chapter 3 presents a systems perspective of the ultrasonic sensing system for the pulse-echo mode of operation. The chapter provides details of the transducer model, the transmitter driver, and the receiver system. Chapter 4 studies the time-optimal transmit optimization problem. The chapter describes the problem formulation, the implementation of the NLP solver to generate numerical solutions, and the PWM synthesis algorithm. Chapter 5 extends the framework developed in Chapter 4 to receiving FUT systems. The tradeoff between the transmit and receive optimization schemes and a robustness analysis is presented. Chapter 6 discusses simple model-free algorithms to enhance the operation of transmitter FUTs by applying damping pulses and receiver FUTs through a masking signal. Chapter 7 outlines the design

of a low-cost sensor array and the processing algorithm based on beamforming to detect multiple reflectors in 3-D space. Chapter 8 discusses the stiffness estimation of an object through a bio-inspired squeeze test procedure. Machine learning-based regressors are trained using simulation data and evaluated on a real-world single degree of freedom experimental hardware. Chapter 9 extends the squeeze test approach to an underactuated tendon-pulley finger mechanism. The chapter outlines a stiffness apparatus for experimental data collection and develops stiffness regressors using the experimentally generated dataset. Chapter 10 concludes the dissertation with a summary of the completed work and topics for future research.

CHAPTER 3

ULTRASONIC SENSING SYSTEM ANALYSIS

This chapter presents a systems perspective of the ultrasonic sensing system for the pulse-echo mode of operation. The chapter discusses a new transducer model that captures the operation of the transducer under both transmission and reception modes. The transformer fed transducer drive circuit used in the research is studied, and the design requirements for the receive signal chain are summarized. The chapter concludes with a description of the data acquisition system used in the experimental work.

3.1 Hardware System Overview

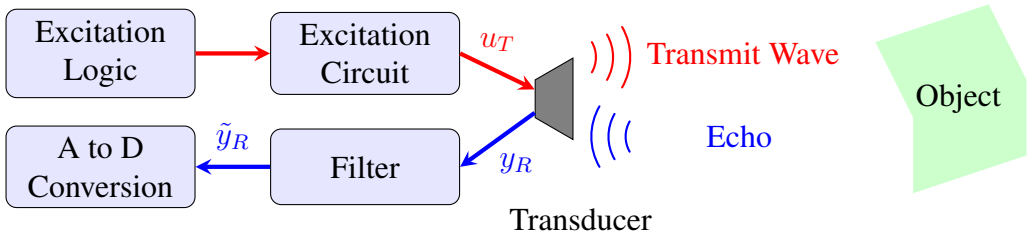

Figure 3.1: Ultrasonic sensing system architecture.

Figure 3.1 shows the architecture of an ultrasonic sensing system. It consists of a transmit path for emitting a pressure wave from a FUT and a receive path to capture and process echoes reflecting off from objects in the scene. The excitation control block issues a time-gated excitation signal and controls switches of an excitation circuit. The excitation circuit includes components, such as a transformer, to improve the power transfer to the FUT. In low-cost applications, PWM peripherals of a MCU implement the excitation logic and realize the desired voltage excitation signal by operating the transistor switches of the excitation circuit. Echoes from reflectors in the scene produce electrical voltages with significantly smaller amplitudes. The signals pass through a bandpass filter designed based

on the resonant frequency of the FUT. An Analog to Digital Converter (ADC), also located within the MCU is used to sample the analog signal for digital processing. The ranging specifications of the system and the desired SNR level of the voltage signals determine the analog filter's gain. The combined use of the transmit and receive paths determine the ToF of echoes, where the start of transducer excitation triggers the data logging process.

3.2 Transducer Model

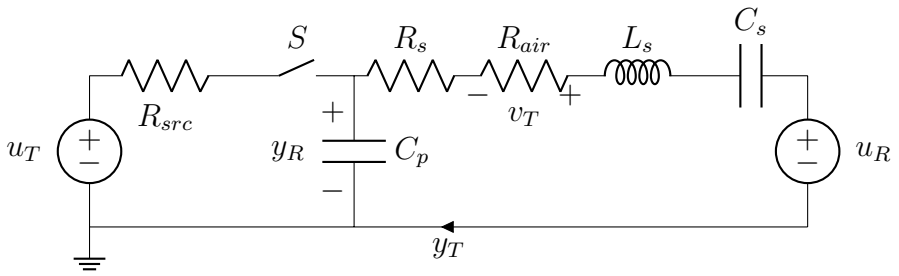

Figure 3.2: Lumped electrical equivalent circuit model of a FUT.

Figure 3.2 shows the electrical equivalent circuit representation of a narrowband FUT. An electrical representation is convenient because a transducer has access only to the electrical terminals; a voltage excitation launches pressure waves, and incoming echoes generate voltages. The model is inspired by the standard Butterworth Van Dyke (BVD) model [44]. The lumped circuit representation is useful and sufficient for sensing system designers, while for a transducer designer, a detailed partial differential equation model of the transducer is essential. The lumped model presented above includes the operation of a transducer during reception and the loading presented by the environment. The oscillatory branch of the transducer is modeled by the series branch components R_s, R_{air}, L_s, and C_s. The values of L_s and C_s determine the resonant frequency f of the transducer. The series resistance R_s represents the damping inherent within the transducer due to the construction. R_{air} represents the electrical equivalent loading presented by air (the radiating medium) on the oscillatory branch. The parallel capacitor branch C_p models the dielectric property of a FUT, as the piezoelectric material is bonded to a metal plate in a FUT. u_T and u_R represent

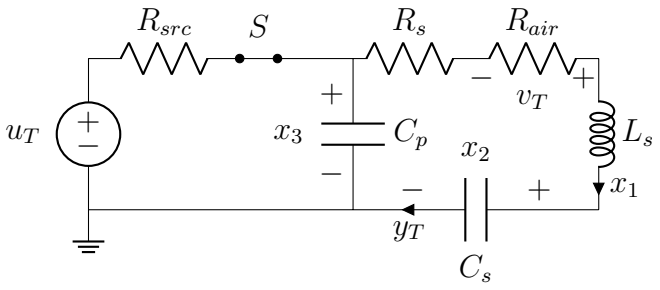

Figure 3.3: Equivalent circuit model of the FUT during transmission. x_1 is current through L_s, $x_2,\ x_3$ are the voltages across C_s and C_p.

the input voltage, and y_T and y_R are the output current and the output voltage during the transmission and reception operations. v_T is the voltage across R_{air} and R_{src} models the resistance of the source. The model is applicable even for an electrostatic transducer, where C_p models the capacitance between the electric foil and the transducer's backplate.

Transmission:

During transmission, $u_R = 0$ and the switch S is closed, resulting in the voltage u_T appearing across the transducer. Figure 3.3 shows the circuit during transmission. Let the state variables x_1 be the current through L_s and $x_2,\ x_3$ be the voltages across C_s and C_p. At resonance, u_T appears across R_s and R_{air}. For a well-designed transmitting transducer, $R_s < R_{air}$, maximizing the power output to the radiating medium. The voltage v_T developed across R_{air} is a scaled version of the acoustic pressure p_T output from the transducer. Equivalently, the current x_1 is a scale factor of the voltage v_T across R_{air}. Therefore, the value of $x_1 = y_T$ can be viewed as a scaled version of the pressure p_T released from the transducer. The state equations of the FUT during transmission with

$\mathbf{x} = [x_1,\ x_2,\ x_3]^T$ are given by

$$\dot{\mathbf{x}} = \begin{bmatrix} -\frac{R_s}{L_s} & -\frac{1}{L_s} & \frac{1}{L_s} \\ \frac{1}{C_s} & 0 & 0 \\ -\frac{1}{C_p} & 0 & -\frac{1}{C_p R_{src}} \end{bmatrix} \mathbf{x} + \begin{bmatrix} 0 \\ 0 \\ \frac{1}{C_p R_{src}} \end{bmatrix} u_T$$
$$y_T = \begin{bmatrix} 1 & 0 & 0 \end{bmatrix} \mathbf{x} \tag{3.1}$$

Reception:

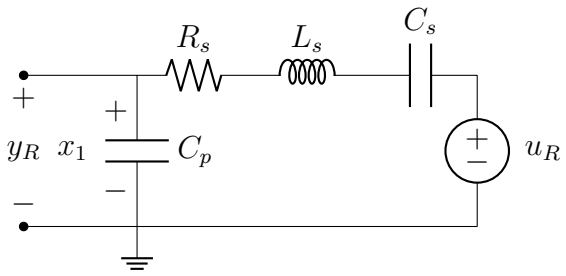

Figure 3.4: Equivalent circuit model of the FUT during reception. x_1 is voltage across C_p and $x_2 = \dot{x}_1$ (not shown). For the RXOPT formulations discussed in Chapter 5, x_5 and x_6 are used instead of x_1 and x_2.

During reception, the switch S is opened, and u_R is the electrical equivalent input voltage induced at the FUT due to the incoming pressure wave p_R. Let x_1 be the voltage generated across the capacitor C_p. y_R is the voltage across the FUT. It is also the input to the receive signal chain, which normally has high input impedance. The state variable $x_2 = \dot{x}_1$ for convenience. x_2 represents a scaled version of current through C_p. The state equations of the FUT during reception with $\mathbf{x} = [x_1,\ x_2]^T$ are given by

$$\dot{\mathbf{x}} = \begin{bmatrix} 0 & 1 \\ -\frac{C_s + C_p}{L_s C_s C_p} & -\frac{R_s}{L_s} \end{bmatrix} \mathbf{x} + \begin{bmatrix} 0 \\ -\frac{R_s}{L_s} \end{bmatrix} u_R$$
$$y_R = \begin{bmatrix} 1 & 0 \end{bmatrix} \mathbf{x} \tag{3.2}$$

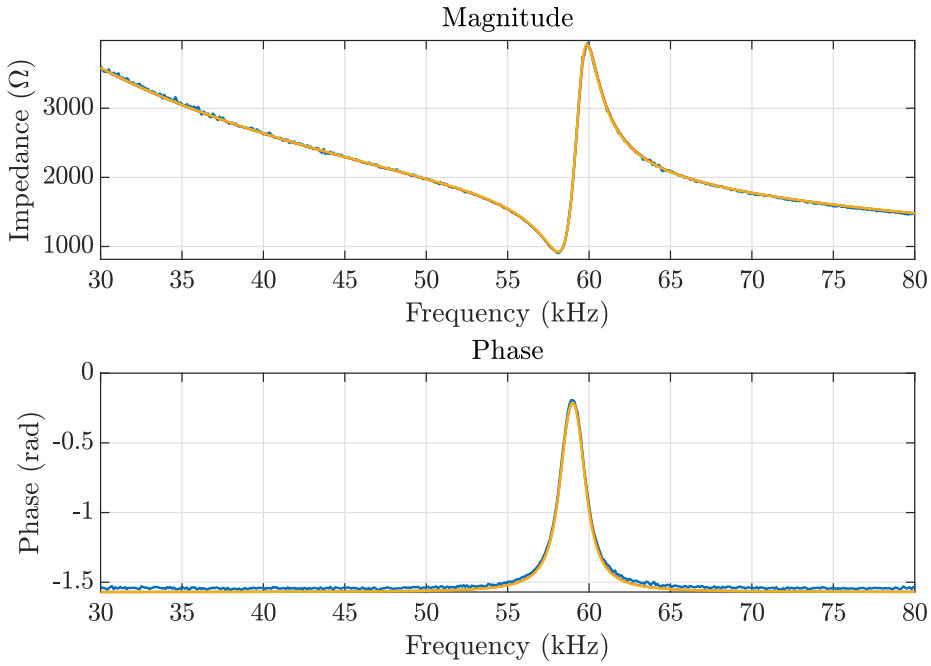

Figure 3.5: Complex impedance measurement data collected by the frequency response analyzer. Data fitting is performed through two nonlinear least squares curve fitting methods. (Measured data [—], data fitting method – 1 [—], data fitting method – 2 [—]).

As only R_s is present in the circuit, which is small, the damping of the FUT during reception is low; this maximizes the sensitivity of the echo generated due to the incoming pressure wave. It is interesting to note that during transmission, the FUT has a model order of 3, whereas, during reception, the FUT has a model order of 2.

3.2.1 Equivalent Circuit Parameter Estimation

The research uses a Murata MA58MF14-7N transducer having a center frequency of 58.5 kHz. The transducer can transmit and receive pressure waves. The equivalent circuit parameters are obtained by using a frequency response analyzer to collect the complex impedance measurement data and fitting the data to the transducer model presented in Section 3.2. The equipment applies electrical excitation to the FUT at several frequencies, and Figure 3.5 shows the impedance response of the transducer. Appendix A discusses the details of the experimental circuit and the procedure used during the data collection step.

Let the measured complex impedance data at the $n = 1, \ldots, N$ discrete frequencies

ω_n be given by $Z_n = A_n + jB_n$. From Figure 3.2 the transducer impedance estimate at frequency ω_n can be computed as

$$\begin{aligned} \hat{Z}_n = \hat{Z}(\omega_n) &= \left[R_s + j\omega_n L_s + \frac{1}{j\omega_n C_s}\right] || \left[\frac{1}{j\omega_n C_p}\right] \\ &= \hat{A}_n + j\hat{B}_n \end{aligned} \tag{3.3}$$

A nonlinear least-squares parameter estimation procedure inspired by [45] is used. An unconstrained nonlinear optimization solver with $g(x)$ as the cost function and x as the set of optimization variables is specified as $\min_x g(x)$. The cost function for the data fitting problem minimizes the error between the measured impedance and the estimated impedance at the ω_n frequencies. The optimization variables, i.e., $R_s,\ L_s,\ C_s$, and C_p, are the unknown model parameters of the transducer. Note that R_s includes the R_{air} component, and decomposition is not possible from the impedance response measurement data. Two different cost function formulations confirm if the parameter estimates converge to the same set of values.

Method 1: Minimization of impedance terms: The Root Mean Square (RMS) error corresponding to the real terms of the estimated and measured impedances, and the RMS error corresponding to the imaginary terms of the estimated and measured impedances, are minimized. The cost function is given by:

$$\text{Cost}(R_s, L_s, C_s, C_p) = \underbrace{\sqrt{\frac{1}{N}\sum_{n=1}^{N}(\hat{A}_n - A_n)^2}}_{\text{RMS error real part}} + \underbrace{\sqrt{\frac{1}{N}\sum_{n=1}^{N}(\hat{B}_n - B_n)^2}}_{\text{RMS error imaginary part}} \tag{3.4}$$

where $\hat{A}_n$ and $\hat{B}_n$ are computed from the optimization variables at the ω_n frequencies.

Method 2: Minimization of impedance magnitudes: In this method, the RMS error between the estimated and measured impedance magnitudes is minimized. The cost function

Table 3.1: Estimated Parameters for the Murata MA58MF14-7N Transducer

Parameter	Symbol	Method 1	Method 2	Units
Oscillatory Branch Resistance	R_s	1185.89	1185.93	Ω
Oscillatory Branch Inductance	L_s	133.16	135.91	mH
Oscillatory Branch Capacitance	C_s	55.72	54.59	pF
Parallel Branch Capacitance (Estimated)	C_p	1.41		nF
Parallel Branch Capacitance (Datasheet)		1.40		nF
Resonant Frequency (Estimated)	f	58.43		kHz
Resonant Frequency (Datasheet)		58.5		kHz

Only C_p and f are specified in the transducer datasheet.

is given by

$$\text{Cost}(R_s, L_s, C_s, C_p) = \sqrt{\frac{1}{N}\sum_{n=1}^{N}(|\hat{Z}_n| - |Z_n|)^2} \tag{3.5}$$

The unconstrained optimization solver `fminsearch` in MATLAB is used to determine the transducer parameters with either method. The termination tolerance is set to 10^{-6}. Through trial and error the initial guesses to each problem are set to $R_s = 500\ \Omega$, $L_s = 100$ mH, $C_s = 20$ pF, $C_p = 500$ pF. The estimated values are shown in Table 3.1. The quality of fit is determined by computing the Normalized Root Mean Square Error (NRMSE). For the measurement Z and the estimate $\hat{Z}$, the fit percent is given by

$$\text{Fit}(Z,\ \hat{Z})\ \% = \left[1 - \frac{||\hat{Z} - Z||}{||\hat{Z} - E(\hat{Z})||}\right] \times 100 \tag{3.6}$$

All N data points are used to compute the Fit % with the above expression. For the methods given by Equation 3.4 and Equation 3.5, the fit percent is 97.2% and 97.6% respectively, indicating a tight fit and a comparable performance as shown in Figure 3.5. The methods result in parameter values that are close to one another. Hence an average is computed from the estimated parameter set. Also, the estimated values for C_p and f agree with the datasheet values.

3.3 Transmit Drive Circuit

The drive circuit block in Figure 3.1 transfers the power from the source to the FUT. It consists of transistor switches connected to passive elements, such as inductors, capacitors, or transformers. Some common drive circuit topologies include the direct drive (shown in Figure 3.3), inductor-capacitor (LC) drive, capacitor-inductor (CL) drive, and transformer drive. The design parameters for the drive circuits can be selected by applying the maximum power transfer principle. From [46], for complex impedances, power transfer is maximized when $Z_{source} = Z^*_{load}$. The research develops algorithms primarily for the transformer-driven transducer circuit. However, the algorithms are also applicable to other drive configurations. Appendix B describes other drive topologies, the physics models, and the design formulas for selecting the drive circuit parameters.

3.3.1 Transformer Equivalent Circuit Model

A step-up transformer with a turns ratio of n is shown in Figure 3.6. Let v_1 and v_2 be the primary and secondary voltages. Based on [47], Figure 3.7 shows the equivalent circuit representation of the transformer in Figure 3.6. The transformer coil's magnetizing inductance at the primary is L_{m1}. The relationship between the transformer's secondary and primary coil inductances can be related by $L_{m2} = n^2 L_{m1}$. R_1 and L_{l1} are the resistance and the leakage inductance at the primary side. R'_2 and L'_{l2} are the resistance and the leakage inductance of the secondary referred to the primary side. They are both given by

$$R'_2 = \frac{R_2}{n^2},\ L'_{l2} = \frac{L_{l2}}{n^2}$$

where R_2 and L_{l2} are the actual resistance and leakage inductance at the transformer's secondary. v'_2 and i'_2 are the secondary voltage and current referred to the primary. The relationship between the actual voltage v_2 and the current i_2, and their referred counterparts

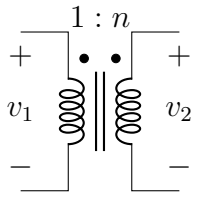

Figure 3.6: Step-up transformer representation.

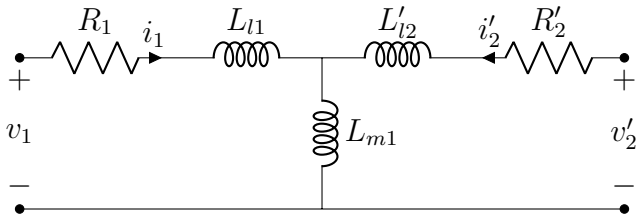

Figure 3.7: Equivalent circuit representation of the transformer.

are given by

$$v'_2 = \frac{v_2}{n},\ i'_2 = ni_2$$

where the secondary circuit components are referred to the primary side of the transformer. The representation of the transformer model in Figure 3.7 using a dependent voltage and a dependent current source is shown in Figure 3.8. The novel representation of the transformer through dependent sources is convenient because the isolation existing between the primary and the secondary terminals of the transformer is preserved. Also, analysis at the primary and the secondary side of the transformer can be performed independently.

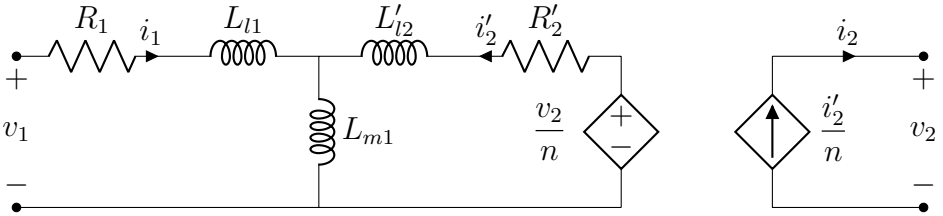

Figure 3.8: Dependent source model of the transformer.

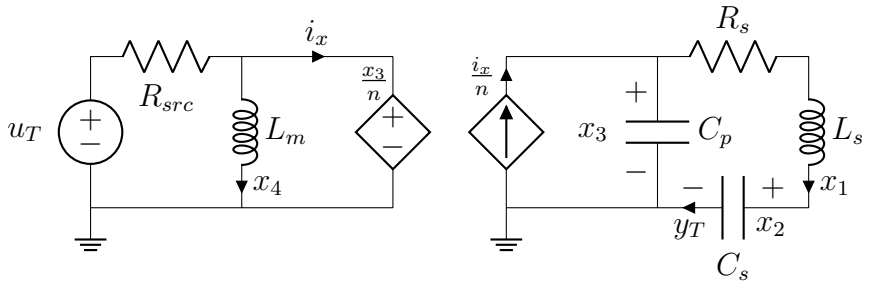

Figure 3.9: Transformer driven transducer circuit. Also, $L_m = L_{m1}$.

3.3.2 Transformer Driven Transducer System

Figure 3.9 shows the transducer circuit driven by the transformer. Modeling simplifications are introduced to the transformer model of Figure 3.8. The leakage inductances L_{l1} and L'_{l2} of the transformer are negligible compared to the coil inductance of the transformer and can be neglected; the model order of the system also reduces. For a well-designed transformer, R_1 and R'_2 are small to minimize copper losses in the transformer. R_{src} lumps the resistances $R_1,\ R'_2$ and the internal resistance of u_T. The subscript 1 in L_{m1} is dropped in Figure 3.9 for notational convenience; therefore, $L_m = L_{m1}$. The state equations of the transformer driven FUT system with $\mathbf{x} = [x_1,\ x_2,\ x_3,\ x_4]^T$ are given by

$$\dot{\mathbf{x}} = \begin{bmatrix} -\frac{R_s}{L_s} & -\frac{1}{L_s} & \frac{1}{L_s} & 0 \\ \frac{1}{C_s} & 0 & 0 & 0 \\ -\frac{1}{C_p} & 0 & -\frac{1}{n^2 C_p R_{src}} & -\frac{1}{nC_p} \\ 0 & 0 & \frac{1}{nL_m} & 0 \end{bmatrix} \mathbf{x} + \begin{bmatrix} 0 \\ 0 \\ \frac{1}{nR_{src}C_p} \\ 0 \end{bmatrix} u_T \tag{3.7}$$

$$y_T = \begin{bmatrix} 1 & 0 & 0 & 0 \end{bmatrix} \mathbf{x}$$

3.4 Baseline Excitation Signal

A voltage excitation is applied to the FUT to emit a pressure wave. The baseline excitation signal (BASE) consisting of n_e excitation cycles at the transducer's resonant frequency f is given by

$$u_T(t) = \begin{cases} +(-1)^i & , \ t \in \mathcal{T}_e \\ 0 & , \ \text{otherwise} \end{cases} \tag{3.8}$$

where the integer i is determined from

$$i = \lfloor 2(t - t_0)f \rfloor, \tag{3.9}$$

t_0 is the time instant at which transmission begins, $\lfloor \cdot \rfloor$ denotes the floor function, and the excitation cycle time intervals are given by

$$\mathcal{T}_e = \left[t_0, \ t_0 + \frac{n_e}{f} \right) \tag{3.10}$$

The signal $u_T(t)$ given by Equation 3.8 results in a rectangular wave excitation, which is suitable for the narrowband FUT used in this research. A bipolar excitation signal is preferable over a unipolar excitation because transducer oscillation occurs about an equilibrium position; bipolar excitation provides twice the peak emission pressure amplitude. Additionally, a DC excitation signal can deform the piezoelectric material permanently due to the high voltages appearing at the FUT's electrical terminals and should be avoided. The transformer drive is AC coupled and protects the FUT compared to the direct drive and LC drive configurations. Research in [7–9] applies a sinusoidal excitation signal to a narrowband FUT, which is not necessary; the excitation signal defined by Equation 3.8 is consistent with low-cost implementations. Also, previous research does not consider the driver stage between the source and the FUT.

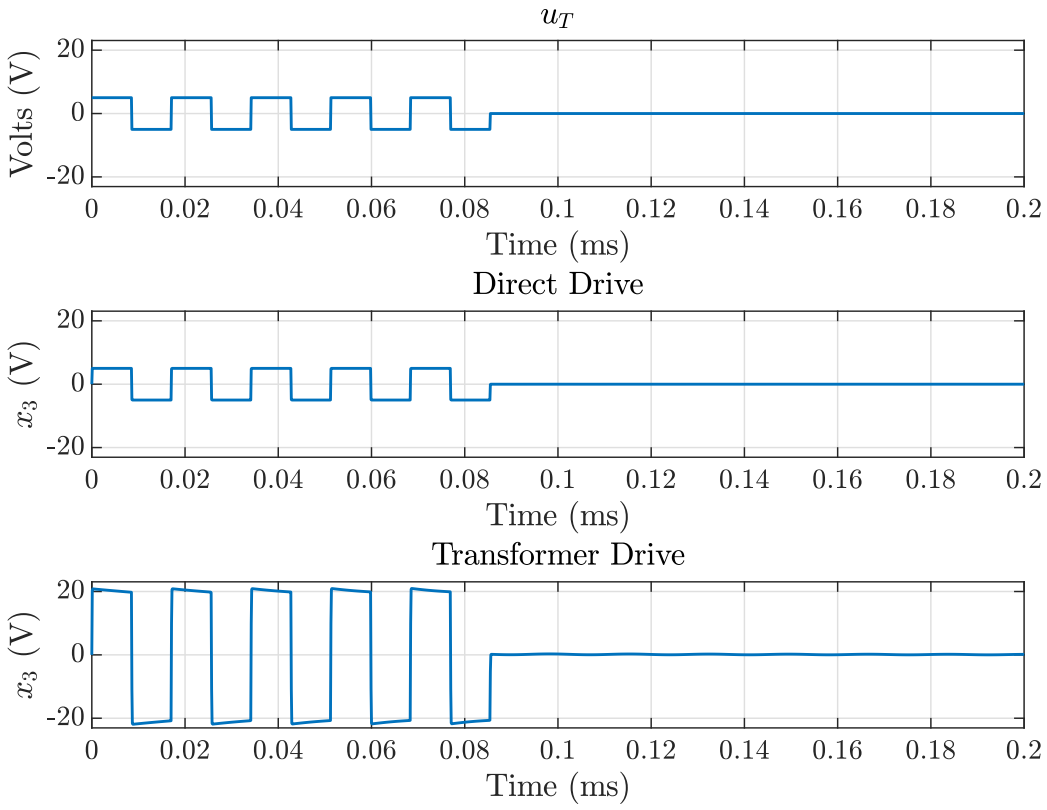

Figure 3.10: Simulation – voltage (x_3) appearing across the FUT.

3.4.1 Simulation

The simulations of the direct-driven and the transformer-driven systems are shown in Figure 3.10 and Figure 3.11. The voltage excitation signal u_T consists of a $n_e = 5$ cycle excitation applied at the resonant frequency f of the FUT with an amplitude of 5 V. The same excitation signal is applied to both configurations in the simulations. The source impedance is assumed to be purely resistive, i.e. $Z_{src} = R_{src}$. The estimated parameters of the transducer listed in Table 3.1 are used in the simulation. The parameters of the transformer are estimated using the procedure in Appendix D and the values are listed in Table D.1. The plots show the state variables x_1 corresponding to the oscillatory branch current representing the emission pressure amplitude and x_3 corresponding to the voltage appearing across the FUT's electrical terminals.

Direct-drive is the simplest topology connecting the source and the FUT as shown in

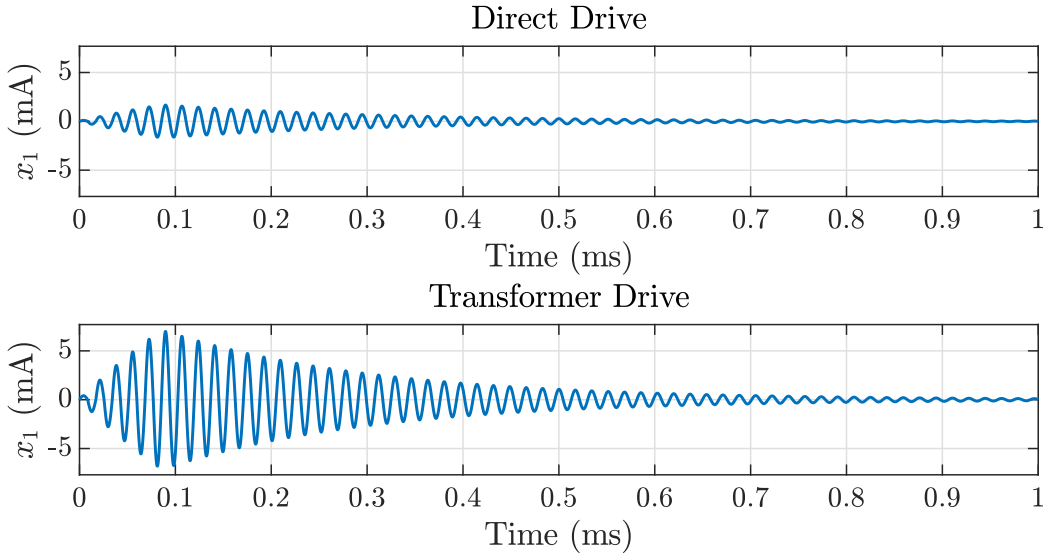

Figure 3.11: Simulation – current (x_1) through the oscillatory branch of the FUT. Current represents the emitted pressure.

Figure 3.3. The excitation signal appears across the FUT, i.e. $u_T \approx x_3$. For the same n_e, the emission pressure amplitude can be increased by increasing the amplitude of u_T. The transformer drive configuration (also LC and CL) can apply voltage excitations with higher amplitudes to the FUT. In Figure 3.10, x_3 has a higher value for the transformer-driven circuit and is scaled by the transformer's turns ratio. Consequently, a higher current x_1 flows through the oscillatory branch, resulting in an increased amplitude of the emitted pressure wave. Note that increasing n_e is another option to increase the amplitude of emission pressure wave; however, the increase obtained is lower when compared to hardware driver circuit solutions.

3.5 Receive Signal Chain

The voltage y_R developed at the receiving FUT in a pulse-echo trial depends on several factors – excitation voltage amplitude, number of excitation cycles, transmitter sensitivity, propagation losses, reflector curvature, material properties of the reflector, multi-path propagation, and receiver sensitivity. A custom analog signal chain is designed to filter and amplify the voltage y_R before analog to digital conversion. Since $f = 58.5$ kHz, a

bandpass filter with passband between 44 – 72 kHz is used. The amplification levels are determined by studying the propagation and attenuation experienced by the emitted signal y_T. Only a few off-the-shelf solutions exist but lack the flexibility a custom receive signal chain offers – cutoff frequency, gain, and synchronizing the operation of multiple receivers with the transmitter.

The emission characteristics are described by a sensitivity parameter. For a transmitter, it is the output pressure for an input excitation amplitude. This parameter is expressed in terms of Sound Pressure Level (SPL) and calibrated against the ANSI/ASA acoustic standard reference pressure with a magnitude of $P_{ref} = 20$ μPa. The SPL of an acoustic device is given by

$$\text{SPL}(r) = 20\log_{10}\left(\frac{P(r)}{P_{ref}(r_{ref})}\right) \tag{3.11}$$

where r is the travel distance, and r_{ref} is the reference distance at which the transducer is calibrated. The propagation of a pressure wave results in spreading losses and $P \propto r^{-1}$. In units of SPL, for a target at r, the pulse-echo response is given by

$$\text{SPL}(r) = \text{SPL}(r_{ref}) - 20\log_{10}\left(\frac{2r}{r_{ref}}\right) - \text{TS} \tag{3.12}$$

where TS is the reflector's target strength that varies with the reflector's shape. The nominal transmit SPL for a 58.5 kHz transducer is 110 dB at 30 cm for a 10 V RMS excitation signal, resulting in an emission pressure of about 6.5 Pa. Assuming a planar reflector, the target strength TS$= 10\log_{10}\frac{r^2}{4}$, based on [48]. The pressure at the receiver is about 0.5 Pa and undergoes a substantial attenuation in its amplitude.

Receiver sensitivity is the parameter that characterizes the voltage developed at the FUT

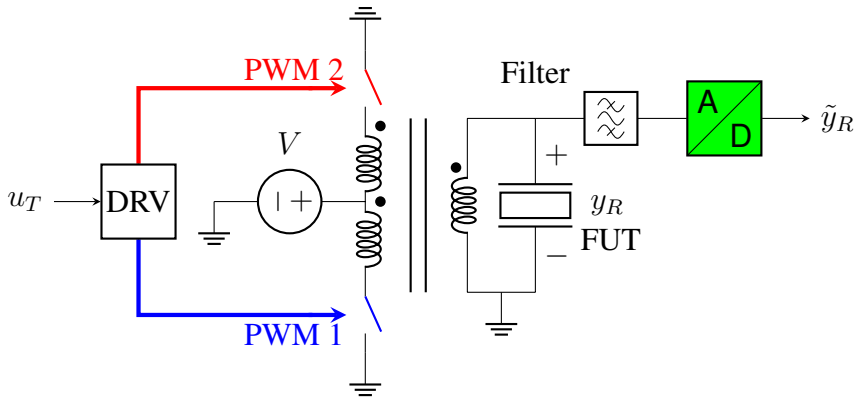

Figure 3.12: Center-tap transformer excitation circuit used to transmit pressure waves. The transmit and receive operations occur on the same device. The experimental system has access only to $\tilde{y}_R$.

for an input pressure. It is specified in dB and is given by

$$\text{Sensitivity}_{\text{dB}} = 20 \log_{10} \left(\frac{\text{Sensitivity}_{\text{V/Pa}}}{\text{Reference}_{\text{V/Pa}}} \right) \tag{3.13}$$

For a nominal receiver sensitivity of -70 dB with the $\text{Reference}_{\text{V/Pa}} = 10$ V/Pa, the voltage developed at the receiver is about 1.5 mV. A single-ended ADC is used and accepts an input voltage between 0 – 3V; the nominal amplification level for achieving full-scale voltage measurements is $\approx$ 1000 V/V. Several fixed gains selected through analog multiplexing support receiver operations up to a maximum range of 1.5 m. Compared to time-varying gains, multiple fixed gains have low complexity and are cost-effective. Appendix C discusses the hardware circuit implementation of the receive signal chain, which consists of several sub-circuits installed on a printed circuit board. The receiver board features an expandable design philosophy where multiple boards can be stacked to provide parallel signal paths, essential for the array mode of operation.

3.6 System Implementation

Figure 3.12 shows the implementation of the sensing system. The circuit uses the Murata MA58MF14-7N FUT and Subsection 3.2.1 discusses the parameter estimation details.

A TDK B78416A2232A003 center-tap step-up transformer drives the transducer and is switched by two Fairchild FQP30N06L MOSFETs connected in a push-pull configuration at the transformer's primary. The body diodes of the MOSFETs are not shown for convenience. The desired input signal u_T is converted to PWM signals which operate the switches through the driver DRV. Although the input signal u_T given by Equation 3.8 – Equation 3.10 can be synthesized without the PWM peripheral, the forthcoming chapters on the time-optimal operation of FUTs produce u_T excitation signals that have arbitrary duty cycles, which requires usage of the PWM peripheral. Also, the PWM peripheral is preferable as dedicated hardware circuits are present within the module to realize edge placements with high timing accuracies (≈10s of ns).

Transmission and reception occur at the same device; both the excitation applied to the transducer and the echo-induced voltage signals developed at the transducer pass through the high gain bandpass filter. y_R is the voltage input to the receive signal chain by the FUT, and $\tilde{y}_R$ is the voltage after filtering and amplification. Appendix C discusses the implementation of the filter circuit. An off-the-shelf evaluation module LAUNCHXL-F28379D from Texas Instruments is used, which has an onboard Texas Instruments TMS320F28379D MCU. The embedded software is executed on the MCU which generates the two PWM signals and acquires the amplified analog voltage signal using the ADC peripheral. The experiment control and data acquisition occur through a serial communication link between the MCU and a host computer. For convenience, Table 3.2 summarizes all the system parameters listed in Table 3.1 and Table D.1.

The signals PWM 1 and PWM 2 are complementary, resulting in the following operating modes:

- PWM 1 = low, PWM 2 = low: As no current will flow through the transformer coils, the voltage induced at the transformer secondary is zero.
- PWM 1 = high, PWM 2 = low: Current flows through the bottom coil of the transformer's primary, inducing a positive voltage at the secondary.

Table 3.2: Summary of Experimental System Parameters for Ultrasonic Sensing

Parameter	Symbol	Value	Units
Transducer Frequency	f	58.4	kHz
Transducer Period	–	17.1	μs
Speed of Sound	v_{sound}	340	m/s
Wavelength of Pressure Wave	λ	5.8	mm
Oscillatory Branch Resistance	R_s	1185.9	Ω
Oscillatory Branch Inductance	L_s	134.7	mH
Oscillatory Branch Capacitance	C_s	55.2	pF
Parallel Branch Capacitance	C_p	1.41	nF
Step-Up Transformer Turns Ratio [Full-Tap]	$1:n$	1:4.17	V/V
Step-Up Transformer Inductance [Full-Tap]	$L_m,\ L_{m1}$	164.1	μH
Step-Up Transformer Resistance [Full-Tap]	$R_1 + R_2'$	2.62	Ω
ADC Sampling Frequency	f_s	250	kHz
ADC Sampling Period	–	4	μs
ADC Resolution	–	12	bits
Receiver Passband Frequencies	–	44–72	kHz
Receiver Passband Gain [Chapter 4 – Chapter 6]	–	1170	V/V
Receiver Passband Gain [Chapter 7]	–	300	V/V
Transmitter Source Voltage	–	5	V
PWM Timebase Period	T_b	4.29	μs
Number of Excitation Cycles	n_e	3 – 10	cycles

- PWM 1 = low, PWM 2 = high: Current flows through the top coil of the transformer's primary, inducing a negative voltage at the secondary.

For completeness, PWM 1 = high, PWM 2 = high will also induce a zero voltage at the transformer's secondary, just like the case when both PWM signals are low; but switch dissipation losses are higher.

Circuits and the state space representation presented in Subsection 3.3.2 are valid even for the center-tap configuration of Figure 3.12 after minor adjustments to the parameter values. For the center-tap transformer (subscript "*ct*"), the primary coil inductance is $L_{m1,\,ct} = \dfrac{L_{m1}}{2}$, and the turns ratio is $n_{ct} = 2n$.

CHAPTER 4
TIME OPTIMAL ENHANCEMENTS FOR TRANSMITTING FLEXURAL ULTRASONIC TRANSDUCERS

4.1 Introduction

Figure 2.1 shows a pulse-echo trial with a 58.5 kHz narrowband FUT. The signal capture exhibits sustained residual vibration long after the excitation has ended, where the total transmission duration consists of two components – the excitation time and the decay time. Section 2.1 discusses how the signal $\tilde{y}_R$ contains two components – the pulse-imposed component and the echo-induced component. The focus of this chapter is on designing a FUT excitation scheme to achieve a rise and decay of the pressure wave in minimum time without compromising the amplitude of the transmitted pressure wave; effectively controlling the FUT's response due to the pulse-imposed component. The work contributes to the knowledge base in several ways. The time-optimal control problem determines the excitation signal minimizing the total transmit time. A step-up transformer fed FUT transmitter system is studied, and the system has fourth-order dynamics as discussed in Subsection 3.3.2. The production of a solution to the Optimal Control Problem (OCP) is non-trivial and requires Nonlinear Programming Problem (NLP) solvers; two NLP solvers are developed – orthogonal collocation and multiple shooting. Consistent with low-cost implementations, an algorithm to synthesize the excitation signal using PWM peripherals is described. Several experiments demonstrate the achieved reduction in the total transmission time, the minimum range, and the range resolution.

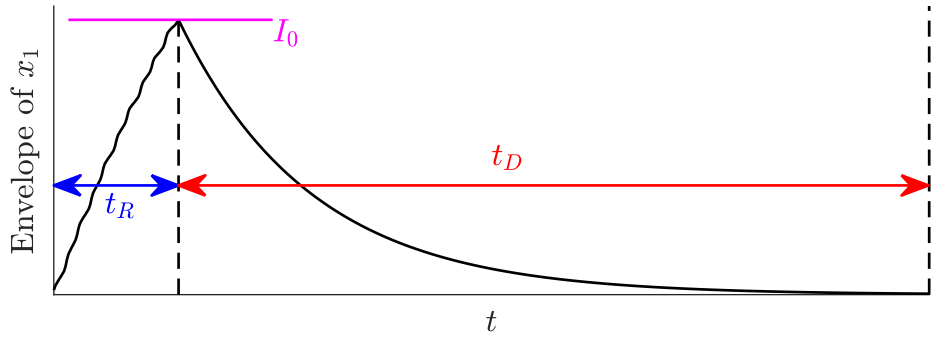

Figure 4.1: Illustration of the transmitter optimization problem.

4.2 Optimization Problem

Figure 3.12 shows the hardware topology of the FUT system, where the FUT is connected to both the transmitter and the receiver circuits. The state-space representation of the transformer-driven transducer is given by Equation 3.7. The excitation signal u_T is applied in an open-loop and is advantageous as additional sensors are not required and reduce the overall system cost and complexity. The downside is the need for an accurate system model, but fortunately, the model parameters do not change with time. Also, [1, 4] demonstrate that open-loop operation is sufficient if the excitation pulses are applied with precise timing.

Figure 4.1 motivates the optimization problem. The current waveform (state x_1) is of interest as its amplitude is proportional to the pressure wave emitted by the FUT as discussed in Section 3.2. In the diagram, the current envelope takes t_R to rise to a target level of I_0 in response to the excitation and t_D to decay down to equilibrium levels from the target level of I_0. Therefore, reducing the total transmission time $t_R + t_D$ allows the FUT to detect echoes earlier, while the specification of a target level I_0 allows the peak transmit pressure strength to be regulated. Additionally, minimizing the total transmission time is equivalent to reducing the length of the blind zone, as the range is the result of scaling time by the speed of sound. There exist two competing problem formulations.

- Formulation 1: Solve the optimization problem as two separate subproblems, where t_R is minimized in the first subproblem with a target current level of I_0, and t_D is

minimized in the second subproblem starting from a target current level of I_0 to achieve equilibrium.

- Formulation 2: Solve the optimization problem as a single equilibrium-to-equilibrium problem where the total time $t_R + t_D$ is minimized while also reaching the target level of I_0 at some intermediate time instant.

Analysis with second-order systems presented in [49] reveals that a small performance degradation in time optimality occurs when formulation 1 is used, but the computation costs with formulation 1 are substantially lower compared to formulation 2. Note that the solutions obtained through either formulation are expected to be different. The two subproblems of formulation 1 are:

Subproblem 1: Rise time minimization:

$$\begin{aligned} &\text{minimize } t_R \\ &\text{subject to } \dot{\mathbf{x}} = \mathbf{A}\mathbf{x} + \mathbf{B}u_T \\ &\quad |u_T| \leq V \\ &\quad \mathbf{x}(0) = \mathbf{0} \\ &\quad |x_1(t_R)| \geq I_0 \end{aligned} \tag{4.1}$$

Subproblem 2: Decay time minimization

$$\begin{aligned} &\text{minimize } t_D \\ &\text{subject to } \dot{\mathbf{x}} = \mathbf{A}\mathbf{x} + \mathbf{B}u_T \\ &\quad |u_T| \leq V \\ &\quad \mathbf{x}(0) = \mathbf{x}(t_R) \\ &\quad |\mathbf{x}(t_D)| \leq \epsilon \end{aligned} \tag{4.2}$$

The input applied to the system is constrained to the rail limits V. The initial conditions

for the decay time minimization subproblem are equal to the values at the end of the rise time minimization subproblem. ϵ is a small value around the equilibrium of the system. The above formulation applies to any choice of drive configurations shown in Figure B.2 with the system dynamics in Table B.2. Determining a closed-form solution to the OCP is challenging. Therefore, the solution to the system of equations is determined through numerical techniques.

4.3 Scaling of the Equation System

Examination of Figure 3.10 and Figure 3.11 shows that the values for the state variables of the equation system differ by several orders of magnitude, and the time scale is on the order of a few milliseconds. Before computing the numerical solution, the state variables, the input, and the time variable are scaled. This intermediate step improves the quality of the solution and the convergence of numerical solvers. Let a reference maximum for the state variable i, the input, and time be X_i, V, and T. The relationships between the scaled ($\mathbf{x}_s$, u_{Ts}, t_s; $\mathbf{A}_s$, $\mathbf{B}_s$) and the unscaled ($\mathbf{x}$, u_T, t; $\mathbf{A}$, $\mathbf{B}$) quantities are given by

$$\begin{aligned} \mathbf{x}_s &= \mathbf{S}^{-1}\mathbf{x}, \;\; \mathbf{S} = \text{diag}\left\{X_i\right\} \\ u_{Ts} &= V^{-1}u_T, \;\; t_s = T^{-1}t \\ \mathbf{A}_s &= T\mathbf{S}^{-1}\mathbf{A}\mathbf{S}, \;\; \mathbf{B}_s = T\mathbf{S}^{-1}\mathbf{B}V \end{aligned} \tag{4.3}$$

Suitable values for the scaling quantities can be determined through the maximum operating conditions expected during regular use. For the transformer driven system with 4$^{\text{th}}$ order dynamics, the values determining $\mathbf{S}$ are $X_1 = 15.73$ mA, $X_2 = 809.69$ V, $X_3 = 20.72$ V and $X_4 = 352.4$ mA. The values are obtained by exciting the system at the supply voltage $V = 5$ V and resonant frequency $f = 58.4$ kHz using 20 excitation cycles (maximum expected during regular use), resulting in $T = 20/f = 342.46$ μs.

4.4 Development of the Numerical Solver

The formulation in Section 4.2 is evaluated numerically. Two possible approaches exist to solve the OCP. The first approach is to apply the optimality principles, which results in the generation of a set of costate equations. Numerical solutions are generated for the combined system consisting of the plant dynamics equations, the costate equations, and the boundary conditions for the state + costate system. The second approach is more direct, which involves converting the problem formulation (dynamic equations) into a set of constraint equations using a discretization scheme. Optimization is then performed on the discretized problem.

The second approach presents several advantages and is preferred. The discretization scheme results in constraint equations describing the state trajectories and the control input, fed into a nonlinear programming problem. The costate equations for the optimal control problem do not need to be derived, unlike the former approach. Input constraints, an important practical aspect, can be easily introduced. A drawback, however, is that the resulting NLP system consists of a large number of constraint equations (about 1000) with a large number of optimization variables (about 30000), requiring computing capability during solution generation. Also, the solver can converge to a local minimum. Therefore, the solver's exit conditions need investigation to determine if the resulting solution is acceptable.

Numerical solutions for each subproblem described by Equation 4.1 and Equation 4.2 are generated by using two different direct optimization methods – Orthogonal Collocation and Multiple Shooting. The use of two approaches allows the verification of the generated optimal excitation signal u_T^*. A NLP takes the following form:

$$\min_x f(x) \qquad \text{subject to: } \begin{cases} g_{lb} \leq g(x) \leq g_{ub} \\ x_{lb} \leq x \leq x_{ub} \end{cases} \tag{4.4}$$

with cost function $f(x)$, optimization variables x having the limits $[x_{lb},\ x_{ub}]$, and inequality

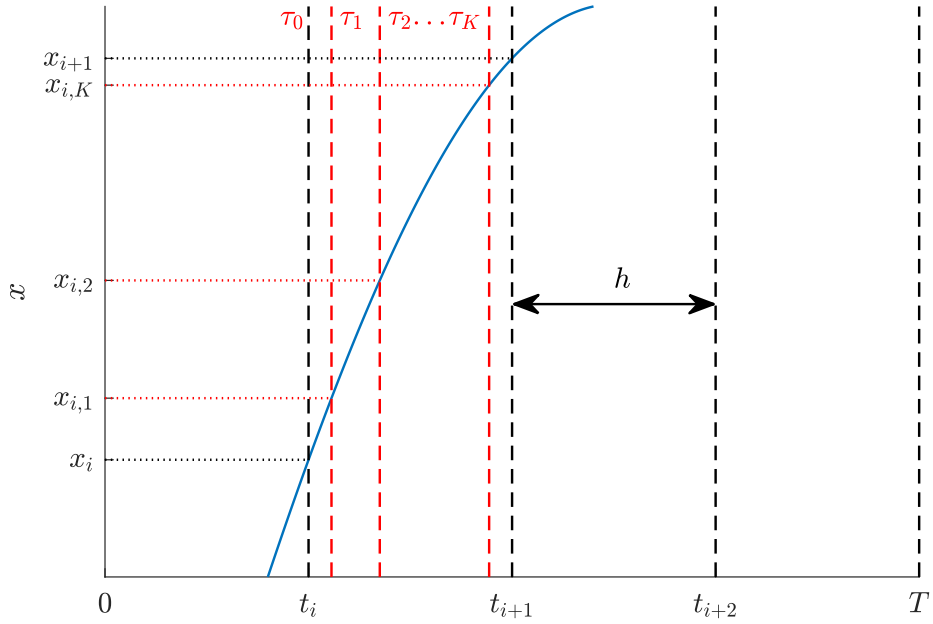

Figure 4.2: Collocation problem setup with fixed step-size h for interval i. The collocation points are denoted by $\tau_1, \ldots, \tau_K$.

constraints $g(x)$ having the limits $[g_{lb},\ g_{ub}]$. Inequality constraints are converted to equality constraints by setting $g_{lb} = g_{ub} = 0$; solvers automatically convert the zero in the equality constraint to a small value depending on the solver configuration. After discretization, the high dimension NLP is numerically solved using a constrained optimization problem solver, such as the open-source IPOPT solver or the FMINCON solver native to MATLAB.

4.4.1 Orthogonal Collocation

The system dynamics in the state-space representation is

$$\frac{dx}{dt} = Ax + Bu = f(x, u) \tag{4.5}$$

For notational convenience, assume a one dimension system. With higher-order systems, the same formulas apply after appropriate adjustments to the dimensions of the system's states x and the matrices A and B. Mathematical details for setting up the collocation problem are described in §10.1–10.3 of [50].

Figure 4.2 illustrates the discretization process. Consider a time duration T over which the solution needs to be computed. The total number of intervals is N, giving the fixed step-size $h = \frac{T}{N}$. Let the intervals be denoted by $i = 1, \ldots, N$. In each interval i of length h from $t_i \leq t \leq t_{i+1}$, a piecewise Lagrange interpolation polynomial of degree K is used to represent the state. The control input is assumed to be piecewise constant throughout the interval i. The Lagrange interpolation profile describing the state is given by

$$x(t) = \begin{bmatrix} l_1(\tau) & \ldots & l_K(\tau) \end{bmatrix} \mathfrak{X}_i \quad , \quad t_i \leq t \leq t_{i+1}, \quad 0 \leq \tau \leq 1 \tag{4.6}$$

where

$$\mathfrak{X}_i = \begin{bmatrix} x_{i,1} & \ldots & x_{i,K} \end{bmatrix}^T \tag{4.7}$$

Therefore, the time $t \in [t_i,\ t_{i+1}]$ can be specified as $t = t_i + h\tau$. The formula for $l_j(\tau)$ is given by

$$l_j(\tau) = \prod_{k=0, \neq j}^{K} \frac{\tau - \tau_k}{\tau_j - \tau_k} \tag{4.8}$$

τ_k are the interpolation points within each interval h, and $x_{i,1}, ...,\ x_{i,K}$ are the values of the state at the K interpolation points as shown in Figure 4.2. The Legendre roots of a degree K Gauss-Jacobi polynomial provides the lowest truncation error of $O(h^{2K})$ [50]. Let $\tau_1, \ldots, \tau_K$ be the K roots of the polynomial, which are also the K interpolation points (also known as collocation points). Let $\tau_0 = 0$. Define the matrices Y_i and M as

$$Y_i = \begin{bmatrix} x_i \\ \mathfrak{X}_i \end{bmatrix}, \quad M = \frac{dL}{d\tau} = \begin{bmatrix} \frac{dl_0}{d\tau}(\tau_1) & \ldots & \frac{dl_K}{d\tau}(\tau_1) \\ \vdots & \ddots & \vdots \\ \frac{dl_0}{d\tau}(\tau_K) & \ldots & \frac{dl_K}{d\tau}(\tau_K) \end{bmatrix} \tag{4.9}$$

Every element of M provides coefficients for the time derivative of the interpolation profile

for the states at the collocation points. For each interval, the collocation equations for the ODE are modeled as equality constraints given by

$$MY_i - hf\left(\mathfrak{X}_i, u_i\right) = 0 \tag{4.10}$$

Equality constraints apply at the end of one interval and the beginning of the next interval. They are given by

$$x_{i+1} - \begin{bmatrix} l_0(1) & \ldots & l_K(1) \end{bmatrix} Y_i = 0 \tag{4.11}$$

The constraint at $t = T$ can be specified as

$$\mathfrak{F} - \begin{bmatrix} l_0(1) & \ldots & l_K(1) \end{bmatrix} Y_i = 0 \tag{4.12}$$

where $\mathfrak{F}$ are the final conditions of the system. The initial conditions $\mathfrak{I}$ of the system at $t = 0$ can be specified as

$$x_{i=1} = \mathfrak{I} \tag{4.13}$$

Summary:

The time-optimal NLP problem with the collocation method after scaling the state variables and the time is given by

$$\begin{aligned} &\min_{u} \; T \\ &\text{subject to:} \quad \begin{bmatrix} MY_i - hf\left(\mathfrak{X}_i, u_i\right) \\ x_{i+1} - \begin{bmatrix} l_0(1) & \ldots & l_k(1) \end{bmatrix} Y_i \\ \mathfrak{F} - \begin{bmatrix} l_0(1) & \ldots & l_K(1) \end{bmatrix} Y_N \end{bmatrix} = \mathbf{0} \end{aligned} \tag{4.14}$$

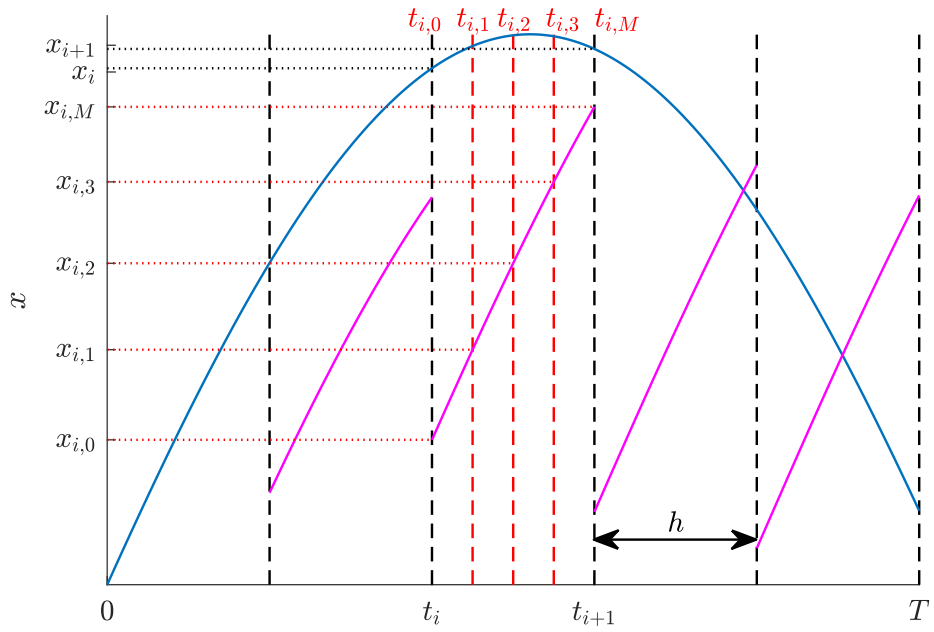

Figure 4.3: Multiple shooting problem setup with fixed step-size h and M sub-steps within each step. Trajectory after convergence [—] and initial trajectory [—].

where the optimization variables are

$$\mathbf{lb} \leq \begin{bmatrix} T & Y_i^T & u_i \end{bmatrix}^T \leq \mathbf{ub} \tag{4.15}$$

ub and **lb** are the upper and lower bounds of the system. For a scaled system the variable limits are $0 \leq T \leq 1$, $-\mathbf{1} \leq Y_i \leq +\mathbf{1}$ and $-1 \leq u_i \leq +1$. The initial and final conditions are given by $\mathfrak{I}$ and $\mathfrak{F}$. Note that T is also one of the optimization variables. This is because of time scaling and is discussed in Section 4.3. The value of the optimization variables in the first solver run can be random and lie anywhere within the variable limits. Convergence of the solver results in the optimal time duration T, the profile for the state, and inputs for the time horizon in which the solution is computed.

4.4.2 Multiple Shooting

Consider the system given by Equation 4.5. §9.1 – 9.4 of [50] discusses mathematical details of the multiple shooting problem. In the single shooting method, during the

integration of an initial value problem, there exists a tendency for the numerical routine to become unstable. Multiple shooting overcomes this issue by splitting the solution interval into smaller intervals, with numerical integration performed in these smaller intervals. The initial conditions for each interval are originally unknown. Equality constraints impose convergence at the interval boundaries resulting in the determination of the solution for the entire interval of interest. The numerical integration is at the heart of the multiple shooting method, and any integration method may be used – Forward/Backward Euler, Trapezoidal Rule, Runge-Kutta. The classic Runge-Kutta 4-step method is used, which gives a truncation error of $O(h^5)$. Figure 4.3 illustrates the multiple shooting method. T is the time duration over which the solution is computed and consists of N intervals. The fixed step size is $h = \frac{T}{N}$. Let the intervals be denoted by $i = 1, \ldots, N$.

To improve numerical accuracy of the IVP and the convergence of the NLP, M sub-steps are taken within each step h starting from x_i. This leads to an equivalent integration step-size of $\delta = \frac{h}{M}$. As shown in Figure 4.3, for the interval i, let the intermediate value of the M steps be $x_{i,j}$ at time $t_{i,j}$ for $j = 0, ..., M$. Perform the M-step numerical integration within the sub-interval i starting with an initial value $x_{i,0} = x_i$ and a step-size of δ. The Runge-Kutta integration steps are

$$\begin{aligned} k_1 &= f(x_{i,j}, u_i) \\ k_2 &= f\left(x_{i,j} + \frac{\delta}{2}k_1, u_i\right) \\ k_3 &= f\left(x_{i,j} + \frac{\delta}{2}k_2, u_i\right) \\ k_4 &= f\left(x_{i,j} + \frac{\delta}{2}k_3, u_i\right) \\ x_{i,j+1} &= x_{i,j} + \frac{\delta}{6}\left(k_1 + 2k_2 + 2k_3 + k_4\right) \end{aligned} \tag{4.16}$$

where $x_{i,j}$ is the state at the interval i and sub-step j, i.e. at time $t = t_{i,j}$. u_i is the value of the control input which is a constant throughout interval i. At the start of the NLP solver, the initial values for each interval may be assigned arbitrary values within the range of the state

variable. Figure 4.3 shows the state trajectory at the initial time interval. Upon convergence of the NLP, $x_{i,M} = x_{i+1}$ resulting in the determination of the state and the control profile for the entire interval. This condition is imposed through the equality constraint

$$x_{i,M} - x_{i+1} = 0 \tag{4.17}$$

The condition at the final time $t = T$ with $\mathfrak{F}$ as the final conditions of the system is specified by the equality constraint

$$x_{i=N,M} - \mathfrak{F} = 0 \tag{4.18}$$

The initial conditions $\mathfrak{I}$ for integration in the interval $i = 1$ starting at $t = 0$ is set as

$$x_{i=1} = \mathfrak{I} \tag{4.19}$$

Summary: The time-optimal NLP problem using the multiple shooting method after scaling the state variables and the time variable is given by

$$\begin{aligned} &\min_{u} \; T \\ &\text{subject to:} \quad \begin{bmatrix} x_{i,M} - x_{i+1} \\ x_{N,M} - \mathfrak{F} \end{bmatrix} = \mathbf{0} \end{aligned} \tag{4.20}$$

where the optimization variables are

$$\mathbf{lb} \leq \begin{bmatrix} T & x_i & u_i \end{bmatrix}^T \leq \mathbf{ub} \tag{4.21}$$

ub and **lb** are the upper and lower bounds of the system. For a scaled system, the variable limits are $0 \leq T \leq 1$, $-1 \leq x_i \leq +1$, and $-1 \leq u_i \leq +1$.

4.4.3 Solution Generation Settings

The solver equations with collocation given by Equation 4.14 and multiple shooting given by Equation 4.20 result in high dimension NLP implementations of the optimal control problem. It is convenient to exploit symbolic math capability in engineering software to implement the relevant equation systems. One open-source tool providing robust symbolic math capability is [51]. NLP solvers are gradient-based techniques. The tool in [51] allows machine precision gradients and Hessians to be determined through automatic differentiation, improving performance and convergence characteristics of the NLP solver. The time horizon T is divided into 4000 intervals in both methods. For a nominal transducer excitation duration of $T = 100$ μs, the edges can be placed with an accuracy of 25 ns, which is also the quantization achieved by the PWM peripheral of the microcontroller. In the collocation method, a 3$^{\text{rd}}$ order polynomial is used, and in multiple shooting 10 sub-steps are used. With the scaled system, the optimality and constraint tolerances of the solver are set to 10^{-6}.

4.5 Simulation Results

For the Baseline Excitation Signal (BASE) defined by Equation 3.8, the system response of the transformer driven transducer system is shown in Figure 4.4 – Figure 4.6. The experimental system parameters are listed in Table 3.2. The parameter values are common to both the simulations and the experiments. For BASE, a $n_e = 5$ cycle voltage excitation is applied at the FUT's resonant frequency f. State x_1 corresponds to the oscillatory branch and responds to the application of u_T. From Figure 4.5, the peak value of the current representing the emitted pressure wave is $x_1 = 6.513$ mA. State x_3 is measured across the electrical terminals of the FUT, which is also connected to the receive signal chain. After the excitation ends, residual vibrations can be observed beyond 0.1 ms, which can interfere with incoming echoes, and are undesirable as shown in Figure 2.1.

The system response with Time Optimal Transmit Excitation Signal (TXOPT) pre-

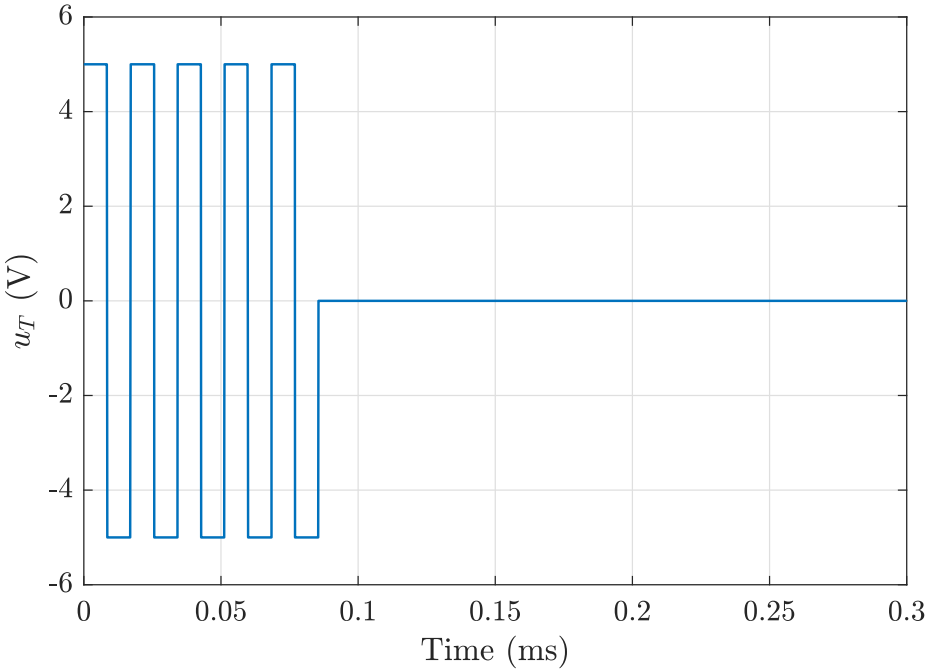

Figure 4.4: Input u_T for BASE.

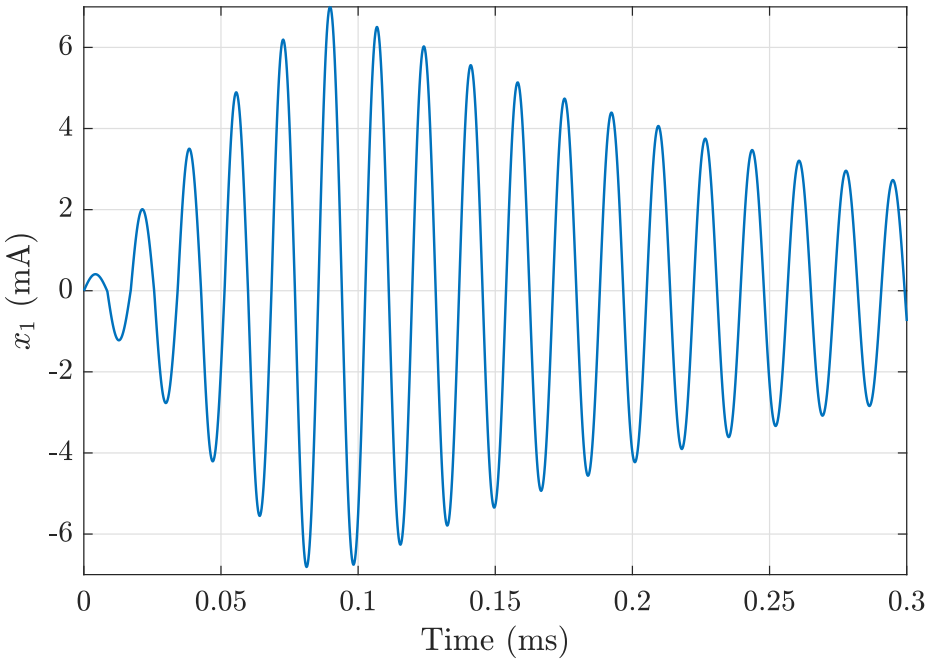

Figure 4.5: State variable x_1 for BASE. The peak current level is $I_0 = 6.513$ mA for the 5 cycle rectangular excitation.

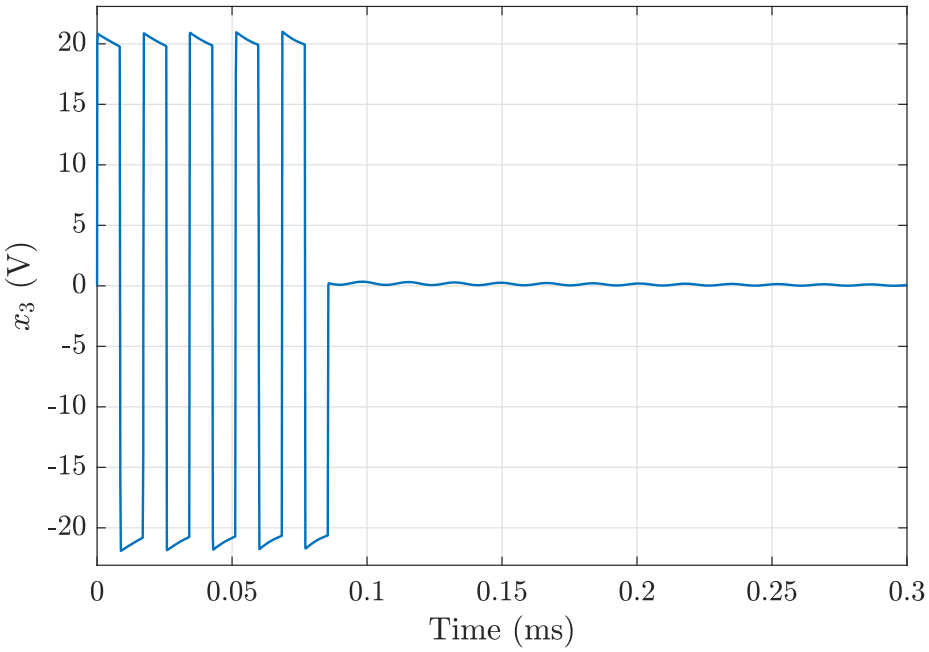

Figure 4.6: State variable x_3 for BASE measured at the transducer terminals.

sented in this chapter is shown in Figure 4.7 – Figure 4.9. The signal u_T^* is assembled by concatenating the results obtained by solving the subproblems given by Equation 4.1 and Equation 4.2. The concatenation time point is shown by the dashed line in Figure 4.7. To compare improvements between TXOPT and BASE strategies, the target current level I_0 is set to 6.513 mA, which is the peak current level obtained with BASE for $n_e = 5$ as shown in Figure 4.5. The u_T^* generated through the numerical evaluation of the optimization problem is shown in Figure 4.7. The optimal excitation signal has a bang-bang pattern switching between the rail limits of $\pm V$, consistent with the theory of time-optimal control for linear time-invariant systems [52]. The u_T^* signal evaluated to the same switching pattern with both the collocation and the multiple shooting approaches confirms the accuracy of the generated signal. The u_T^* pattern up until the dashed line obtained by solving subproblem 1 allows the current x_1 to rise to the target current level more quickly than BASE. The TXOPT approach applies a phase shift at $t = 0$ and a final short pulse around the dashed black line. The u_T^* pattern beyond the dashed line obtained by solving subproblem 2 accelerates the decay of x_1 to steady-state. The intermediate full-width rectangular pulses are at the FUT's resonant

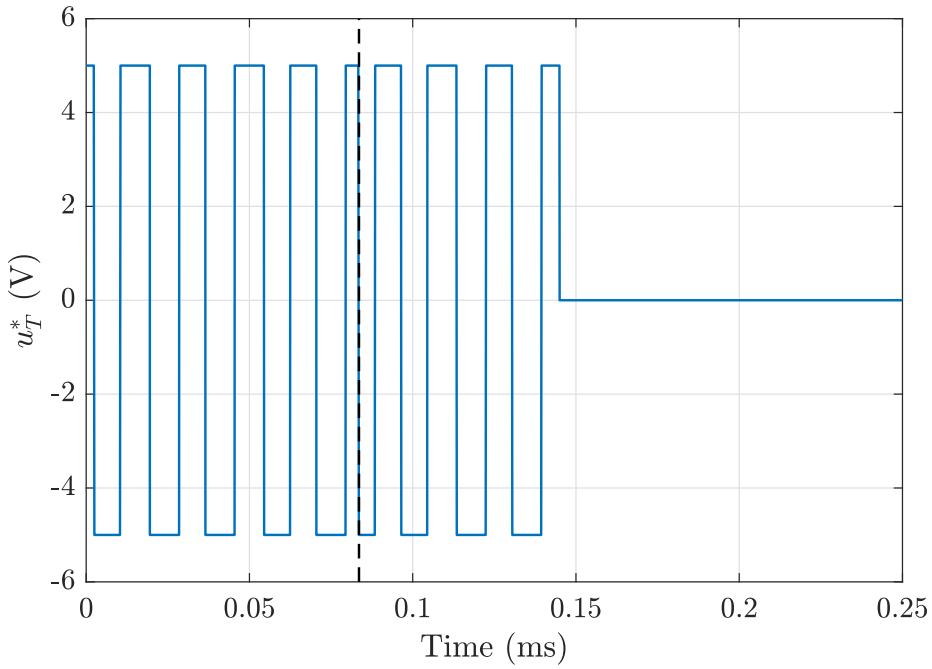

Figure 4.7: Input u_T^* for TXOPT.

frequency f. The current waveform with u_T^* is shown in Figure 4.8, and a comparison of the current envelopes with respect to BASE is shown in Figure 4.10. Comparison of Figure 4.5 and Figure 4.8 shows that steady-state conditions are reached with TXOPT at 0.15 ms when the excitation is stopped, while residual vibrations persist with BASE.

4.6 PWM Excitation Waveform Synthesis

The synthesized time-dependent bang-bang excitation signal u_T^* is realized using the waveform synthesis procedure to verify and validate the TXOPT scheme. Figure 3.12 presents the hardware realization of the transformer-fed circuit, where the transistor switches are operated with the MCU's PWM peripherals to apply the excitations to the FUT. The PWM can place signal transitions with high timing accuracy (about 25 ns).

Figure 4.11 shows the operation of the PWM peripheral. The main components required during signal synthesis are – 1. timebase reference, 2. timebase period T_b, 3. time quantization determining the edge placement, 4. edge placement action. The timebase reference is a periodic signal, such as a sawtooth waveform operating at a frequency of $\frac{1}{T_b}$.

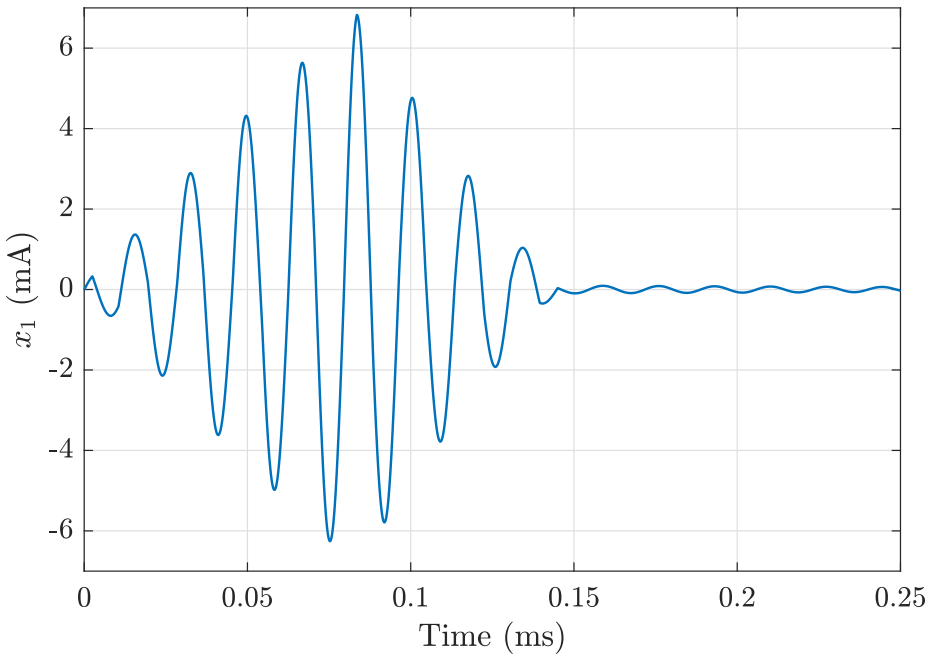

Figure 4.8: State variable x_1 for TXOPT. The target current level is $I_0 = 6.513$ mA, which is the same peak level as BASE with $n_e = 5$ of Figure 4.5.

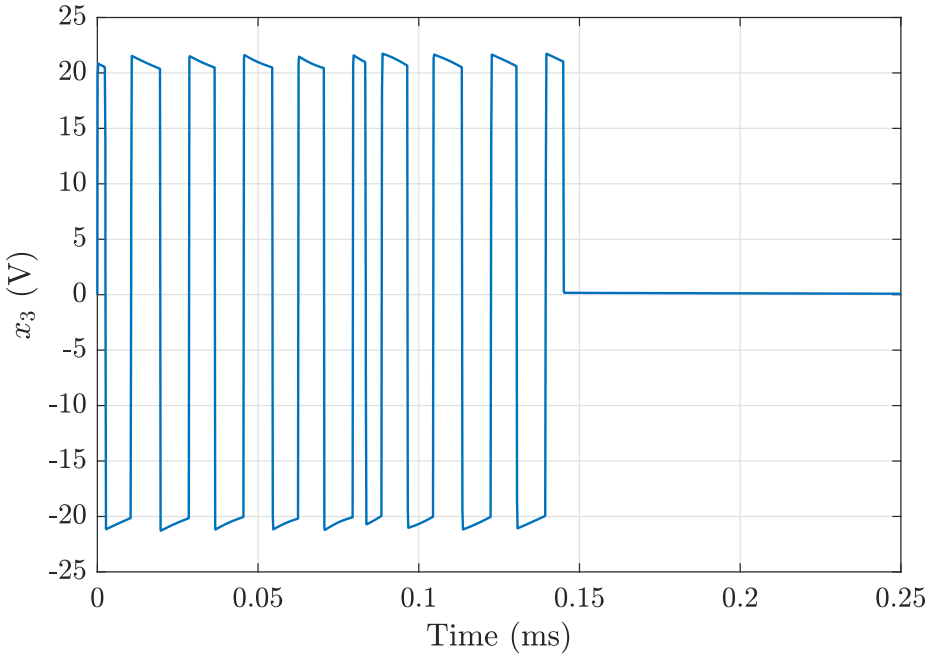

Figure 4.9: State variable x_3 for TXOPT at the FUT's terminals.

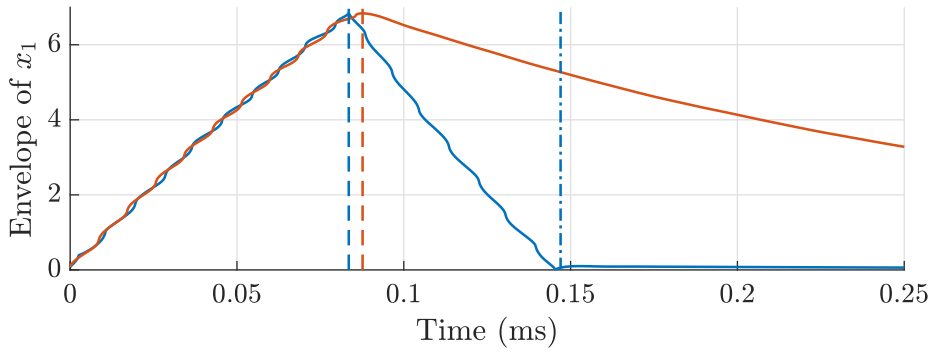

Figure 4.10: Current (x_1) envelope comparison with BASE [—] and TXOPT [—].

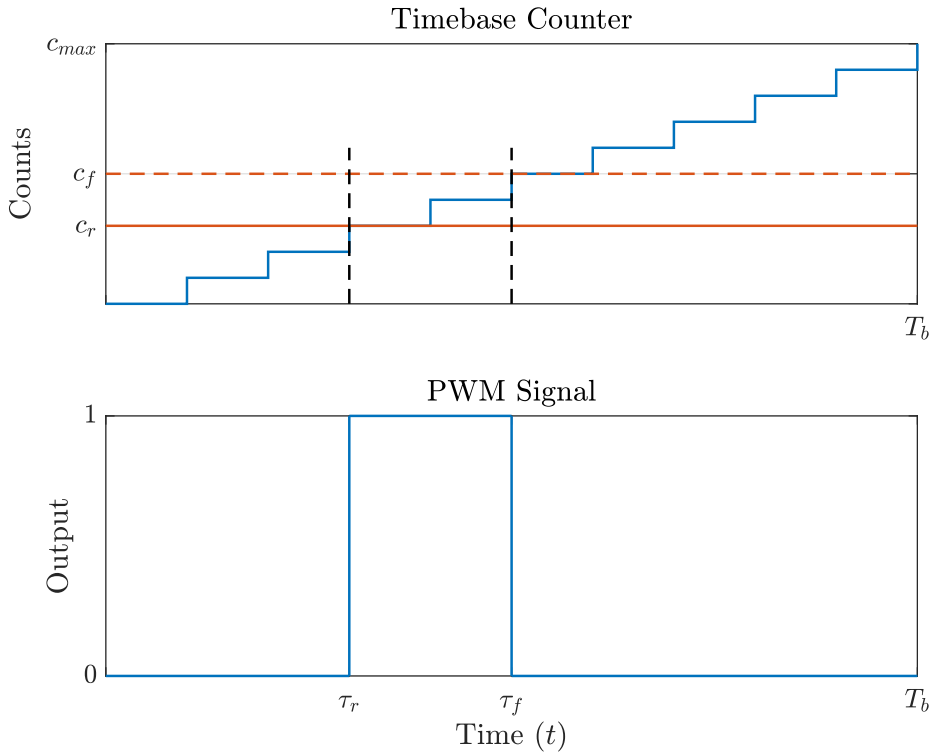

Figure 4.11: Operation of the PWM peripheral.

The sawtooth waveform is digitally implemented as a counter. An up-counting timebase takes c_{max} counter steps to complete one period. The counter is reset to zero at $t = T_b$. The counter values c_r and c_f determine the action at a digital output pin of the MCU; c_r is programmed to apply a rising edge transition ($0 \rightarrow 1$) at the time instant τ_r, while c_f is programmed to apply a falling edge transition ($1 \rightarrow 0$) at the time instant τ_f. The relationship between the counter values c and the edge placement at the time instant τ is given by

$$c = \tau C, \text{ where } C = \frac{c_{max}}{T_b} \tag{4.22}$$

As a bidirectional excitation signal needs to be synthesized, two PWM peripherals are employed. The synthesis algorithm leverages the superposition principle to generate the transistor gating signals. The peripheral PWM1 applies gating signals to generate positive voltages specified by $(c_{1r},\ c_{1f})$, and the peripheral PWM2 applies gating signals to generate negative voltages specified by $(c_{2r},\ c_{2f})$. In scaled voltage units, three levels $(0,\ +1,\ -1)$ describing the excitation signal and the transitions occurring between each level can be synthesized. Consider the signal synthesis example shown in Figure 4.12, where the desired signal spans between 0 and $3T_b$.

Interval $0 \leq t < T_b$: A rising edge transition $0 \rightarrow +1$ occurs, and c_{1r} determines the transition instant. Setting $c_{1f} = c_{max}$ maintains a positive signal level for the remainder of the interval. $c_{2r} = c_{2f} = 0$ as no negative voltage appears in the interval.

Interval $T_b \leq t < 2T_b$: In this interval the desired signal is positive initially, and then transitions to a negative voltage level. $c_{1r} = 0$ allows a positive voltage to be maintained at $t = T_b$. As a $+1 \rightarrow -1$ transition occurs, setting c_{1f} and c_{2r} to a suitable value with $c_{1f} = c_{2r}$ determines the transition point within the interval. Setting $c_{2f} = c_{max}$ maintains the negative voltage level for the remainder of the interval.

Interval $2T_b \leq t < 3T_b$: In this interval the desired signal is negative initially, and then

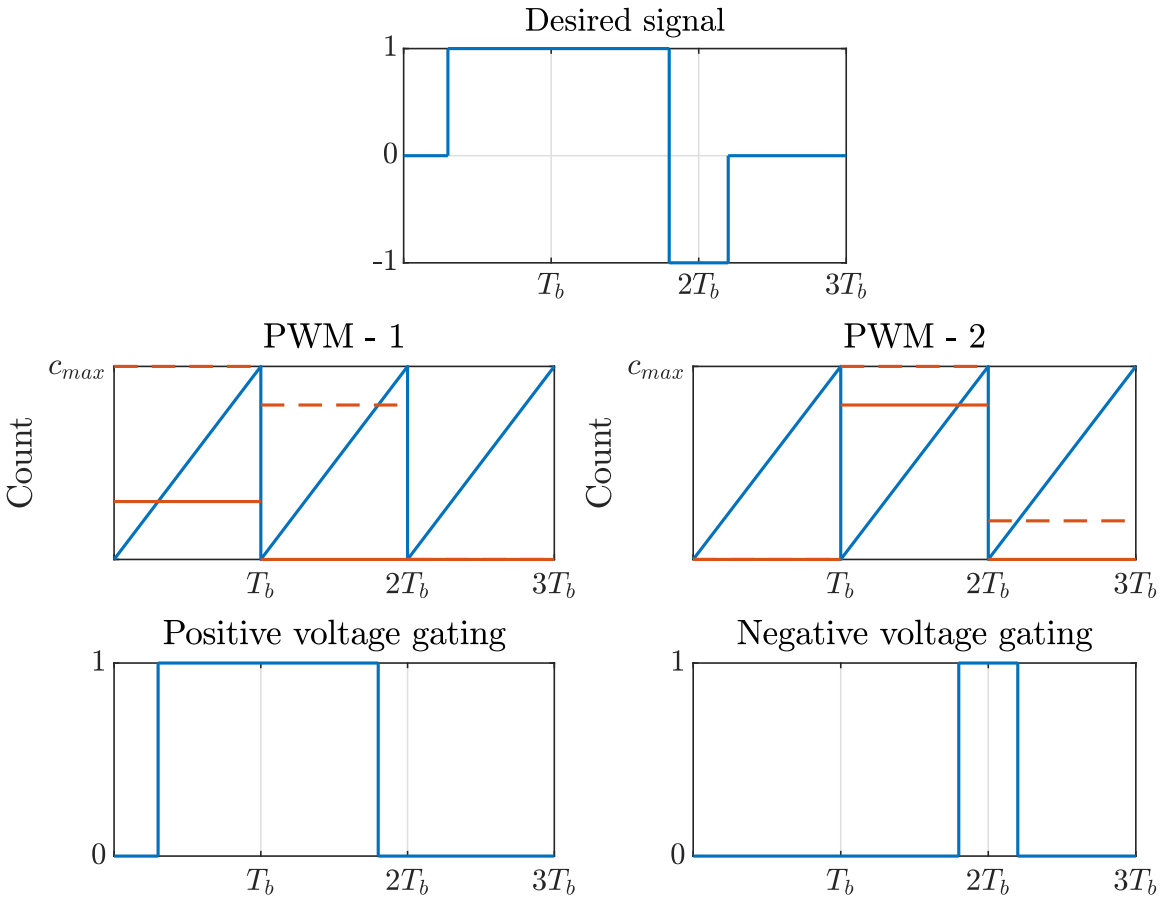

Figure 4.12: Red solid line = duty cycle for rising edge, red dashed line = duty cycle for falling edge.

transitions to a zero voltage level. $c_{2r} = 0$ allows a negative voltage to be applied at $t = 2T_b$. A $-1 \rightarrow 0$ transition occurs in the interval, and c_{2f} determines the transition point within the interval. $c_{1r} = c_{1f} = 0$ because no positive voltage needs to be generated.

Within each timebase period, the set of allowable transitions is summarized in Figure 4.13, where up to three different voltage levels $(-1, 0, +1)$ can be synthesized. However, the transitions $+1 \rightarrow -1 \rightarrow +1$ and $-1 \rightarrow +1 \rightarrow -1$ occurring within a single timebase period are disallowed. This limitation exists because only two counter values $(c_r,\ c_f)$ per PWM peripheral are used to synthesize the desired signal.

The signal u_T^* has several transitions, and it is preferable to automate the process of determining the counter values for the gating signal. Algorithm 1 describes the synthesis procedure. The inputs to the algorithm are the timebase period, the desired excitation signal,

and the duration of the excitation signal. The algorithm outputs the counter values for the gating signals, which can be directly loaded into the registers controlling the PWM peripheral's operation. The transducer is a resonant device and operates at the fundamental frequency f; the majority of the pulses in u_T^* generated in Section 4.2 are full-width pulses and have a duration of $\frac{1}{f}$. Switching transitions for full-width pulses occur at intervals of $\frac{1}{2f}$. Figure 4.7 shows that it is also possible to produce pulses that have widths shorter than $\frac{1}{2f}$ at the beginning of excitation, the end of excitation, and also during the transition from startup to shutdown. Based on simulations, setting $T_b = \frac{1}{4f}$ is sufficient to meet the needs of u_T^*.

In Algorithm 1, based on the superposition principle, the signal is decomposed into positive and negative pulse segments in line 5 – line 7. This step isolates the signals that the PWMs generate in each timebase period. In line 8 – line 13, the time instants when the rising and falling edges occur are determined by looking for step level changes in the signal. The time instants where the edges occur are converted to PWM counter values in line 14 – line 16.

A multi-mode PWM formulation is studied in [49], where $T_b = \frac{1}{2f}$ is used. This choice allows edge placements to occur with twice the precision of edge placements of Algorithm 1. However, this choice requires a special alignment procedure; the transition interval shown by the dashed line in Figure 4.7 needs to be aligned with the timebase signal of the PWM peripheral. Such an alignment is not feasible with the excitation waveforms described in Chapter 5, where two such transition events occur with pulse edges shorter than $\frac{1}{2f}$. Algorithm 1 is applicable for the methods presented in both Chapter 4 and Chapter 5.

4.7 Experimental Results

Figure 3.12 shows the hardware circuit for the experimental verification. Experiments evaluate improvements in the minimum range and the range resolution when the TXOPT

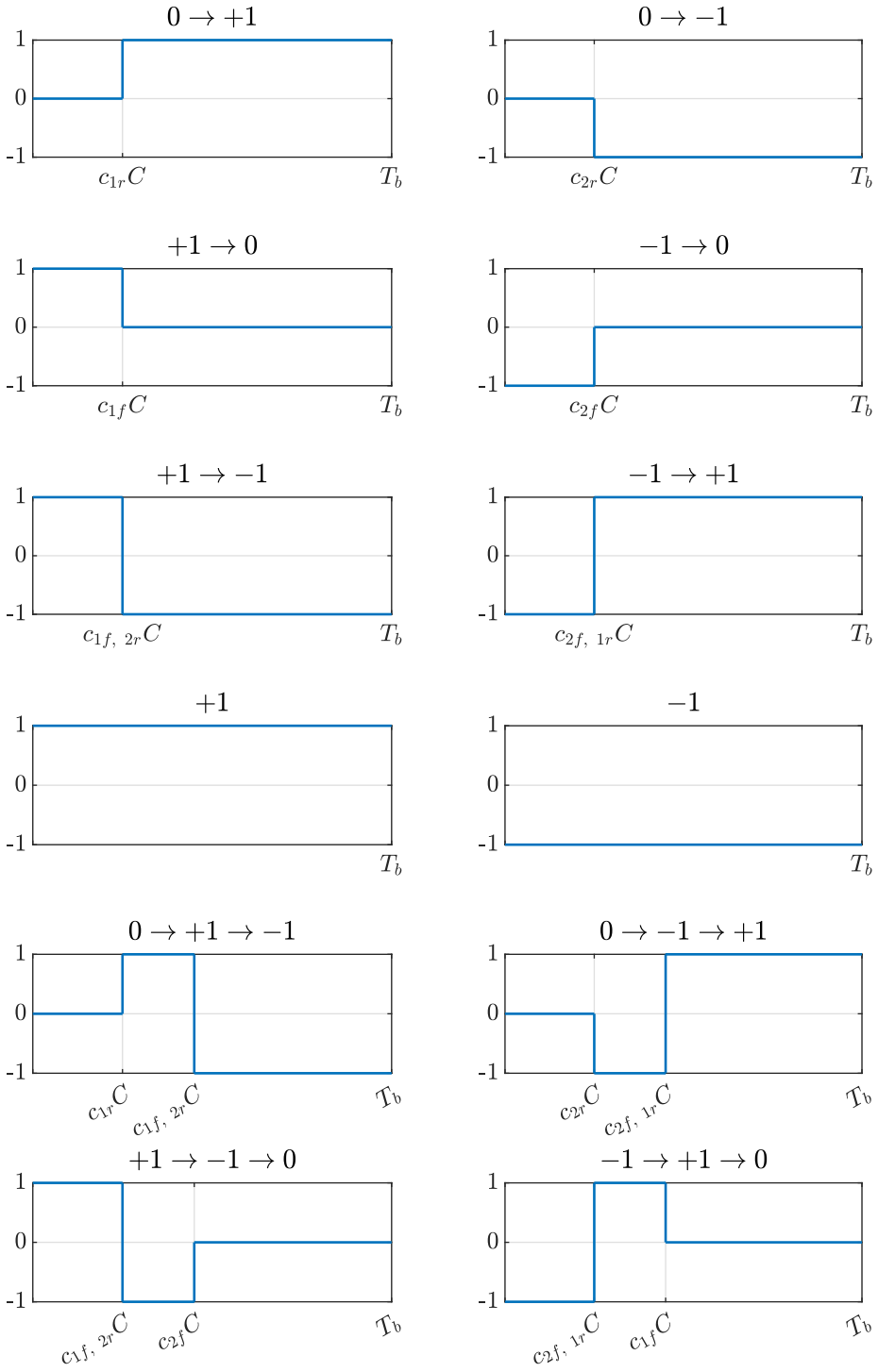

Figure 4.13: Voltage levels synthesized in one time base period. $C = \dfrac{T_b}{C_{max}}$. To synthesize $+1$ (or -1) starting at $t = 0$, $c_{1r} = 0$ (or $c_{2r} = 0$). If the signal remains at $+1$ (or -1) for the remainder of the time base period, the duty cycle $c_{1f} = 1$ (or $c_{2f} = 1$).

Algorithm 1: PWM Excitation Waveform Synthesis

Inputs:

T_b: Timebase period (in seconds)

c_{max}: Maximum counter value

$u(t)$: Desired signal. $u, t \in R^m$

t_m: Excitation signal duration

Outputs:

Counter values $\in R^p$

For positive voltage synthesis by PWM - 1: $(c_{1r},\ c_{1f})$ and

For negative voltage synthesis by PWM - 2: $(c_{2r},\ c_{2f})$

Determine the number of timebase period segments when $u(t)$ is active, i.e.

$p :=$ ceil $\left(\frac{t_m}{T_b}\right)$

Set $C :=$ ceil $\left(\frac{c_{max}}{T_b}\right)$

for $k \leftarrow 1$ **to** p **do**

  Step 1: $u_k(\tau) := u(\tau)$ where $\tau \in [(k-1)T_b,\ kT_b]$ and

    $u_k(\tau) \in R^l$, $l =$ length of u_k

  Step 2: Decompose signal into positive and negative pulse segments

    $u_+(\tau) = 1\ (\{\tau : u_k(\tau) \geq 0\})$ for PWM - 1

    $u_-(\tau) = 1\ (\{\tau : u_k(\tau) < 0\})$ for PWM - 2

  Step 3: Determine rising and falling edges for $u_+(\tau)$ and $u_-(\tau)$:

    Rising edge detection:

      $\tau_{(r,\ P)} := \tau$ s.t. $\tau_{l-1} = 0$ and $\tau_l = 1$

    Falling edge detection:

      $\tau_{(f,\ P)} := \tau$ s.t. $\tau_{l-1} = 1$ and $\tau_l = 0$

    where $P = (u_+(\tau),\ u_-(\tau))$

  Step 4: Determine the counter values for each segment:

    $c_{(r,\ P)} := C\tau_{(r,\ P)}$

    $c_{(f,\ P)} := C\tau_{(f,\ P)}$

end

excitation is applied. The target current level I_0 is set equal to the peak current level obtained when the FUT is excited with BASE for $n_e = 5$, similar to Figure 4.4 and Figure 4.7. The measurements as seen by the ADC after analog filtering and amplification are shown in Figure 4.14. When u_T^* is applied, the decay time reduces. To measure the reduction in the total transmission duration, the time instant when the envelope goes below the threshold is determined. Since the ADC is single-ended, for a threshold of 10% of the positive signal range of the ADC (i.e., 0 – 2047 counts) corresponding to the noise floor of the ADC, the envelope with TXOPT crosses the threshold about 0.4 ms earlier than BASE. The optimal excitation does not cause $\tilde{y}_R$ to reach noise floor levels immediately at the end of excitation because of amplification, nonlinearities in the dynamics of the transformer-fed FUT system, plant parameter estimation error, and imperfections in actuation.

The detection of echoes from reflectors near the FUT was tested by placing a flat object at a distance of 15 cm in front of the FUT. Pulse-echo trials were conducted by applying both BASE and TXOPT excitations to the FUT. The improvement in minimum range and the ability to detect nearby objects is shown in Figure 4.15. With the TXOPT approach, an echo from the reflector is detected, while with the BASE excitation, the echo is not detected. This occurs because the vibration amplitude of the FUT as it decays to steady-state is larger than the amplitude of the incoming echo, resulting in detection losses.

Figure 4.16 demonstrates the range resolution enhancement. Two flat objects are present in the scene at a distance of 35 cm and 38 cm in front of the FUT. Application of the TXOPT excitation scheme results in the detection of both objects, whereas the application of BASE results in the detection of only one object. The echo with BASE has an extended envelope because of the slow decaying tail of the transmitted pressure wave. Equation E.4 discusses how the range resolution depends on the pulse width. With TXOPT, since the pulse width of the transmitted pressure wave reduces due to the shorter decaying tail, the pulse width of the voltage induced by the echoes also reduces, improving the range resolution of the sensing system.

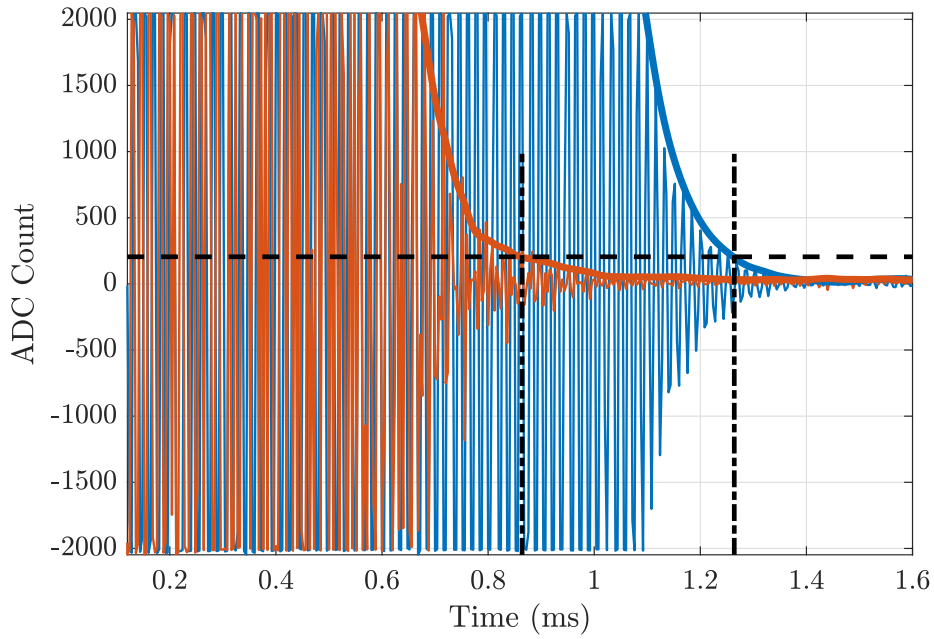

Figure 4.14: Experiment 1: Residual vibrations and envelope after analog filtering and amplification with no reflector. (BASE [—], TXOPT [—], threshold [- -], and total transmission duration [- .].

Figure 4.17 shows the experimental performance improvement in the minimum range of the TXOPT case over the BASE case. The range is computed by scaling ToF by half the speed of sound as given by Equation 1.1. The minimum range is the range corresponding to the time instant when the decaying tail goes below a threshold as shown in Figure 4.14. The minimum range improves by an average of 32% with TXOPT when compared to BASE.

4.8 Summary and Conclusion

In this chapter, time-optimal control principles are applied to design the excitation signals of an FUT to minimize the residual vibrations. The control problem formulation requires the current through the oscillatory branch to reach a specified level. Two numerical solvers – collocation and multiple shooting are developed, and numerical solutions to the control problem are determined. Although the solution generation process requires a PC, the PWM waveform synthesis algorithm allows the computed excitations to be translated into a list of counter values for application using the PWM peripherals found in many low-cost MCUs.

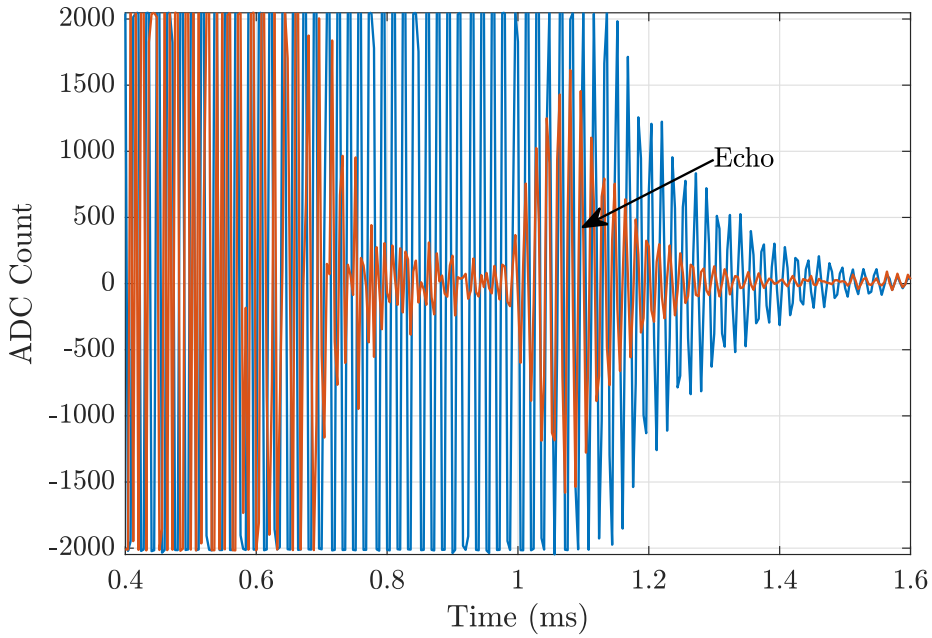

Figure 4.15: Experiment 2: Echo detection with the optimal excitation signal demonstrating minimum range enhancement. One reflector at 15 cm. (BASE [—], and TXOPT scheme [—]).

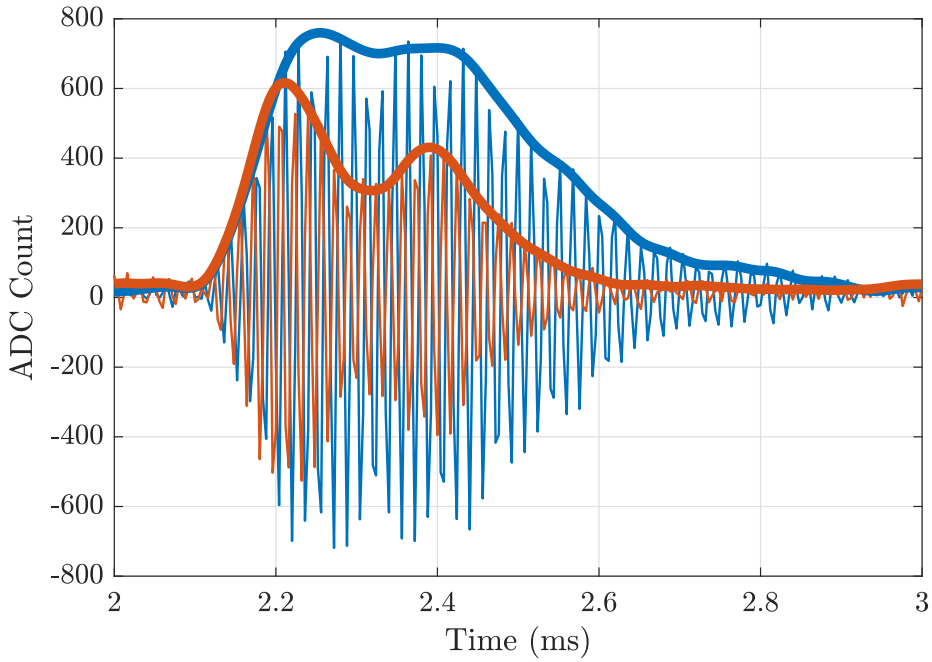

Figure 4.16: Experiment 3: Range resolution enhancement with the optimal excitation signal. Two reflectors in the scene at 35 cm and 38 cm. (BASE [—], and TXOPT scheme [—]).

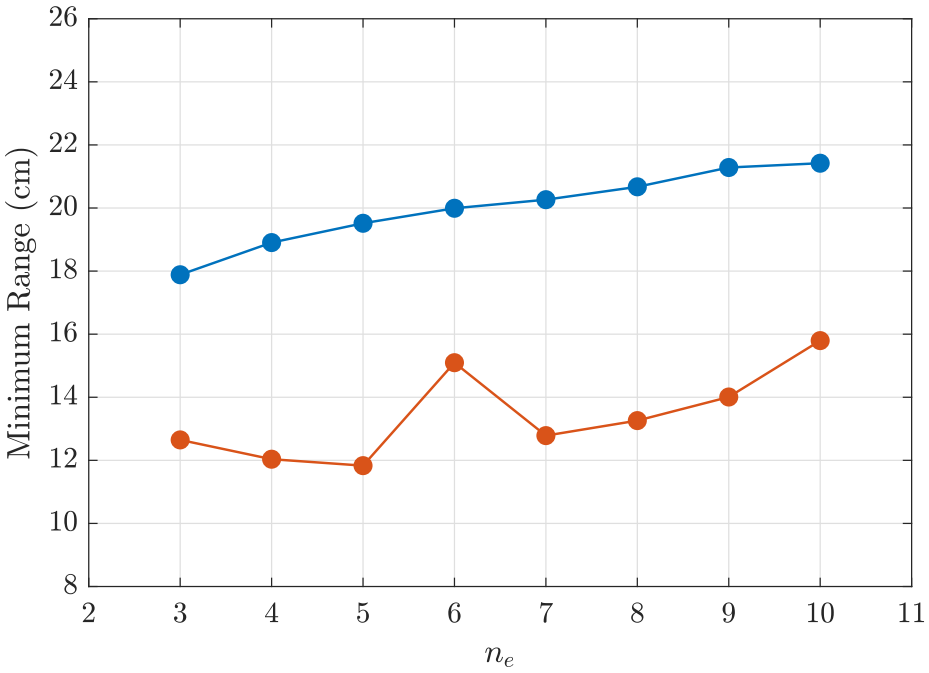

Figure 4.17: Experimental minimum range improvement of TXOPT [—] over BASE [—]. Target current I_0 for u_T^* is set to the peak current value obtained with BASE.

The advantages of applying optimal excitations were demonstrated through simulations and experiments. The reduction in the decay time allows the detection of objects located near the FUT. The work presented in this chapter resulted in the publication [53].

CHAPTER 5
TIME OPTIMAL ENHANCEMENTS FOR RECEIVING FLEXURAL ULTRASONIC TRANSDUCERS

5.1 Introduction

In Chapter 4 the focus was on reducing the residual vibrations through time-optimal control for a transmitting transducer (TX-FUT). The designed optimal excitation (TXOPT) accelerated the damping of the TX-FUT. Consequently, the length of the blind zone reduced, improving the sensing system's minimum range and range resolution. This chapter extends the results developed in the previous chapter by studying the influence of an incoming pressure wave on a receiving transducer (RX-FUT), which is also a dynamic system. Figure 5.1 clarifies the focus of this chapter. Through time-optimal control principles, this chapter develops a solution to synthesize excitations u_T for the TX-FUT to cancel the dynamics of the RX-FUT so that y_R has a sharp rise to the peak followed by a sharp fall to the noise floor level. As the range is a scaled version of the time axis, by Equation E.4, echoes at the RX-FUT with shorter pulse widths yield improvements in the range resolution of the sensing system.

The problem formulation achieves the temporal width reductions while maintaining the peak amplitude of the echoes. The approach applies to both monostatic and bistatic sensing configurations, and the system under study results in a high model order (6^{th} order). Numerical solution methods developed in Chapter 4 produce the excitation profile for the TX-FUT. The chapter also compares the two competing problem formulations studied in this research (TXOPT and RXOPT) and the impact on the minimum range and the range resolution. The experiments demonstrate improvements in the sensor's performance metrics while illustrating the tradeoffs.

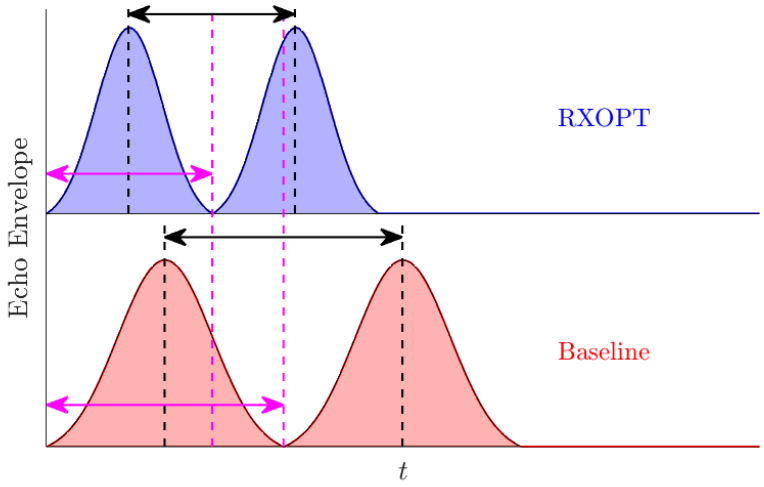

Figure 5.1: Comparison of echoes at RX-FUT. Reduced pulse width of echoes (y_R) improves the range resolution of the sensing solution. Peak echo amplitude at RX-FUT is maintained.

5.2 System Physics

The system under study consists of a dedicated transmitting device fed by a transformer (TX-FUT) and a dedicated receiving device (RX-FUT). Figure 3.9 shows the electrical equivalent circuit for a transformer-fed transducer, and the corresponding state-space representation is given by Equation 3.7. During reception, Figure 3.4 describes the equivalent circuit of the RX-FUT with the state-space representation given by Equation 3.2. Figure 1.1 illustrates the pulse-echo mode of operation, which can be modeled as a linear process. By the pressure $\leftrightarrow$ voltage analogy, the pressure wave p_T and p_R are proportional to the voltages v_T and u_R respectively. Section 3.2 discusses how p_T is also proportional to the current y_T flowing in the oscillatory branch of the FUT. Therefore, the pressure wave received by the RX-FUT $u_R(t)$ may be modeled as a scaled and time-shifted copy of the emitted pressure wave $y_T(t)$ and can be written as

$$u_R(t) = \alpha y_T(t - \tau) \tag{5.1}$$

where α is a scale factor that accounts for the propagation losses due to the reflector's location, shape, and material properties. On the other hand, τ encodes the round-trip travel distance of the pressure waves. The input u_R to the RX-FUT cannot be determined in advance as both α and τ are unknown. The reflector's characteristics are also unknown. Note that the transducer experiences electrical $\leftrightarrow$ mechanical $\leftrightarrow$ acoustic conversion losses as discussed in Section 3.5.

Modeling simplifications are possible by setting τ to a constant, implying that the pressure waves travel a fixed distance between the transmitting and the receiving devices. One good option is to set $\tau = 0$. As the α parameter encodes the reflective properties of the scatterer, one choice is to set $\alpha = 1$, implying a lossless reflection. Section 3.2 describes how the current x_1 through the oscillatory branch of the transmitter model represents the emitted pressure wave. Therefore, $u_R = y_T = x_1$. Since two identical transducers from the same batch are used, one to transmit and one to receive pressure waves, the parameter values are assumed to be the same. The combined state-space model of the transmit-receive system is a 6$^{\text{th}}$ order dynamic system – 4$^{\text{th}}$ order dynamics describe the transformer-fed transmitter, and 2$^{\text{nd}}$ order dynamics describe the receiver. The state variables for the transmitter system are $[x_1, \ldots, x_4]$ and given by Equation 3.7. Let x_5 and x_6 be the new state variables for the receiver system given by Equation 3.2. With reference to Figure 3.4, x_5 models the voltage across the capacitor C_p, and $x_6 = \dot{x}_5$ models a scaled version of the current through the capacitor C_p. In the state-space representation, the $\mathbf{A}$ matrix has the dimension 6×6, and the $\mathbf{B}$ matrix has the dimension 6×1. The $(i,\ j)^{\text{th}}$ entry of the sparse matrices defining the

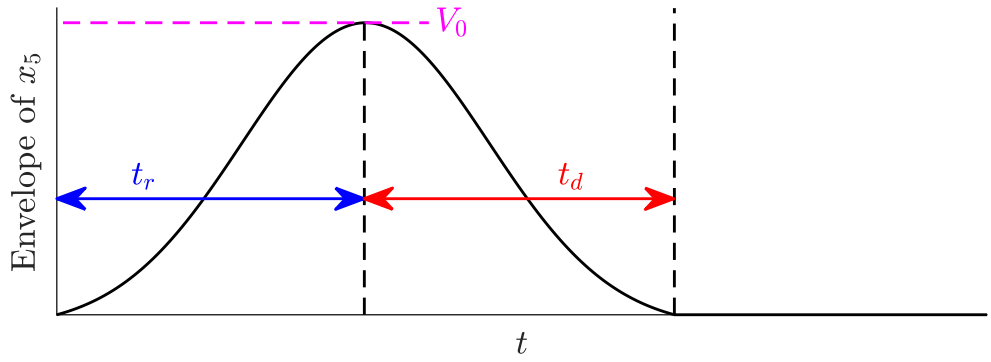

Figure 5.2: Illustration of the receiver echo shape optimization problem. x_5 represents the voltage at the receiver across the capacitor C_p.

combined TX-RX system is given by

$$\begin{gathered} a_{11} = \frac{-R_s}{L_s},\ a_{12} = \frac{-1}{L_s},\ a_{13} = \frac{1}{L_s},\ a_{21} = \frac{1}{C_s}, \\ a_{31} = \frac{-1}{C_p},\ a_{33} = \frac{-1}{n^2 R_{src} C_p},\ a_{34} = \frac{-1}{nC_p},\ a_{43} = \frac{1}{nL_m}, \\ a_{56} = 1,\ a_{61} = \frac{\alpha}{L_r C_p},\ a_{65} = \frac{-(C_s + C_p)}{L_s C_s C_p},\ a_{66} = \frac{-R_s}{L_s}, \\ \text{and } b_{31} = \frac{1}{nR_{src}C_p} \end{gathered} \tag{5.2}$$

5.3 Receive Optimization Problem

Figure 5.2 motivates the optimization problem. The echo takes a time t_r to rise to a voltage level of V_0 from equilibrium conditions, after which it decays back to the noise floor in time t_d. As shown by Figure 5.1, reducing the total time duration of the echo, i.e. $t_r + t_d$, is equivalent to improving the range resolution characteristics of the sensor by Equation E.4. Similar to Section 4.2, a two subproblem optimization setup is preferred, solved in sequence. In the first subproblem, the rise time is minimized, and in the second subproblem, the decay time is minimized.

The input u_T to the transducer is constrained to a maximum rail voltage of V. The peak level of the echo is V_0 and introduced into the formulation through an inequality constraint.

The state variables for the decay time minimization problem are initialized with the values of the state variables at the end of the rise time minimization problem. Additionally, let ϵ be the noise floor level. The two subproblems for the receive optimization problem RXOPT are given by

Subproblem 1: Rise time minimization of the echo

$$\begin{aligned} &\text{minimize } t_r \\ &\text{subject to } \dot{\mathbf{x}} = \mathbf{A}\mathbf{x} + \mathbf{B}u_T \\ &\quad |u_T| \leq V \\ &\quad \mathbf{x}(0) = \mathbf{0} \\ &\quad |x_5(t_r)| \geq V_0 \end{aligned} \tag{5.3}$$

Subproblem 2: Decay time minimization of the echo

$$\begin{aligned} &\text{minimize } t_d \\ &\text{subject to } \dot{\mathbf{x}} = \mathbf{A}\mathbf{x} + \mathbf{B}u_T \\ &\quad |u_T| \leq V \\ &\quad \mathbf{x}(0) = \mathbf{x}(t_r) \\ &\quad |\mathbf{x}(t_d)| \leq \epsilon \end{aligned} \tag{5.4}$$

The numerical techniques orthogonal collocation and multiple shooting discussed in Section 4.4 are employed to determine the optimal solution to each subproblem. As the state variables in the system differ by several orders of magnitude, and the time axis is on the order of milliseconds, scaling discussed in Section 4.3 is performed to improve the numerical convergence. Just as before, the numerically synthesized excitation signal u_T is applied to the TX-FUT in an open loop. Also, the optimality and constraint tolerances of the solver are set to 10^{-6}.

5.4 Simulation Results

The system is simulated with the model parameters listed in Table 3.2. The parameter values are common to both the simulations and the experiments. The TX-FUT and the RX-FUT are identical copies from the same batch. Although the resistance of the transducer's oscillatory branch is expected to be slightly different during reception and transmission operations, they are assumed to be equal due to reciprocity. Moreover, the estimation of the receiver's resistance requires sophisticated instrumentation. The simulation study considers three cases:

1. **Baseline Excitation Signal (BASE)**: Applies a voltage excitation u_T at the TX-FUT with $n_e = 3$ given by Equation 3.8 at the resonant frequency f.

2. **Time Optimal Transmit Excitation Signal (TXOPT)**: Applies the voltage excitation u_T^* at the TX-FUT synthesized through the numerical solution for the formulations given by Equation 4.1 and Equation 4.2. I_0 is set equal to the peak transmit current at the TX-FUT (state variable x_1) when BASE is applied.

3. **Time Optimal Receive Excitation Signal (RXOPT)**: Applies the voltage excitation u_T^* at the TX-FUT synthesized through the numerical solution for the formulations given by Equation 5.3 and Equation 5.4. V_0 is set equal to the peak echo voltage at the RX-FUT (state variable x_5) when BASE is applied.

Figure 5.3 – Figure 5.5 shows the excitation input u_T applied to the TX-FUT, the state variable x_1 representing the transmitted pressure, and the state variable x_5 representing the echo voltage generated at RX-FUT with each excitation scheme. The total time taken by the transmitted pressure and the received echo reveals important performance parameters of the ultrasonic sensing system, such as the minimum range and the range resolution. The metrics

to compare the three schemes are given by

$$\begin{aligned} t_{TX} &= \min(\tau) \text{ where } \{\tau : |x_1(\tau)| \leq \epsilon_{TX}\} \text{ and} \\ t_{RX} &= \min(\tau) \text{ where } \{\tau : |x_5(\tau)| \leq \epsilon_{RX}\} \end{aligned} \tag{5.5}$$

where t_{TX} and t_{RX} determine the total transmission and reception durations, ϵ_{TX} and ϵ_{RX} are threshold values above zero indicative of the equilibrium levels of the system. The two quantities provide the total time to rise to a peak value and decay back to equilibrium conditions. The metric t_{TX} characterizes the minimum range, and the metric t_{RX} characterizes the range resolution of the system. A smaller t_{TX} reduces the length of the blind zone as illustrated by Figure 1.1 and allows reflectors to be closer to the sensor system. A smaller t_{RX} implies a smaller separation between two objects as clarified by Figure 5.1. The values for ϵ_{TX} and ϵ_{RX} are set to 10% of the peak value of x_1 and x_5 respectively. This provides a reasonable threshold level to estimate the timing metrics and study the relative system performance with different excitation schemes.

In BASE, a short excitation is applied to the TX-FUT, which consists of $n_e = 3$ cycles at the resonant frequency as shown in Figure 5.3a. The resulting signal y_T at the TX-FUT and the echo y_R generated at the RX-FUT have an extended decaying tail as shown in Figure 5.4a and Figure 5.5a. Both minimum range and range resolution of the system degrades due to a large t_{TX} and t_{RX} value.

For the RXOPT excitation scheme, the numerical results are generated through the solution of Equation 5.3 and Equation 5.4. The peak echo voltage V_0 obtained from the state variable x_5 of RX-FUT has the same amplitude when compared to the BASE excitation scheme. Figure 5.3c shows the excitation input to the TX-FUT. It is a bang-bang signal, switching between the rail limits, which is characteristic of linear time-invariant systems [52]. Compared to the BASE excitation scheme, the RXOPT scheme lasts for a substantially longer duration. Figure 5.4c shows the pressure wave (current waveform x_1) emitted by the TX-FUT with the RXOPT scheme, and Figure 5.5c shows the corresponding voltage at

the RX-FUT. The current in the oscillatory branch shows a sequence of two pressure bursts emitted by the TX-FUT. The first burst is responsible for building up the voltage signal at the RX-FUT to the desired voltage level V_0, while the second burst causes the voltage signal in the RX-FUT to decay back to equilibrium conditions. The echo voltage signal given by x_5 shows a sharp rise to the peak followed by a sharp drop to equilibrium levels. The width of the echo has been reduced substantially by about 68% when compared with BASE, which results in a corresponding improvement in the range resolution of the system with RXOPT. It is interesting to note that the peak transmit pressure level with the RXOPT scheme is higher compared to the BASE scheme due to the additional excitation cycles. In the echo, small levels of residual vibrations with an amplitude less than ϵ_{RX} exist and are in the noise floor regime. Another interesting aspect is the coupled nature of the problem; u_T is applied to the TX-FUT to launch a pressure wave p_T (signal y_T) that interacts with the dynamics of the RX-FUT to bring improvements to y_R. With RXOPT, both the transmitted pressure and the received echo transition to equilibrium conditions immediately after the excitation input ends.

The resulting excitation u_T with the TXOPT scheme is shown in Figure 5.3b, where the peak current I_0 is the same as that of the BASE excitation scheme. The transmitted pressure wave has a sharp rise to the peak amplitude level, followed by a sharp fall to equilibrium levels. With the TXOPT scheme t_{TX} is smaller compared to both the BASE and the RXOPT schemes. This aspect improves the minimum range of the ultrasonic sensing system as the length of the blind zone reduces. On the other hand, the echo waveform of the RX-FUT has an amplitude reduction of about 52% compared to the BASE and the RXOPT schemes. Also, the t_{RX} for the echo is about 1.6 times larger than the RXOPT scheme but is about 19% smaller than BASE. The range resolution improves even with the TXOPT scheme, but the improvement comes at the expense of the peak echo amplitude.

In summary, the RXOPT scheme provides the best improvement in the range resolution of the system, with a marginal improvement in the minimum range of the system. On the

other hand, the TXOPT scheme provides the best improvement in the minimum range of the system and marginal improvement in the range resolution of the system.

5.5 Experimental Results

The experiments use two identical 58.5 kHz narrowband Murata MA58MF14-7N FUTs located side-by-side as shown in Figure 1.1 with a separation of 3 cm between the TX-FUT and the RX-FUT. Note that the FUTs are capable of monostatic operation, i.e., the same device can be used to both transmit and receive pressure waves. The voltages appearing at the terminals of both FUTs pass through the receive signal chain described in Appendix C. The dedicated receive signal paths use a gain of 1170 V/V to study the effect of the three excitation schemes. The TX-FUT is also connected to the transmitter hardware circuit as shown in Figure 3.12, allowing the excitation-imposed decay characteristics to be studied. The RX-FUT is only connected to the receive signal chain to comply with the model given by Equation 5.2. The PWM synthesis procedure described in Algorithm 1 translates the generated excitation signals into PWM counter values for experimental verification.

The experimental results are shown in Figure 5.6 – Figure 5.8 and compare the performance of the three excitation schemes discussed in Figure 5.3. The plots show the measurements after removing the bias (2047 ADC counts for a 12-bit ADC). Figure 5.6 shows the signal capture at the TX-FUT and is used to compare the minimum range for monostatic systems, the main focus of Chapter 4. The reduction in the total transmission time is determined by the time instant when the envelope goes below the threshold (shown by the dashed line in Figure 5.6). For a threshold at about 10% of the maximum signal level, the envelope decays about 0.34 milliseconds earlier with the TXOPT scheme when compared to the BASE scheme, improving the minimum range. With the RXOPT excitation scheme, there is a marginal improvement when compared to the BASE excitation scheme because, as shown in the simulations, the peak transmit pressure is higher in RXOPT resulting in a longer decay. The TXOPT excitation gives the best minimum range. For bistatic systems,

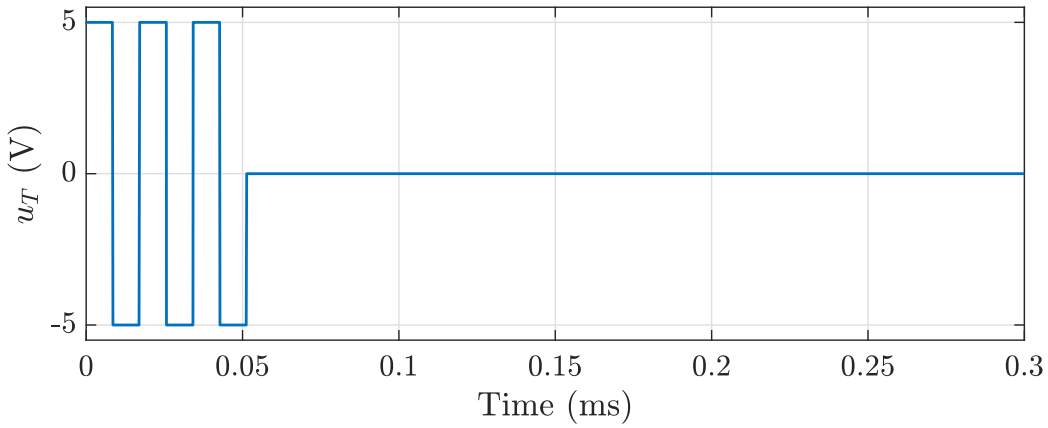

(a) BASE excitation for $n_e = 3$. Results in peak transmit current $I_0 = 4.56$ mA and peak echo voltage $V_0 = 2.74$ mV.

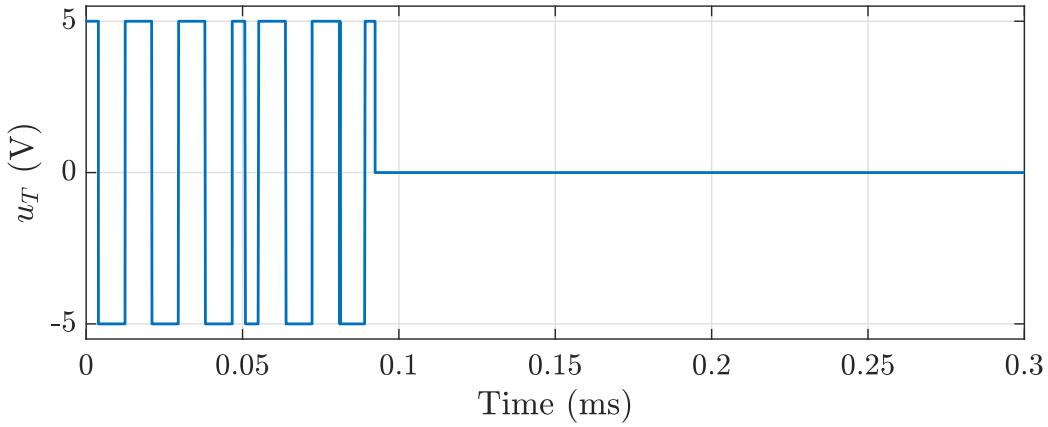

(b) TXOPT excitation signal. Results in peak transmit current $I_0 = 4.56$ mA.

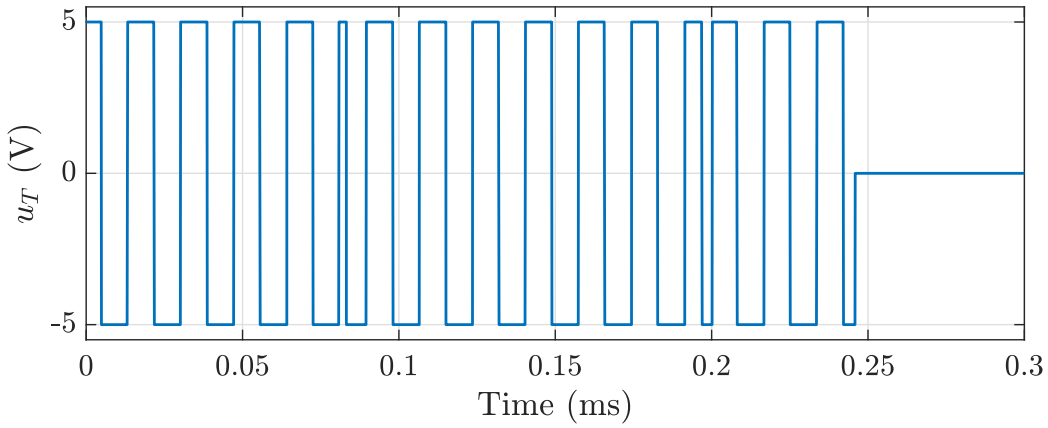

(c) RXOPT excitation signal. Results in peak echo voltage $V_0 = 2.74$ mV.

Figure 5.3: Voltage excitation u_T applied to the TX-FUT.

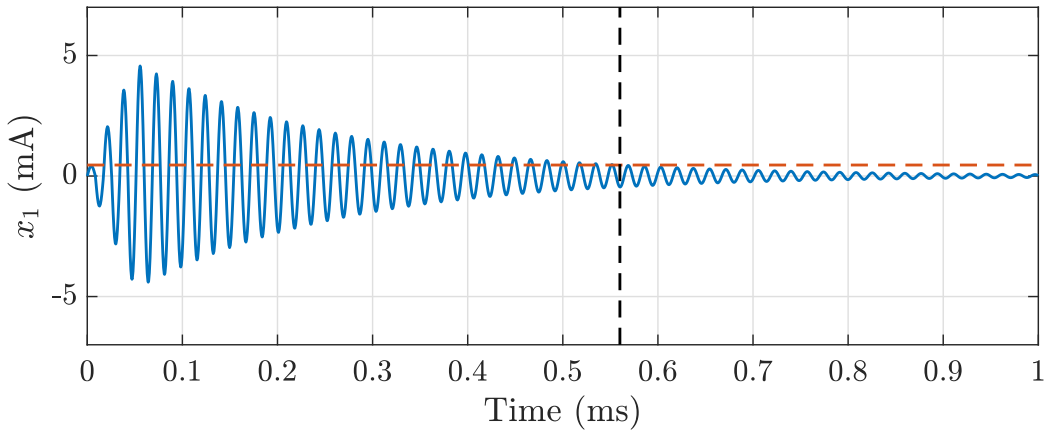

(a) BASE excitation. $t_{TX} = 0.56$ ms. Peak transmit current = 4.56 mA.

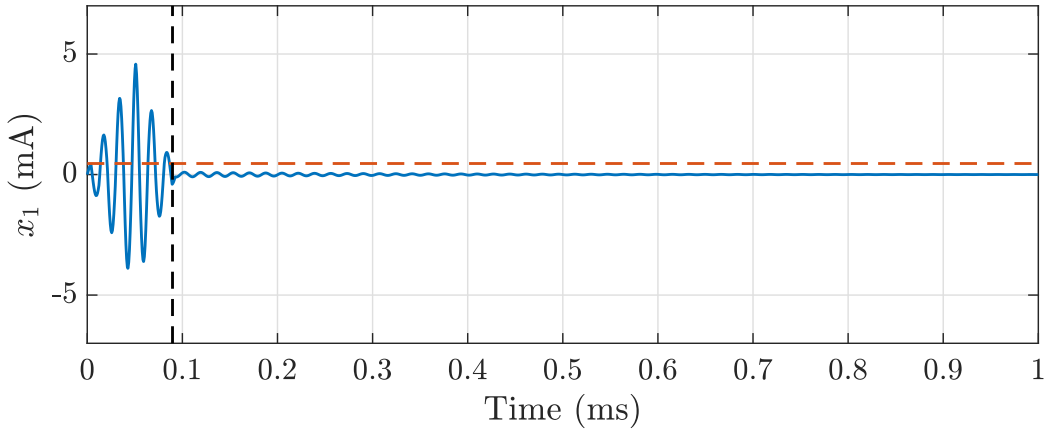

(b) TXOPT excitation. $t_{TX} = 0.089$ ms. Peak transmit current = 4.56 mA. Results in the shortest transmit duration.

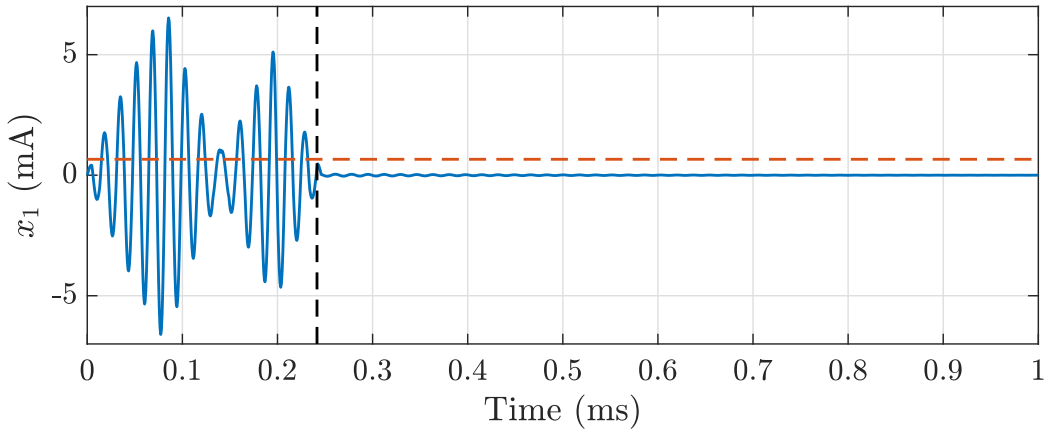

(c) RXOPT excitation. $t_{TX} = 0.242$ ms. Peak transmit current = 6.53 mA. Results in a higher peak amplitude w.r.t BASE. Second emission burst accelerates damping of RX-FUT.

Figure 5.4: The current x_1 of the TX-FUT represents the emission pressure wave with each excitation scheme.

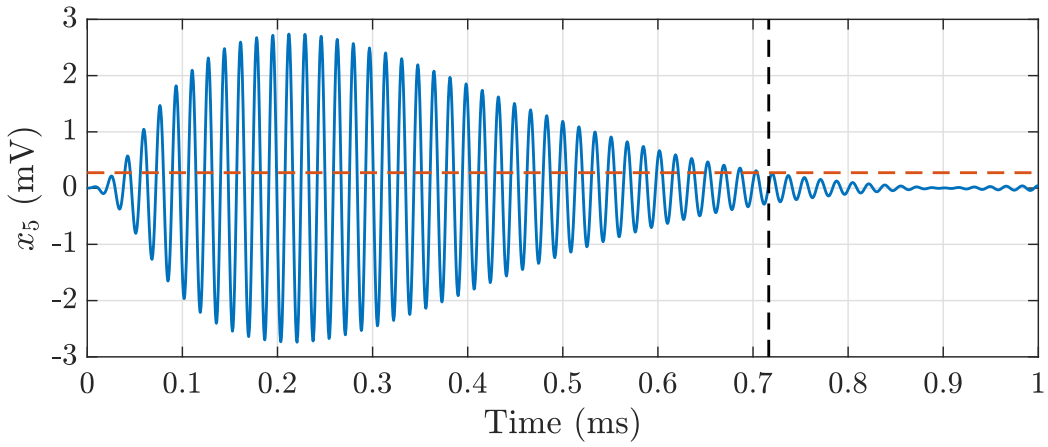

(a) BASE excitation. $t_{RX} = 0.717$ ms. Peak echo voltage = 2.74 mV.

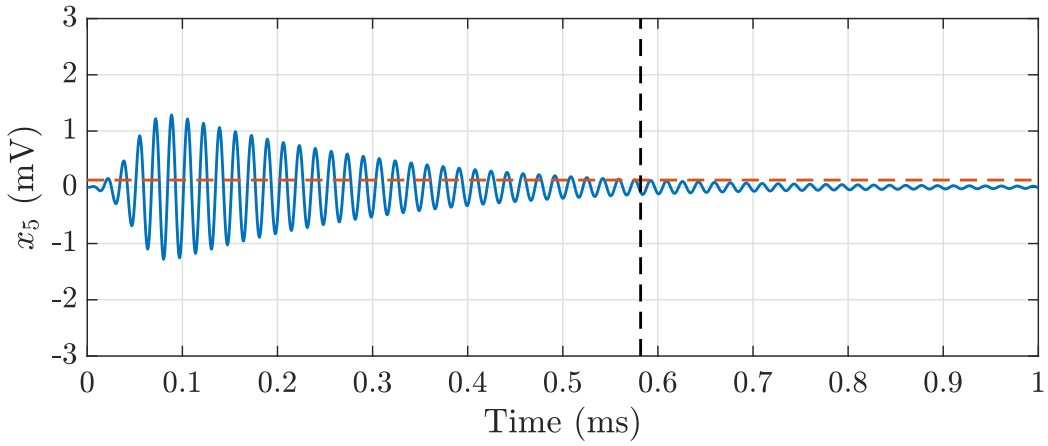

(b) TXOPT excitation. $t_{RX} = 0.581$ ms. Peak echo voltage = 1.29 mV.

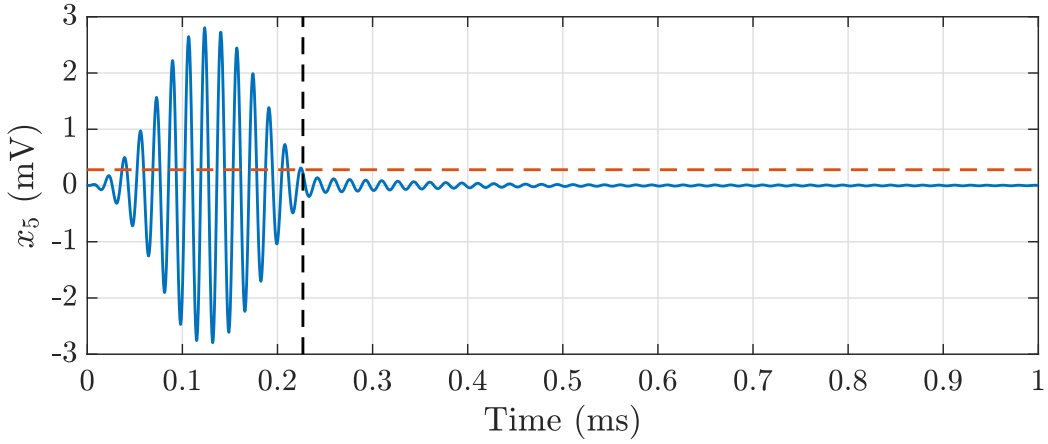

(c) RXOPT excitation. $t_{RX} = 0.227$ ms. Peak echo voltage = 2.74 mV. RXOPT achieves same peak amplitude w.r.t BASE, but has a much shorter t_{RX}.

Figure 5.5: The voltage x_5 at the RX-FUT represents the induced echo with each excitation scheme.

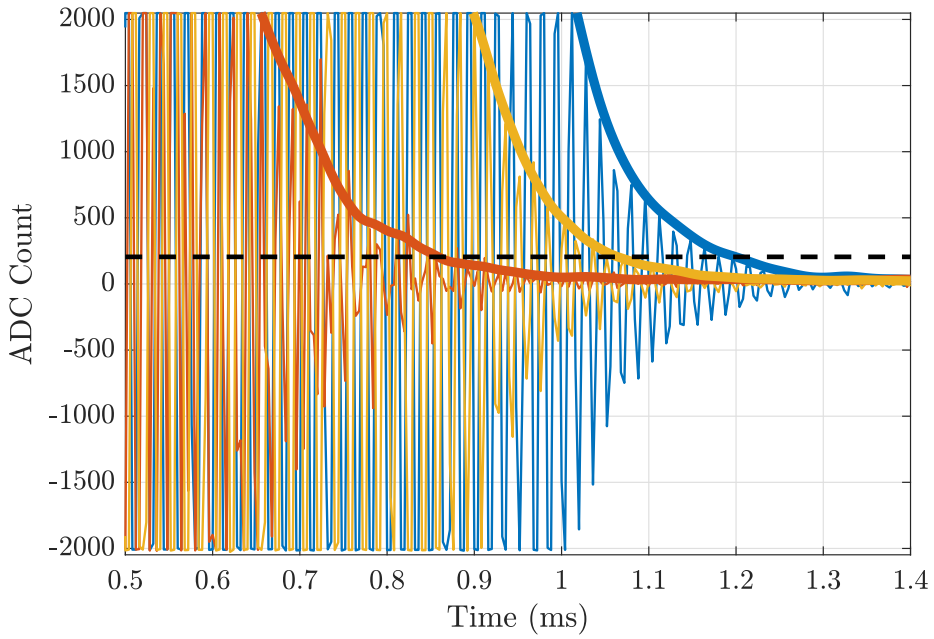

Figure 5.6: Experiment 1: Measurements at the TX-FUT. Transmitter decay determines the minimum range. (BASE [—], TXOPT [—], RXOPT [—], Threshold [- -]). TXOPT provides the best minimum range.

the minimum range enhancement depends on the separation between the TX-FUT and the RX-FUT, the receiver's sensitivity, and the directionality of the devices. Since the separation between the TX-FUT and the RX-FUT is comparatively large (3 cm), and the RX-FUT also has a low receive sensitivity, the minimum range improvements with TXOPT excitation in a bistatic configuration is marginal. However, Figure 7.8 illustrates that for a sensitive omnidirectional receiver, the TXOPT excitation scheme accelerates the damping in the receiver reducing the blind zone of the sensing system.

Figure 5.7 and Figure 5.8 show the performance comparisons at the RX-FUT when the excitations are applied at the TX-FUT. In Figure 5.7 a single reflector is present in the scene. Horizontal dashed lines indicate the threshold corresponding to each excitation scheme, while vertical dashed lines indicate the time instants when the signal envelope goes below the threshold. With the RXOPT excitation, the echoes have a sharp rise to the peak, followed by a fast decay to the noise floor level when compared with BASE and TXOPT. For a threshold at 10% of the peak echo amplitude, the width of the echo has been reduced

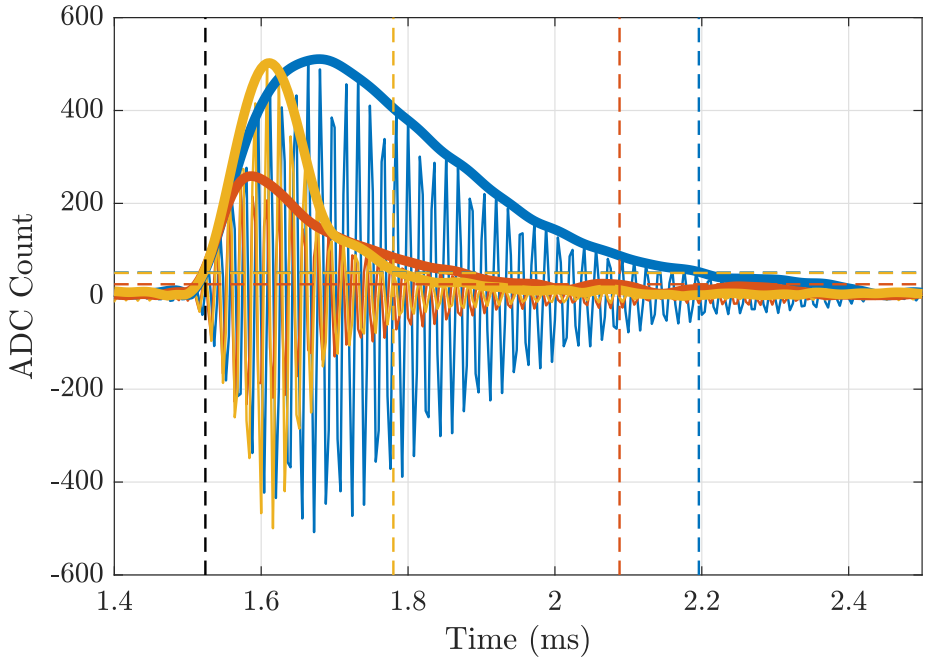

Figure 5.7: Experiment 2: Measurements at the RX-FUT. Echoes are received from a single flat reflector in the scene located 27.5 cm from the sensing system. (BASE [—], TXOPT [—], RXOPT [—], Echo start [- -]). RXOPT has shortest echo and maintains peak amplitude when compared to BASE.

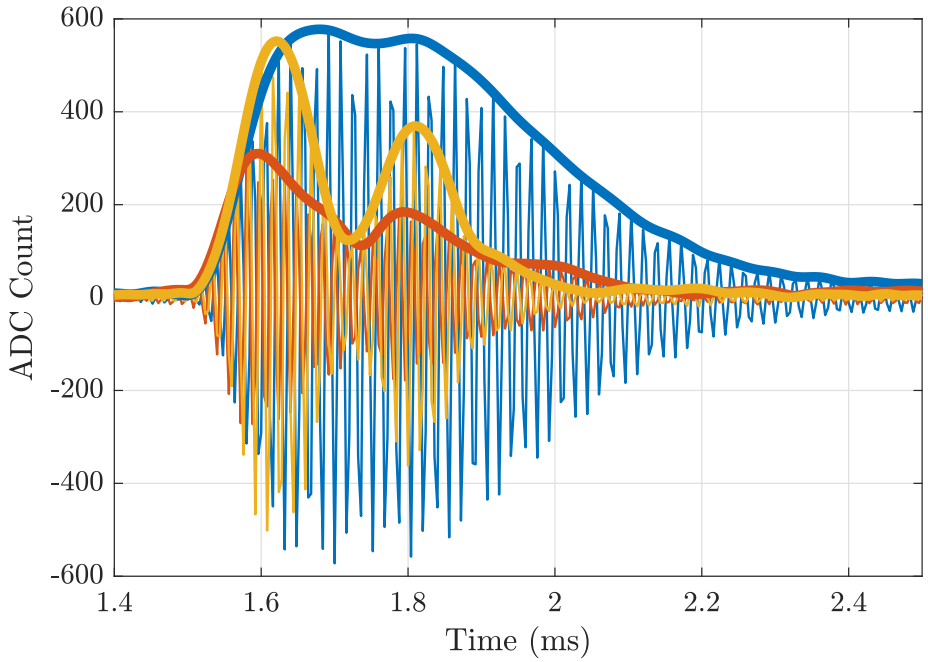

Figure 5.8: Experiment 3: Measurements at the RX-FUT. Echoes are received from two flat reflectors in the scene located at 27.5 and 30.5 cm from the sensing system. (BASE [—], TXOPT [—], RXOPT [—]). TXOPT and RXOPT improve range resolution when compared to BASE.

by about 60% with the RXOPT scheme and by about 16% with the TXOPT scheme when compared to BASE. But an important difference is that the echo with the RXOPT scheme has the same peak amplitude when compared to BASE. With the TXOPT scheme, however, the improvement comes at the expense of a reduction in the peak echo amplitude, which drops by about 49% when compared to BASE. The amplitude drop of the echo with the TXOPT scheme is due to a shorter decaying tail of the transmitted pressure wave. For the RXOPT scheme, the echo shows a faster rise to the peak compared to the BASE and the TXOPT excitation schemes, demonstrating the minimization of the rise time to peak for the echo. On the other hand, the TXOPT scheme has a peak occurring about 0.1 ms earlier compared to BASE, which is because the rise time of the transmitted pressure wave is minimized in the TXOPT scheme.

Figure 5.8 shows improvements in the range resolution due to the shortening of the width of the echoes. Two flat reflectors are present in the scene with a 3 cm separation. The experiments show detection of both reflectors in the case of RXOPT and TXOPT excitation schemes. On the other hand, with the BASE excitation scheme, the signal capture has an extended envelope due to the superposition of the echoes from the two reflectors. Therefore, detecting the echo from the reflector located farthest away from the sensing system poses challenges when compared to both TXOPT and RXOPT methods.

Note that $\alpha = 1$ for the simulations and the excitation signal applied to the TX-FUT. In actual pulse-echo experiments, $\alpha << 1$. Also, the value of α is unknown and determined by the experimental conditions. In both experiments shown by Figure 5.7 and Figure 5.8, α is maintained the same for all the three excitation schemes. The experiments consider a bistatic mode of operation as the designed excitations are for a receiver connected directly to the analog receive signal chain. However, the RXOPT methodology applies even to monostatic systems. For such situations, the transformer's secondary coil will need to be decoupled during reception to remove its influence on the receiver's dynamics. The other option is to model the transformer's secondary coil connected to the receiver during reception.

Additional improvements may be obtained with a more accurate parameter estimation of the RX-FUT as the transmitter and receiver parameters are assumed to be equal.

5.6 Excitation Signal Sensitivity

This section studies the impact of model parameter variations on key sensor performance metrics – $t_{TX},\ a_{TX},\ t_{RX},\ a_{RX}$, where $a_{TX} = \max(|y_T|)$ and $a_{RX} = \max(|y_R|)$. The analysis summarizes the sensitivity of the experimental system to simulation-generated excitation commands with errors in the model parameter values. The excitation signal (TXOPT or RXOPT scheme) synthesized for the system with a nominal set of parameters is applied to a system with a slightly different set of model parameters to study the effect on the metrics. Equation 5.2 gives the model for synthesizing the RXOPT excitation signals, which is an extended version of the model for synthesizing the TXOPT excitation signal given by Equation 3.7. Hence analysis with the RXOPT scheme is sufficient to understand the behavior with the TXOPT scheme. Recall from Subsection 3.3.1, that the parameters of the ultrasonic sensing system can be organized into three blocks – the parameters of the source and the transformer driver circuit $(R_{src},\ L_m)$, the parameters of the TX-FUT $(R_t,\ L_t,\ C_t,\ C_{tp})$, and the parameters of the RX-FUT $(R_r,\ L_r,\ C_r,\ C_{rp})$. Note that parameter variations of the TX-FUT influence both the TX-FUT and the RX-FUT, whereas parameter variations of the RX-FUT do not influence the TX-FUT. The study does not consider the transformer turns ratio (n) as the parameter scales the metrics under consideration.

Figure 5.9 – Figure 5.11 plot the variation of the four sensor performance metrics when subjected to model parameter variations. It is useful to consider normalized units when studying the effects due to parameter variations. The nominal system is the system for which the RXOPT excitation is synthesized, corresponding to no parameter variations, and the plots show the amount of variation observed with each metric when compared to the nominal system. Recall that t_{TX} provides a measure of the time to reach equilibrium after

excitation of the TX-FUT, determining the minimum range of the system. A reduction of t_{TX} is preferable as it improves the minimum range of the system. The a_{TX} provides a measure of the peak transmit amplitude. It is preferable to have an increase of a_{TX} as it improves the maximum range while also reducing the amplification requirements of the receiver's analog signal chain. The t_{RX} assesses the range resolution of the system, and as per Appendix E, a smaller t_{RX} improves the range resolution of the sensor system. Lastly, a_{RX} provides a measure of the amplitude at the RX-FUT. An increase in a_{RX} is preferable and provides an improved SNR of the echo at the RX-FUT. In the simulation-based analysis, the X-Axis of the graphs determines the level of parameter variations, while the Y-Axis determines the variation of the metric under consideration. Note that the scale values are different for each plot as each parameter affects the system differently.

Source and Transformer Driver Circuit: Figure 5.9 shows the corresponding effects.

- R_{src}**:** There is a marginal impact on the system's performance metrics due to the variation of R_{src}. For observable effects, R_{src} needs to be modified by a large magnitude. At higher values of R_{src}, the losses at R_{src} increase and reduce the power delivered to the TX-FUT. Therefore, a_{TX} and t_{TX} both reduce as the magnitude of the transmitted pressure wave decreases. The metrics a_{RX} and t_{RX} reduce because of dependence on the transmitted pressure wave. Moreover, the R_{src} parameter does not alter the oscillatory characteristics of the TX-FUT.

- L_m**:** Variation of L_m has a limited impact on the system's performance metrics. Higher values of L_m reduce the current drawn from the source during excitation intervals, allowing a slightly more efficient power delivery to the FUT.

Transmitting FUT: Figure 5.10 shows the corresponding effects.

- R_t**:** Increasing the value of R_t increases the damping in the oscillatory branch of the TX-FUT. Also, since the voltage across R_t represents the magnitude of the emitted pressure wave, a higher R_t results in a higher a_{TX} value. Because of increased

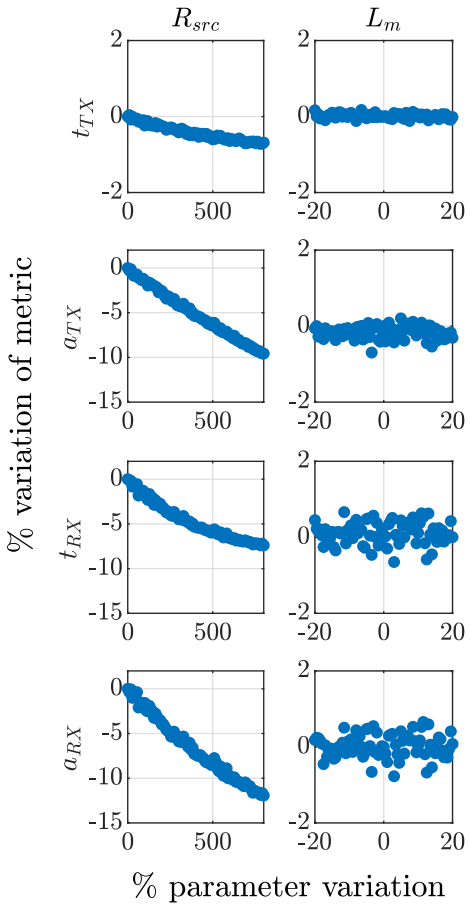

Figure 5.9: Variations of the source and the transformer driver circuit's model parameters: $R_{src},\ L_m$.

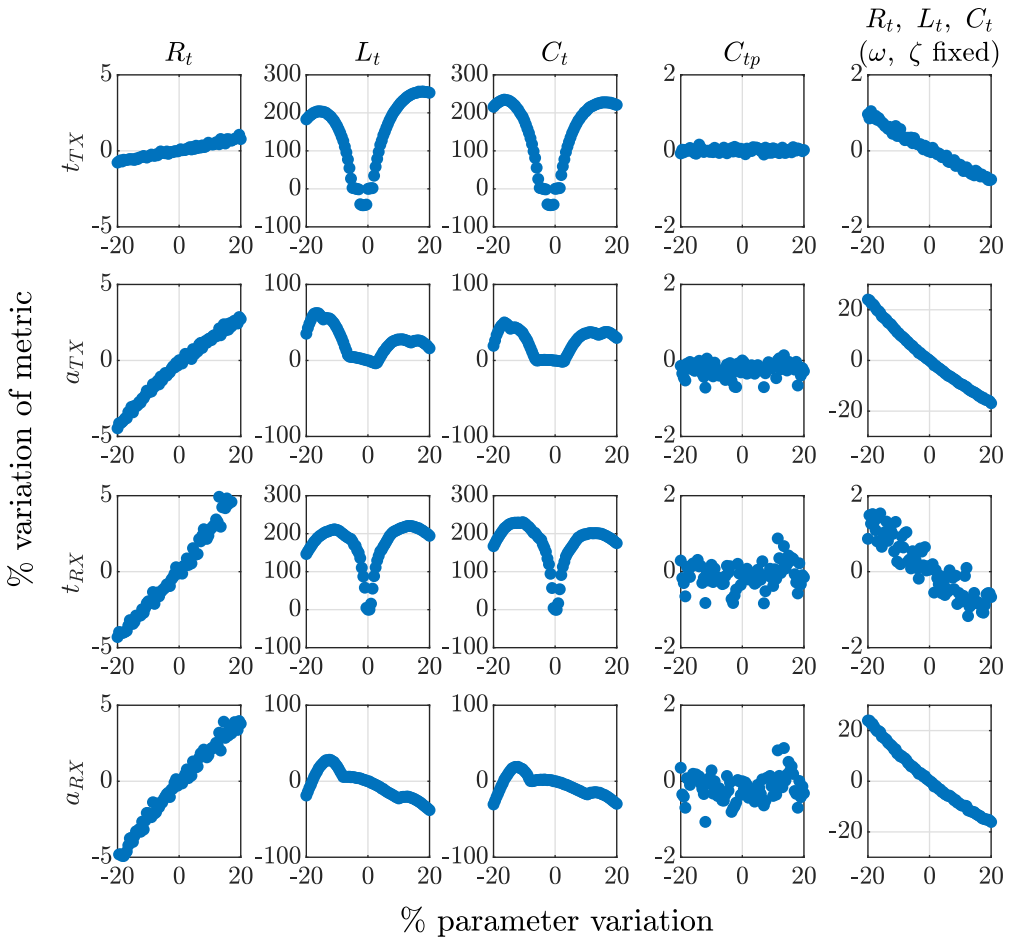

Figure 5.10: Variations of the TX-FUT's model parameters: $R_t,\ L_t,\ C_t,\ C_{tp}$. ω and ζ are the resonant frequency and the damping ratio of the TX-FUT.

damping, the t_{TX} metric is only marginally affected at higher a_{TX} values. Both a_{RX} and t_{RX} are higher as the emitted pressure increases as R_t increases.

- L_t and C_t**:** Since L_t and C_t determine the resonant frequency of the TX-FUT, it is helpful to study them together. Any variations in either parameter modify the resonant frequency of the TX-FUT, in which case, the RX-FUT's resonant frequency also differs from the TX-FUT's resonant frequency creating a mismatch. A small 5% change can result in the t_{TX} value changing by more than 25%. Hence, it is essential to estimate the L_t and C_t parameters accurately. With an increased t_{TX}, the t_{RX} metric also increases because of an increased length of the transmitted pressure wave. The value of a_{TX} shows non-monotonic variations at higher parameter discrepancies because multiple pulse bursts exist. Consequently, the trends for a_{RX} are also non-monotonic as it depends on the emitted pressure wave.

- C_{tp}**:** Changes to the value of C_{tp} do not affect any of the sensor's performance metrics because C_{tp} represents the bulk capacitance of the piezoelectric material and is not responsible for influencing the oscillatory characteristics of the FUT.

- $R_t,\ L_t,\ C_t$ vary with fixed ω and ζ**:** In this special case, all the parameters of the oscillatory branch vary, but the resonant frequency and the damping ratio are constant. Variation in a_{TX} occurs because R_t changes when L_t and C_t vary in order to maintain a constant damping ratio of the oscillatory branch. Higher values of R_t result in higher values of both a_{TX} and a_{RX}. Because of increased damping, the t_{TX} metric varies marginally. The t_{RX} metric also has marginal variations because the oscillatory branch is excited at the same resonant frequency and preserves the envelope of the emitted pressure wave, which is not the case when only ζ or ω change.

Receiving FUT: Figure 5.11 shows the corresponding effects. Since changes to the RX-FUT's parameters do not affect the TX-FUT's metrics a_{TX} and t_{TX}, they are not displayed in the plots.

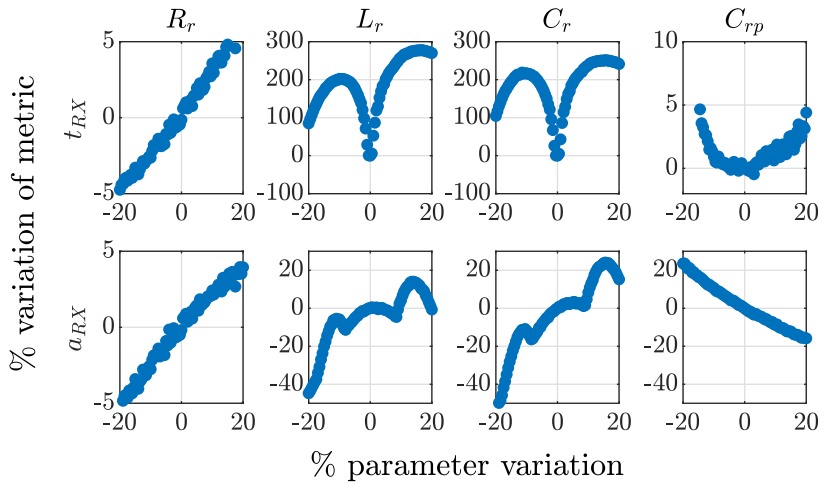

Figure 5.11: Variations of the RX-FUT's model parameters: R_r, L_r, C_r, C_{rp}.

- R_r: By circuit analysis of Figure 3.4, an increase in R_r results in a higher value of a_{RX} and t_{RX}. The increased damping in the RX-FUT prevents a large increase of the t_{RX} value when a_{RX} increases.

- L_r, C_r**:** Similar to the TX-FUT, changes to either L_r or C_r alters the resonant frequency of the RX-FUT; any small changes to either parameter result in large variations of the t_{RX} value. The a_{RX} metric has non-monotonic changes because it is possible to induce echoes consisting of multiple bursts at the RX-FUT when a frequency mismatch occurs. Such behavior is not preferable as the range resolution degrades.

- C_{rp}**:** From Figure 3.4, smaller values of C_{rp} are preferable because the C_{rp} capacitor charges more quickly, presenting larger voltages at the output of the RX-FUT. The t_{RX} value has a marginal impact because changes to C_{rp} do not alter the resonant characteristics of the RX-FUT.

5.7 Summary and Conclusion

In this chapter, time-optimal control principles are applied to design the excitation signals of a TX-FUT to influence the damping of an RX-FUT. The RXOPT control problem

minimizes the width of the voltage y_R induced at the RX-FUT by the incoming echoes. The chapter also compares the RXOPT scheme with the TXOPT scheme of Chapter 4. Experiments show a reduction in the width of the induced voltage by about 60% with the RXOPT scheme and by about 16% with the TXOPT scheme when compared with the BASE scheme. The RXOPT scheme maintains the peak amplitude of the echoes at the receiver, whereas the TXOPT scheme has a 49% drop in the peak amplitude of the echo voltage. The RXOPT scheme provides the best improvement in the range resolution followed by the TXOPT scheme when compared with BASE. For the minimum range, the TXOPT scheme provides the best improvement, while the RXOPT scheme provides a marginal improvement over BASE. A high-order transformer fed FUT along with the receiver's dynamics is considered. The solution to the 6^{th} order control problem is non-trivial and determined through numerical techniques presented in Section 4.4. The sensitivity of the excitation signal to variations in the system parameters is summarized. The research develops a math-based solution and emphasizes the tradeoffs between the three excitation schemes. For comparison, recent research presented in [8] discusses an undisclosed sub-optimal manual tuning procedure.

CHAPTER 6
MODEL FREE ENHANCEMENTS FOR FLEXURAL ULTRASONIC TRANSDUCERS

6.1 Introduction

This chapter presents two methods to improve the performance of ultrasonic transducers actuated by a pulse timing signal u_T consisting of an integer number of excitation cycles followed by an integer number of out-of-phase damping cycles. Note that the PWM peripheral with arbitrary duty cycles is not essential to realize this simplified design concept. Figure 2.1 shows the excitation response when a single FUT is used to both transmit pressure waves and receive echoes. As discussed in Section 2.1, the signal y_R contains two components – a pulse induced component (v_T) and an echo-induced component (u_R), where $y_R = v_T + u_R$. The constrained form of u_T is consistent with low-cost implementations. The first method is a transmitter enhancement; motivated by the time-optimal problem formulations of Chapter 4, a number of out-of-phase damping cycles are appended to the desired number of excitation cycles to minimize the settling time of v_T without reducing the peak value of v_T. The second method is a receiver enhancement; the echo-induced transducer voltage u_R is isolated from the pulse-imposed transducer voltage v_T by subtracting a stored masking signal from the acquired receiver signal. The proposed methods rely on a simple learning procedure that does not require a mathematical model of the system or the use of a nonlinear programming solver, as discussed in Section 4.4. Because this procedure is executed on an embedded microcontroller, the proposed methods are insensitive to variations in components or parameters. Experiments demonstrate improvements in minimum range and range resolution; measurements using one and two reflectors are discussed.

The first method involving out-of-phase damping cycles goes beyond existing literature

in several ways: an embedded low-cost solution is developed, thereby eliminating the need for laboratory instrumentation and the reliance on highly specialized v_T waveforms; explicit procedures are given that automatically produce the optimal number of damping cycles for a desired number of excitation cycles, thereby eliminating the ambiguity arising from undisclosed manual tuning processes used in existing work; circuit modifications and component variations are both easily accommodated without any need for microcontroller reprogramming, due to the model-free self-tuning framework. The second method, which uses a stored masking signal to estimate the echo-induced voltage via $u_R = y_R - v_T$, is not presented in the published literature.

6.2 Proposed Enhancements

In this section, the proposed enhancements are described with a level of detail sufficient to enable their use by others. It is assumed that the resonant frequency f and hence period $T = \dfrac{1}{f}$ of the transducer have been determined, e.g. using methods from [54]; embedded solutions are possible.

6.2.1 Transmitter Enhancement: Damping

Recall from Figure 3.12 that $u_T(t)$ is the pulse timing signal generated by the microcontroller. Consistent with low-cost implementation, $u_T(t)$ is constrained to take the form

$$u_T(t) = \begin{cases} +(-1)^i & , \; t \in \mathcal{T}_e \\ -(-1)^i & , \; t \in \mathcal{T}_d \\ 0 & , \; \text{otherwise} \end{cases} \tag{6.1}$$

where the integer i is determined from

$$i = \lfloor 2(t - t_0)/T \rfloor, \tag{6.2}$$

t_0 is the time instant at which transmission begins, $\lfloor \cdot \rfloor$ denotes the floor function, and the excitation and damping cycle time intervals are given by

$$\mathcal{T}_e = [t_0, t_0 + n_e T) \tag{6.3}$$

$$\mathcal{T}_d = [t_0 + n_e T, t_0 + (n_e + n_d) T) \tag{6.4}$$

where n_e is the integer number of excitation cycles and n_d is the integer number of out-of-phase damping cycles. According to Equation 6.1 – Equation 6.4, the only variables available to influence $v_T(t)$ are n_e and n_d, implying that the precise shape of $v_T(t)$ cannot be directly manipulated. The maximum range of the sensor is proportional to n_e (over the usable range of n_e), and the goal of the proposed transmitter enhancement is to determine the n_d that minimizes the settling time of $v_T(t)$ for a given n_e.

6.2.2 Receiver Enhancement: Masking

Recall from Figure 3.12 that $\tilde{y}_R(t)$ is the signal sampled by the microcontroller for purposes of echo detection and processing. Since $\tilde{y}_R(t)$ represents $y_R(t)$ after passing through a high-gain bandpass filter, it inherits from y_R the decomposition

$$\tilde{y}_R(t) = \tilde{v}_T(t) + \tilde{u}_R(t) \tag{6.5}$$

where $\tilde{v}_T(t)$ represents the pulse-imposed component of the measurement and $\tilde{u}_R(t)$ represents the echo-induced component of the measurement. If no reflectors are in the field of view, then the signal components $\{\tilde{v}_T(t),\ \tilde{u}_R(t)\} = \{\tilde{y}_R(t),\ 0\}$ will depend on $(n_e,\ n_d)$ in a consistent and predictable way. For any $(n_e,\ n_d)$ of interest, it is possible to record $\tilde{y}_R(t)$ with no reflectors present during commissioning to obtain an estimate $\hat{v}_T(t)$ of $\tilde{v}_T(t)$ for

subsequent use, i.e.

$$\hat{v}_T(t) = \begin{cases} \tilde{y}_R(t) & , \ t \in [t_1, t_2) \\ 0 & , \ \text{otherwise} \end{cases} \tag{6.6}$$

where $\tilde{y}_R(t)$ is measured with no reflectors present, t_1 is the first time instant for which the peaks of $\tilde{y}_R(t)$ fall below the voltage saturation level, and t_2 is the first time instant for which the peaks of $\tilde{y}_R(t)$ fall below the voltage noise level. In subsequent experiments involving reflectors, Equation 6.5 – Equation 6.6 establish that the signal $\tilde{u}_R(t)$ may be estimated using the measured $\tilde{y}_R(t)$, the previously stored $\hat{v}_T(t)$, and the relationship

$$\hat{u}_R(t) = \begin{cases} 0 & , \ t \in [0, t_1) \\ \tilde{y}_R(t) - \hat{v}_T(t) & , \ \text{otherwise.} \end{cases} \tag{6.7}$$

An echo may be reliably detected from $\hat{u}_R(t)$ beginning at t_1, or from $\tilde{y}_R(t)$ beginning at t_2. The blind zone for reliable echo detection has been reduced because $t_1 < t_2$. The signal $\hat{v}_T(t)$ is called a mask, since it potentially hides detectable echoes from nearby reflectors. The objective of the proposed receiver enhancement is to record the mask $\hat{v}_T(t)$ for desired values of (n_e, n_d), to improve minimum range via Equation 6.7.

6.2.3 Commissioning Algorithms

The enhancements defined in Subsection 6.2.1 and Subsection 6.2.2 are enabled by a sensor commissioning procedure that involves pulse-echo experiments conducted with no reflectors present. In this procedure, transmitter parameters $(n_e, \ n_d)$ are inputs and receiver signal samples $y[k] = \tilde{y}_R(kT_s)$ are outputs, where k is the sampling index and T_s is the sampling period. Given an initial index K, a window length L and a threshold value Y, the

signal $y[k]$ is characterized by a settling index k_s, defined as the smallest value of k such that

$$|y[i]| \leq Y, \quad i \in [k,\ k+L), \quad k \geq K \tag{6.8}$$

The commissioning procedure relies on two algorithms. The first algorithm systematizes the evaluation of settling index k_s by finding the smallest k satisfying Equation 6.8, whereas the second algorithm uses settling index values to obtain the information needed to implement the proposed enhancements. An auxiliary result of the second algorithm is a set of metrics quantifying achievable improvements in sensor performance.

Algorithm 2 takes a receiver signal $y[k]$, which is generated by the transmitter using Equation 6.1 – Equation 6.4 with $(n_e,\ n_d)$, and extracts the settling index k_s of that signal. Three parameters provide some flexibility in the specification of k_s: the initial index K should be such that $KT_s \geq t_0$ to limit the search to the active transmitter interval; the window length L should be such that $LT_s \geq T$ to ensure at least one cycle of oscillation is accounted for; and threshold level Y should be set to either a large value, say Y_{large} corresponding to saturation level, or a small value, say Y_{small} corresponding to noise level, depending on use case. Line 4 requires that signal magnitude be below the threshold for all samples in the window. The left window edge defines the settling index k_s, implying that $y[k_s]$ is the first sample of $y[k]$ to settle below threshold level Y.

Algorithm 3 determines and stores the information needed to implement the transmitter enhancement (damping) and the receiver enhancement (masking); i.e. the optimal $(n_e,\ n_d)$ pairs subject to transmitter operating constraints Equation 6.1 – Equation 6.4, and the corresponding signals $\hat{v}_T[k]$ defined in Equation 6.6. For each n_e value of interest, a range of n_d values results in a sequence of no-reflector experiments and resulting receiver signals $y[k]$. Each receiver signal is evaluated to determine two settling indexes, k_1 and k_2, using Algorithm 2; the first uses a saturation-level threshold $Y = Y_{\text{large}}$ to determine when $y[k]$ settles below saturation, whereas the second uses a noise-level threshold $Y = Y_{\text{small}}$ to

Algorithm 2: Settling Index Evaluation for $(n_e,\ n_d)$

Input:

- signal $y[k]$ from $(n_e,\ n_d)$, parameters K, L, Y

Outputs:

- settling index k_s

```
1  Initialize q ← 1
2  Initialize k ← K
3  while q = 1 do
4  |  if |y[i]| ≤ Y for all i ∈ [k, k + L) then
5  |  |  k_s ← k
6  |  |  q ← 0
7  |  else
8  |  |  k ← k + 1
9  |  end
10 end
11 return k_s
```

determine when $y[k]$ settles below noise. For each n_e, line 1 defines the range of n_d under consideration, and line 7 selects from this range the value n_d^* that provides minimum settling index k_1 or k_2. The search range $n_d \in [0,\ n_e]$ is consistent with the need to balance the energy contributions of n_e (positive) and n_d (negative). The values obtained for n_d^* by minimizing either k_1 or k_2 will be the same, for appropriate choices of $(K,\ L,\ Y)$. Line 8 stores the corresponding mask signal $\hat{v}_T[k]$, which is nonzero over $k \in [k_1,\ k_2]$, for use in echo detection. Line 9 stores the corresponding values $(k_1,\ k_2)$ as performance metrics.

The settling indexes provided by Algorithm 2 and Algorithm 3 quantify the performance improvements enabled by the proposed transmitter enhancement (damping) and the proposed receiver enhancement (masking). Algorithm 2 returns a settling index k_s that functionally depends on five parameters:

$$k_s = f(n_e,\ n_d,\ K,\ L,\ Y) \tag{6.9}$$

Algorithm 3 explicitly returns settling indexes k_1 and k_2, but it also implicitly returns another

Algorithm 3: Learning Procedure for Damping and Masking

Input:

- parameter range $n_e \in [n_{e,\min},\ n_{e,\max}]$

Outputs:

- $(n_e,\ n_d^*)$ pairs and associated $\hat{v}_T[k]$ masks

```
for n_e ← n_e,min to n_e,max do
    for n_d ← 0 to n_e do
        acquire y[k] using (n_e, n_d)
        evaluate k_1 using Algorithm 2 with Y_large
        evaluate k_2 using Algorithm 2 with Y_small
    end
    determine n_d* as the n_d that minimizes k_1 or k_2
    store v̂_T[k] mask corresponding to (n_e, n_d*)
    store (k_1, k_2) metrics corresponding to (n_e, n_d*)
end
return (n_e, n_d*) and v̂_T[k] for n_e ∈ [n_e,min, n_e,max]
```

settling index k_3, and all of these settling indexes are special cases of Equation 6.9 via

$$k_1 = f(n_e,\ n_d^*,\ K,\ L,\ Y_{\text{large}})$$

$$k_2 = f(n_e,\ n_d^*,\ K,\ L,\ Y_{\text{small}})$$

$$k_3 = f(n_e,\ 0,\ K,\ L,\ Y_{\text{small}})$$

with $k_0 < k_1 < k_2 < k_3$ where transmitter operation begins at $t_0 = k_0 T_s$. An echo may be reliably detected beginning at $t_3 = k_3 T_s$ for the baseline system, at $t_2 = k_2 T_s$ with damping enabled, or at $t_1 = k_1 T_s$ with damping and masking enabled.

6.3 Experimental Results

Figure 3.12 shows the hardware circuit for experimental verification. The significant parameters of the experimental setup are summarized in Table 3.2. The Table 6.1 provides the parameters for executing the model-free algorithms. With just 4.25 samples per cycle and 12-bit resolution, the implementation intentionally emphasizes low cost applications; the relatively low sampling frequency is visually evident in the data plots that follow. Threshold

Table 6.1: Model Free Algorithm Parameters

Parameter	Symbol	Value
Initial Index	k_0, K	30
Window Length	L	10
Saturation Threshold	Y_{large}	2030
Noise Threshold	Y_{small}	204

values are listed without units, since sample values $y[k]$ are interpreted as signed integers between -2048 and 2047 (even though signal $\tilde{y}_R(t)$ is a voltage). All experiments use the same transmitter source voltage, the same receiver passband gain, and (when present) the same flat wooden reflectors.

The commissioning procedure defined in Algorithm 3 was applied to the experimental system with no reflectors present, using the parameters listed in Table 6.1. The window length L corresponds to 2.35 cycles, and the chosen threshold values Y_{large} and Y_{small} result in identical $(n_e,\ n_d^*)$ pairs using either k_1 or k_2 minimization in line 7; moreover, the resulting $(n_e,\ n_d^*)$ pairs remain the same for all neighboring parameter choices. The performance metrics obtained from Algorithm 3 are summarized in Table 6.2. The values listed in the k_3, k_2, and k_1 columns represent the earliest sampling indexes for which an echo may be reliably detected, for the cases of baseline, damping alone, and damping with masking, respectively. Minimum range is

$$r_{\min} = \frac{1}{2} v_{sound}(k_i - k_0)T_s, \quad i \in \{1, 2, 3\} \tag{6.10}$$

For $n_e = 5$, Equation 6.10 yields $r_{\min} \in \{11.1,\ 14.6,\ 18.8\}$ cm. Using Equation 6.10, the final two columns show the extent to which the proposed transmitter and receiver enhancements improve minimum range over the baseline system for each n_e; damping alone yields measured $r_{\min}$ improvements of 18 – 28%, whereas damping with masking yields measured $r_{\min}$ improvements of 31 – 44%.

In the sequence of plots presented below, the focus is on a comparison of sensing system

Table 6.2: Measurements of Performance Metrics

n_e	n_d^*	k_1	k_2	k_3	$\frac{k_3 - k_1}{k_3 - k_0}$	$\frac{k_3 - k_2}{k_3 - k_0}$
3	2	180	237	289	0.42	0.20
4	3	199	248	302	0.38	0.20
5	3	193	245	306	0.41	0.22
6	4	221	261	315	0.33	0.19
7	4	192	239	319	0.44	0.28
8	4	219	263	332	0.37	0.23
9	5	242	282	336	0.31	0.18
10	5	237	273	340	0.33	0.22

performance for two particular transmitter parameter pairs. The choice $(n_e,\ n_d) = (5,\ 0)$ leads to baseline performance (BASE), whereas the choice $(n_e,\ n_d) = (5,\ 3)$ leads to enhanced performance. Figure 6.1 shows the pulse timing signal $u_T(t)$ for the $(n_e,\ n_d)$ pairs of interest, generated by Equation 6.1, where transmitter operation begins at 0.12 ms.

Figure 6.2 reveals the effect of damping alone, using measured $y[k]$ versus kT_s plots; Figure 6.2a corresponds to the no-reflector commissioning experiments, whereas Figure 6.2b corresponds to experiments with a reflector located 15 cm from the transducer (round-trip time of 0.882 ms). The transmitter begins at 0.12 ms, so the echo arrives around 1 ms. When the baseline parameters $(n_e,\ n_d) = (5,\ 0)$ are used, the echo cannot be detected. On the other hand, when the preferred parameters $(n_e,\ n_d) = (5,\ 3)$ are used, the echo is clearly detectable in Figure 6.2b. Therefore, damping alone has a favorable impact on the sensor's minimum range.

Figure 6.3 – Figure 6.4 reveals the effect of damping and masking together, using measured $y[k]$ versus kT_s plots; Figure 6.3 corresponds to the no-reflector commissioning experiments, whereas Figure 6.4 corresponds to experiments with a reflector located 11.1 cm from the transducer (round-trip time of 0.65 ms). The transmitter begins at 0.12 ms, so the echo arrives around 0.77 ms.

The preferred parameters $(n_e,\ n_d) = (5,\ 3)$ are used in Figure 6.3 – Figure 6.4, but

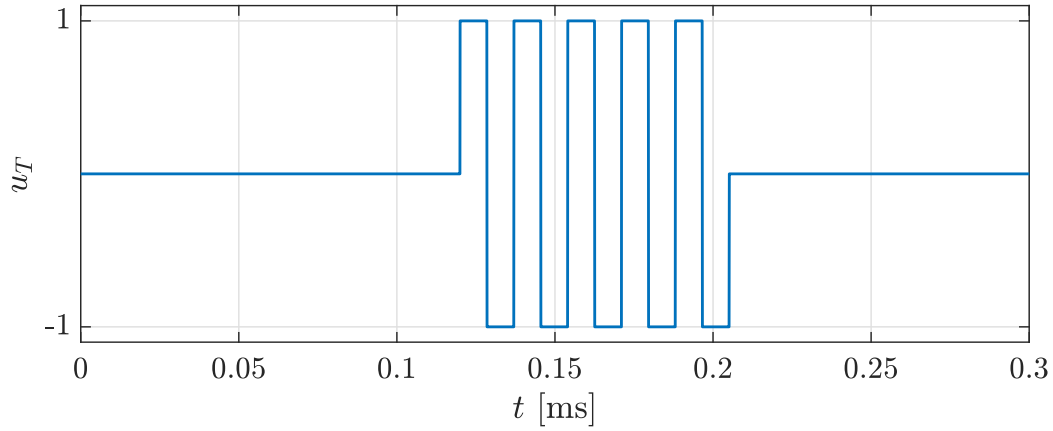

(a) Signal $u_T(t)$ using $(n_e,\ n_d) = (5,\ 0)$.

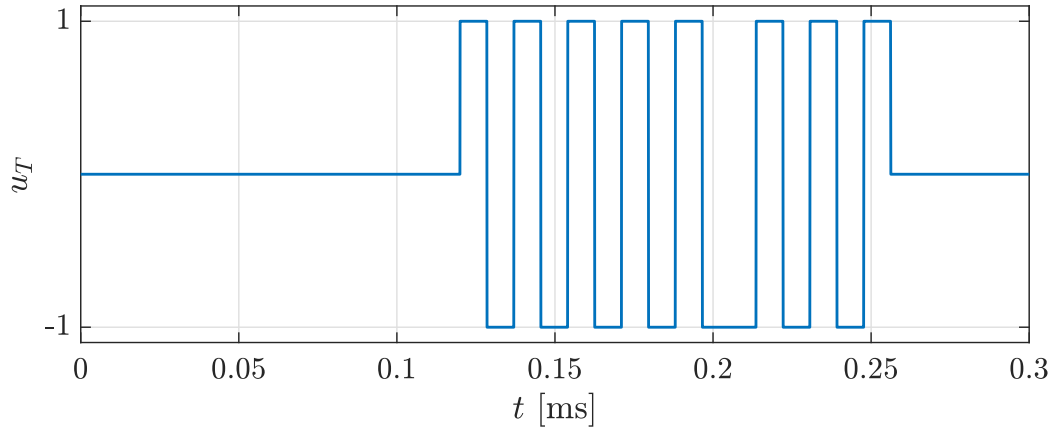

(b) Signal $u_T(t)$ using $(n_e,\ n_d) = (5,\ 3)$.

Figure 6.1: Pulse timing signal without and with damping.

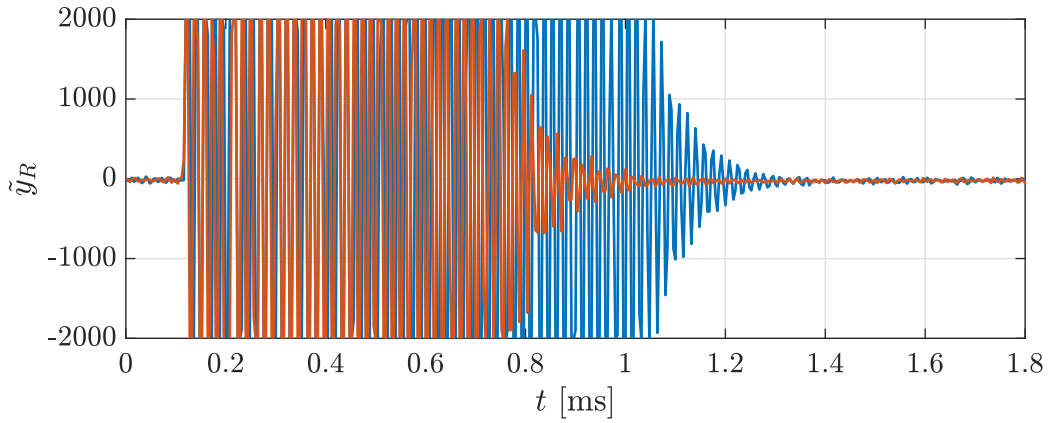

(a) No-reflector commissioning signal for damping.

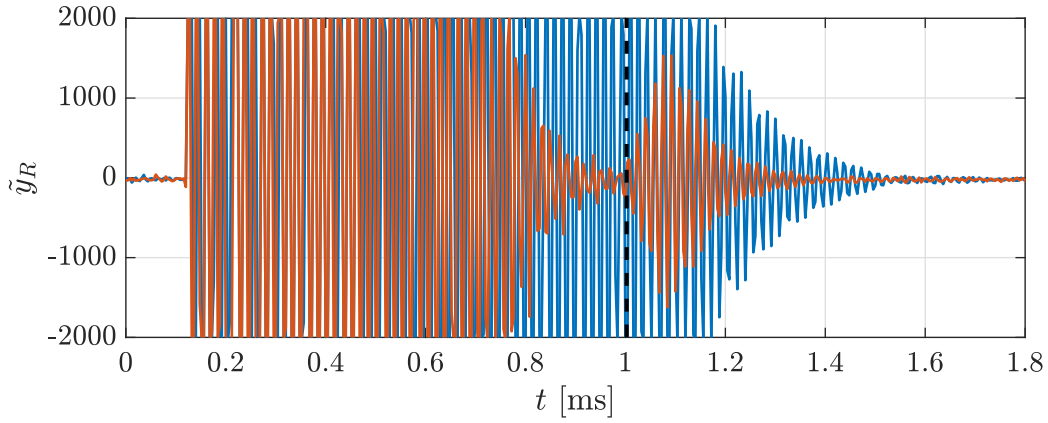

(b) One reflector at 15 cm. Echo detected from $\tilde{y}_R$ for $(n_e,\ n_d) = (5,\ 3)$.

Figure 6.2: Plots reveal the benefits of damping. Signal $\tilde{y}_R$ for $(n_e,\ n_d) = (5,\ 0)$ [—]. Signal $\tilde{y}_R$ for $(n_e,\ n_d) = (5,\ 3)$ [—].

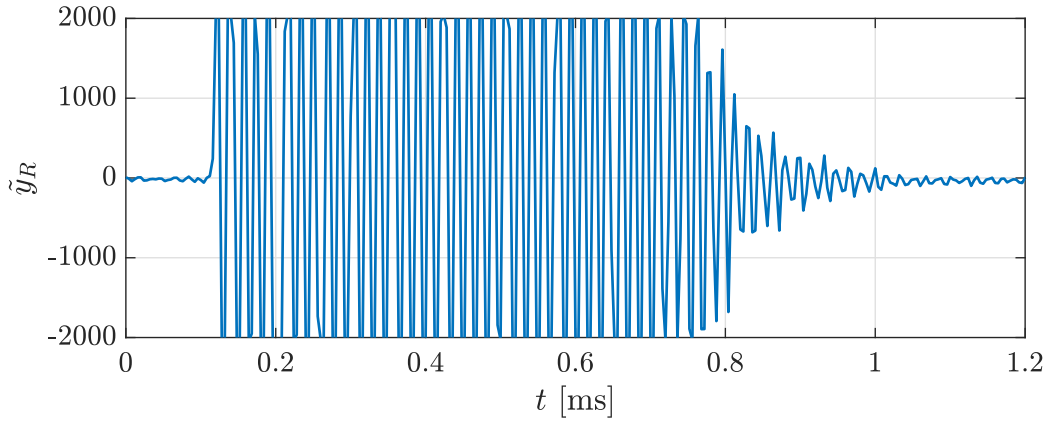

(a) $(n_e,\ n_d) = (5,\ 3)$, commissioning signal $\tilde{y}_R$.

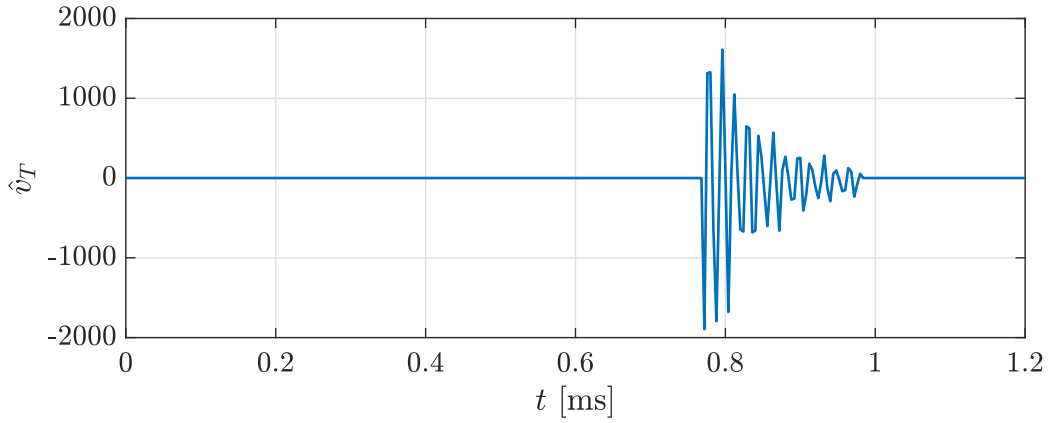

(b) $(n_e,\ n_d) = (5,\ 3)$, commissioning signal $\hat{v}_T$.

Figure 6.3: No-reflector commissioning experiment for masking.

the echo cannot be detected from $y[k]$ in Figure 6.4a. The mask signal $\hat{v}_T[k]$ shown in Figure 6.3b is used to compute the echo signal $\hat{u}_R[k]$ shown in Figure 6.4b which clearly reveals the otherwise hidden echo. Therefore, masking in combination with damping further improves the sensor's minimum range.

Figure 6.5 reveals the influence of damping on echo duration. In Figure 6.5a there is one reflector at 38 cm, whereas in Figure 6.5b there are two reflectors at 35 cm and 38 cm (round-trip separation time of 0.176 ms). In Figure 6.5, comparing $n_d = 0$ and $n_d = 3$, the echo duration has been reduced by damping, offering a greater possibility for detecting the presence of two closely spaced reflectors. From Appendix E, the range resolution can be

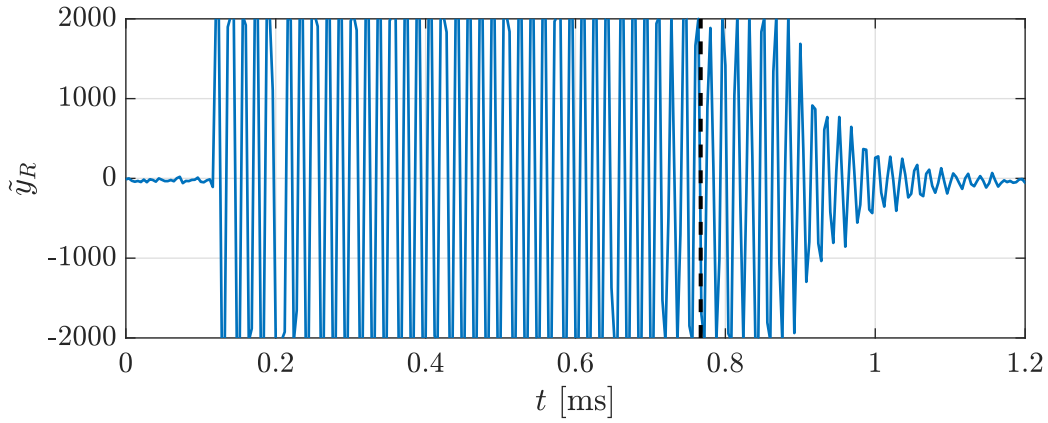

(a) $(n_e,\ n_d) = (5,\ 3)$, echo not detected from $\tilde{y}_R$.

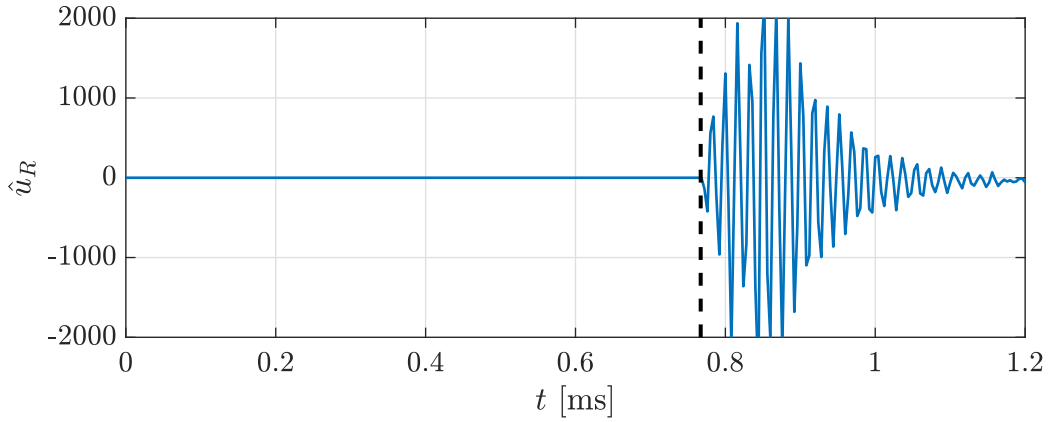

(b) $(n_e,\ n_d) = (5,\ 3)$, echo detected from $\hat{u}_R$.

Figure 6.4: Plots reveal the benefits of masking with one reflector at 11.1 cm.

quantified from measured echoes according to

$$\Delta r_{\min} = \tfrac{1}{4} v_{sound} \left(k_R - k_L\right) T_s \tag{6.11}$$

where k_R and k_L are the right and left indexes that determine echo duration, using magnitude bound $Y_{\text{small}} = 100$ and window length L, as shown in Figure 6.5. Values of $\Delta r_{\min}$ from Equation 6.11 are 3.94 cm for Figure 6.5a and 2.35 cm for Figure 6.5b, so damping provides a 41% improvement. Reflector separation in Figure 6.5b is 3 cm, so $n_d = 0$ will fail but $n_d = 3$ will succeed. These predictions are correct, since the measurement of $y[k]$ in Figure 6.5b with $n_d = 0$ shows a single-peak envelope, whereas the measurement of $y[k]$ with $n_d = 3$ shows a two-peak envelope.

6.3.1 Comparison of Damping with TXOPT

Figure 6.6 and Figure 6.7 compare the damping obtained with the three schemes – BASE, the TXOPT scheme of Chapter 4, and the model-free damping approach of this chapter. The BASE and the model-free damping methods apply the excitation $(n_e,\ n_d) = (5,\ 0)$ and $(n_e,\ n_d) = (5,\ 3)$ respectively as shown in Figure 6.1, and the TXOPT excitation scheme applies the excitation signal shown in Figure 4.7. The TXOPT scheme has the best decay characteristics, which is closely followed by the model-free damping scheme as shown in Figure 6.6a. The TXOPT excitation applies fractional width pulses and provides the additional enhancement in the decay characteristics when compared with the model-free damping scheme which applies an integral number of full-width pulses. With a single reflector at 15 cm in front of the sensor system, the TXOPT and the model-free schemes achieve comparable performance as shown by Figure 6.6b. Note that the TXOPT scheme's envelope has slightly faster rise and decay characteristics compared to the model-free scheme. The peak amplitude with the TXOPT scheme is marginally higher compared to the model-free damping scheme.

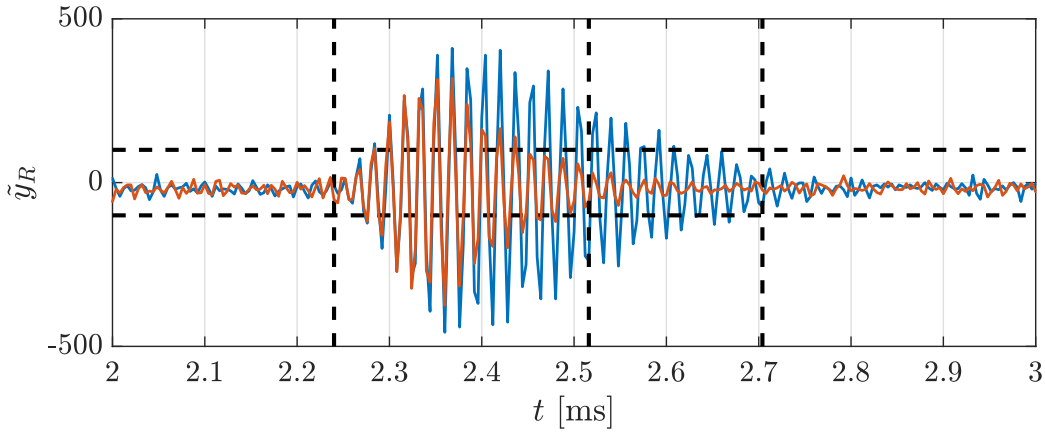

(a) One reflector at 38 cm. $(n_e,\ n_d) = (5,\ 0)$, echo has longer duration. $(n_e,\ n_d) = (5,\ 3)$, echo has shorter duration. Horizontal dashed lines are at ± 100.

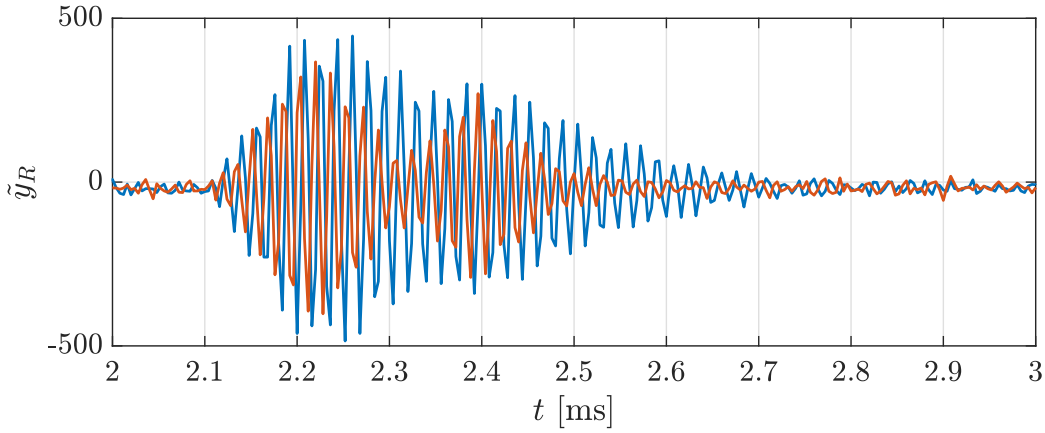

(b) Two reflectors at 35 cm and 38 cm. $(n_e,\ n_d) = (5,\ 0)$, envelope shows one peak. $(n_e,\ n_d) = (5,\ 3)$, envelope shows two peaks.

Figure 6.5: Interval between vertical dashed lines is $(k_R - k_L)\, T_s$. Echo duration is reduced by damping. $(n_e,\ n_d) = (5,\ 0)$ is shown in [—], and $(n_e,\ n_d) = (5,\ 3)$ in [—].

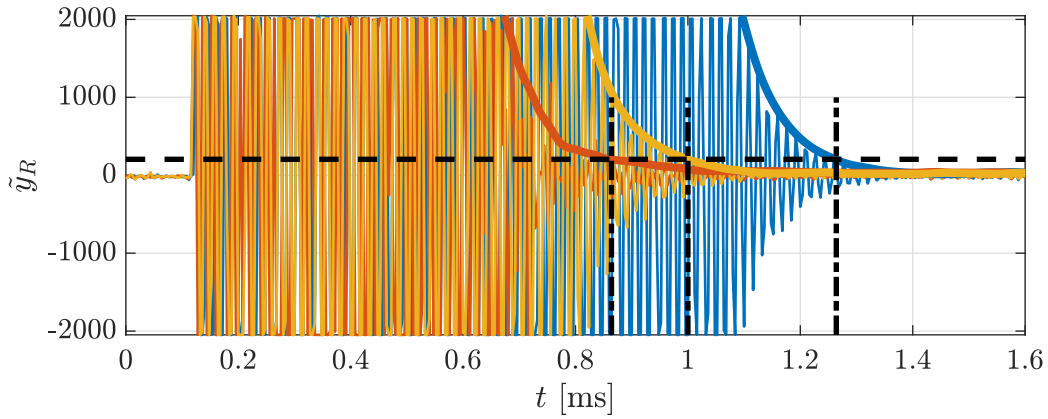

(a) Residual vibrations and the envelope after exciting the FUT. No reflector in the scene.

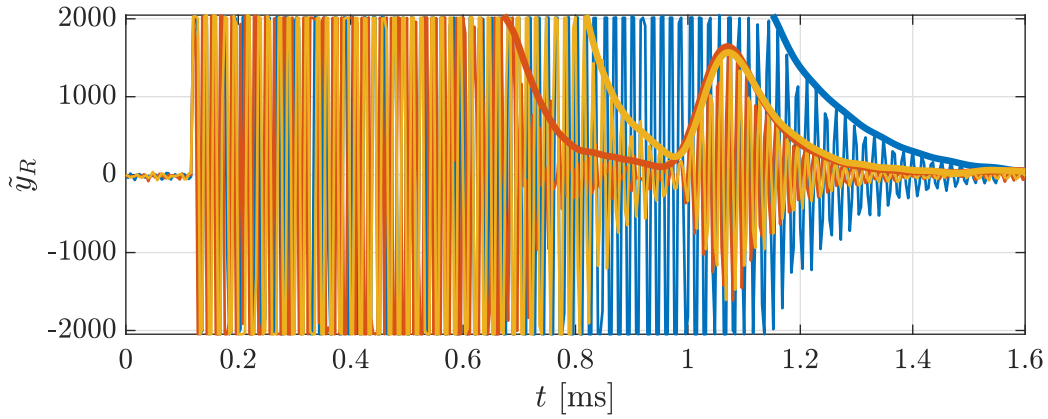

(b) Echo detection with a single reflector at 15 cm.

Figure 6.6: Experiment: Plots compare BASE for $n_e = 5$ [—], TXOPT scheme [—], and the Model-Free damping scheme for $(n_e,\ n_d) = (5,\ 3)$ [—].

Figure 6.7 compares the minimum range with the three schemes under consideration. The indices (k_3) returned by Algorithm 3 for the model-free damping scheme are converted to range estimates using Equation 1.1. The TXOPT scheme provides the best minimum range (decay characteristics) with an average improvement of about 32%, whereas the model-free approach provides an average improvement of about 22%. The model-free damping is approximately time-optimal and is simpler to implement compared to the TXOPT approach, which requires a math model of the system, knowledge of system parameter values, and the use of NLP solvers to determine the numerical solution to an OCP.

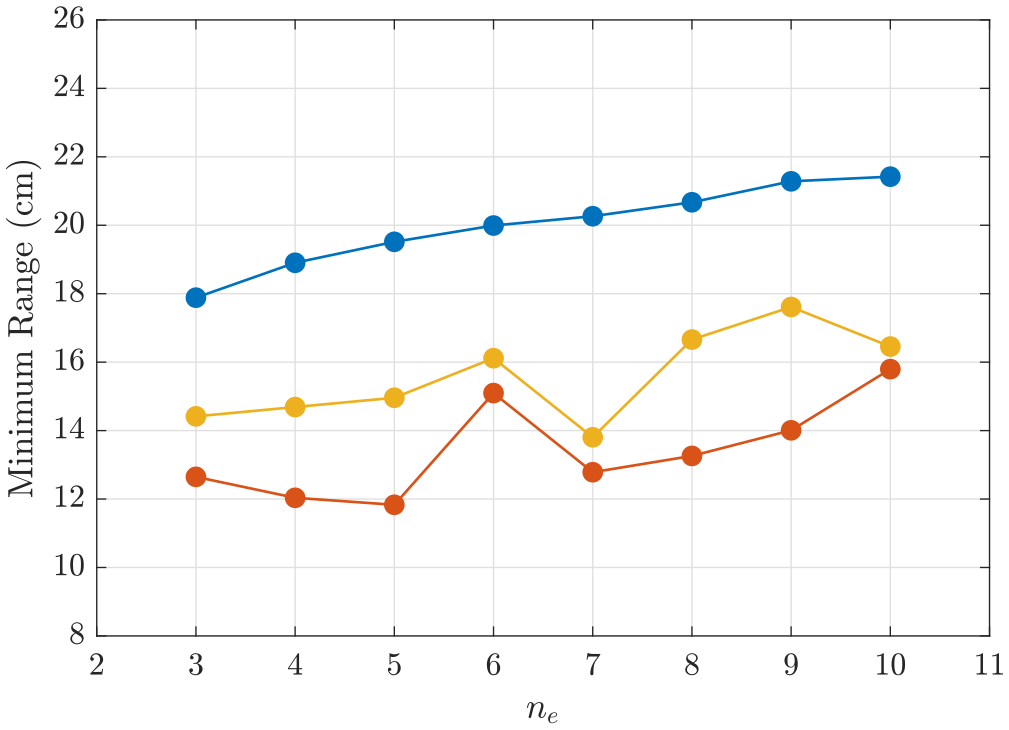

Figure 6.7: Experimental minimum range improvement of the TXOPT [—] and Model-Free Damping [—] schemes over BASE [—]. Target current I_0 for u_T^* in the TXOPT scheme is set to the peak current value obtained with BASE.

6.4 Summary and Conclusion

Two enhancements, referred to as damping and masking, have been developed to avoid the undesired consequences of residual vibrations in monostatic sensing systems that use flexural ultrasonic transducers. Out-of-phase damping cycles are applied subsequent to the excitation cycles during transmitter operation to reduce the time duration of oscillation without sacrificing the peak amplitude of oscillation. Masking signals that are measured and stored during commissioning are used to modify the signals obtained during receiver operation to reveal reflector echoes that would otherwise remain hidden. These two enhancements improve the sensor's minimum range and range resolution, as verified by experiments.

The proposed enhancements represent novel contributions that are broadly applicable and simple to implement. There is no significant restriction on the type of transducer or circuitry being used, there is no need for a system model or parameter values aside from the

maximum number of allowed excitation cycles, and the commissioning procedure is fully defined by two algorithms that can be easily realized using low-resource microcontrollers. The self-tuning capability resulting from the embedded implementation of these algorithms automatically provides minimum settling time, subject to the constraints on transmitter operation adopted here. The work presented in this chapter resulted in the publication of the journal paper [55].

CHAPTER 7
3-D ULTRASONIC IMAGING

7.1 Introduction

Previous chapters focused on improving ranging capabilities (the minimum range and the range resolution) of ultrasonic sensors by controlling the residual vibrations of an FUT. In the example of Figure 1.1, the objects $(1,\ 2,\ 3)$ are located at different radial distances but also in different directions. The transducer configurations already studied can estimate only the reflector's range. This chapter addresses the design of an ultrasonic sensor utilizing multiple transducers and a beamforming-based processing algorithm to determine the reflector positions in 3-D space, estimating both the range and the bearing.

The sensor consists of a single narrowband FUT for transmitting pressure waves and a small number of analog MEMS microphones for receiving the pressure waves. Fewer receiving elements reduce the overall cost to manufacture the array, the associated computation cost, and the data storage requirements. The processing algorithm allows data acquisition to occur at high update rates of up to 45 Hz, comparable to a vision-based system. The sensor also has a small footprint making it suitable for use in applications that have space constraints. The chapter describes end-to-end system design aspects such as sensor array design and analog and digital processing requirements. The processing algorithm is designed to be executed rapidly on low-cost embedded devices and uses a single pulse-echo trial to resolve multiple reflectors. Computation cost details specify requirements for dedicated single-chip solutions. Experiments demonstrate array design and algorithm performance in a scene consisting of several reflectors.

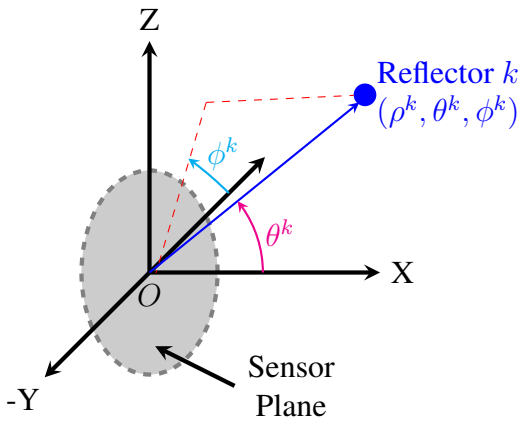

Figure 7.1: Schematic of the sensor's workspace. The reflector k is located at the point $(\rho^k, \theta^k, \phi^k)$, where ρ^k is the radial distance, ϕ^k, and θ^k are the azimuth and polar angles.

7.2 Sensor System

Figure 7.1 clarifies the sensor's workspace. The elements of the sensor are located in the YZ plane. The k reflectors are at the spherical coordinate $(\rho^k, \theta^k, \phi^k)$, where ρ^k is the radial distance, ϕ^k, and θ^k are the azimuth and polar angles measured from the origin of the array to each reflector. The array's normal is along the positive X-axis. The designed array is shown in Figure 7.2 and consists of a single narrowband FUT (Murata MA58MF14-7N) operating at the resonant frequency (f_e) of 58.5 kHz, and an array of wideband MEMS microphones (Knowles SPV08A0LR5H-1). The FUT is used only for emitting pressure waves and is driven by the transformer network of Figure 3.12. The pressure wave is launched by exciting the FUT with an integral number of cycles n_e at the resonant frequency f_e given by Equation 3.8 – Equation 3.10. The receiver array consists of M low-cost MEMS microphones to collect echoes from the scene and are installed on a printed circuit board. Appendix F provides the schematic of the receiver array and the board layout.

The transmitter and the microphones have a circular aperture, and the Airy function

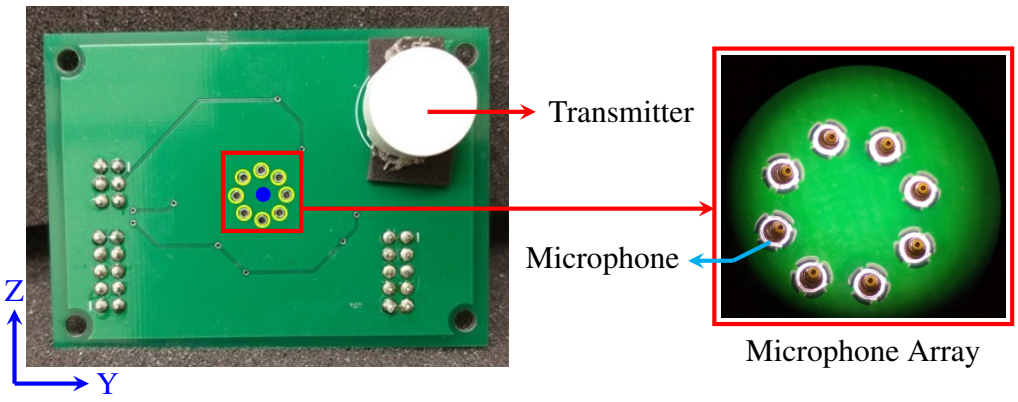

Figure 7.2: Ultrasonic sensor. The transmitter and the elements of the microphone array are located in the YZ plane with the origin situated at the center of the microphone array.

describes the radiation pattern. From [28], it is given by

$$H(\theta) = \frac{J_1\left(\frac{2\pi}{\lambda} a \sin(\theta)\right)}{\left(\frac{2\pi}{\lambda} a \sin(\theta)\right)} \tag{7.1}$$

where J_1 is a Bessel function of the first kind, λ is the wavelength, and a is the radius of the aperture. The radiation pattern functionally depends only on the polar angle (θ) due to the symmetry of the circular aperture about the azimuth. The distribution of microphone elements is a design choice. A uniform circular arrangement is preferable because of symmetry, routing of the circuit traces on the printed circuit board, and suitability for manually installing sensor elements. Uniform circular arrays also have lower levels of beam broadening compared to other arrangements as the look direction is varied [28, 56].

Figure 7.3 plots the normalized radiation pattern of the transmitter element, the receiver element, and the operation of the sensor array using the parameters listed in Table 7.1. The region of interest is the front of the sensor array, i.e., a sweep range of $\theta \in [-90,\ +90]$ degrees. The span of the main lobe determines the active region of a transducer, determined using the -3 dB definition in the literature [28]. In Figure 7.3, it is represented by the line at -3 dB w.r.t the maximum amplitude. The transmitter insonifies a region of space between $\pm 12.5^o$. On the other hand, the microphone has an omnidirectional response; because

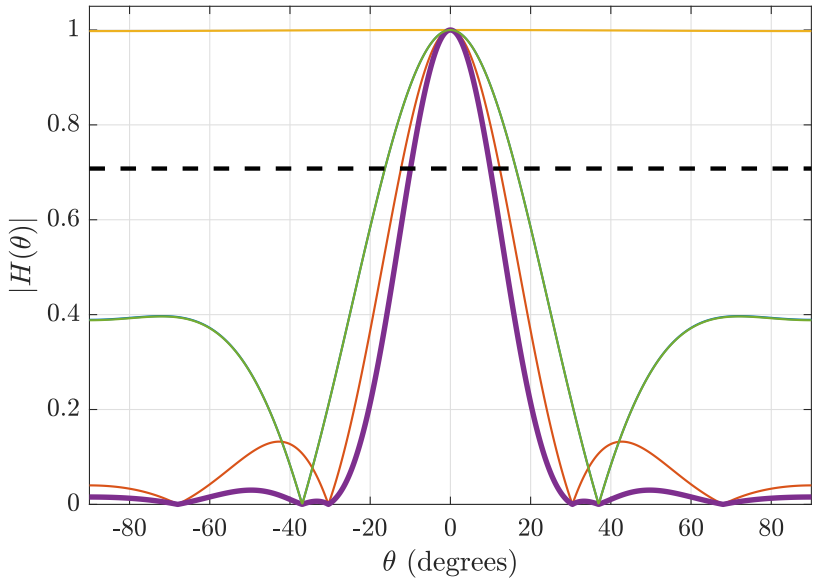

Figure 7.3: Normalized radiation pattern. Element factor of the FUT (H_t) [—], element factor of the microphone (H_m) [—], array factor (AF) and the receiver array radiation pattern (H_r) [—], two-way radiation pattern (H_{tr}) [—], and -3 dB line [- -]. As $|H_m| \approx 1$, $|H_r| \approx |AF|$.

$|H_m(\theta)| \approx 1$, echo reception is possible from anywhere in front of the array.

For the circular microphone array, two design freedoms exist – the number of elements (M) and the radius of the ring containing the elements. For the choice of $M = 8$, the microphone elements have an angular separation of 45^o between them. To effectively suppress grating lobes occurring in the visible region, based on [28, 56] array elements require a separation smaller than $\frac{\lambda}{2}$. For the circular array, the radius of the ring on which

Table 7.1: Array Design Parameters

Parameter	Value	Units
Transducer Radius (datasheet)	7	mm
Microphone Radius (datasheet)	0.25	mm
Receiver Array Radius	3.7	mm
Number of elements (M)	8	-
Transducer's Center Frequency (f_e)	58.5	kHz
Speed of Sound (v_{sound})	340	m/s
Wavelength (λ)	5.81	mm

the elements are located is given by

$$\text{Radius of the Ring} = \frac{\lambda/2}{2\pi/M} \tag{7.2}$$

Using the specifications of Table 7.1, the radius of the ring is 3.7 mm. It is interesting to note that the 8 microphone elements are located on a ring that is about one-half the radius of the transmitter FUT. The receiver array's response is given by

$$H_r = AF \times H_m \tag{7.3}$$

where AF is the array factor determined by the location of each microphone element in the receiver array. The array factor AF is given by

$$AF = \sum_{m=1}^{M} \exp\left[j\frac{2\pi}{\lambda}\left(x_m u + y_m v + z_m w\right)\right] \tag{7.4}$$

where $(x_m,\ y_m,\ z_m)$ are the locations of the M microphone elements. The unit vectors $(u,\ v,\ w)$ of the spherical coordinate system defined in Figure 7.3 can be written as

$$u = \cos(\theta),\ v = \sin(\theta)\cos(\phi),\ w = \sin(\theta)\sin(\phi) \tag{7.5}$$

Because the microphone elements have an omnidirectional response, $|H_r| \approx |AF|$. In the pulse-echo mode of operation, the two-way transmit-receive radiation pattern defines the operating region of the sensor array and is given by

$$H_{tr} = H_t \times H_r \tag{7.6}$$

From Figure 7.3, the transmitting FUT limits the operating region of the sensor array. Also, the side lobes are 97% smaller than the main lobe resulting in high detection SNR. The theoretical angular resolution (azimuth and polar) is 19.8^o based on the 3 dB definition from

[28, 30]. Increasing the number of elements allows better angular resolution but has several disadvantages. Each microphone requires a dedicated receive signal path and memory for storing the microphone data, increasing the hardware cost. Additionally, several steps during digital processing involve complex matrix math computations; the overall compute costs grow approximately as a square of the number of receiver elements, reducing the sensor's throughput. Employing fewer microphones is beneficial for low-cost space-constrained applications operating on a power budget.

7.3 Processing Algorithm

Figure 7.4 illustrates the various steps of the processing algorithm. Broadly the algorithm is organized into pre-processing steps, the beamforming step, followed by several post-processing steps. Data logging begins when the transmitter emits a pressure wave in response to a voltage excitation consisting of n_e cycles (TXOPT or RXOPT schemes may also be applied). The algorithm takes in the digital signal capture as the input and outputs the 3-D positions of multiple reflectors in the scene.

7.3.1 Pre-processing Steps

The analog voltage signal containing the echoes at each microphone first passes through a bank of bandpass filters discussed in Appendix C. The M dedicated filters use a fixed gain of 300 V/V to amplify the signal, which is sampled by a 12-bit ADC of a MCU at a sampling frequency of f_s. The integer-valued signal at the ADC after adjusting for bias has a range between -2048 and 2047. The signal capture for the M microphones is given by

$$\boldsymbol{s}(t) = [s_1(t), \ldots, s_M(t)]^T, \qquad 0 \leq t < T \tag{7.7}$$

where T is the time duration of the signal capture, giving a total capture length of $N = Tf_s$. The noise component is assumed to be small in $\boldsymbol{s}(t)$; explicit representation of noise in

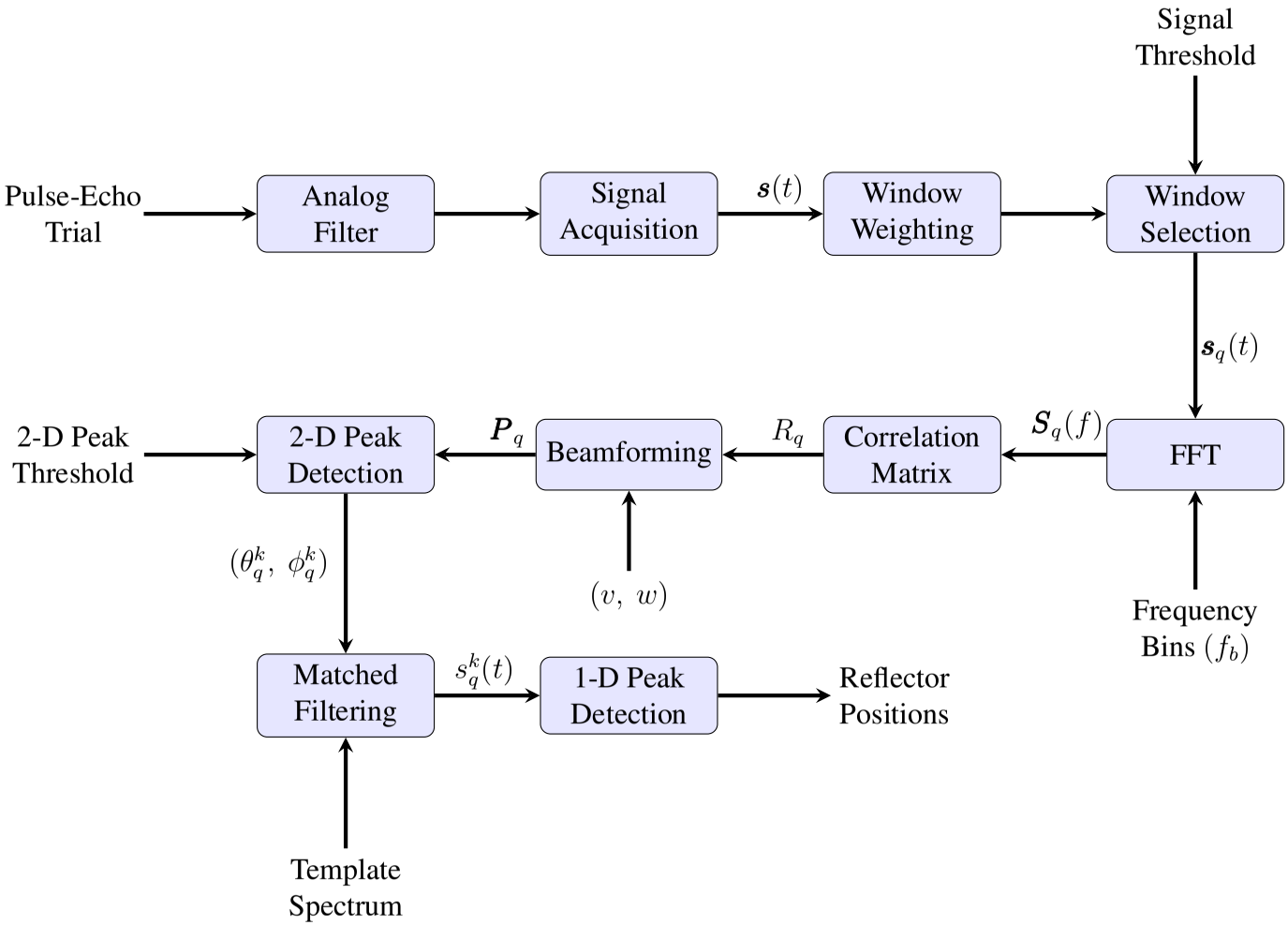

Figure 7.4: Steps in the processing algorithm. Signal $\boldsymbol{s}(t)$ is a concatenation of the signals corresponding to the M microphones of the receiver array.

Equation 7.7 is suppressed for notational convenience. The maximum range is obtained by scaling T by the speed of sound as given by Equation 1.1. The signal capture is split into multiple smaller-length windows to detect several reflectors in the scene. Let Q be the total number of windows, and $q = 1, \ldots, Q$. For a window length of L and an overlap length of αL between subsequent windows, where $\alpha \in [0, 1]$, the number of windows is computed as

$$Q = \frac{N - \alpha L}{L(1 - \alpha)} \tag{7.8}$$

The parameters (N, L, α) impact the memory requirements and the computation cost. A smaller window length reduces the memory utilization during subsequent processing steps but increases the computation cost as all the downstream steps of the algorithm will need to be repeated for each window. After partitioning the length N signal, each window is weighted using a length L window function defined as $h(t)$ for $0 \leq t < \frac{L}{f_s}$; $h(t)$ is a Hanning window. The corresponding operations are given by

$$\begin{gathered} \boldsymbol{s}_q(t) = \boldsymbol{s}(t)h(t - \mathcal{T}_q^s), \quad \mathcal{T}_q^s \leq t < \mathcal{T}_q^s + \frac{L}{f_s} \\ \text{where } \mathcal{T}_q^s = \frac{(q-1)\alpha L}{f_s}, \quad q = 1, \ldots, Q \end{gathered} \tag{7.9}$$

The weighting reduces the discontinuities at the boundary between two windows and the associated spectral leakages. The microphone signals will have echoes of sufficient amplitude only during some time intervals. At other time intervals, the signal level of $\boldsymbol{s}(t)$ will be around the noise floor level of the system. To eliminate redundant computations and boost the sensor throughput when echoes of sufficient amplitude are not present, a window selection is performed as

$$\boldsymbol{s}_q(t) = \begin{cases} \boldsymbol{s}_q(t), & \exists \ |\boldsymbol{s}_q(t)| > \mu, \ \mathcal{T}_q^s \leq t < \mathcal{T}_q^s + \frac{L}{f_s} \\ 0, & \text{otherwise} \end{cases} \tag{7.10}$$

where μ is the threshold. For an embedded application, to determine the windows that need to be processed, a 1-D peak detector is applied and is outlined in Algorithm 4. The algorithm takes in a signal vector and a threshold value as inputs. It outputs the number of peaks, the time instants when they occur, and the peak values. Line 4 of the algorithm checks if the current signal index has a higher value compared to the adjacent indices while also satisfying the threshold criterion. To perform the selection, one of the length L signals of $\boldsymbol{s}_q(t)$ is fed as input to Algorithm 4. If the peak detector returns more than one peak, the downstream steps of Figure 7.4 are evaluated one window at a time.

Algorithm 4: 1-D Multiple Peak Detector

Inputs:

- $s(t)$: Input signal of length L
- μ: Threshold

Outputs:

- k: Number of peaks
- t_k: Time at peak k
- p_k: Value of peak k at time t_k

```
1 Initialize loop variable i := 0
2 Initialize peak counter k := 0
3 for i ← 1 to L − 1 do
4 |   if s(t_i) > s(t_{i−1}) and s(t_i) > s(t_{i+1}) and s(t_i) > μ then
5 |   |   k := k + 1
6 |   |   p_k = s(t_i)
7 |   |   t_k = t_i
8 |   i := i + 1
9 end
```

Frequency-domain beamforming is preferable for determining the directions of arrival of echoes because it offers computational efficiency. The L-point FFT of $\boldsymbol{s}_q(t)$ is computed, resulting in a frequency spectrum that has a length of $\frac{L}{2}$ spanning between 0 and $\frac{f_s}{2}$. Both the transmitted acoustic pressure waves and the received echoes are narrowband. Hence it is beneficial to retain only a subset of the spectral content corresponding to the frequency range f_b for the remaining processing steps. The frequency spectrum computation can be

written as

$$\boldsymbol{S}_q(f) = \text{FFT}(\boldsymbol{s}_q(t)), \text{ where } f \in f_b \tag{7.11}$$

The $M \times M$ spatial correlation matrix R_q for window q is essential for the beamforming step and may be derived by computing the output power of Equation 2.1. The R_q matrix is given by

$$R_q = \boldsymbol{S}_q(f)\boldsymbol{S}_q^H(f), \qquad f \in f_b \tag{7.12}$$

7.3.2 Beamforming

Figure 2.2 and Section 2.2 clarify the operation of a beamformer. Time delays that functionally depend on the look direction are applied to process the signals at the receiver in Equation 2.1 and Equation 2.2. For a specific set of time delays, the power of Equation 2.1 is maximized, which determines the object's direction. To detect the two unknown angles (polar, azimuth), define the $M \times 1$ length steering vector as

$$\psi(u,\ v,\ w) = \begin{bmatrix} \exp\left[j\dfrac{2\pi}{\lambda}\left(x_1u + y_1v + z_1w\right)\right] \\ \vdots \\ \exp\left[j\dfrac{2\pi}{\lambda}\left(x_Mu + y_Mv + z_Mw\right)\right] \end{bmatrix} \tag{7.13}$$

where $(u,\ v,\ w)$ are the unit vectors in the spherical coordinate system given by Equation 7.5, and $(x_m,\ y_m,\ z_m)$ are the positions of the microphones in the receiver array. The unit vectors $(u,\ v,\ w)$ are functions of $(\theta,\ \phi)$ and correspond to the arrival direction of the pressure waves. In Figure 7.2, the microphone elements are located on the YZ plane. Therefore $x_1, \ldots, x_M = 0$, resulting in Equation 7.13 reducing to $\psi(v,\ w)$.

Beamforming is at the core of the processing flow in Figure 7.4. The signal power is computed along several look directions determined by the uniformly spaced $(v,\ w)$ values

defining a 2-D search grid as illustrated by Figure 7.5b. Local maxima are then determined from the power computations to identify the arrival directions $(v^l,\ w^l)$. Figure 7.5 also clarifies that the $(v,\ w)$ grid and the $(\theta,\ \phi)$ grid are related by Equation 7.5; correspondingly the identified $(v^l,\ w^l)$ directions are converted to $(\theta^l,\ \phi^l)$ identifying the directions of arrival of echoes. The span of the main lobe in the two-way radiation pattern shown in Figure 7.3 defines the grid's limits. Theoretical foundations of beamforming are discussed in [29], and only aspects relevant to the processing algorithm are outlined. The three beamforming methods considered in this work to determine the power matrix are:

1. **DAS**: The power is computed as

$$P_q(v,\ w) = \psi^H(v,\ w) R_q \psi(v,\ w) \tag{7.14}$$

   where $(\cdot)^H$ denotes the complex conjugate transpose of a matrix. The DAS approach is non-adaptive and requires low computation resources. A downside is the lower angular resolution. Figure 2.2 discusses the DAS beamformer.

2. **MVDR**: This approach is adaptive, where a weighting matrix $\eta(v,\ w)$ suppresses the power computations from directions that do not coincide with the echo's arrival directions. In directions that coincide with the echo's arrival directions, the weighting matrix is kept constant. The MVDR problem is formulated as an optimization problem as

$$\begin{aligned} &\min_{\eta(v,\ w)} \ \eta^H(v,\ w) R_q \eta(v,\ w) \\ &\text{subject to } |\eta^H(v,\ w)\ \psi(v,\ w)| = 1 \end{aligned} \tag{7.15}$$

   Fortunately, the optimization problem has a closed-form solution that determines the optimal direction-dependent weights, first determined by Capon [29]. It is given by

$$\eta(v,\ w) = \frac{R_q^{-1}\ \psi(v,\ w)}{\psi^H(v,\ w)\ R_q^{-1}\ \psi(v,\ w)} \tag{7.16}$$

The power computation with the optimal weights applied is given by

$$P_q(v,\ w) = \frac{1}{\psi^H(v,\ w) R_q^{-1} \psi(v,\ w)} \tag{7.17}$$

Because weighting is applied, the resolution with MVDR improves when compared to DAS.

3. **MUSIC**: This adaptive approach involves several steps. First, the eigendecomposition of the correlation matrix R_q is determined. The eigenvalues Λ_m are arranged, say, in increasing order; ν_m are the corresponding eigenvectors. Define the columns of the matrix η as

$$\eta := \nu_m \ \forall \ (\Lambda_m < \text{Threshold}) \tag{7.18}$$

where Threshold $= \alpha \times \max\{\Lambda_1, \ldots, \Lambda_M\}$ and $\alpha = [0,\ 1]$. Therefore, η defines a matrix of eigenvectors corresponding to the smallest eigenvalues. Note that η will have fewer than M columns after the thresholding operation. The eigenvalues corresponding to the noise subspace are orders of magnitude smaller than the eigenvalues of the signal subspace, and an $\alpha \approx 0.1$ is sufficient to identify all the eigenvectors. Other methods such as AIC or BIC discussed in [29] may be employed to perform eigenvalue selection. However, the thresholding approach is simple and produces a similar level of performance compared to AIC or BIC. The estimated correlation matrix determined with the eigenvectors of the noise subspace is given by

$$R_{q,MUSIC} = \eta\eta^H \tag{7.19}$$

The power computations with MUSIC is given by

$$P_q(v,\ w) = \frac{1}{\psi^H(v,\ w)\ R^{-1}_{q,MUSIC}\ \psi(v,\ w)} \tag{7.20}$$

P_q computed using Equation 7.14, Equation 7.17, and Equation 7.20 is a function of $(v,\ w)$, which is evaluated at several points on a uniformly spaced 2-D search grid. Let the matrix $\boldsymbol{P}_q$ aggregate the signal power computed at all the 2-D grid locations.

7.3.3 Post-processing Steps

The matrix $\boldsymbol{P}_q$ may contain several local maxima, each representing an arrival direction of the pressure waves. Algorithm 5 describes a 2-D peak detection algorithm to identify the maxima. The algorithm accepts a 2-D matrix and a threshold value as inputs. It outputs the number of peaks, the coordinates where the peaks occur, and the peak values. Figure 7.6 clarifies the condition on Line 4 – Line 5 of the algorithm. The condition checks if the value at the center of a 3×3 matrix of points is the highest. The threshold condition ensures that only maxima above the noise floor level of the matrix $\boldsymbol{P}_q$ are detected. Note that Line 2 and Line 3 of the algorithm add a boundary of zeros to the 2-D input matrix to simplify the peak finding logic and allow for detection to occur at the edges of the input matrix.

When $\boldsymbol{P}_q$ is determined on a uniformly spaced $(\theta,\ \phi)$ grid, the $\boldsymbol{P}_q$ values have a spherical variation. Figure 7.5a clarifies that adjacent values of θ correspond to different heights, while adjacent values of ϕ correspond to points on a circle; the automatic detection of 2-D peaks in $\boldsymbol{P}_q$ will require a spherical-to-Cartesian conversion. On the other hand, for a uniformly spaced grid of $(v,\ w)$ values, as shown in Figure 7.5b, the $\boldsymbol{P}_q$ matrix has a direct mapping to each grid point; the automatic detection of 2-D peaks can occur without any intermediate operations. After the peak values $(v,\ w)$ are identified, conversion to $(\theta,\ \phi)$ is made using Equation 7.5. Therefore, evaluation of the matrix $\boldsymbol{P}_q$ on the $(v,\ w)$ grid is computationally efficient and preferable. Note that a uniformly spaced $(v,\ w)$ grid results in

Algorithm 5: 2-D Multiple Peak Detector

Inputs:

- M: Input 2-D matrix of size $V \times W$
- μ: Threshold

Outputs:

- k: Number of peaks
- $(i_k,\ j_k)$: Location of peak k
- p_k: Value of peak k at $(i_k,\ j_k)$

Initialize peak counter $k := 0$
for $i \leftarrow 0$ **to** $V + 1$ **do**
  for $j \leftarrow 0$ **to** $W + 1$ **do**
    if $M(i,\ j) > M(q,\ r)$ and $M(i, j) > \mu$, where
    $\{q\ \in [i - 1,\ i + 1],\ r \in [i - 1,\ i + 1],\ (q,\ r) \neq (i,\ j)\}$ **then**
      Update $k := k + 1$
      Update $p_k = M(i,\ j)$
      Update $(i_k,\ j_k) = (i,\ j)$
  end
  $i := i + 1$, $j := j + 1$
end

Indexing for matrix $M(i,\ j)$ is in the range $i = 1, \ldots, V$ and $j = 1, \ldots, W$. For $i = \{0,\ V + 1\}$ and $j = \{0,\ W + 1\}$, an outer boundary of zeros is added to the matrix M.

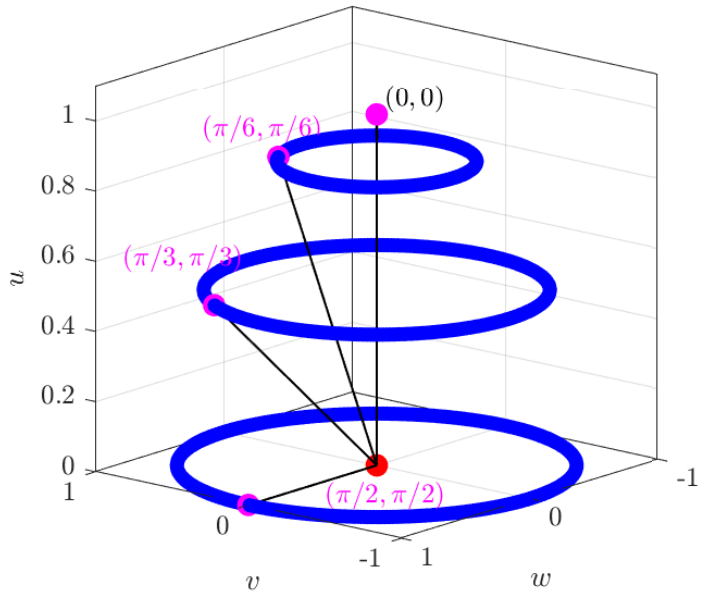

(a) Points on a uniformly spaced 2-D $(\theta,\ \phi)$ grid result in a spherical variation. Variation of θ results in circular contours at various heights. Variation of ϕ covers the circle.

$(v_1,\ w_1)$	$\dots$	$(v_V,\ w_1)$
$\vdots$	$\ddots$	$\vdots$
$(v_1,\ w_W)$	$\dots$	$(v_V,\ w_W)$

$(v,\ w)$ grid

(b) Matrix representation of the 2-D $(v,\ w)$ grid with uniform grid spacing between adjacent matrix entries.

Figure 7.5: Relationship between $(\theta,\ \phi)$ grid and $(v,\ w)$ grid.

a non-uniformly spaced $(\theta,\ \phi)$ grid. This aspect requires a 2-D interpolation procedure to improve the accuracy of the identified peak's location.

2-D peak interpolation

The beamformed power spectrum $\boldsymbol{P}_q$ results in a 2-D matrix, which is a function of the discretized 2-D grid points $(v,\ w)$. Several local maxima representing maximum constructive interference are present in the power spectrum. The locations $(i_k,\ j_k)$ of the k local maxima are returned by the 2-D peak detector given by Algorithm 5 and correspond to

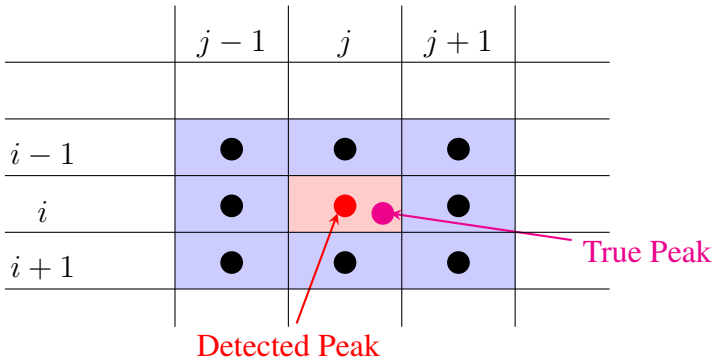

Figure 7.6: 2-D peak detection and interpolation to determine fractional indices.

the polar and azimuth angles $(\theta_k,\ \phi_k)$. As $(v,\ w)$ are discretized with a uniform separation of Δv and Δw, the indices $(i,\ j)$ of the matrix can be used instead of the actual values $(v,\ w)$ to derive closed-form expressions interpolating the 2-D peak. In the graphic shown in Figure 7.6, the identified indices returned by the peak detector are located at $(i,\ j)$, whereas the true peak is present at an off-grid location. Determining the true peak location will result in indices containing fractional values. The corresponding values of $(\hat{v},\ \hat{w})$ evaluate to an intermediate point between the grid points resulting in increased angular estimation accuracy. The fractional peak location is estimated by fitting a paraboloid of the form

$$f(i,\ j) = Ai^2 + Bij + Cj^2 + Di + Ej + F \tag{7.21}$$

where $A, \ldots,\ F$ are the coefficients of the approximating paraboloid. As shown in Figure 7.6, the peak and the 8 neighbouring points surrounding the peak in the 3×3 block are considered, where the power spectrum values at the indices $\{i-1,\ i,\ i+1\}$ and $\{j-1,\ j,\ j+1\}$ are utilized. The coefficients $A, \ldots,\ F$ are determined through least-squares curve fitting of the 9 points. For computations, temporarily set $(i,\ j) = (0,\ 0)$; the indices take the values $\{-1,\ 0,\ 1\}$, resulting in an over-determined system of dimension

9×6 for the 9 points of Figure 7.6 and is given by

$$\begin{bmatrix} p^2 & pq & q^2 & p & q & 1 \end{bmatrix} \begin{bmatrix} A \\ \vdots \\ F \end{bmatrix} = \begin{bmatrix} f(p,\ q) \end{bmatrix} \tag{7.22}$$

$$\text{where } p = \{-1,\ 0,\ 1\},\ q = \{-1,\ 0,\ 1\}$$

The values of $A, \ldots, F$ after computing the pseudo-inverse is given by

$$\begin{bmatrix} A \\ \vdots \\ F \end{bmatrix} = \begin{bmatrix} \frac{1}{6} & \frac{1}{6} & \frac{1}{6} & -\frac{1}{3} & -\frac{1}{3} & -\frac{1}{3} & \frac{1}{6} & \frac{1}{6} & \frac{1}{6} \\ \frac{1}{4} & 0 & -\frac{1}{4} & 0 & 0 & 0 & -\frac{1}{4} & 0 & \frac{1}{4} \\ \frac{1}{6} & -\frac{1}{3} & \frac{1}{6} & \frac{1}{6} & -\frac{1}{3} & \frac{1}{6} & \frac{1}{6} & -\frac{1}{3} & \frac{1}{6} \\ -\frac{1}{6} & -\frac{1}{6} & -\frac{1}{6} & 0 & 0 & 0 & \frac{1}{6} & \frac{1}{6} & \frac{1}{6} \\ -\frac{1}{6} & 0 & \frac{1}{6} & -\frac{1}{6} & 0 & \frac{1}{6} & -\frac{1}{6} & 0 & \frac{1}{6} \\ -\frac{1}{9} & \frac{2}{9} & -\frac{1}{9} & \frac{2}{9} & \frac{5}{9} & \frac{2}{9} & -\frac{1}{9} & \frac{2}{9} & -\frac{1}{9} \end{bmatrix} \begin{bmatrix} f(-1,\ -1) \\ f(-1,\ 0) \\ f(-1,\ +1) \\ f(0,\ -1) \\ \vdots \\ f(1,\ 1) \end{bmatrix} \tag{7.23}$$

The equation of the paraboloid has now been fully determined. In Equation 7.23, the values of $f(i,\ j)$ on the RHS are known and evaluate to points in the 3×3 window. The values of $A, \ldots,\ F$ are computed by weighting the values of $f(i,\ j)$. The peak location is obtained from the gradient of Equation 7.21 and is given by

$$\begin{aligned} \frac{\partial f}{\partial i} &= 0 = D + 2Ai + Bj \\ \frac{\partial f}{\partial j} &= 0 = E + Bi + 2Cj \end{aligned} \tag{7.24}$$

Solving Equation 7.24 results in the values for $(\hat{i},\ \hat{j})$ as

$$\hat{i} = \frac{2CD - BE}{B^2 - 4AC} \text{ and } \hat{j} = \frac{2AE - BD}{B^2 - 4AC} \tag{7.25}$$

The values $A, \ldots, F$ are given by Equation 7.23, and the values for $\hat{v}$ and $\hat{w}$ where the interpolated 2-D peak occurs is given by

$$\hat{v} = v + \hat{i}\Delta v \;\text{ and }\; \hat{w} = w + \hat{j}\Delta w \tag{7.26}$$

The approach presented in this section determines a closed-form expression for a uniformly spaced grid. The procedure requires low computing resources and is suitable for embedded implementations as only elementary operations, such as multiplications and additions, are needed. The interpolation procedure discussed in [57] does not consider the additional simplifications introduced by a uniform 2-D grid. Also, the approach in [57] requires iterative techniques to determine a least-squares solution to the fitting problem, resulting in additional computations compared to the above method.

Radial distance determination

After obtaining the interpolated locations of the k peaks in window q as $(\hat{v}_q^k,\ \hat{w}_q^k)$, the polar and azimuth angles $(\hat{\theta}_q^k,\ \hat{\phi}_q^k)$ are determined by manipulating Equation 7.5. The radial distance ρ_q^k is the only quantity that remains to be estimated. Recall from Equation 2.1 that the output of the beamformer is a sum of all the input signals after applying the time delays that depend on the look direction. Also, recall from Equation 7.13 that the vector $\psi(v,\ w)$ corresponds to the look direction $(v,\ w)$, in the frequency domain, the output spectrum of the beamformer is given by

$$\boldsymbol{S}_q^k(f) = \psi^H(\hat{v}_q^k,\ \hat{w}_q^k)\boldsymbol{S}_q(f) \tag{7.27}$$

The radial distance is estimated by using Equation 1.1, which scales the round trip ToF by the speed of sound. Several algorithms exist to determine the ToF, and matched filtering (also known as cross-correlation) is applied as the SNR is maximized. The cross-correlation

operation is given by

$$\mathcal{C}_q^k(f) = \mathbb{S}^*(f)\boldsymbol{\mathcal{S}}_q^k(f) \tag{7.28}$$

where $\mathbb{S}(f)$ is the known template spectrum of an echo, and $(\cdot)^*$ denotes the complex conjugate. There are two options to generate the template – from models presented in Section 3.2 or through experimental measurements. Experimental measurements provide an accurate representation of an echo. But, model-based generation of a template can be synthesized easily in software and can apply modifications when needed without relying on new experimental measurements. A disadvantage of the model-based generation approach is the need for accurate knowledge of the system's model parameters.

The complex-valued time-domain representation of Equation 7.28 is determined through an inverse FFT and is written as

$$c_q^k(t) = \text{IFFT}(C_q^k(f)) \tag{7.29}$$

Based on [58], the signal envelope is determined by computing the absolute value of Equation 7.29, i.e. $|c_q^k(t)|$. The 1-D peak detector discussed in Algorithm 4 is applied to $|c_q^k(t)|$ to obtain the time instant t_q^k where the signal envelope achieves a maximum. The offset introduced due to windowing by Equation 7.9 needs to be accounted. The radial distance ρ_q^k to each reflector is computed as

$$\rho_q^k = (\mathcal{T}_q^s + t_q^k)\frac{\upsilon_{sound}}{2} \tag{7.30}$$

With this step, all three quantities that define the position of a reflector in spherical coordinates $(\rho_q^k,\ \hat{\theta}_q^k,\ \hat{\phi}_q^k)$ have been estimated. The corresponding Cartesian coordinates can be

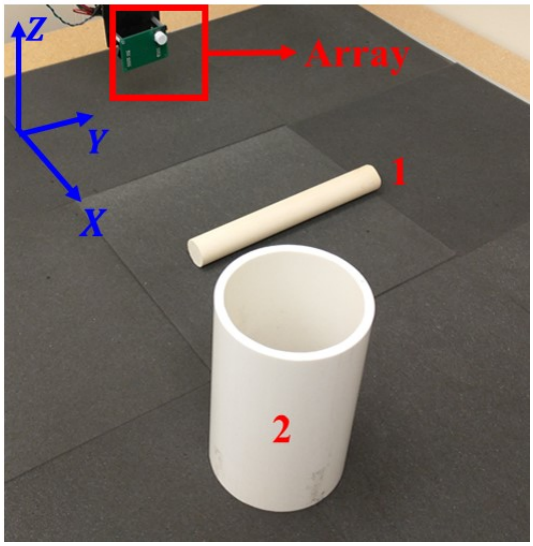

Figure 7.7: Sensor's workspace consisting of two reflectors.

Table 7.2: Ground Truth Location of the Reflectors

Reflector	Reflector Radius (cm)	Ground Truth (x, y, z) cm
Reflector - 1	1.5	$(27, 0, -8.5)$
Reflector - 2	5.75	$(50, -17, 0)$

computed using Equation 7.5 as

$$x_q^k = \rho_q^k \hat{u}_q^k, \qquad y_q^k = \rho_q^k \hat{v}_q^k, \qquad z_q^k = \rho_q^k \hat{w}_q^k \tag{7.31}$$

7.4 Algorithm Evaluation

Consider the workspace consisting of two reflectors as shown in Figure 7.7. The sensor is located 10 cm above the floor. Reflector 1 rests on the floor of the workspace, and reflector 2 is located at an angle. The ground truth locations of the reflectors are in Table 7.2. The processing algorithm of Section 7.3 uses the parameters listed in Table 7.3.

The signals at each step of the processing algorithm are shown in Figure 7.8 – Figure 7.13. A $n_e = 5$ cycle voltage excitation is applied to the transmitter to emit a pressure wave at the resonant frequency $f_e = 58.5$ kHz. The positions of both reflectors are determined with a

Table 7.3: Processing Algorithm Parameters

Parameter	Symbol	Value	Units
Excitation Cycles	n_e	5	cycles
Filter Gain	–	300	V/V
Signal Capture Length	N	1792	samples
Window Length	L	512	samples
Overlap Fraction	α	0.5	–
Threshold	μ	0.1	normalized
Frequency Bins	f_b	$[51,\ 66]$	kHz
Grid Size	$V \times W$	32x32	–
Polar Angle Range	–	$[-45,\ 45]$	deg
Azimuth Angle Range	–	$[0,\ 180]$	deg

single pulse-echo trial. The analog echo-containing signals pass through a bank of dedicated custom analog bandpass filters discussed in Appendix C. Note that the receiver microphones have ≈ 30 dB better sensitivity when compared to the FUT. Hence, a lower gain of 300 V/V is sufficient.

The amplified signal is sampled by a 12-bit single-ended ADC at a sampling frequency of $f_s = 250$ kHz, about four times the operating frequency of the sensor system, and is shown in Figure 7.8a. The integer-valued signal at the ADC after removing the bias has a range between -2048 and 2047 counts, as shown in Figure 7.8b. The signal captures for all eight microphones is superimposed. The capture shows an initial decaying tail which occurs due to the residual oscillations of the transmitter after its excitation. Therefore, the initial portion of the signal up to 0.9 ms is not processed. Methods presented in Chapter 4 – Chapter 6 address the decaying tail issue and may be applied to reduce the minimum range and enhance the range resolution of the sensor system. Two echoes of sufficient amplitude around 1.7 and 3 ms are present that correspond to the two reflectors in the workspace. As the analog filter is well-designed, the captured signal has low levels of in-band noise, obviating the need for digital filtering, which is a computation-intensive process.

The signal capture has a length of 1792 samples (7.192 milliseconds), translating to a maximum range of about 1.2 meters. A window length of 512 samples with a 50%

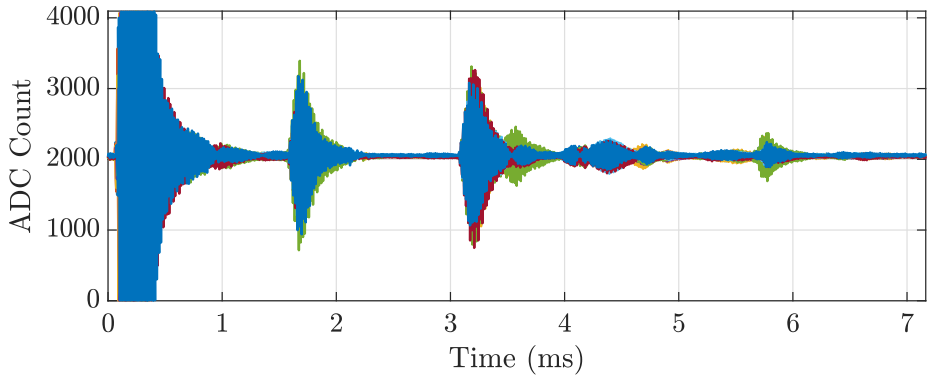

(a) Signal captured by the single-ended 12-bit ADC.

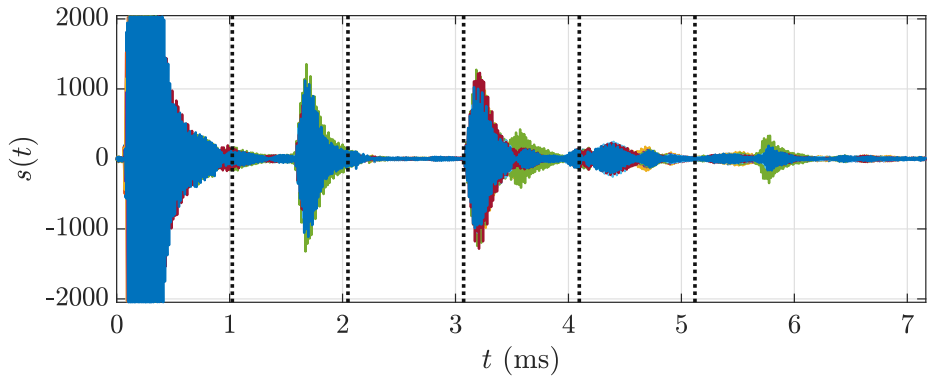

(b) Signal $\boldsymbol{s}(t)$ after bias compensation. Vertical dashed lines indicate the start of each window.

Figure 7.8: Acquired microphone signals. The data from all 8 microphones are superimposed.

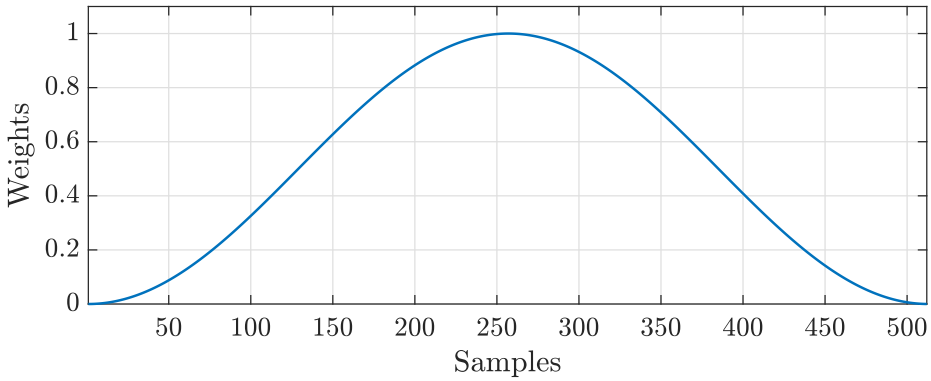

Figure 7.9: Hanning weighting function.

overlap between the windows gives a good balance between memory and compute cost. In Figure 7.8b, the dashed lines indicate the start of each window, and the signal trace consists of a total of six windows. The window $q = 1$ exists between $0 \leq t < 2.048$ milliseconds, window $q = 2$ between $1.024 \leq t < 3.072$ milliseconds, and so forth.

The Hanning function shown in Figure 7.9 weights the signal samples in each window as given by Equation 7.9 and has the same length as the window. The weighting coefficients are close to zero at the interval boundaries (sample indices 1 and 512) and have a value of 1 around the middle of each interval (sample index 256). Since the overlap between the windows is 50% (256 samples), the presence of a signal spanning two windows is not a concern. With weighting, the signal is emphasized in one of the windows while suppressed in the other windows. For example, consider the signal at around 3 milliseconds in Figure 7.8b. In the windows, $1.024 \leq t < 3.072$ milliseconds and $3.072 \leq t < 5.12$ milliseconds, the window weights suppress the signal because it is close to the interval boundaries and in the window $2.048 \leq t < 4.096$ milliseconds, the signal is approximately at the center of the window and is emphasized as shown in Figure 7.10.

As there are only two echoes of sufficient amplitude in the signal trace, windows $q = 2$ and $q = 3$ are retained by the window selection step and advanced through the remaining compute-intensive stages. Figure 7.10 shows the isolated windows after applying the 1-D peak detector of Algorithm 4 during window selection.

After the window selection, the downstream operations are performed window-by-window, first for the window $q = 2$ and then for window $q = 3$. As the sensor utilizes narrowband pressure waves with a bandwidth of ≈ 3 kHz, only a subset of frequency bins $f_b = [51,\ 66]$ kHz are retained. This step reduces the compute cost and the memory requirements by about eightfold in this case.

The uniform $(v,\ w)$ grid has a size of 32×32 and the grid limits are determined by the two-way radiation pattern shown in Figure 7.3. The sweep limits for the polar angles are $[-45^o,\ 45^o]$, and the azimuth between $[0^o,\ 180^o]$. Figure 7.11 and Figure 7.12

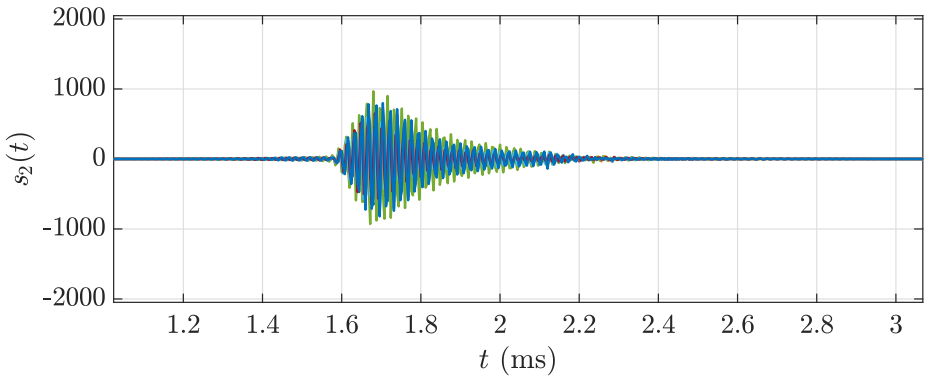

(a) Signals $\boldsymbol{s}_2(t)$ corresponding to window 2 after the weighting step.

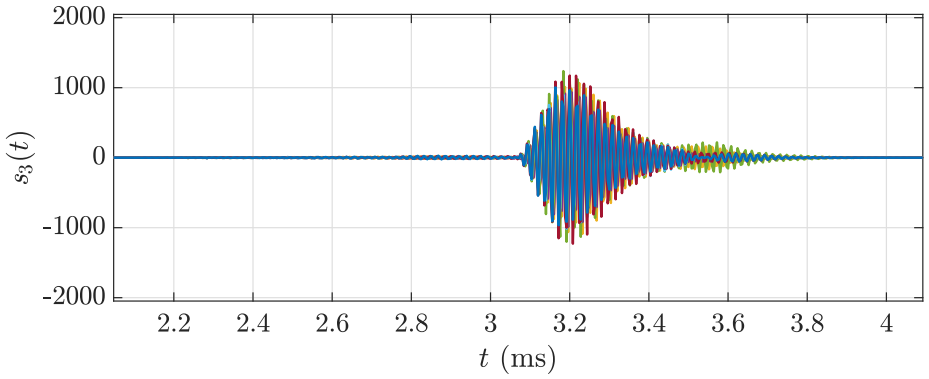

(b) Signals $\boldsymbol{s}_3(t)$ corresponding to window 3 after the weighting step.

Figure 7.10: Signals after window weighting and selection.

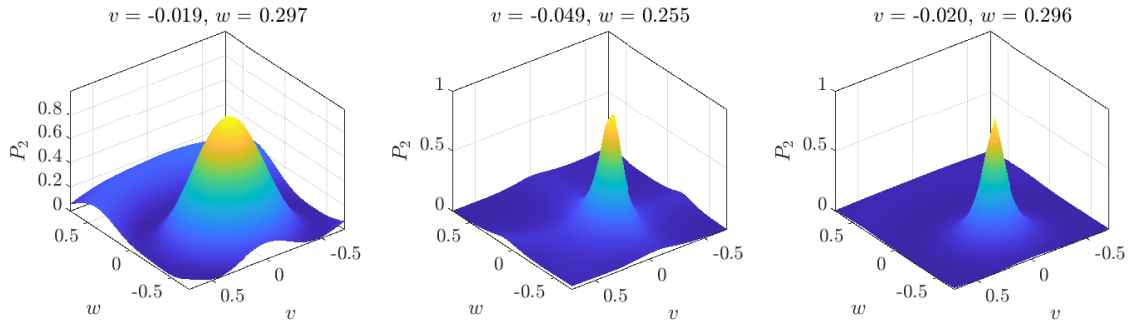

(a) DAS. (b) MVDR. (c) MUSIC.

Figure 7.11: Beamformer output power $\boldsymbol{P}_2$ for window 2.

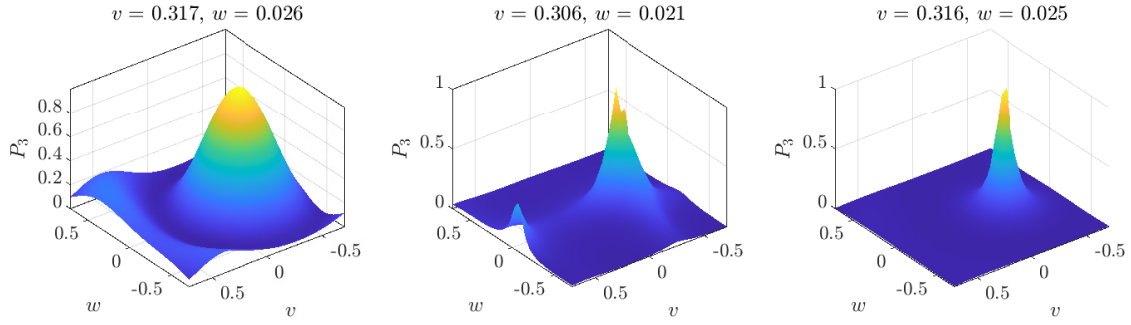

(a) DAS. (b) MVDR. (c) MUSIC.

Figure 7.12: Beamformer output power $\boldsymbol{P}_3$ for window 3.

show the normalized power matrix $\boldsymbol{P}_q$ for windows $q = 2$ and $q = 3$ with the three beamformers – DAS, MVDR, and MUSIC. As only a single dominant echo exists in each window corresponding to the physical object, only a single 2-D peak is present in each window.

The beamformer performance is compared using experimental measurements. Angular resolution and noise floor level characterize the performance of the ultrasonic sensor. The

Table 7.4: Beamformer Performance Comparison

Beamformer	Angular Resolution (deg)	Noise Floor (dB)
DAS	24.84	-12
MVDR	8.17	-24.4
MUSIC	6.26	-30.5

smallest detectable separation between two objects in the azimuth or the polar directions determines the angular resolution of a sensor array. For a uniform circular array, due to symmetry, they are both equal. The main lobe's beamwidth determined by the 3 dB criterion discussed previously provides the resolution. A smaller beamwidth yields a higher angular resolution. Noise floor level, on the other hand, is the nominal level of power in the $\boldsymbol{P}_q$ matrix and determines the separation between the peak value of $\boldsymbol{P}_q$ and the residual level. Both these metrics – better angular resolution and a smaller noise floor level improve the detection and discrimination of multiple objects within each window. Table 7.4 summarizes the experimental performance of the beamformers.

The DAS beamformer has the lowest angular resolution and the highest noise floor level compared to the other two adaptive beamformers. The MVDR beamformer has an improved angular resolution and noise floor level as it applies a direction-dependent weighting factor to the acquired signal data during processing. The MUSIC beamformer has the best angular resolution and the lowest noise floor levels providing the best detection capability among the three beamformers. From a computation perspective, the DAS beamformer has the lowest computation cost. Both MVDR and MUSIC achieve a higher resolution with an increased computation cost. The MVDR requires the inverse of the correlation matrix R_q, while MUSIC requires the eigenvalue decomposition of R_q and a matrix inversion. These additional steps need matrix factorizations of R_q increasing the computation cost.

From Figure 7.11 and Figure 7.12, the 2-D peak interpolation operation is apparent as the identified values of $(v,\ w)$ at which the peaks occur are slightly different with each method and do not correspond to discretized locations on the $(v,\ w)$ grid. Figure 7.13 shows the resulting matched filtered signal envelope $c_q^k(t)$ after progressing through the remaining post-processing steps. Applying the 1-D peak detector of Algorithm 4 determines the time instant at which the maximum value occurs. The 1-D peak detector identifies only one peak in $c_q^k(t)$ as it is derived from the 2-D peak at $(\hat{v}_q^k,\ \hat{w}_q^k)$. The identified reflector locations are listed in Table 7.5, demonstrating a high detection accuracy of the processing algorithm.

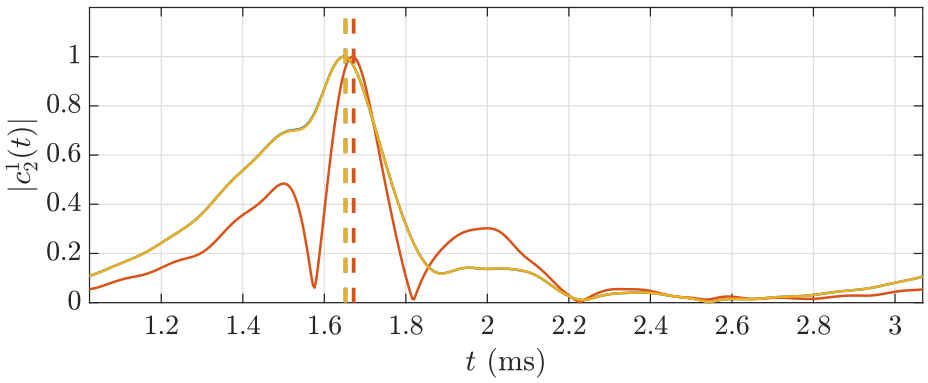

(a) Signal envelope corresponding to window 2.

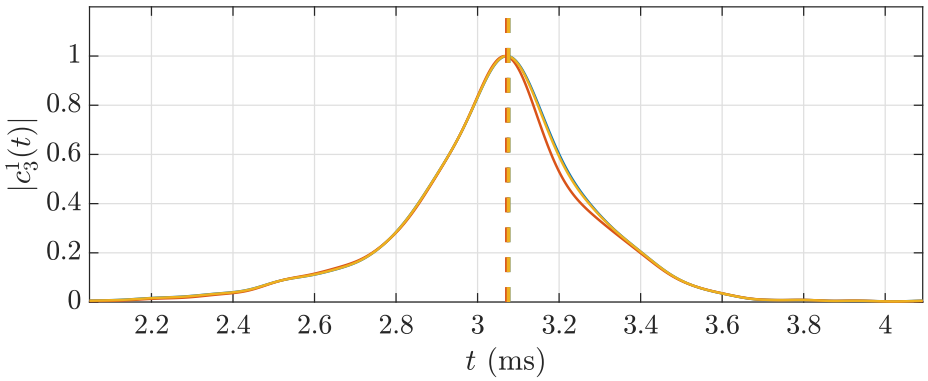

(b) Signal envelope corresponding to window 3.

Figure 7.13: Signal envelope after matched filtering.
(DAS [—], MVDR [—], and MUSIC [—]).

The error with the MVDR beamformer is slightly higher because of the adaptive look direction-dependent weighting value computations. MUSIC achieves the best performance and has higher resolving capability compared to DAS. Also, the small discrepancies in the estimates are due to the reflector's curvature and multi-path propagation effects.

7.5 Embedded Implementation

A high update rate (i.e., rate of pulse-echo trials) is essential for real-world robotic applications, such as workspace mapping or object tracking. The processing algorithm of Figure 7.4 is implemented on the Texas Instruments TMS320F28379D MCU to determine the computing requirements for dedicated chip solutions. This step also avoids the exchange of large volumes of data through serial communication, which is used extensively during

Table 7.5: Processing Algorithm Performance

Reflector	Ground Truth (ξ) $(x,\ y,\ z)$ cm	Beamformer	Estimate ($\hat{\xi}$) $(\hat{x},\ \hat{y},\ \hat{z})$ cm	Error % $\left\lvert \frac{\lvert\lvert\xi\rvert\rvert - \lvert\lvert\hat{\xi}\rvert\rvert}{\lvert\lvert\xi\rvert\rvert} \right\rvert \times 100$
Reflector - 1	$(27, 0, -8.5)$	DAS	$(26.81, 0.54, -8.34)$	0.79
		MVDR	$(27.52, -1.21, -7.26)$	0.66
		MUSIC	$(26.82, 0.55, -8.33)$	0.79
Reflector - 2	$(50, -17, 0)$	DAS	$(49.58, -16.58, -1.35)$	0.98
		MVDR	$(49.71, -15.97, -1.10)$	1.11
		MUSIC	$(49.61, -16.5, -1.32)$	0.98

Reflector - 1 radius = 1.5 cm, Reflector - 2 radius = 5.75 cm. Mean of 5 pulse-echo trials is reported as the estimated position.

experiments in the previous chapters. For comparison, to exchange 1792 samples of signal data from 8 elements of the microphone with each sample represented using 16 data bits, the total data exchanged after each pulse-echo trial is about 229 Kbits. For a nominal serial communication speed of 4 MBaud, the data transmission duration takes about 60 milliseconds. Since the operating system schedules the software running on a host PC, the maximum update rate achieved for PC-based processing is about 5 – 8 Hz; the low update rate is unsuitable for applications that require real-time object detection.

The MCU consists of two processing cores and two control law accelerator cores, and all the cores operate at the maximum clock frequency of 200 MHz. The Table 7.6 lists the computation cost per window of the processing algorithm, and all the steps use single precision floating point math. The beamforming step, as expected, is the most computation-intensive step requiring about 10 milliseconds to run as beamforming requires complex math computations at each coordinate in the 2-D $(v,\ w)$ grid. Using all four cores of the MCU to process the pulse-echo measurement data in parallel minimizes the computation load due to the beamforming step, improving the sensor's throughput. The other processing steps consume only about 8% of the MCU's time and have a negligible impact. The fully embedded solution requires a total of 64 – 70 kilobytes of memory; the memory-intensive aspects are – the analog signal data, the complex-valued FFT spectra, the coordinates of the 2-D grid $(v,\ w)$ points, the correlation matrix, and the output power matrix of the beamformer. For a processor utilization of 80%, the sensor achieves a throughput between 20 and 45 Hz. The throughput varies depending on the number of windows that need to be processed. Although the processing loop can achieve higher throughputs, the maximum rate is limited due to the manufacturer prescribed maximum cycle rate of the TX-FUT. Note that the computation requirements scale as the square of the number of microphone elements. Hence it is beneficial to use an array consisting of a small number of microphones. For comparison, other solutions utilize several expensive and powerful processors [24, 25] and graphic processing units [26, 31] operating at high clock speeds (few GHz) with large

Table 7.6: Computation Cost per Window

Processing Step	Cycles	% of Total Cycles
Window Weighting	7348	0.37
Window Selection	8195	0.41
FFT	14643	0.73
Correlation Matrix	23765	1.19
Beamforming	1852324	92.91
2-D Peak Detection	33791	1.69
Matched Filtering	45408	2.28
1-D Peak Detection	8194	0.41
Total Cycles	1993668	

The clock frequency of the microcontroller is 200 MHz. The processing steps use 32-bit floating point math.

memory (few gigabytes).

7.5.1 Experimental Evaluation

Figure 7.14 shows the experimental setup to demonstrate the sensor array's ability to track moving objects. The scene consists of a single spherical reflector (a ball) mounted at the end of a motorized arm. The Dynamixel XM430-W210R smart servo motor used in Chapter 8 and Chapter 9 provides the rotational capability, while the motor's onboard position encoder provides ground truth position measurements. The spherical reflector is present in front of the sensor and is above the sensor's center. The scene also consists of other surfaces that can produce reflections and are covered with foam to enhance the echoes arising from the spherical reflector. However, it is still possible to capture reflections from parts of the rotary arm, leading to different distance estimates.

Figure 7.15 and Figure 7.16 display the point cloud measurements obtained with the sensor array. The motor commands result in the spherical reflector tracing a circular arc in the XY plane. The repositioning event occurs at a constant speed, and measurement data from both the motor and the ultrasonic sensor array are collected simultaneously. Figure 7.15a shows a 2-D view comparing the points detected by the sensor array with that

Figure 7.14: Experiment setup evaluating the embedded implementation of the processing algorithm.

of the encoder measurements. The point cloud data provided by the sensor approximately follows a circular path. Since the scattering mechanism of ultrasonic pressure waves is predominantly specular, only a small region of points on the spherical reflector within the main beam of the two-way radiation pattern produce reflections. In the 3-D view of the same experimental data shown in Figure 7.15b, the majority of the points are at a height from the sensor array, and some of the points indicate reflections arising from the rotary arm. Figure 7.15b emphasizes both the spatial and temporal aspects measured by the ultrasonic sensor, where the 3-D Cartesian coordinates estimated by the sensor array are compared with the encoder measurements. The 10-second log contains estimates from 400 points (each point is from a pulse-echo trial), providing continuous 3-D point cloud measurements of the moving reflector.

7.6 Summary and Conclusion

A low-cost ultrasonic sensor consisting of a single narrowband transducer to insonify a robot's scene is used with an array of MEMS microphone receivers to determine the positions of multiple reflectors in the sensor's scene. The chapter discusses end-to-end system design considerations of the sensor, analog signal chain, and the digital processing of the received

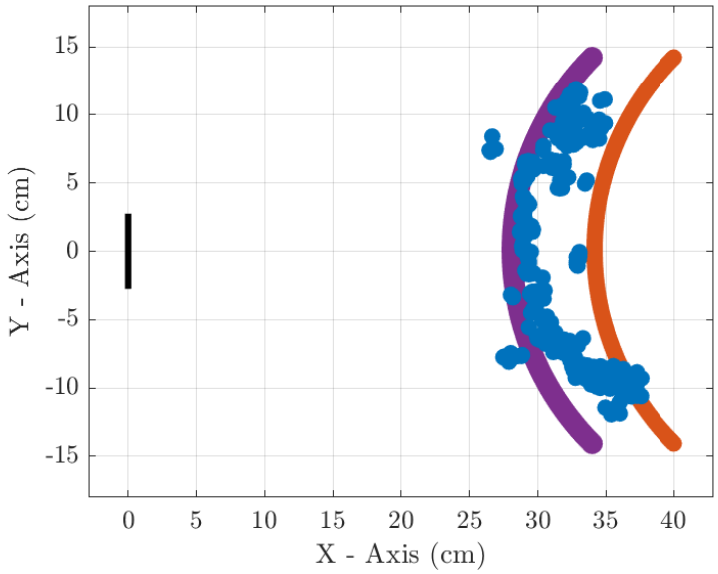

(a) XY plane. The sensor is located at $x = 0$.

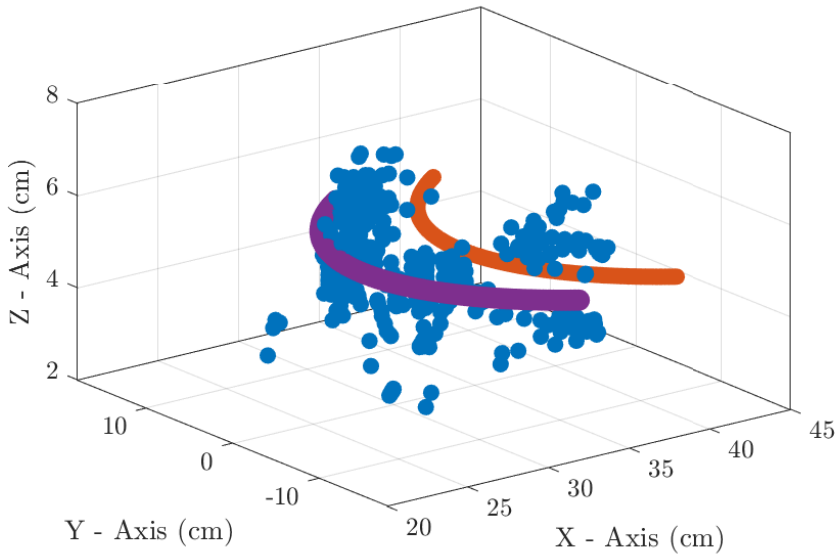

(b) 3-D view.

Figure 7.15: Sensor point cloud for the tracking experiment. (Sensor measurements [•], center of the spherical reflector [•], outer periphery of the spherical reflector [•]).

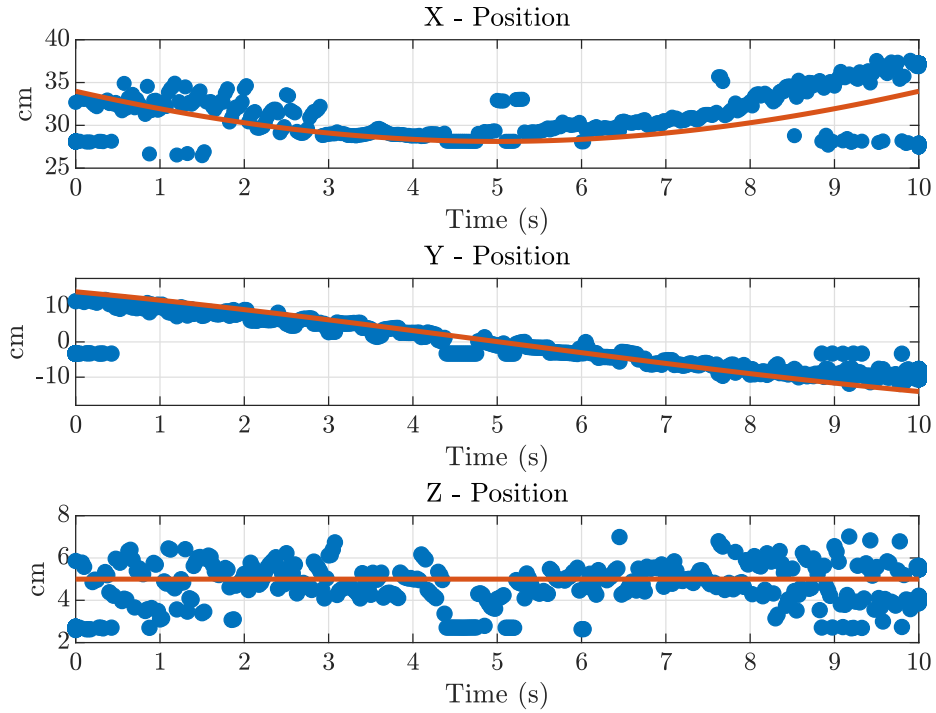

Figure 7.16: Spatio-temporal plot of the 3-D point cloud data. Sensor measurements [•], ground truth encoder measurements [—].

signals. The use of fewer receivers reduces the overall cost of the sensor hardware, the computation and memory requirements (the processing algorithm requires only kilobytes of memory), and the overall power consumption. Experimental results illustrate the ability to detect multiple objects in a 3-D space simultaneously with high accuracy. Experimental results also demonstrate the detection and tracking of a moving object.

Tactile Sensing

CHAPTER 8

STIFFNESS ESTIMATION IN SINGLE DEGREE OF FREEDOM SYSTEMS

8.1 Introduction

This chapter focuses on estimating stiffness, an essential quantity in tactile sensing. Consider the simplified representation of a gripper consisting of two jaws as shown in Figure 1.2. Only one gripper jaw is actuated, and the actuator has a position and current sensor. Sensor measurements are obtained after achieving a grasp through a squeeze test, which involves changing the position (or force) applied to the object by the mechanism. This chapter extends the knowledge base by developing a sensing solution that uses only position and current measurements to estimate an object's unknown stiffness. In contrast, prior work in [33, 35, 38] utilizes tactile sensor arrays mounted on the gripper's jaws to obtain force measurements. Machine learning-based regressor models the relationship between the position and current sensor measurements and the stiffness value in SI units. Stiffness outputs from the regressor are continuously valued, while prior research only classifies input data into stiffness classes, i.e., high, moderate, or low stiffness. Virtual datasets are generated through simulation models of the system to train regressors, which are later evaluated on a representative single degree of freedom experimental hardware system to assess the real-world stiffness estimation performance. The chapter also studies how dry friction in the mechanism and the gripper's actuation can influence the sensor measurements, and how regressors can overcome the introduced effects.

8.2 System Physics

8.2.1 Stiffness Estimation Model

The model of the gripper grasping an object with unknown stiffness k_o shown in Figure 1.2 can be represented by a second-order system as shown in Figure 8.1. The unknown linear spring stiffness is k_o, while M is the lumped mass of the object and the linear actuator's shaft, F is the force applied by the actuator onto the object representing the grasping force, and F_f models the lumped friction force arising due to the gripper mechanism and the object under grasp.

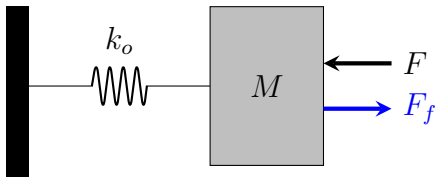

Figure 8.1: Linear model for stiffness estimation.

Figure 8.2 shows the rotational version of the second-order system of Figure 8.1 modeling the single degree of freedom gripper mechanism. It consists of a torsion spring of unknown stiffness k_o that needs to be determined using the squeeze test, and J is the inertia of the actuator's shaft and the rotary arm driving the torsion spring. τ is the torque applied by the rotary actuator, and τ_f is the lumped friction torque present in the system.

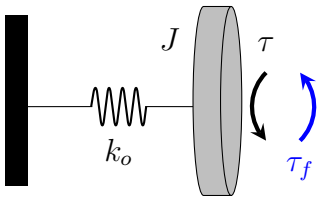

Figure 8.2: Rotational model for stiffness estimation.

8.2.2 Actuator Model

For simplicity, a rotary DC motor is considered and generates the torque τ. For a squeeze test, one possible method is to modify the position of the jaws. This method applies

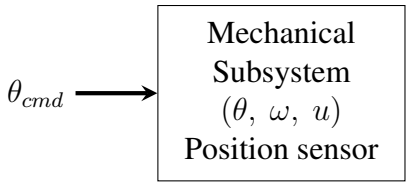

Figure 8.3: Single stage position controller. $\theta =$ motor position, and $\omega =$ motor velocity are the state variables. $u =$ input motor voltage. $\theta_{cmd} =$ commanded position.

increasing compression onto the object under grasp and translates to the operation of the DC motor under the position control mode. The alternate approach modifies the compression applied to the object, which translates to the current control mode of operation. The set of equations modeling the electromechanical characteristics of a rotary DC motor is given by

$$\begin{aligned} \text{Electrical subsystem: } u &= iR + L\frac{di}{dt} + K_m\frac{d\theta}{dt} \\ \text{Mechanical subsystem: } K_m i &= J_m\frac{d^2\theta}{dt^2} + b_m\frac{d\theta}{dt} + \tau_l \end{aligned} \tag{8.1}$$

where u is the voltage applied to the motor, i is the motor current, θ is the angular position, and $\omega = d\theta/dt$ is the angular velocity of the rotor. R and L are the winding resistance and inductance. J_m and b_m are the inertia and the mechanical damping of the actuator's shaft. τ_l is the load torque on the motor. Coupling exists between the electrical and the mechanical subsystems through the motor constant K_m. The equation system given by Equation 8.1 has an order of three. There exist two possible position controller implementation options, and [59] provides detailed discussions about the design. Only aspects essential to the research are summarized.

Single stage position controller

The high level representation of a single-stage position controller is illustrated in Figure 8.3. In this approach, the input voltage applied to the motor controls the motion of the rotor to a target position of θ_{cmd}. This design requires only one sensor – to measure the rotor position. As the electrical system's dynamics are faster than the mechanical system's

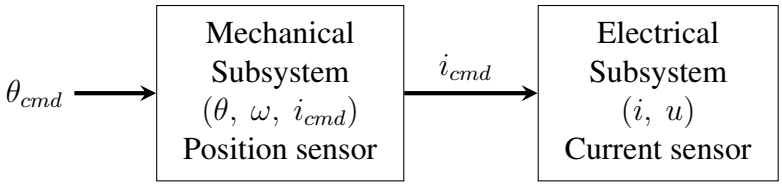

Figure 8.4: Two-stage position controller. θ = motor position, ω = motor velocity, and i = motor current are the state variables. u = input motor voltage. θ_{cmd} = commanded position, and i_{cmd} = commanded current issued by the mechanical subsystem to the electrical subsystem.

dynamics, model order reduction is possible through a quasi-static approximation of the electrical system. Setting $\frac{di}{dt} = 0$ reduces Equation 8.1 to a second-order system. The resulting current equation is given by

$$i = \frac{u - K_m\omega}{R} \tag{8.2}$$

With u as the voltage input to the motor and the load torque w_m modeled as a disturbance input, the DC motor's plant in state-space form for designing the single-stage position controller is

$$\frac{d}{dt}\begin{bmatrix}\theta \\ \omega\end{bmatrix} = \begin{bmatrix}0 & 1 \\ 0 & -\alpha\end{bmatrix}\begin{bmatrix}\theta \\ \omega\end{bmatrix} + \begin{bmatrix}0 \\ \beta\end{bmatrix}u + \begin{bmatrix}0 \\ \frac{-1}{J_m}\end{bmatrix}w_m \tag{8.3}$$

where $\alpha = \frac{K_m^2 + b_m R}{J_m R}$ and $\beta = \frac{K_m}{J_m R}$. The single-stage position controller results in a simpler implementation. However, a drawback of this approach is the possibility of operating the motor outside of its current limits.

Two stage position controller

The two-stage approach has two control loops that allow the operation of the motor within its current limits. Figure 8.4 illustrates the high-level function which exploits the separation existing between the electrical and mechanical subsystems in Equation 8.1. The inner control loop regulates the faster electrical subsystem, and the outer control loop

regulates the slower mechanical subsystem. This design requires a second sensor to monitor the current in addition to a position sensor. i_{cmd} is the commanded signal issued to the current control regulator by the mechanical subsystem, and w_m is the disturbance load torque input to the mechanical subsystem. The plant equations for designing the slower mechanical subsystem performing position regulation are given by

$$\frac{d}{dt}\begin{bmatrix}\theta\\ \omega\end{bmatrix} = \begin{bmatrix}0 & 1\\ 0 & -\dfrac{b_m}{J_m}\end{bmatrix}\begin{bmatrix}\theta\\ \omega\end{bmatrix} + \begin{bmatrix}0\\ \dfrac{K_m}{J_m}\end{bmatrix} i_{cmd} + \begin{bmatrix}0\\ \dfrac{-1}{J_m}\end{bmatrix} w_m \tag{8.4}$$

The outer position control loop issues current command requests i_{cmd} to the inner current control loop. The current regulator applies voltage inputs u to the motor. The motor's speed ω from the mechanical system is treated as a disturbance input to the current control loop and denoted by w_e. The plant model for designing the faster current regulator is given by

$$\frac{di}{dt} = \left[-\frac{R}{L}\right] x_3 + \left[\frac{1}{L}\right] u + \left[\frac{-K_m}{L}\right] w_e \tag{8.5}$$

Due to multiple control loops, the design complexity is higher when compared to the single-stage architecture but allows for the motor's operation within its current limits.

8.2.3 Simulation Model for Data Generation

With reference to Figure 8.2, the motor torque relates to the motor current and is given by $\tau = K_m i$. During an exploratory procedure (squeeze test), the DC motor is operated with an increasing position command, and the current is monitored, which is proportional to the applied torque. The motor current level changes in response to overcome the torsion spring stiffness, the friction torque, and the inertial torque. Assuming a two-stage position controller, the state-space representation of Figure 8.2 with the state variables $[\theta,\ \omega]$, input

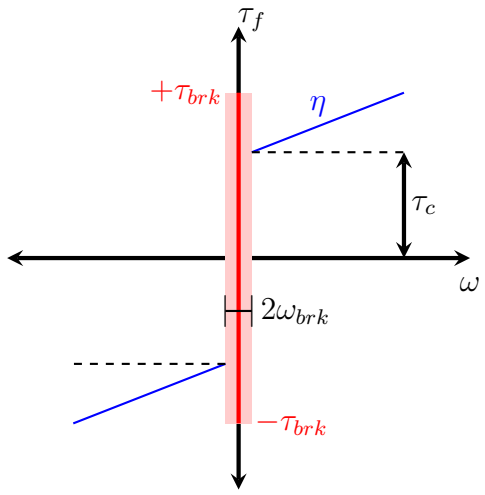

Figure 8.5: Stick-slip friction law.

current i, and friction torque disturbance τ_f is given by

$$\frac{d}{dt}\begin{bmatrix}\theta \\ \omega\end{bmatrix} = \begin{bmatrix}0 & 1 \\ -\frac{k_o}{J} & 0\end{bmatrix}\begin{bmatrix}\theta \\ \omega\end{bmatrix} + \begin{bmatrix}0 & 0 \\ \frac{K_m}{J} & -\frac{1}{J}\end{bmatrix}\begin{bmatrix}i \\ \tau_f\end{bmatrix} \tag{8.6}$$

Note that J represents the lumped inertia of the actuator's shaft and the grasped object, while τ_f represents the lumped friction forces in the system. Equation 8.6 is similar to Equation 8.4, but accommodates the lumped friction torque in the system and the spring stiffness of the object. Also, Equation 8.6 follows directly from the mechanical subsystem description of Equation 8.1 and formulates the simulation model as a second-order system instead of a third-order system. This is because the current regulator in the two-stage position controller eliminates the need to model the electrical dynamics. Another advantage is that only parameters corresponding to the mechanical system need to be known, i.e., $(K_m,\ J)$. The current loop's saturation effects and the quantization effects of the position and current sensors are included to improve the accuracy of the simulation model.

8.2.4 Friction Model

Modeling of friction effects is also critical. Some friction models employ a smooth variation of friction torque around $\omega = 0$, resulting in a unique one-to-one mapping between friction torque and angular velocity [60]. However, many systems exhibit stick-slip behavior, wherein a discontinuity in friction torque exists at $\omega = 0$. The Karnopp friction model is used to account for stick-slip friction; with this model, simulations can be performed with high fidelity at a low computation cost [60, 61].

The Karnopp friction model summarized in Figure 8.5 requires only four parameters, whereas other friction models require up to eight parameters [60]. Figure 8.5 illustrates two modes, "stick" mode corresponding to $\omega = 0$ and $|\tau_f| \leq \tau_{brk}$ and "slip" mode corresponding to $|\omega| \geq \omega_{brk}$ and $\tau_f = \tau_c \,\text{sign}\{\omega\} + \eta\,\omega$. The breakaway torque τ_{brk} represents the static friction level in the system, whereas the breakaway speed ω_{brk} represents a small but non-zero speed. τ_c is the Coulomb friction torque and η is the viscous friction coefficient. For simulation of the system given by Equation 8.6 with the friction model of Figure 8.5, the friction torque in the system is given by

$$\tau_f = \begin{cases} K_m i - k_o \theta & \text{, during stick} \\ \tau_c \,\text{sign}\{\omega\} + \eta\,\omega & \text{, during slip} \end{cases} \tag{8.7}$$

Transition from stick to slip is triggered by the condition $|K_m i - k_o \theta| > \tau_{brk}$. On the other hand, the transition from slip to stick is triggered by the condition $|\omega| < \omega_{brk}$. When the system given by Equation 8.6 is restricted to pure viscous friction, under equilibrium conditions the stiffness may be directly computed as $k_o = \dfrac{K_m i_{\text{eq}}}{\theta_{\text{eq}}}$; this simple approach does not apply when stick-slip behavior — notoriously difficult to predict or characterize in real-world applications — is significant. This is one of the motivations for leveraging machine learning methods for stiffness estimation.

Table 8.1: System Parameters

Parameter	Symbol	Value	Units
Inertia	J	2.28×10^{-3}	kg-m^2
Motor Constant	K_m	1.30	N-m/A
Position Sensor Quantization	–	2π/4096	rad
Current Sensor Quantization	–	2.69×10^{-3}	A
Supply Voltage	–	12	V
Sampling Frequency	f_s	1	kHz

8.3 Simulation

The experimental system utilizes a Dynamixel XM430-W210R smart servo DC motor. The smart servo is designed to be used as a black-box actuator and implements several control algorithms – position, velocity, and current. To simulate and generate datasets for regression, several parameters of the single degree of freedom rotation system, shown in Figure 8.2 and governed by Equation 8.6 and Equation 8.7 need to be determined. The parameter estimates are determined through experiments on the unloaded DC motor, and Appendix G provides details of the estimation procedure. The parameters are listed in Table 8.1 and are common for the simulations, dataset synthesis, and experiments. A designed persistently exciting speed command signal is applied to the motor, and the motor's position, current, and voltage are measured. Two methods are used to fit the measurement data – linear least squares and the greybox parameter identification tool of MATLAB. Only the viscous friction component is estimated for the motor, and the Coulomb friction and the stick-slip friction, although present in the unloaded motor, are assumed to be small and neglected. Moreover, the estimation of the motor's friction parameters is computationally challenging and is subject to change when an object, i.e., when a torsion spring is introduced into the system.

Figure 8.6 – Figure 8.11 shows the simulation response of the system when the DC motor's position control loop is subjected to a position reference command. Two actuation commands are considered – ramp and staircase. The increasing position reference command

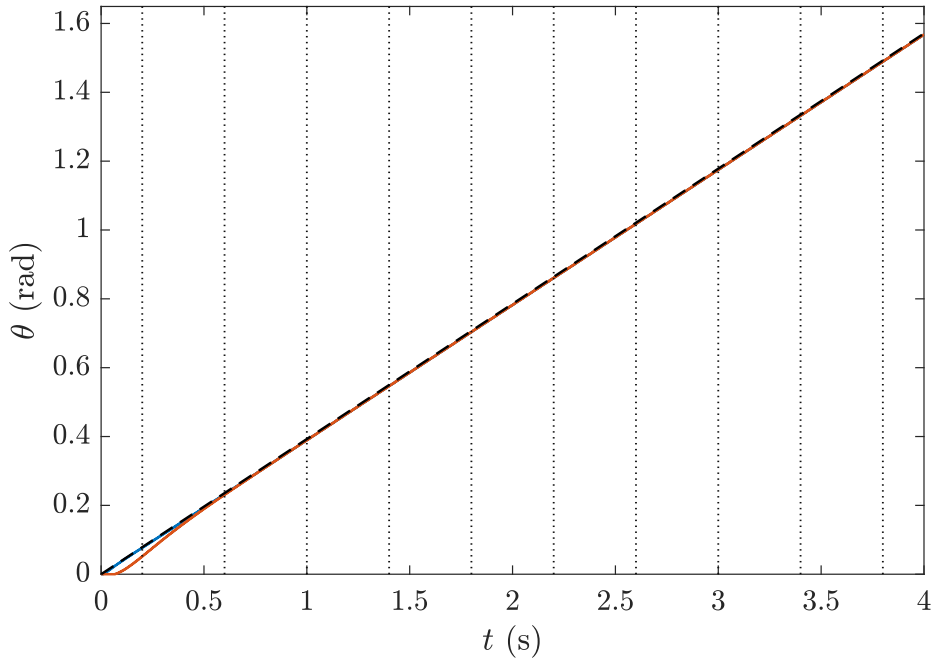

Figure 8.6: Simulated ramp position command to $\pi/2$ rad
(without friction [—], with friction [—], position command [**- -**], regressor inputs [**:**]).

results in the compression of the torsion spring, which is equivalent to an increased amount of squeezing of the object in the single degree of freedom gripper application with the grasp maintained. The simulation parameters are: $k_o = 111$ N-mm/rad, $\tau_{brk} = 200$ N-mm, $\tau_c = 150$ N-mm, $\eta = 50$ N-mm-s/rad, $\omega_{brk} = 10^{-3}$ rad/s. Note that the vertical dotted lines in the figures indicate the sampling instants used as input to the regressor discussed later.

For the ramp position actuation in Figure 8.6, the current through the motor shown in Figure 8.7 rises smoothly in response. However, under friction, a small error in the position can be seen initially up to $t = 0.2$ seconds due to some small stick-slip behavior as the system begins to move from rest. When the system is under motion, the current waveform for the system with friction has an offset compared to the system without friction. As the spring moves at a constant velocity, it results in a constant level of Coulomb and viscous friction torque as shown by Figure 8.8, with the offset in the current proportional to the friction level in the system.

Figure 8.10 shows the current waveform when the system is subjected to a staircase position actuation command shown in Figure 8.9. For the frictionless system, as the spring

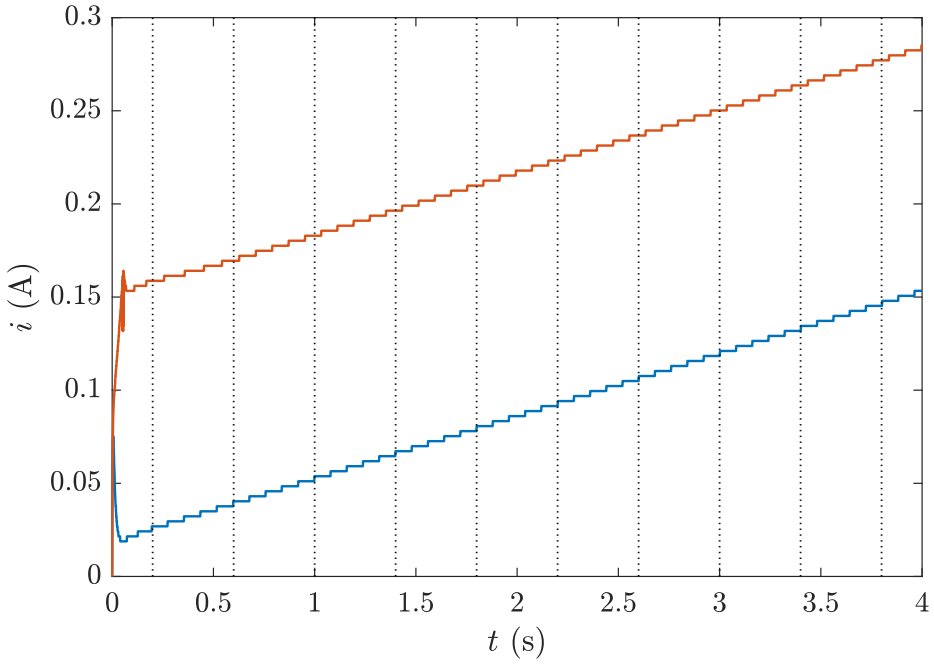

Figure 8.7: Simulated current measurement with ramp actuation (without friction [—], with friction [—], regressor inputs [:]).

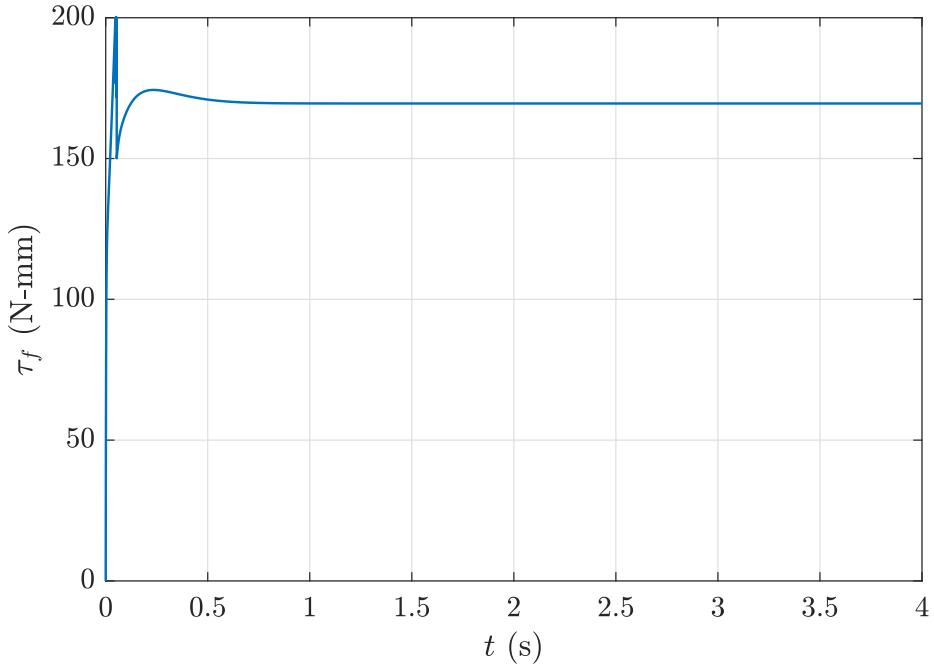

Figure 8.8: Friction torque with simulated ramp command.

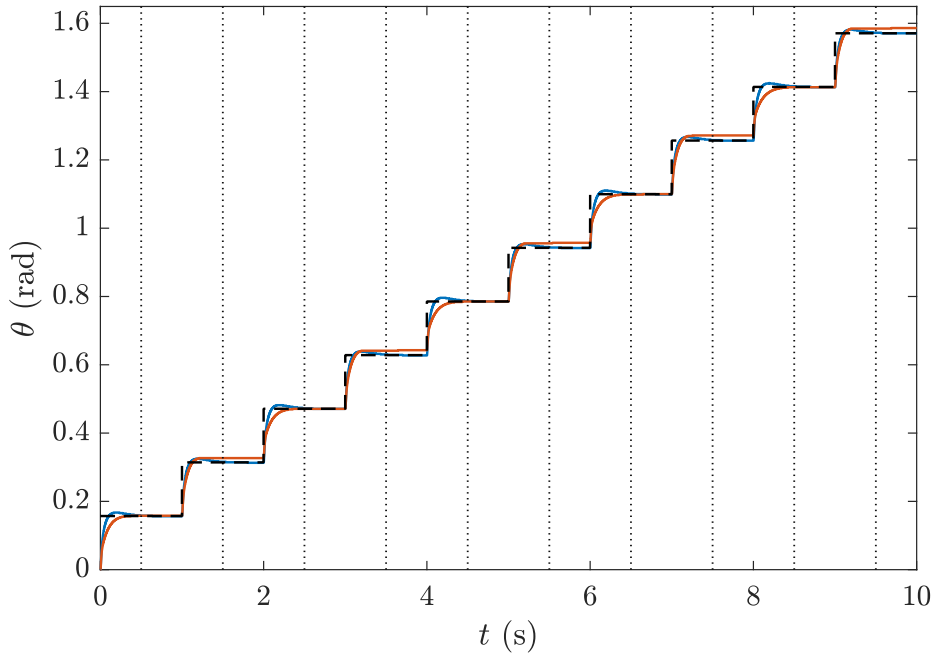

Figure 8.9: Simulated step position command to $\pi/2$ rad, 10 steps
(without friction [—], with friction [—], position command [**- -**], regressor inputs [**:**]).

is compressed, the motor current also increases in steps, with a constant current existing between each step. Under friction, the motor position closely tracks the position commands like the frictionless case. However, the current waveform exhibits a memory effect due to stick-slip friction behavior occurring between two subsequent steps. As motion ceases to exist after a steady-state is reached, with each step position change, the current takes on any value over a large range as given by Equation 8.7. This results in non-monotonic variations in the current waveform when the spring is compressed, as the additional current is used to overcome the friction effects as shown in Figure 8.11. The current spikes occur at the start of each repositioning step command event as the system begins to move from rest. The response to the staircase actuation is simulated for a longer duration to allow the position reference command to settle to steady-state before the next repositioning event and to study the regressor's performance under dry friction conditions.

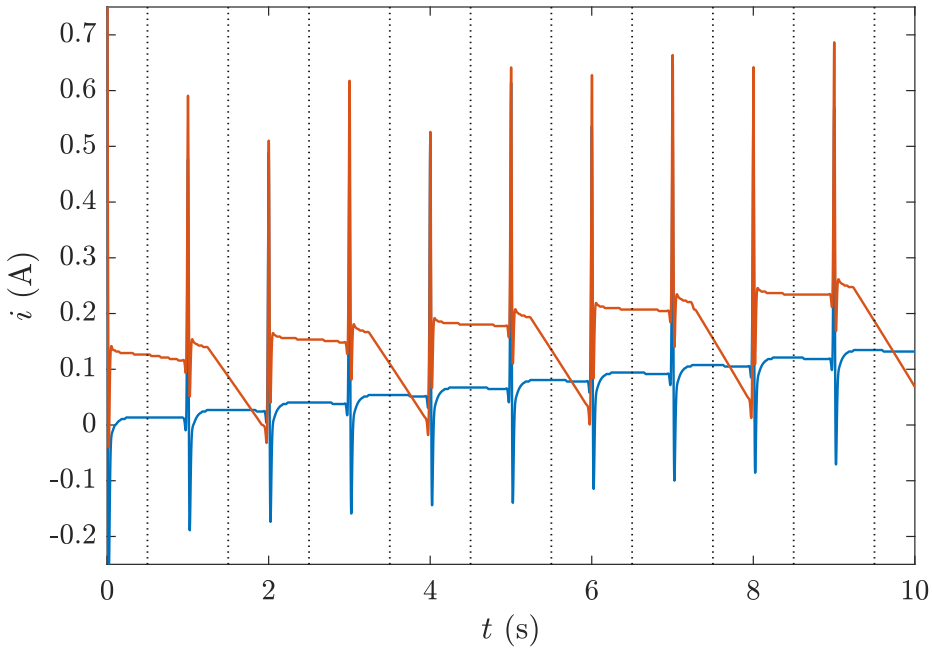

Figure 8.10: Simulated current measurement with step actuation (without friction [—], with friction [—], regressor inputs [:]).

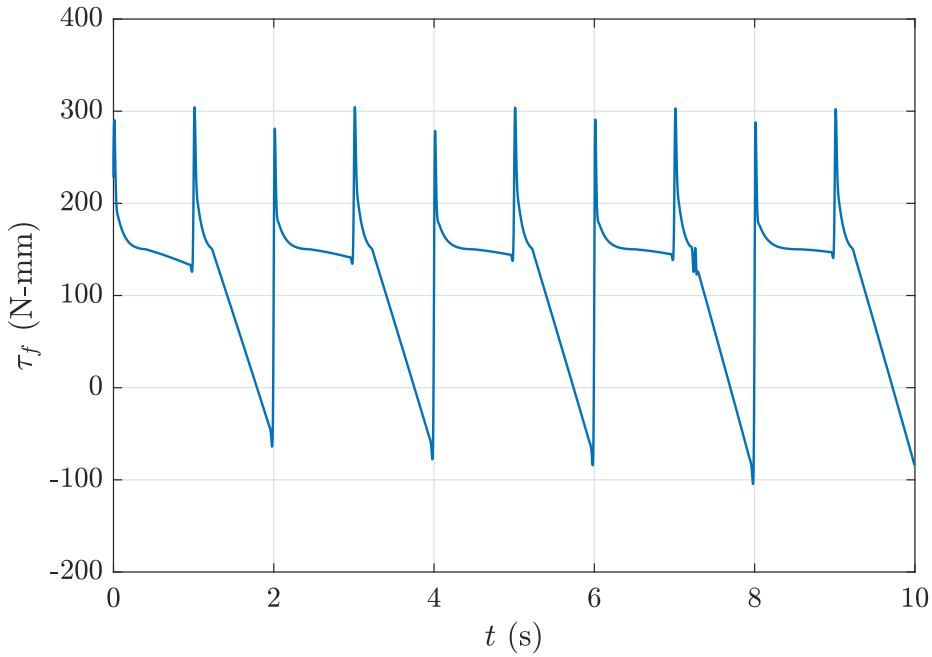

Figure 8.11: Friction torque with simulated step command.

8.4 Stiffness Regression

Through simulations, Section 8.3 establishes that the determination of the stiffness of an object as a ratio of the change in current to a change in position is applicable only for systems without friction at equilibrium. For stiffness estimation, the plant and the friction parameters change when a spring is introduced into the system, leading to an incorrect stiffness estimate if it is calculated as a ratio. Classical parameter estimation approaches can be employed to estimate the value of the unknown stiffness k_o. Although other parameters of the system can also be simultaneously estimated along with the unknown stiffness, classical approaches have several disadvantages. They require a knowledge of the plant physics to establish the estimation equations, a persistently exciting signal for the simultaneous estimation of multiple parameters [62], and have a higher computation cost when high bandwidth parameters related to friction are involved. Moreover, the design of persistently exciting signals needs care in situations such as grasping, as the object under a grasp can be ejected out of a grasp.

Inspired by data-driven machine learning approaches, regressors are developed and evaluated. The regressor models a function f between the input and the output data. As shown in Figure 8.12, the regressor accepts position and current measurements each of length L as the input and outputs a measure of stiffness. In the first step, referred to as the training step, the coefficients modeling the regressor function f are determined from the dataset consisting of the inputs and the ground-truth stiffness values. In the second step, the coefficients modeling f in the first step estimate the unknown object stiffness k_o. Since data approximates the function to estimate the stiffness, obtaining an accurate stiffness value from the trained regressor requires a large dataset [41, 42]. A simulation of the plant and friction parameters given by Equation 8.6 and Equation 8.7 is utilized to generate the dataset. A portion of the simulation dataset, referred to as the test dataset, is held out to evaluate the regressor function, where only the inputs (position and current) are provided, and the

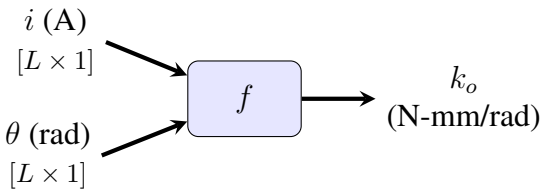

Figure 8.12: Estimating stiffness through regression.

accuracy of the stiffness estimate is computed. Regressors trained on datasets generated through simulations are also evaluated with experimental measurement data.

Although the synthesis of the virtual dataset requires an accurate physical description of the plant, the plant parameter values, its variability, and computing power during the dataset synthesis and regressor training phases, several benefits exist. A large virtual dataset can be more easily generated as a batch process with limited human intervention when compared to the work in Chapter 9; previous research in [32, 33, 39] also use experiments to generate sparse datasets. Based on [41, 42] a large dataset also helps prevent the overfitting of the regressor function f. In the virtual world, high bandwidth phenomena (friction) can be simulated with high fidelity, which can be challenging to introduce in an experimental setup. Since mechanisms are comprised of multiple parts manufactured to a tolerance specification, the part-to-part variability is another aspect that can be injected during virtual synthesis. This minimizes performance degradation when regressors trained on virtually generated datasets are used on real-world experimental data. Moreover, a trained regressor can be deployed onto low-cost embedded solutions as the evaluation of stiffness requires only elementary operations that can be performed rapidly.

8.4.1 Dataset Synthesis Settings

Several datasets are synthesized using the simulation model to study the ability of regressors to estimate stiffness in the presence of dry friction effects and variations in the plant parameters for the two actuation commands – ramp and staircase. Each dataset consisted of N unique items, where each item corresponded to a different stiffness value.

Table 8.2: Dataset Generation Parameters

Parameter	Symbol	Value	Units
Dataset Size	N	2000	–
Training:Testing Ratio	–	60:40	–
Sensor Measurement Length	L	10	–
Stiffness Range	k_o	$[1,\ 500]$	N-mm/rad
Ramp Actuation Duration	–	4	s
Staircase Actuation Duration	–	10	s
Breakaway Friction Range	τ_{brk}	$[1, 300]$	N-mm
Coulomb÷Breakaway Friction Range	α	$[0.45,\ 0.95]$	–
Viscous Friction Range	η	$[1, 300]$	N-mm-s/rad
J and K_m Tolerance	–	5	%

Additional variations are introduced to the friction parameters, i.e. $\tau_{brk},\ \tau_c,\ \eta$, and the DC motor's nominal plant parameters J and K_m listed in Table 8.1. A uniformly distributed random number generator provides the parameters for each simulation based on the operating range listed in Table 8.2. The dataset statistics for the various parameter values is shown in Figure 8.13. As per the Karnopp friction model, since $\tau_c < \tau_{brk}$, the value for τ_c is determined as a randomly generated fraction of the value of τ_{brk}, i.e., $\tau_c = \alpha\tau_{brk}$. The position controller's gains were tuned based on a nominal set of plant parameters and kept unchanged throughout the dataset generation process.

8.4.2 Regressor Evaluation

A Support Vector Machine (SVM) regressor with a linear kernel is considered. Mathematical details of the regressor are discussed in [41, 42]. The regressor accepts position and current sensor inputs each of length L, which controls its size. Other regressor architectures developed for time-series data and exploiting the sequential nature of the sensor measurements may be employed with similar performance. Since the simulations generate data on a dense time axis, the time instants at which the L position and current measurements are obtained is another design choice. For the dataset synthesis in this work, the L sampling

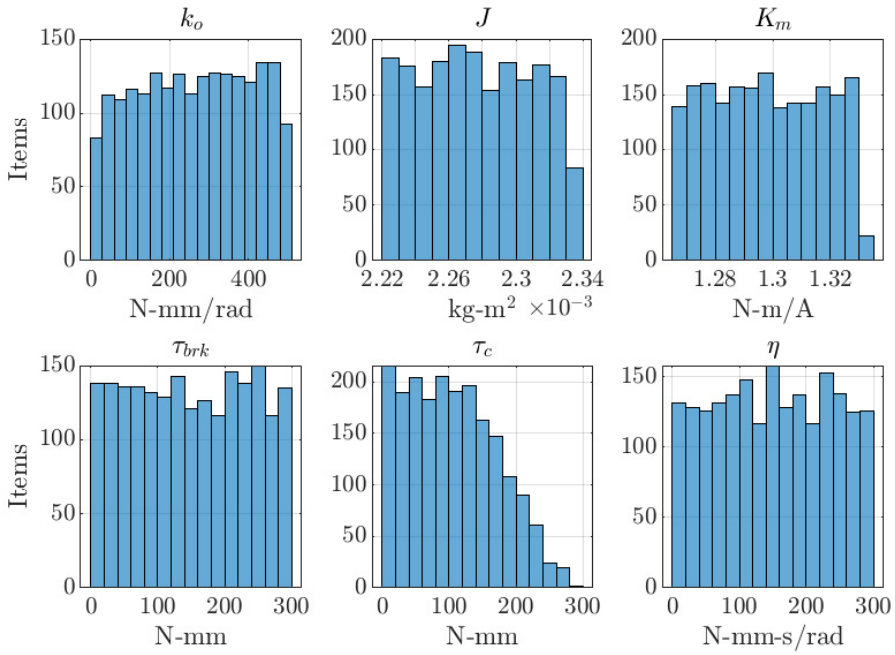

Figure 8.13: Statistics for the randomly generated set of parameter values. Each simulation run has a different set of parameters.

instants on the time axis shown by the vertical dotted lines in Figure 8.6 – Figure 8.7 and Figure 8.9 – Figure 8.10 are used. For the ramp actuation, the first point is logged at an offset to ensure that the system is in motion. Subsequent points are logged at equal intervals. For the staircase actuation, the L points are logged at the middle of each step. The datasets synthesized for each actuation are:

- Dataset D1: No friction or parameter variation
- Dataset D2: Friction without parameter variation
- Dataset D3: Parameter variation without friction
- Dataset D4: Both friction and parameter variation

A regressor is trained for each dataset corresponding to each actuation signal. Built-in routines in MATLAB from the Statistics and Machine Learning Toolbox are used during the

training stage. The regressor's performance is evaluated by computing the metric

$$\% \text{ Error} = \frac{|k_{Estimate} - k_{Truth}|}{k_{Truth}} \times 100 \tag{8.8}$$

where $k_{Estimate}$ is the regressor predicted stiffness value, and k_{Truth} is the ground truth stiffness used to generate the data. The datasets are abbreviated as Dx, while the corresponding regressors are abbreviated as Rx, where $x = 1, \ldots, 4$. Figure 8.14 shows the performance of the regressors designed for operation with the ramp position actuation, and Figure 8.15 shows those designed for operation with the staircase position actuation command. The mean performance error for the two actuation commands are tabulated in Table 8.3 and Table 8.4 respectively. Each cell corresponds to the performance when regressor Rx is evaluated on the dataset Dx. During regressor training, the datasets are partitioned into a training set and a test set based on the ratio listed in Table 8.2. So two performance measures corresponding to the training and testing set are listed for the diagonal entries in the tables. For the off-diagonal entries, the full dataset of length N is used to evaluate the regressor's performance, and therefore only one performance measure is listed in the table. However, for the Figure 8.14 and Figure 8.15, only the performance with the test dataset is displayed.

The dataset D1 represents the ideal scenario. Errors during the experimental identification of the system's parameters and due to part-to-part variation for manufactured components are both neglected. Regressor R1 applied to dataset D1 demonstrates that stiffness is accurately predicted with the position and current measurement data. In dataset D2, the friction effects are included and represent a situation closer to the experimental system. When regressor R1 is evaluated on dataset D2, there is a significant deterioration in the stiffness estimates with both the ramp and staircase actuation. For the ramp actuation, Figure 8.7 shows that the degradation is because of the offset in the current waveform due to Coulomb and viscous friction. For the staircase actuation, due to the presence of stick-slip behavior, the current waveform has non-monotonic changes as shown in Figure 8.10. Perfor-

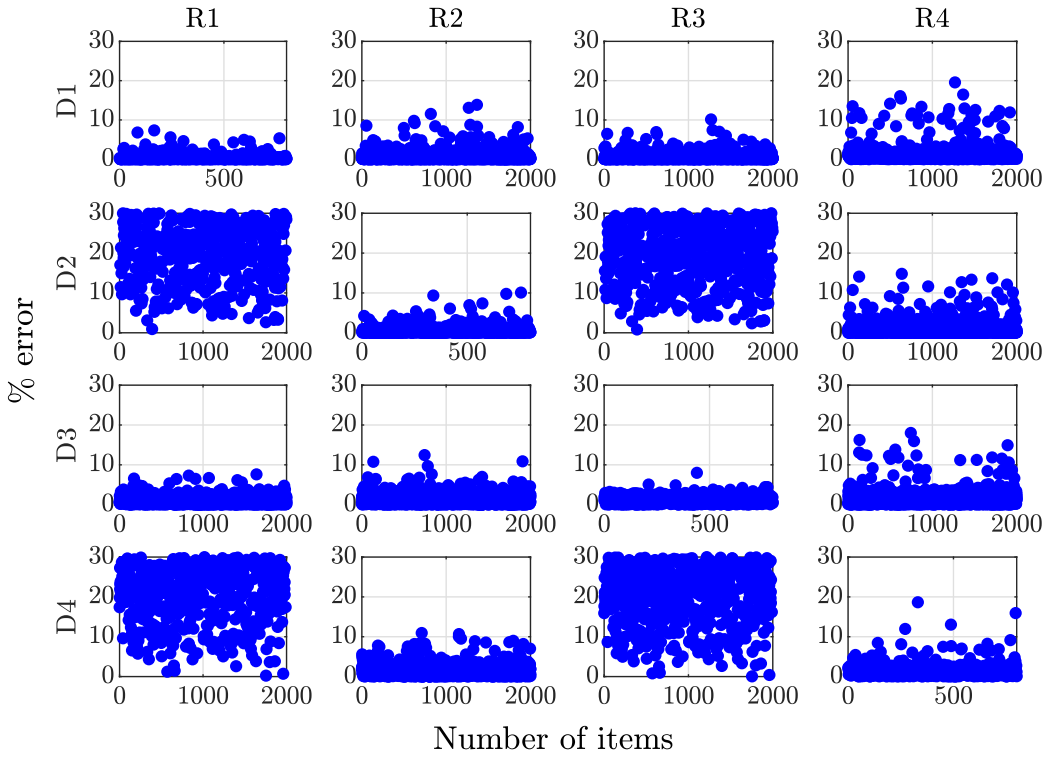

Figure 8.14: Stiffness regression performance on simulation datasets with ramp actuation.

mance degradation also occurs when regressor R1 is tested on dataset D4, which shows the importance of modeling friction phenomena in the system. When regressor R1 is applied to dataset D3, the performance degradation is mainly due to parameter variation introduced into the dataset. Friction has a more significant impact on the accuracy of stiffness estimation than the variation of simulation model parameters.

When the regressor R2 trained on dataset D2 that includes friction effects is evaluated on dataset D1 that does not have friction effects, performance comparable to the situation when regressor R1 is tested on dataset D1 is obtained. Moreover, the regressor R2 evaluated on dataset D2 shows that an SVM with a linear kernel can overcome the friction effects, which is predominantly viscous for the ramp actuation, and predominantly stick-slip for the staircase actuation. Similarly, regressor R2 applied to dataset D4 demonstrates good stiffness prediction accuracy. The performance degradation when regressor R2 is tested on dataset D3 is mainly because of the errors introduced due to the parameter variations. Hence, dataset D2 is a good starting point. Regressor R3 modeled on dataset D3 containing

Table 8.3: Mean % Error for Simulation Datasets with Ramp Actuation

	% Error			
Regressor/ Dataset	R1	R2	R3	R4
D1	0.29* 0.32	0.53	0.39	1.20
D2	96.06	0.51* 0.54	86.68	0.84
D3	1.34	1.43	1.32* 1.33	1.64
D4	103.55	1.46	93.45	1.58* 1.64

* performance of the training dataset only

Table 8.4: Mean % Error for Simulation Datasets with Staircase Actuation

	% Error			
Regressor/ Dataset	R1	R2	R3	R4
D1	0.37* 0.43	3.16	0.24	0.85
D2	61.49	3.06* 3.23	58.28	2.28
D3	1.43	3.86	1.32* 1.33	1.71
D4	56.70	3.72	53.67	2.95* 3.16

* performance of the training dataset only

only parameter variations performs poorly when evaluated on datasets D2 and D4 due to friction in both datasets.

The regressor R4 trained on dataset D4 containing both friction and parameter variation has an all-round performance similar to regressor R2 modeled on a dataset that considers only friction. Dataset D4 is a superset of all the datasets D1 – D3. As an SVM approximates a nominal set of coefficients from the underlying dataset, regressor R4 modeled on dataset D4 shows a slight performance degradation when used on other datasets. The percent errors for the staircase actuation are higher than the percent errors for the ramp actuation. This is

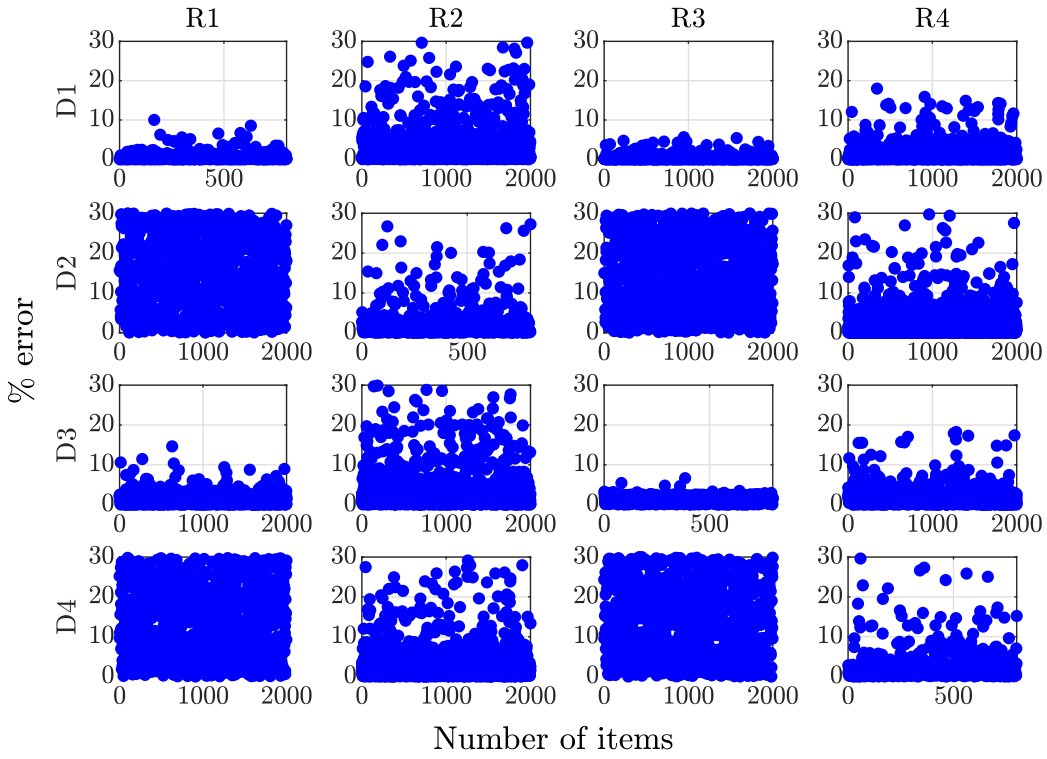

Figure 8.15: Stiffness regression performance on simulation datasets with staircase actuation.

because of the stick-slip phenomena with staircase actuation. Coulomb and viscous friction can be made more dominant by lubricating mechanical systems to reduce stick-slip friction and selecting actuations having a smooth motion, such as a ramp. Also, it is essential to include friction phenomena occurring in the system during virtual dataset synthesis.

8.5 Experimental Results

Figure 8.16 shows a CAD rendering of the experimental setup of the rotational system. It consists of a 3-D printed frame and a rotary arm installed on a Dynamixel XM430-W210R smart servo motor's shaft. The motor operates in the current-based position control mode. A Texas Instruments TMS320F28379D microcontroller issues time-periodic commands via a serial communication interface to the motor and logs the motor's position and current sensor measurement data at a rate of f_s. The axes of the motor and an off-the-shelf left-hand wound torsion spring are aligned. The experimental setup emulates a single degree of freedom gripper system. One end of the spring contacts the frame, and the other end of

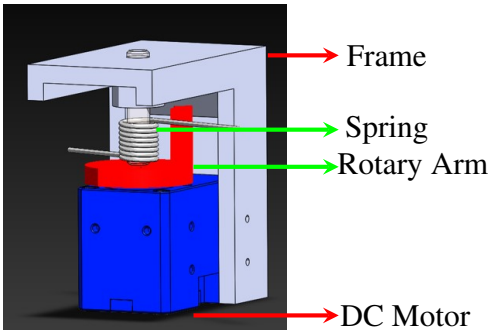

Figure 8.16: CAD rendering of the setup for experimental evaluation.

the spring contacts the rotary arm. Compression of the spring occurs between the frame and the rotary arm. The smart servo is commanded with a ramp and staircase actuation profile, similar to the commands used during the simulation and the dataset generation steps. Figure 8.17 – Figure 8.20 show the experimental measurement data with each actuation profile for torsion springs of two different stiffness values. The experiments show trends similar to the simulations. Since spring 2 has higher stiffness, the motor current for spring 2 is higher when compared to spring 1. Also, similar to the simulations, Figure 8.20 shows the presence of dry friction effects in the current measurement data with step actuation. A subset of the data log containing the L input points at the defined time instants shown by the dotted vertical lines is the input to the regressor. As the motor and the torsion springs have friction, the regressor modeled on the dataset with both friction and parameter variations is used.

Table 8.5 tabulates the experimental results and evaluates regressor R4. The regressor is trained on virtually synthesized dataset D4 and contains both friction and parameter variation. Off-the-shelf springs from McMaster-Carr Supply Co. are used (Spring 1 Part No. 9271K708, Spring 2 Part No. 9271K232). The tables list the mean of 5 trials for each case. The worst-case stiffness estimation accuracy for ramp actuation is 3.4%, and for the staircase actuation is 5%.

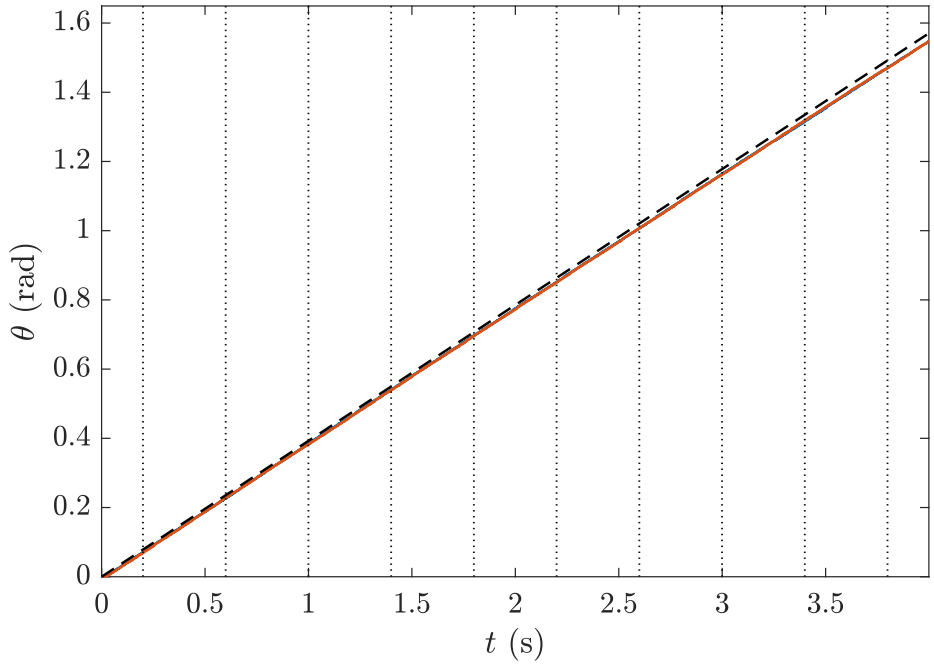

Figure 8.17: Experimental ramp position command to $\pi/2$ rad
(Spring 1 [—], spring 2 [—], position command [- -], regressor inputs [:]).

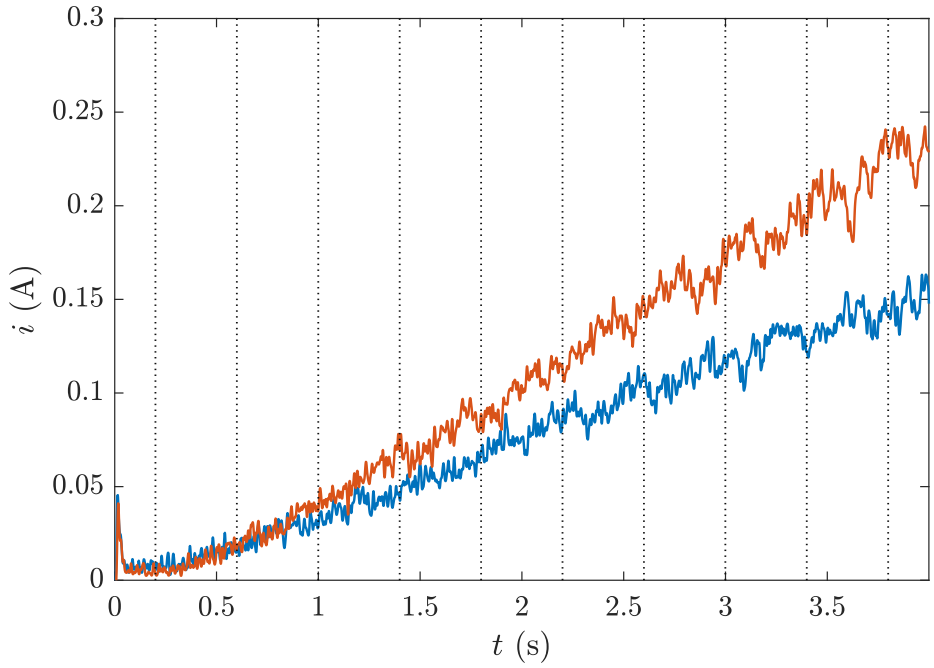

Figure 8.18: Experimental current measurement with ramp actuation
(Spring 1 [—], spring 2 [—], regressor inputs [:]).

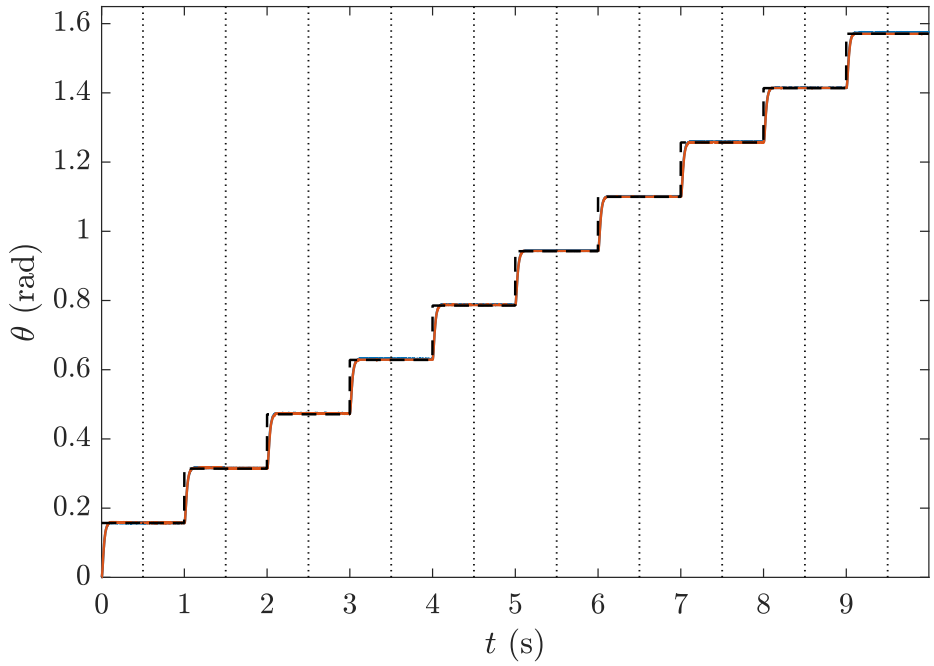

Figure 8.19: Experimental step position command to $\pi/2$ rad, 10 steps (Spring 1 [—], spring 2 [—], position command [- -], regressor inputs [:]).

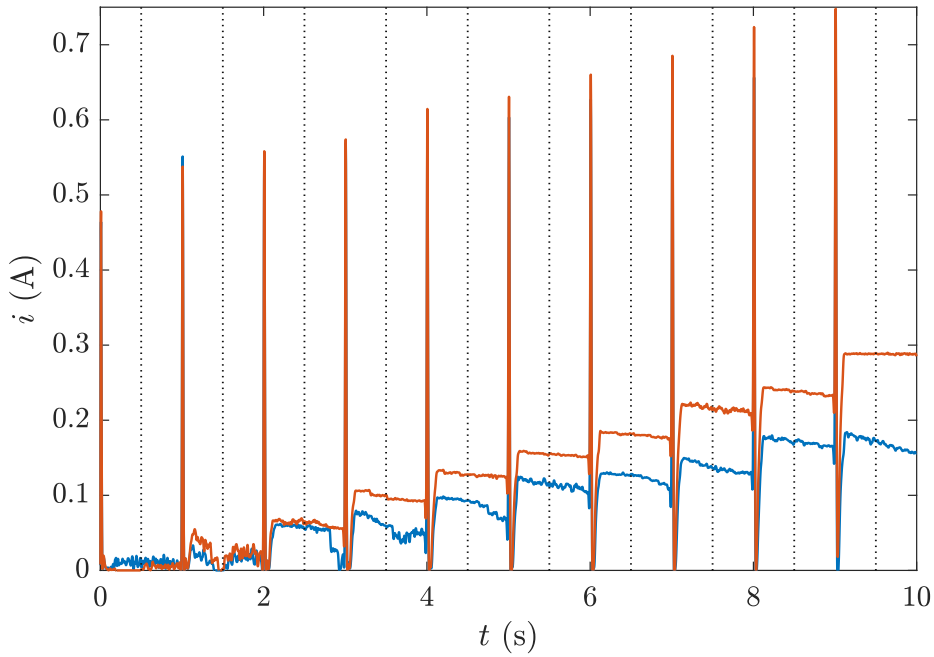

Figure 8.20: Experimental current measurement with step actuation (Spring 1 [—], spring 2 [—], regressor inputs [:]).

Table 8.5: Performance with Experimental Data

Ground Truth (N-mm/rad)	Spring 1 111.5		Spring 2 161.8	
Regressor	Estimate N-mm/rad	Error %	Estimate N-mm/rad	Error %
Ramp actuation	110.4	0.9	167.3	3.4
Staircase actuation	117.0	4.9	169.9	5.0

Datasheet specified ground truth tolerance = 10%.

8.6 Summary and Conclusion

This chapter considers a single degree of freedom gripper mechanism and demonstrates how only actuator position and current measurements can determine the unknown stiffness of an object, i.e., a spring, using regression. The chapter also discusses the synthesis of datasets for training regressors through simulation and the aspects that need consideration. Simulation allows the generation of large datasets as a batch process, which prevents overfitting issues during regressor training. The chapter exposes how nonlinear effects, such as dry friction, can be incorporated during the dataset generation process to improve the regressor's prediction accuracy. Regressors improve stiffness estimation performance when dry friction and parameter variation are present in the mechanism. Also, regressors trained on simulation datasets can accurately estimate the stiffness when fed experimental measurements. The work presented in this chapter resulted in the publication [63].

CHAPTER 9

STIFFNESS ESTIMATION WITH UNDERACTUATED TRANSMISSION MECHANISMS

9.1 Introduction

Research in [32, 33, 36] presents grippers that have multiple jaws that resemble human fingers. The finger mechanisms utilize an underactuated transmission mechanism to achieve motion. Figure 9.1 shows a schematic representation of a finger driven by a tendon-pulley transmission mechanism inspired from [32, 33]. A single actuator drives the two-link mechanism; the tendon starts at the pulley attached to the motor, runs continuously through the body of link-1, and terminates at link-2. From [64], the kinematic constraint that relates the motor's position and the link angles is given by

$$\theta_m r_m = \theta_1 r_1 + \theta_2 r_2 \tag{9.1}$$

where $r_m,\ r_1,\ r_2$ and $\theta_m,\ \theta_1,\ \theta_2$ are the pulley radii and positions of the motor and links 1 and 2 respectively. Equation 9.1 illustrates the coupled motion of the two links due to the tendon-pulley mechanism. The application of an increasing motor torque allows the taut tendon to transfer torques to the two links causing a rotation, say in one of the directions as indicated in the schematic. During contact between an object and the finger, an increasing motor torque transfers a compressive force onto the object under a grasp. It is interesting to note that the rotation of the motor can cause motion of the links only in one of the directions (counter-clockwise in the graphic). Torsion springs are located along the link axes and cause motion of the links in the opposite direction (clockwise in the graphic). When the motor torque is removed, the restoring torque provided by the springs returns the links to their equilibrium position. Other designs described in [64] utilize additional tendon pulley

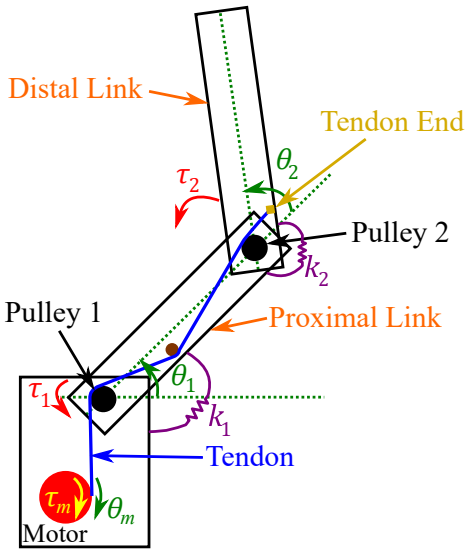

Figure 9.1: Schematic of the underactuated tendon-pulley transmission mechanism.

transmission trains to cause rotations in the opposite direction to restore the links but result in fully actuated mechanisms.

Underactuated mechanisms in grippers are increasing in popularity because control algorithms have low levels of complexity resulting in open-loop operation. Fewer sensors are needed, which reduces the overall cost of grippers, i.e., joint position and torque sensors are not required. Equation 9.1 also illustrates the adaptability of the finger to an object's shape. For a given θ_m and assuming a taut tendon, θ_1 and θ_2 can change based on the object's shape. This feature is suitable for applications where object manipulation is essential. The reduced control complexity also comes at a price, where it is not possible to enforce control of both links $(\theta_1,\ \theta_2)$ simultaneously, which may be desirable for some applications. Reorientation of the gripper pose could result in a drop in the tendon tension resulting in a loss of grasp. On the other extreme, it is also possible to apply forces that damage the object or eject it out of a grasp. Compared to fully actuated mechanisms, the operating workspace of the underactuated gripper is reduced and requires care during the design phase [36].

The focus of this chapter is to extend the squeeze test approach presented in Chapter 8 to underactuated fingers driven by tendon-pulley transmission mechanisms as shown in Figure 9.1. The finger has access only to position and current sensor measurements from the

actuator that drives the transmission train. For comparison, prior research work in [32, 33, 35] utilize force sensor arrays mounted on the finger to classify stiffness into a few categories (high, medium, low stiffness). The chapter designs regressors for the underactuated finger mechanism to provide a continuous-valued linear stiffness output in SI units. The dataset to train and evaluate the regressor is obtained through automated squeeze test experiments and provides a comparison with the approach presented in Chapter 8, which uses simulations to generate the dataset to train the regressor. Since a large dataset is needed to train the regressor, an apparatus that simulates stiffness is developed. The apparatus presents a standardized and calibrated stiffness to the underactuated finger mechanism during data collection and can be adjusted electronically. The approach overcomes the challenges of previous research in [32, 33, 35]; in [33], a small dataset (about 75 items) is obtained from objects made from polyurethane foam of different linear stiffness, and [35] uses everyday objects during data collection. It is essential to retain the object's shape when stiffness is varied, as classifiers can exploit attributes that characterize the shape during machine learning. The stiffness apparatus systematizes the data collection process and allows only the stiffness to vary.

9.2 Stiffness Apparatus

The apparatus to emulate linear stiffness is shown in Figure 9.2. It consists of parallel plates driven by a linear DC motor. A load cell is located between the actuator and the plates to measure the normal forces applied to the apparatus by the gripper's fingers. The linear actuator operates in a position control loop. Stiffness regulation is achieved by commanding a position to the linear actuator using the load cell's readings. Direct measurement of the applied external force obviates the need to model the friction and backlash arising in the linear actuator, which can be significant.

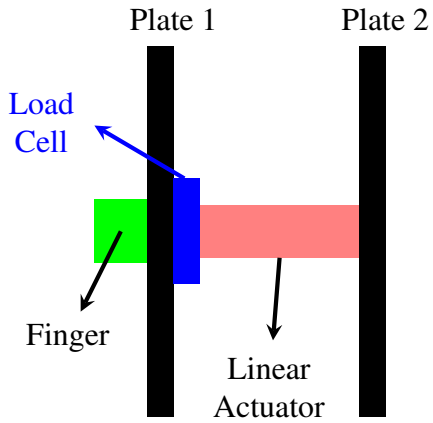

Figure 9.2: Cross-section of the stiffness apparatus for electronically generating linear stiffness during data collection.

9.2.1 Stiffness Control Loop

The stiffness control loop architecture is shown in Figure 9.3. The design model follows the single-stage position control formulation discussed in Subsection 8.2.2 and based on [59]. An Actuonix L12-P DC motor with a 3 cm pitch operates the parallel plate device. The Texas Instruments TMS320F28379D MCU implements the embedded controller. PWM signals generated by the MCU apply voltage input to the DC motor through an H-Bridge (DRV8305 booster pack). The rail voltage of the H-Bridge is set to $V = 6$ V. Analog position feedback provided by the motor is logged using an ADC peripheral. A 5 kg load cell TAL220B connects to a load cell amplifier HX711 and provides digital force measurements to the MCU through serial communication. The HX711 provides measurements at a maximum rate of 80 Hz.

In Figure 9.3, k_{ref} is the desired stiffness of the apparatus, F and y are the measurements from the force and the position sensor. Equation 8.3 provides the plant model used to design the controller gains $(K_{11},\ K_{12},\ K_2)$ and the estimator gains (L_1, L_2) for the position control loop. Note that Equation 8.3 lists the plant physics for a rotary motor, but the same equations apply even to a linear motor by interpreting the parameters in terms of their linear analogues. $\hat{\mathbf{x}} = [\hat{x}_1\ \ \hat{x}_2]^T$ are the estimator's states corresponding to the linear position and velocity.

σ is the state variable associated with the integrator. y_{ref} is an equilibrium position of the apparatus. Force sensor measurements modify the command issued to the position control loop w.r.t. the equilibrium position. The pre-saturated control input $u^*[k]$ at the current instant k is computed as

$$u^*[k] = -K_{11}\hat{x}_1[k] - K_{12}\hat{x}_2[k] - K_2\sigma[k] \tag{9.2}$$

The control input to the actuator is limited to a maximum rail voltage of V. Actuator saturation is achieved by

$$u[k] = \begin{cases} V, & u^*[k] > V \\ -V, & u^*[k] < -V \end{cases} \tag{9.3}$$

For a control loop rate of h, applying forward Euler discretization, the integration equations are given by

$$\hat{x}_1[k+1] = \hat{x}_1[k] + h\left(\hat{x}_2[k] - L_1(\hat{x}_1[k] - y[k])\right) \tag{9.4}$$

$$\hat{x}_2[k+1] = \hat{x}_2[k] + h\left(-\alpha\hat{x}_2[k] + \beta u[k] - L_2(\hat{x}_1[k] - y[k])\right) \tag{9.5}$$

where α and β are the motor's parameters. The integrator update equation with anti-windup compensation is implemented as

$$\sigma[k+1] = \sigma[k] + \begin{cases} 0 & , \ |u^*[k]| > V \\ h\left(y[k] + \dfrac{F[k]}{k_{ref}} - y_{ref}[k]\right) & , \ |u^*[k]| \leq V \end{cases} \tag{9.6}$$

The H-Bridge applies the voltage across the motor, and the duty cycle applied for an

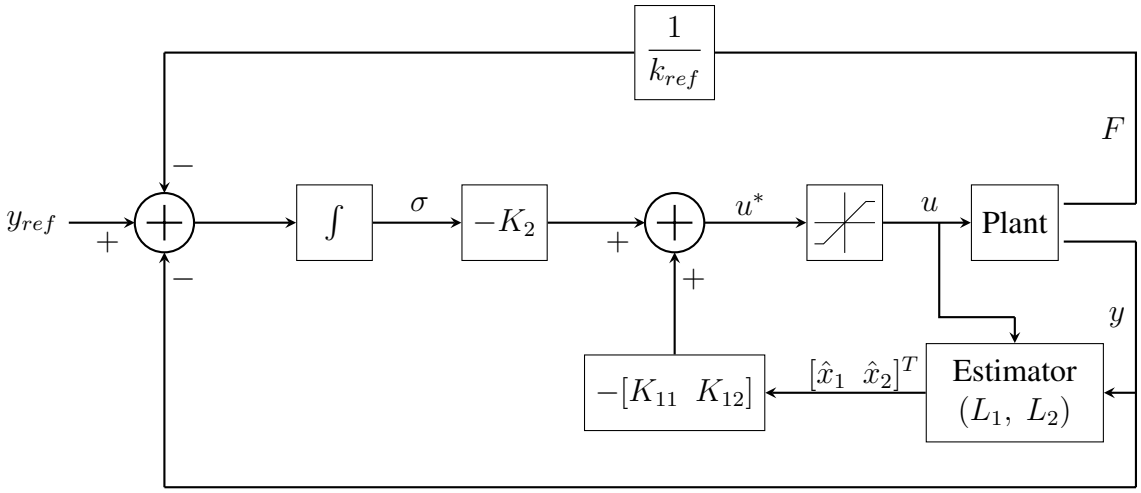

Figure 9.3: Stiffness control loop implementation. k_{ref} sets the stiffness level of the apparatus.

up-down time-base counter is determined by

$$d[k] = \frac{1}{2}\left(1.0 + \frac{u[k]}{V}\right) \tag{9.7}$$

Based on [59], with the regulator and estimator parameters λ_r and λ_e, the formulas for the loop gains are given by

$$\begin{gathered} K_{11} = \frac{3\lambda_r^2}{\beta}, \quad K_{12} = \frac{3\lambda_r - \alpha}{\beta}, \quad K_2 = \frac{\lambda_r^3}{\beta} \\ L_1 = 2\lambda_e - \alpha, \quad L_2 = (\lambda_e - \alpha)^2 \end{gathered} \tag{9.8}$$

9.2.2 Stiffness Loop Experimental Evaluation

The linear motor's parameters are obtained experimentally with the procedure detailed in Chapter H and the identified parameters are listed in Table H.1. The embedded controller implements the equations listed in Subsection 9.2.1. The control loop is operated at a rate of 1 kHz ($h = 1$ ms) with the gain values set to $\lambda_r = 30$ rad/s and $\lambda_e = 120$ rad/s. Note that the position sensor's measurements are sampled at the control loop's rate of 1 kHz, while

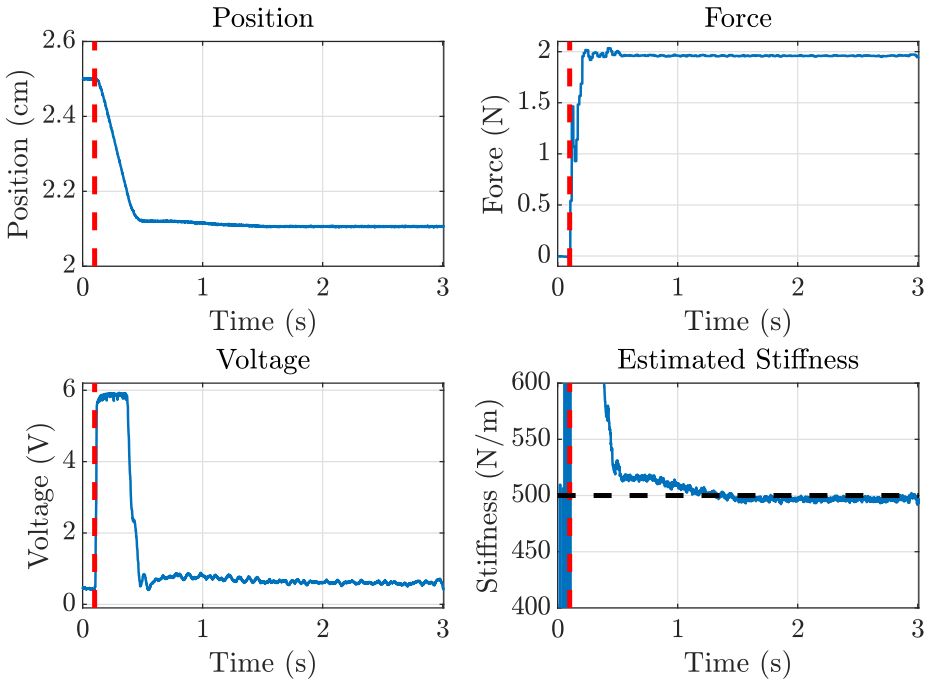

Figure 9.4: Stiffness loop performance for $k_{ref} = 500$ N/m. Force of 1.96 N through a 200 g test mass is introduced at $t \approx 0.1$ s. Onset of loading [- -], commanded stiffness [- -].

the force sensor's measurements are sampled at 80 Hz. During the periodic execution of the control loop, for approximately 12 samples, the same force sensor reading is used during the integration of the state equations described in Subsection 9.2.1. The PWM peripheral uses a timebase frequency of 25 kHz.

The operation of the stiffness loop is shown in Figure 9.4, where the stiffness level is set to $k_{ref} = 500$ N/m. The stiffness apparatus is subjected to a force of 1.96 N (test mass of 200 g) at about 0.1 seconds. The initial reference position of the stiffness apparatus is at 2.5 cm, and the application of force results in a compression of about 3.9 mm, settling approximately 0.32 seconds later. The mean steady-state error in stiffness due to the step force application in the example is ≈ 1.2 N/m.

9.3 Stiffness Data Collection

Figure 9.5 shows the snapshot of the underactuated finger applying compressive forces to the stiffness apparatus. The finger hardware and the stiffness apparatus were 3-D printed

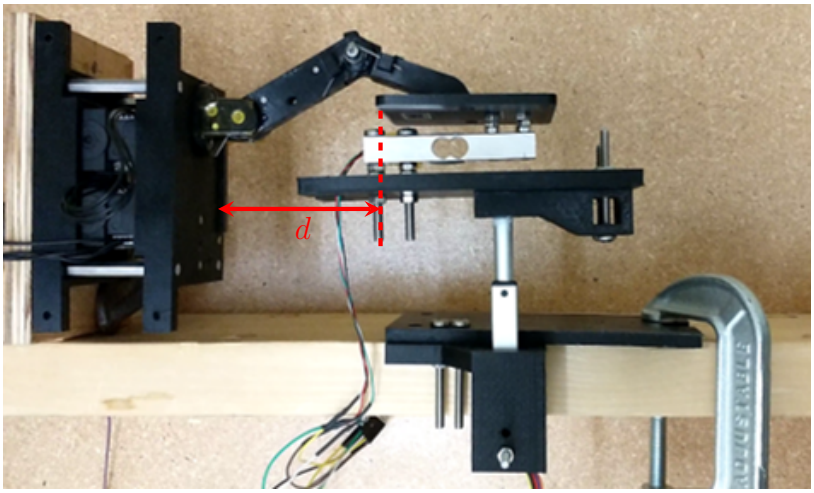

Figure 9.5: Underactuated finger applying compressive forces onto the stiffness apparatus during a squeeze test.

using ABS plastic. The stiffness apparatus implements hardware and algorithms discussed previously to behave like a linear spring. Since the squeeze test involves no manipulation during grasping (i.e., lifting, relocating the object), the finger assembly and the stiffness apparatus are clamped to the table. The finger design is inspired by [32] but makes several upgrades through simulations of the finger's physics. The restoring mechanisms connecting the links use a torsion spring instead of a linear spring used in [32, 33], minimizing contact between various components. Lubrication is introduced at the joints to make viscous friction effects dominant. As clarified by Equation 9.1, an increasing motor position (tendon tension) results in a coupled motion of both links.

The MCU connects to a host PC through the serial communication interface and exchanges stiffness settings and the finger actuator's measurement data during each squeezing experiment. Apart from the linear stiffness, the setup also allows variations in the distance between the gripper and the apparatus (d in Figure 9.5). The two experimental conditions are used to build the dataset and permit some degree of automation during data collection. The finger-apparatus contact can occur in several ways – fingertip contacts, proximal or distal links contact at an interior point, or both links contact. The data collection considers only fingertip contacts, and the separation distance (d) between the gripper and the apparatus

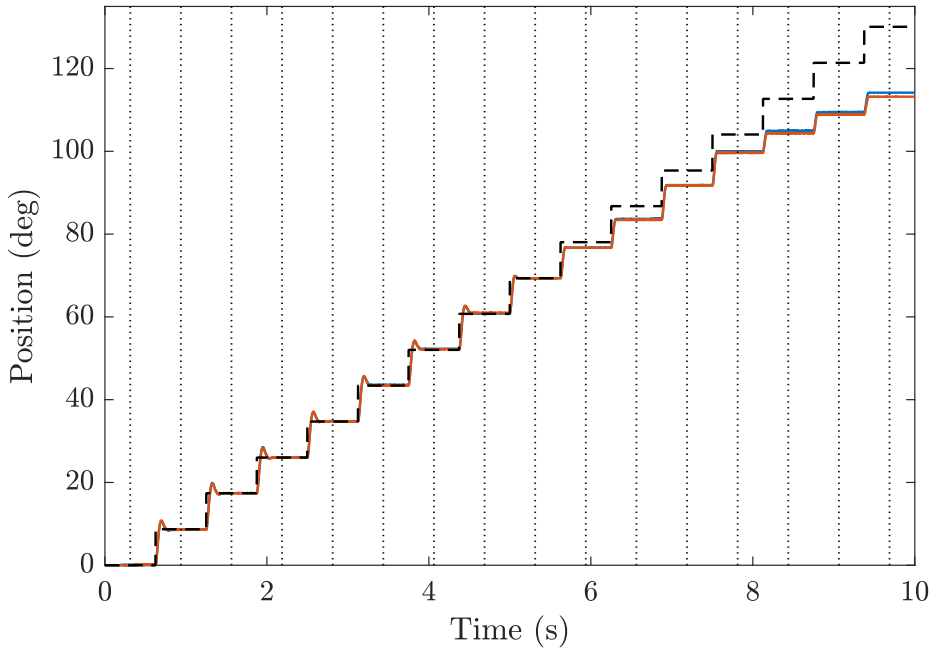

Figure 9.6: Position measurements during squeeze test (stiffness $k_{ref} = 400$ N/m [—], stiffness $k_{ref} = 600$ N/m [—], position command [- -], regressor inputs [:]).

is selected to meet the constraint. Also, contacts that transition to a fingertip contact are not considered.

Similar to Chapter 8, the Dynamixel XM430-W210R smart servo motor drives the underactuated finger of Figure 9.5. The motor operates in the position control mode during data collection. The controller gains are tuned to a nominal set of parameters based on trial-and-error and are unchanged throughout the dataset generation process. A Texas Instruments TMS320F28379D MCU issues serial commands to the servo motor and obtains the motor's position and current sensor data. Figure 9.6 – Figure 9.7 show the measurements when a staircase position command is applied by the motor controlling the gripper's finger. Both links are initially at an equilibrium position and do not contact the object. As the position command increases, the underactuated finger closes in on the object and makes initial contact. With increasing compression of the object, the current through the motor also increases. Figure 9.7 shows that the finger-object contact occurs at around 4.75 seconds, after which the finger applies compressive forces.

The approach phase is an additional element in the underactuated finger experiments,

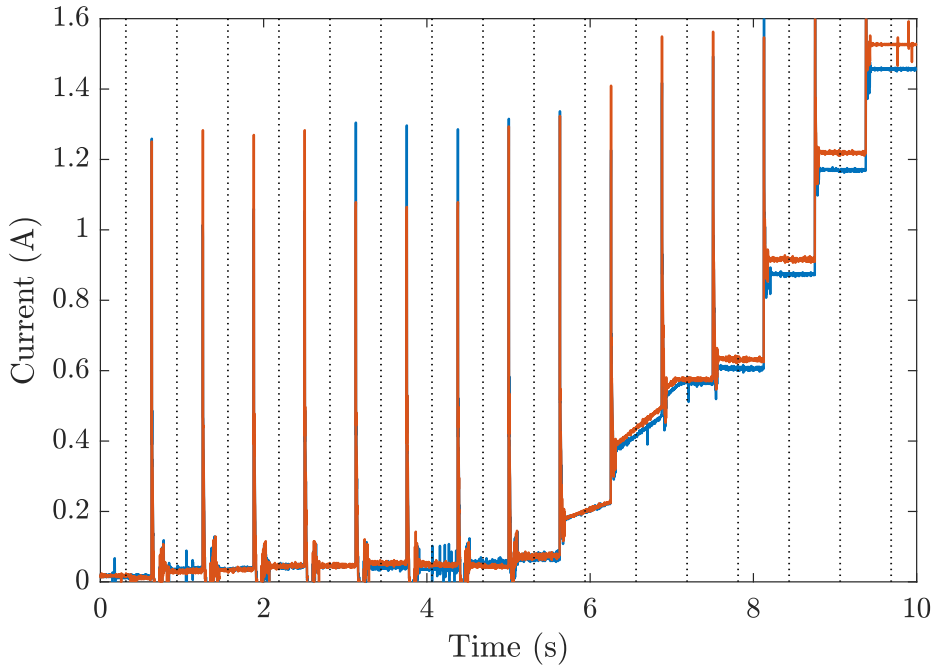

Figure 9.7: Current measurements during squeeze test (stiffness $k_{ref} = 400$ N/m [—], stiffness $k_{ref} = 600$ N/m [—], regressor inputs [:]).

while in Chapter 8, the spring and the jaw are in contact throughout the data collection phase. The position, current, and the contact instant also include attributes characterizing the object's size and the location within the finger's workspace. As the stiffness apparatus maintains the same object size, it ensures that the regressor learns only components that affect the stiffness. In the figures, as the stiffness increases, the discrepancy between the commanded position and the measured position also increases. The controller attempts to bridge the position gap with the increased current flow, features leveraged by the regressor-based stiffness estimation approach. Some small non-monotonic behavior is visible in the current waveform, which is attributable to low levels of dry friction in the mechanism; dry friction appears due to contact between the links and tendon-link contact.

The data collection settings are summarized in Table 9.1. Chapter 8 discusses the effects of dry friction and the selection guidelines for an actuation signal. However, a staircase actuation signal is selected to provide a conservative estimate of the stiffness regression performance for the underactuated finger mechanism. The L vertical dashed lines

Table 9.1: Data Collection Settings with the Underactuated Finger

Parameter	Symbol	Value	Units
Dataset Size	N	750	items
Training:Testing Ratio	-	0.8	-
Staircase Actuation Duration	-	10	s
Number of Staircase Steps	-	15	-
Sensor Measurement Length	L	16	-
Sampling Frequency	f_s	1	kHz
Stiffness Range	k_o	$[400, 1800]$	N/m
Position Range	d	$[6,\ 10]$	cm

in Figure 9.6 – Figure 9.7 indicate the time instants when the data is sampled for regressor input, similar to Chapter 8. The staircase actuation duration, the position command, and the number of steps are the design criteria for the actuation signal; selected based on the stiffness range, the gripper's workspace, and to allow for equilibrium to be achieved in the position and current measurements before the samples for the regressor inputs are obtained.

The dataset consists of N items, and each item corresponds to data from a unique experiment (stiffness setting, distance change). The stiffness range models a wide variety of objects. The linear stiffness range between $[400,\ 1800]$ N/m is selected based on the results presented in [33], where the values at the lower bound correspond to compressible objects (ex. foam), while those at the upper bound correspond to rigid objects (ex. wood block). A uniformly distributed random number generator programs a reference stiffness level k_{ref} for each trial. Additionally, the dataset diversity is increased by modifying the separation d between the gripper's base and the stiffness apparatus as shown in Figure 9.5 every 75 trials by 0.4 cm.

9.4 Regression Performance

Figure 8.12 illustrates the high-level representation of the regression architecture. Position and current, each of length L, are the inputs to the function f. The L data points correspond to the values at the time instants shown by the vertical dashed lines in Figure 9.6 – Figure 9.7. The function f outputs a measure of the linear stiffness in N/m. Since the finger

consists of multiple links driven by the tendon-pulley transmission mechanism, the physics of the finger involves trigonometric terms. This motivates the use of a nonlinear function to model f from the regression dataset. The function f consists of three layers – an input layer, a network layer, and an output layer. The input layer mainly formats the data and performs normalization. For the network layer, two competing options exist – a single layer Neural Network (NN) and a single layer Long Short Term Memory (LSTM), each having a size of 50. References [41, 42] discuss the theoretical details of the NN and the LSTM networks. The design choices considered in this chapter are referred to as shallow networks. On the other hand, for example, the network layer for deep networks is characterized by multiple copies of NN or LSTM layers. The output layer consists of a fully-connected layer to provide the linear stiffness estimate in SI units.

The dataset is divided into a training set and a test set, and the test set is held out during the training phase. This process is analogous to training a regressor and deploying the trained model into the gripper for live validation with new measurement data under different experimental conditions $(k_{ref},\ d)$. The networks are designed and trained with built-in libraries from MATLAB's Deep Learning Toolbox. Figure 9.8 summarizes the performance during the training and testing phase, where the predicted stiffness is compared with the ground truth stiffness for each item in the datasets. The deviation from the nominal value, i.e., ground truth = estimate and shown by the dashed red line, indicates the estimation error. The performance error in the stiffness measurements is determined using Equation 8.8, and Table 9.2 summarizes the mean prediction accuracy. Regressor-based stiffness estimation achieves comparable performance with both networks – NN and LSTM.

The performance with the test dataset suggests that the regressor can generalize well to new test scenarios that the regressor has not seen. Since the staircase actuation is applied, the measurement data contain effects due to dry friction in the mechanism and provide conservative performance estimates. Additionally, the measurement data also includes effects due to the stiffness apparatus. Because stiffness = force change/compression, higher

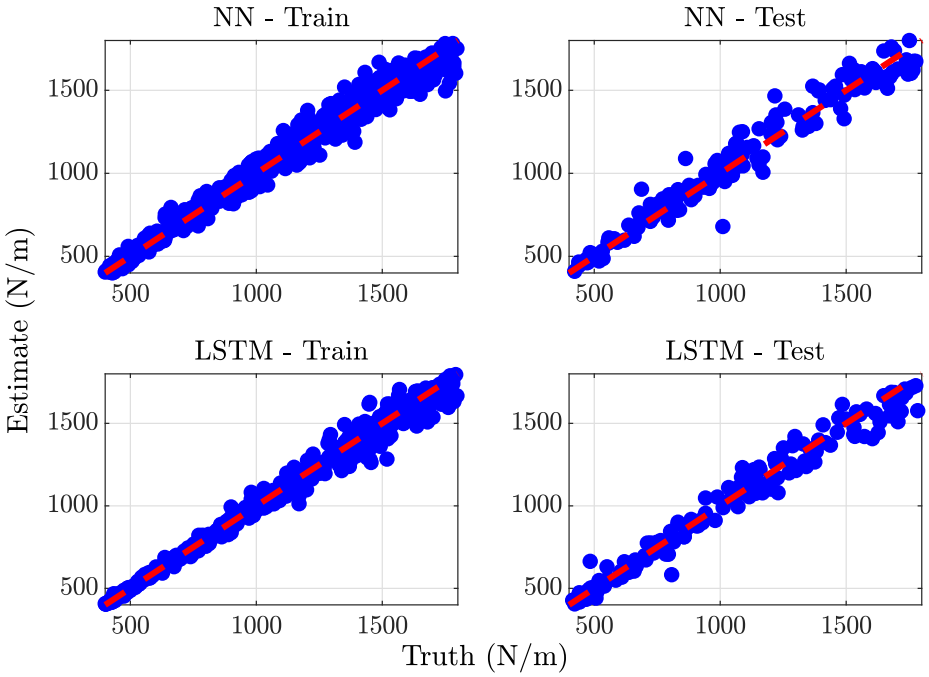

Figure 9.8: Regressor performance comparison between estimated and ground truth stiffness. The nominal estimation performance with no error is represented by [- -].

Table 9.2: Regressor Performance with the Underactuated Finger

Regressor	% Error	
	Train	Test
Neural Network	4.01	5.55
LSTM Network	2.59	5.05

stiffness values require larger forces to be applied to the stiffness apparatus to induce a detectable compression. After all the data collection logic disallows multiple grasps of the object to permit adaptation of the staircase profiles based on initial measurements and uses the same staircase actuation command for low and high stiffness levels, the errors increase at higher stiffness levels. The performance of the LSTM regressor is slightly better compared to the NN regressor because the LSTM is suitable for modeling relationships occurring in sequential data [42], and the position and current data are time-series measurements.

9.5 Summary and Conclusion

This chapter studies an underactuated finger driven by a tendon-pulley transmission mechanism and extends the squeeze test approach presented in Chapter 8. The work demonstrates that position and current measurements are sufficient to determine the unknown stiffness of an object using regression. Experiments generate the dataset to train and test the regressor, with the finger actuated by a staircase command signal to achieve and maintain a fingertip grasp. An electronically controlled stiffness apparatus is discussed that systematizes the data collection process and allows the acquisition of multiple measurements from the experimental setup. Regressors using single layer NN and LSTM networks trained on experimental datasets accurately estimate the stiffness presented to the finger by the apparatus.

CHAPTER 10

CONCLUSION

10.1 Contributions

This research addresses several key issues to enhance the operation of ultrasonic transducers. Time optimal control principles are applied to study a transformer-driven transducer system, which results in a high order of the system. The resulting excitation scheme maintains the amplitude of the transmitted pressure wave and improves the minimum range and the range resolution by shortening the length of the decaying tail of the TX-FUT. The OCP formulation consists of a sequence of two sub-problems, and numerical solutions are determined through a high dimension NLP. The PWM excitation synthesis procedure exploits the superposition principles to realize the excitation schemes on the bench using low-cost MCUs. Although the studies focus on a transformer-driven configuration, the developed methods apply to other drive configurations as outlined in Appendix B. Experimental results achieve an average improvement in the minimum range by about 32% versus the baseline excitation strategy, which applies an integral number of pulses at the FUT's resonant frequency. The range resolution of the system also shows a similar improvement.

Time optimal formulation is also applied to enhance the shape characteristics of an echo at a receiving FUT by manipulating the voltage excitation applied to a transmitting FUT. The math-based formalism considers the transmitter and the receiver dynamics (results in a 6^{th} order system). The transmitter excitation scheme obtained through the numerical solutions results in echoes with a sharp rise to the peak followed by a fast fall to equilibrium. Experimental evaluations show an improvement of about 60% in the pulse width resulting in improved range resolution. The enhancements maintain the peak amplitude level of the echo when compared to the baseline excitation that applies an integral number of cycles to the transmitting FUT at the resonant frequency. The research illustrates tradeoffs in the

minimum range, range resolution, amplitude of the transmitted pressure, and received echo with the two competing time-optimal schemes.

Two simple model-free algorithms – damping and masking, are developed for transmitter and receiver enhancements. The algorithms can run on low-cost, resource-constrained embedded devices. The model-free approaches remove the need for a mathematical model of the system and an accurate knowledge of the system's parameters. The algorithms can use any excitation driver circuit topology between the source and the FUT as discussed in Appendix B, can capture sensor installation conditions, and also self-tune depending on the pressure $\leftrightarrow$ voltage sensitivity of the FUT. The transmitter damping approach improves both minimum range and range resolution and achieves approximate time-optimality by appending out-of-phase damping cycles. On the other hand, the masking algorithm improves the minimum range of the FUT, where the echo-induced voltage component is isolated from the pulse-imposed voltage component by subtracting a stored masking signal from the acquired signal. Because the commissioning procedure can run within a short duration, both algorithms can execute whenever recalibration is needed.

The research presents an ultrasonic sensor array that uses a single narrowband transmitter and a receiver array consisting of MEMS microphones to detect multiple objects in 3-D space. A small number of microphone elements is beneficial, as it allows for a significant reduction in the system cost and computing requirements while also boosting the sensor's throughput. Several phased array algorithms (DAS, MVDR, MUSIC) determine the directions of arrival, where Chapter 7 discusses beamforming in a transformed $(v,\ w)$ space. The post-processing algorithms outline the extraction of multiple local maxima from an array and interpolation to improve the detection accuracy of the sensor. Experimental results demonstrate the high throughput of the sensor system, comparable to a vision system when the processing algorithm runs on an embedded device. The sensor system, processing architecture, and a detailed computation cost analysis provide requirements for dedicated single-chip solutions.

In the tactile sensing area, the research studies the problem of estimating the stiffness

of a grasped object. The squeeze test exploratory procedure uses only position and current measurements to determine the unknown stiffness of the grasped object. The overall system implementation is cost-effective as the system does not use contact force sensors on the gripper's jaws (fingers). The research addresses if regression can estimate object stiffness and provide a continuous-valued stiffness output in the presence of dry friction and parameter variation effects. The performance of regressors trained with simulation-generated datasets on real-world experimental measurement data is also evaluated. The regression approach is extended by successfully estimating the stiffness with an underactuated finger consisting of a tendon-pulley transmission mechanism. Chapter 9 describes an apparatus that systematizes the generation of linear stiffness for collecting experimental data and training regressors instead of relying on everyday objects as stiffness sources.

The research resulted in the following publications:

- A. Balasubramanian, K. Sastry, D. Magee, and D. Taylor, "Time Optimal Operation of Flexural Ultrasonic Transducers For Enhanced Ranging," *IEEE Industrial Electronics Society Conference*, pp. 1–6, 2021.
- A. Balasubramanian, D. Magee, and D. Taylor, "3-D Ultrasonic Sensing in Air with a Narrowband Transmitter and a Receiver Microphone Array," *IEEE Industrial Electronics Society Conference*, pp. 1–6, 2021.
- A. Balasubramanian, D. Magee, and D. Taylor, "Stiffness Estimation in Single Degree of Freedom Mechanisms using Regression," *IEEE Industrial Electronics Society Conference*, pp. 1–6, 2021.
- A. Balasubramanian, K. Sastry, D. Magee, and D. Taylor, "Transmitter and Receiver Enhancements for Ultrasonic Distance Sensing Systems," *IEEE Sensors Journal*, vol. 22, no. 11, pp. 10692–10698, 2022.

Results from Chapter 5 on the operation of transmitting FUTs to enhance the echo shape at a receiving FUT will be submitted to a journal for publication.

10.2 Future Work

The research uses low-cost hardware to excite the transducer, and the excitation schemes are constrained to the rail limits. The design of hardware topologies that allow transducer excitations with less constrained inputs is a potential focus area. The application of excitations in a closed-loop setting is another candidate area. Analysis of the relationship between the excitations synthesized through time-optimal schemes presented in the research and pulse compression schemes is a prospect. The synthesis of excitation schemes through system inversion is another investigation opportunity. The model-free algorithm self-tunes only transmitting FUTs; a model-free self-tuning algorithm enhancing receiver operation for results in Chapter 5 is another candidate. The ultrasonic array operation for detecting multiple objects performs beamforming at the receiver. Transmit beamforming will allow for a higher field of view, but the transmitter size is a limiting factor. MEMS-based design of transducer arrays can address the limitations of transmitter/receiver array designs. The research discusses an architecture for the processing algorithm and provides computing requirements to achieve throughputs comparable to a vision system. The design of dedicated chip solutions and accelerators for compute-intensive beamforming is a valuable next step. The 3-D sensor array provides point cloud data; the classification of objects using ultrasonic point clouds and sensor fusion with multiple ultrasonic sensor arrays or vision sensors is another potential research area.

The stiffness estimation work focuses on a single underactuated finger and considers fingertip contact. Extension to multi-fingered underactuated mechanisms that consider other grasp types utilizing multiple squeeze tests to adapt the actuation signal is a natural next step. The compression tests assume that the application of forces retains the object's shape. Stiffness estimation allowing object shape changes is an investigation opportunity. The design of a dynamic model of the underactuated system and the influence of the dynamics on stiffness estimation is another candidate for exploration. Transferring regressors

trained for underactuated gripper systems using simulation data for use with real-world experimental measurements is a natural extension. The stiffness apparatus introduces systematic stiffness emulation facilitating the collection of a large-sized experimental dataset suitable for regression and classification architecture design. The adaptation of pre-trained regression architecture to new applications is an opportunity.

Appendices

APPENDIX A

TRANSDUCER PARAMETER ESTIMATION PROCEDURE

An AP Instruments Model 300 frequency response analyzer collects the frequency response data from the FUT. Figure A.1 shows the connection details of the electrical circuit during data collection. The equipment applies calibrated electrical voltage excitation of $V_{in}(\omega)$ to the circuit. A reference resistor R_{ref} connects in series with the FUT's electrical terminals. During the data collection step the measurement probes connect across the reference resistor as shown by the probing points **A** and **B** in Figure A.1. A PC-based software supplied by the equipment manufacturer, AP Instruments, controls the analyzer. The input voltage during measurements is set to $V_{in}(\omega) = 1.77$V RMS for each center frequency and the reference resistor value $R_{ref} = 1$ kΩ for the FUT is programmed in the tool. The device performs a frequency sweep between 30 kHz and 80 kHz in steps of 100 Hz, and the bandwidth of the instrumentation system is 10 Hz, with a gain of 6 dB. Measurement data is averaged 50 times to reduce the noise at each frequency. The tool automatically performs pre-processing based on the configurations to provide the complex impedance measurements of the FUT.

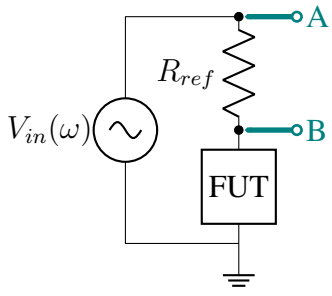

Figure A.1: Circuit for collecting frequency response measurements for an FUT. The transformer parameter estimation in Appendix D also uses the same circuit, and the transformer's primary terminals connect to R_{ref} in place of the FUT.

APPENDIX B

TRANSMIT DRIVE CIRCUIT CONFIGURATIONS

Figure B.1 shows an overview of the excitation circuit, and Figure B.2 provides the detailed version. A driver circuit exists between the source and the FUT for transferring power. With Z_{src} and Z_{load} as the complex source and load impedances, from [46], power transfer is maximized when $Z_{src} = Z^*_{load}$. Some common drive circuit choices have multiple combinations of passive elements (inductors, capacitors, or transformers) but increase the overall system order, cost, and complexity. For a narrowband FUT the four suitable drive configurations are – direct drive, transformer drive, CL, and LC drive.

Applying the maximum power transfer principle to each configuration results in an ideal set of design parameters for each drive circuit and is summarized in Table B.1. The LC and CL drive configurations are obtained by rearranging the locations of the inductor and the capacitor elements. The transformer drive configuration, which this research emphasizes, is modeled using dependent sources as discussed in Subsection 3.3.1. Table B.1 lists two design options for the transformer drive system. The first design option specifies the ideal value for both the transformer coil inductance L_{m1} and the turns ratio n, resulting in a less realizable design. The second option specifies only the transformer coil inductance L_{m1} and provides flexibility in the choice of the turns ratio n. The state-space representations for each drive configuration are summarized in Table B.2. The addition of driver circuits has the effect of canceling the bulk capacitance C_p of the FUT.

The transformer drive and the CL drive configurations are AC coupled and protect

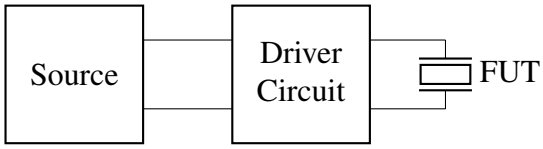

Figure B.1: Excitation circuit overview.

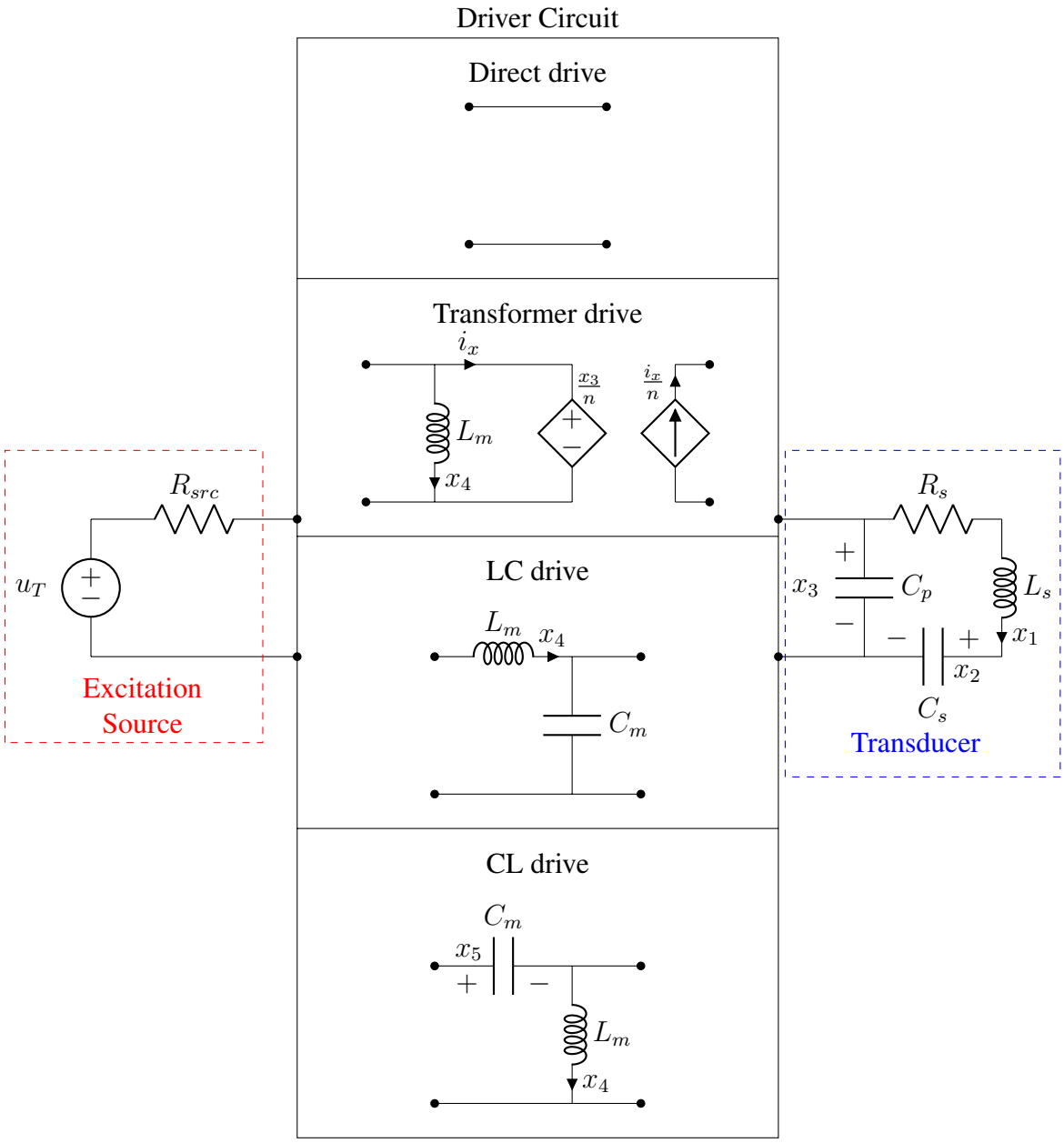

Figure B.2: Detailed excitation circuit. Drive configurations choices – direct, transformer, CL and LC drive. One of the four choices is connected between the excitation source and the transducer. For simplicity, $X_{src} = 0$.

Table B.1: Ideal Drive Design Parameters

System Configuration	Parameter Values
LC drive	$L_m = \frac{R_{src}Q - X_{src}}{\omega}; C_m = \frac{Q}{\omega R_s} - C_p$
CL drive	$L_m = \frac{R_s}{\omega\left(\omega R_s C_p + Q\right)}; C_m = \frac{1}{\omega\left(QR_{src} + X_{src}\right)}$
Transformer drive	Option 1: $L_{m1} = \frac{R_{src}^2 + X_{src}^2}{\omega\left(R_{src}R_s\omega C_p - X_{src}\right)}; n = \sqrt{\frac{R_s R_{src}}{R_{src}^2 + X_{src}^2}}$
	Option 2: $L_{m2} = \frac{R_s R_{src}}{\omega\left(R_{src}R_s\omega C_p - X_{src}\right)} = n^2 L_{m1}$

Formulas for different system configurations are obtained through impedance matching. $\omega = \frac{1}{\sqrt{L_s C_s}}$ and $Q = \sqrt{\frac{R_s}{R_{src}} - 1}$. X_{src} is included in the derivations for completeness.

the FUT compared to the direct drive and LC drive configurations; the application of DC voltages to the FUT can cause permanent deformations of the piezoelectric material [65]. The direct drive results in the lowest model order of 3, whereas the CL drive results in a system that has an order of 5. Prior research [7–9] utilizes a sinusoidal excitation signal to excite a narrowband FUT, which may not be necessary. Since the FUT is bandpass, a square wave voltage is sufficient and requires simpler hardware to synthesize the excitation signal (using H-Bridge circuits). Previous research also does not consider the intermediate driver stage. The vibration control methods and experiments study the transformer-driven system, but the methods also apply to the other drive configurations listed in Figure B.2.

The simulations for the direct drive and the transformer drive configurations are shown in Figure 3.10 and Figure 3.11. For the transformer drive configuration, using the design formulas provided by the design option 1 in Table B.1 result in the parameter values: $L_{m1} = 4.88$ μH and $n = 32.8$. This design is not practically realizable as the value for L_{m1} is small (close to leakage inductance levels) and the transformer has a high turns ratio. With

Table B.2: State-Space Representation of Transmit Circuit Configurations

System Configuration	A-Matrix	B-Matrix
Direct drive	$\begin{bmatrix} -\frac{R_s}{L_s} & -\frac{1}{L_s} & \frac{1}{L_s} \\ \frac{1}{C_s} & 0 & 0 \\ -\frac{1}{C_p} & 0 & -\frac{1}{C_p R_{src}} \end{bmatrix}$	$\begin{bmatrix} 0 \\ 0 \\ \frac{1}{C_p R_{src}} \end{bmatrix}$
Transformer drive	$\begin{bmatrix} -\frac{R_s}{L_s} & -\frac{1}{L_s} & \frac{1}{L_s} & 0 \\ \frac{1}{C_s} & 0 & 0 & 0 \\ -\frac{1}{C_p} & 0 & -\frac{1}{n^2 C_p R_{src}} & -\frac{1}{nC_p} \\ 0 & 0 & \frac{1}{nL_m} & 0 \end{bmatrix}$	$\begin{bmatrix} 0 \\ 0 \\ \frac{1}{nR_{src}C_p} \\ 0 \end{bmatrix}$
LC drive	$\begin{bmatrix} -\frac{R_s}{L_s} & -\frac{1}{L_s} & \frac{1}{L_s} & 0 \\ \frac{1}{C_s} & 0 & 0 & 0 \\ -\frac{1}{C_p + C_m} & 0 & 0 & \frac{1}{C_p + C_m} \\ 0 & 0 & -\frac{1}{L_m} & -\frac{R_{src}}{L_m} \end{bmatrix}$	$\begin{bmatrix} 0 \\ 0 \\ 0 \\ \frac{1}{L_m} \end{bmatrix}$
CL drive	$\begin{bmatrix} -\frac{R_s}{L_s} & -\frac{1}{L_s} & \frac{1}{L_s} & 0 & 0 \\ \frac{1}{C_s} & 0 & 0 & 0 & 0 \\ -\frac{1}{C_p} & 0 & -\frac{1}{C_p R_{src}} & -\frac{1}{C_p} & -\frac{1}{C_p R_{src}} \\ 0 & 0 & \frac{1}{L_m} & 0 & 0 \\ 0 & 0 & -\frac{1}{C_m R_{src}} & 0 & -\frac{1}{C_m R_{src}} \end{bmatrix}$	$\begin{bmatrix} 0 \\ 0 \\ \frac{1}{C_p R_{src}} \\ 0 \\ \frac{1}{C_m R_{src}} \end{bmatrix}$

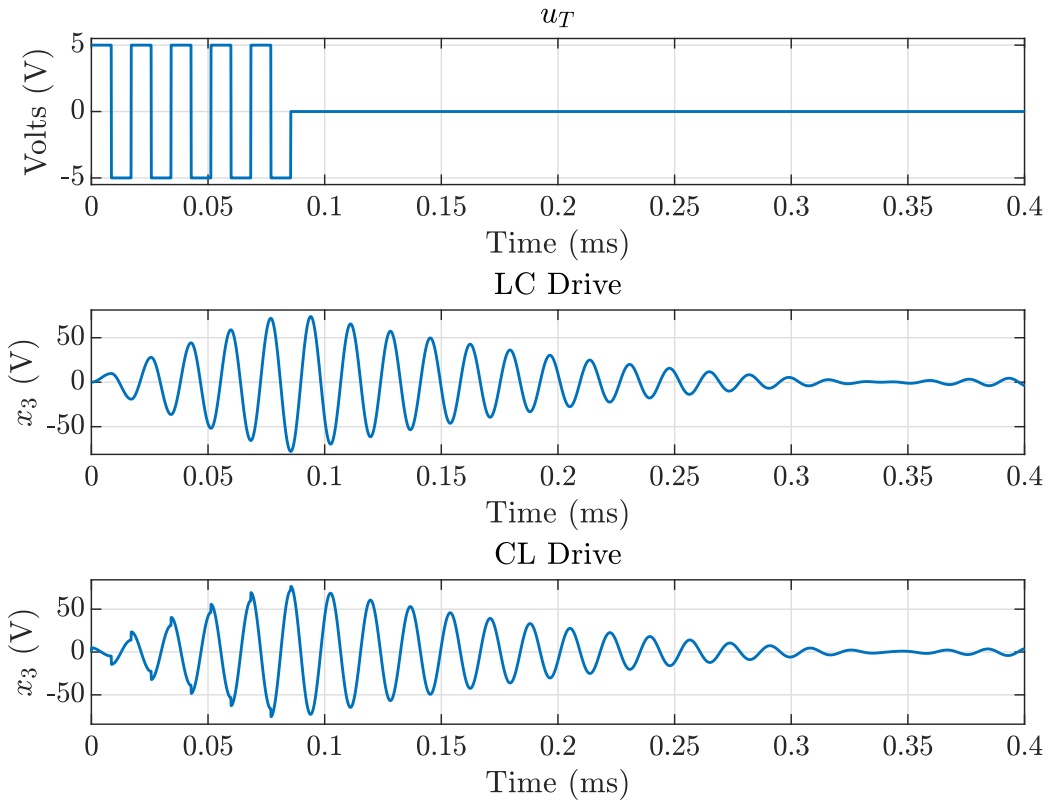

Figure B.3: Simulation – voltage (x_3) appearing across the FUT.

the design option 2 the transformer's turns ratio is a free parameter giving the secondary inductance value of $L_{m2} = 5.3$ mH. The transformer used in the experimental work is selected based on this guideline and has $L_{m2} = 3$ mH as listed in Table D.1.

Figure B.3 and Figure B.4 show the simulations for the LC and CL drive systems where the excitation defined by Equation 3.8 – Equation 3.10 with $n_e = 5$ is applied. Ideal design values for the inductor and the capacitor based on the design formulas in Table D.1 are selected for the LC and CL networks. Both networks achieve comparable performance; the peak amplitude of the current x_1 (transmitted pressure wave) is higher when compared to the direct drive simulations of Figure 3.11 for the same u_T because of a better power transfer from the source to the load. For the transformer-driven network, a higher turns ratio can provide similar peak current amplitudes as the ideal LC or CL-driven networks.

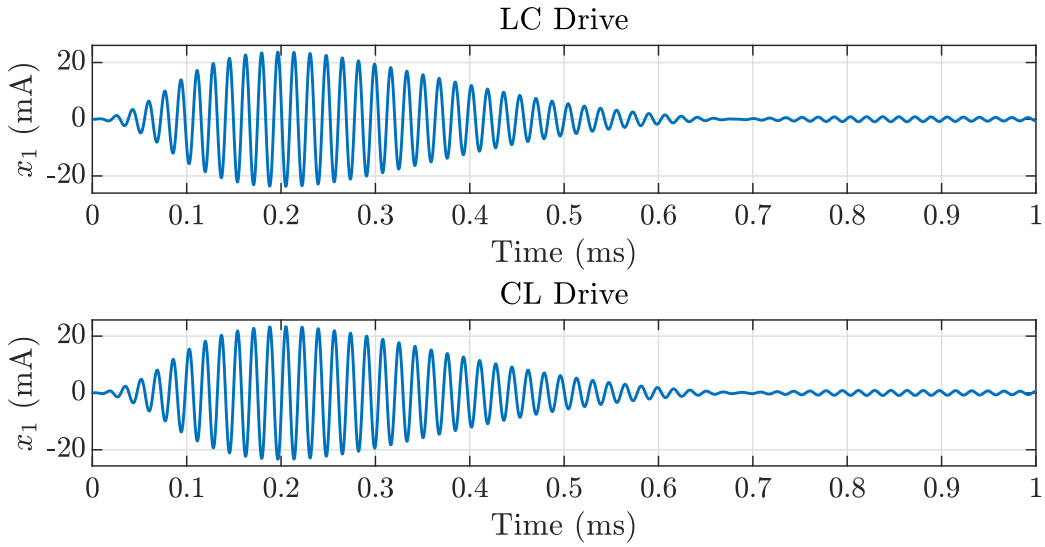

Figure B.4: Simulation – current (x_1) through the oscillatory branch of the FUT. Current represents the emitted pressure.

APPENDIX C

RECEIVER BOARD DESIGN

Figure C.2 shows the schematic of the custom receiver designed especially for the needs of this research, and Figure C.1 shows the hand-assembled receiver. A custom receiver is essential for analog signal processing, data collection, and experimental evaluation of the developed algorithms. Only a few commercial solutions provide access to the analog signal data (Texas Instruments PGA460), offering limited customization and without synchronized data collection, which is essential when using multiple receiver elements. The receiver amplifies and filters in two stages to allow for flexibility while also meeting the specifications of the low-noise opamp. The amplifier has four selectable gains for the first stage, introduced through analog multiplexing, and the second stage provides a fixed gain, allowing net input-output amplifier gains of $\{300,\ 600,\ 1170,\ 1800\}$ V/V. Multiple amplifier gains allow operation with different input devices (microphone or FUT), receive sensitivity variations (microphone has $\approx$ 30 dB better sensitivity compared to the FUT), and accommodate modifications to the operating range of the sensor. The bandpass filter has a net passband frequency between $[44,\ 72]$ kHz and is tuned to operate around the FUT's resonant frequency of 58.5 kHz.

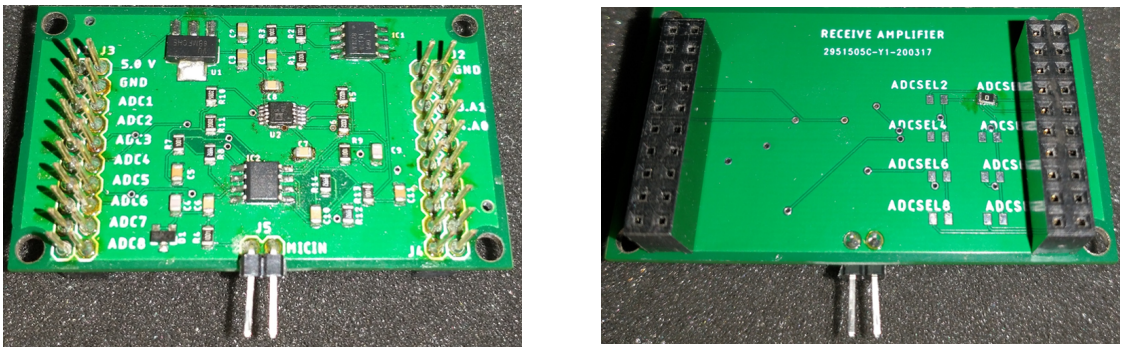

(a) Front. (b) Back.

Figure C.1: Assembled receiver board.

The receiver board has several circuits – an onboard voltage regulator to provide a fixed rail supply of 3 V to the filtering and the amplification stages; a bias generator to provide a fixed reference level at 1.5 V for converting bipolar voltage signals $[-1.5,\ 1.5]$ V into a unipolar signal $[0,\ 3]$ V before feeding a single-ended ADC. As shown in Figure C.1, the header pins allow the stacking of multiple boards on top of one another, which is suitable for the array mode of operation. Each receiver board feeds a dedicated ADC pin on the TMS320F28379D MCU. The opamp's output signal can be routed to one or more header pins feeding the MCUs ADC channel by shorting the ADCx and ADCSELx traces, where $x = 1, \ldots, 8$. In the assembled board shown in Figure C.1, ADCSEL1 is shorted and connects the opamp output to channel ADC1.

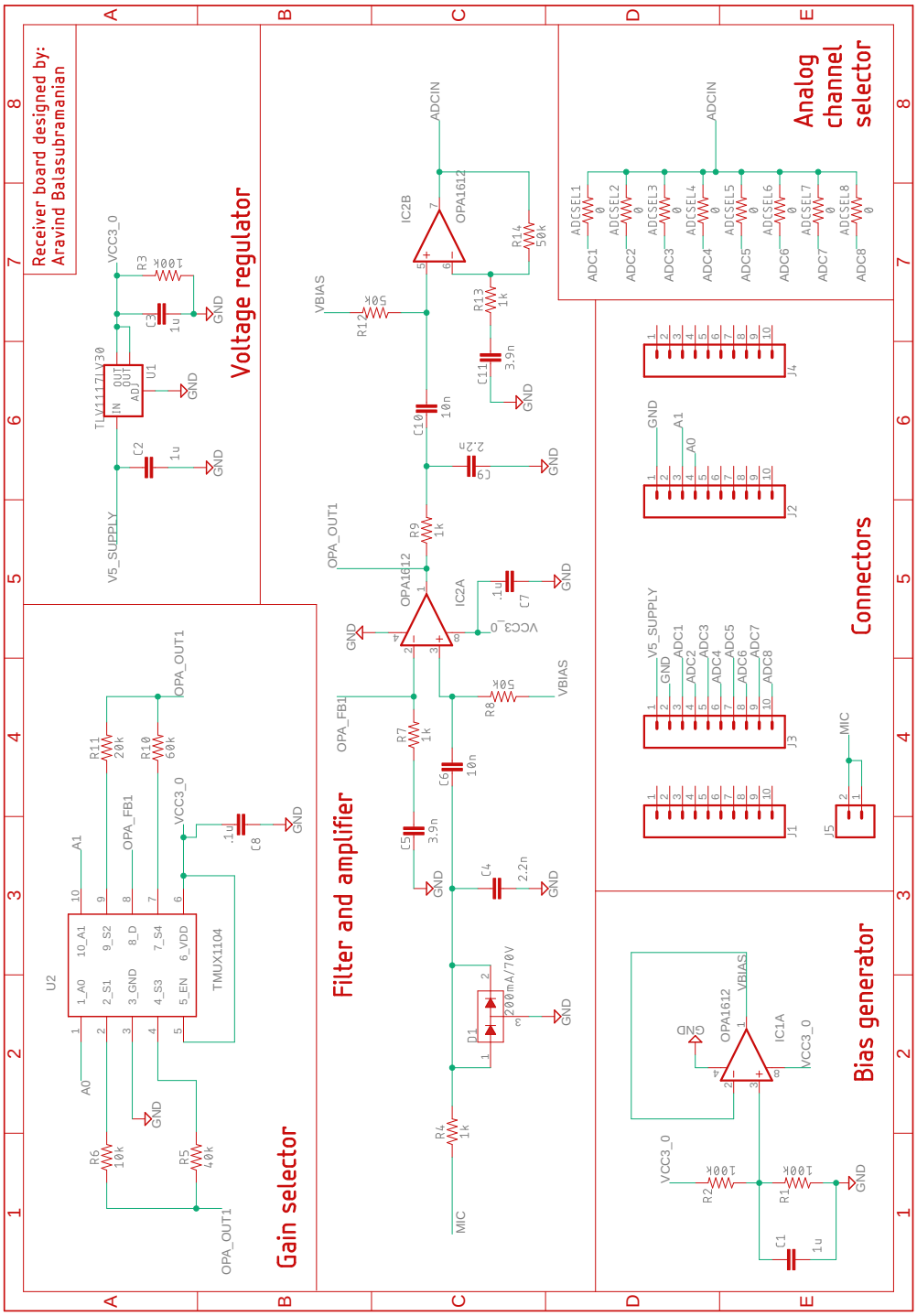

Figure C.2: Receiver board schematic. Passband frequency: $[44,\ 72]$ kHz, and selectable gains: $\{300,\ 600,\ 1170,\ 1800\}$ V/V.

APPENDIX D

TRANSFORMER PARAMETER ESTIMATION

A TDK EPCOS B78416A2232A003 step-up pulse transformer is the driver stage between the excitation source and the FUT. The data collection circuit is shown in Figure A.1 with $R_{ref} = 10\,\Omega$. The transformer is the device under test, and the transformer's primary terminals connect between the ground and R_{ref}. Two impedance measurement tests provide the data to obtain the parameters of the circuit of Figure 3.8 – short-circuited secondary and open-circuited secondary; Figure D.1 plots the resulting data. The effective impedance measured by each test is given by

$$\begin{gathered}\text{Open-circuit secondary: } Z_{\text{OC}} = (R_1 + R_2') + j\omega(L_{l1} + L_{l2}' + L_{m1}) \\ \text{Short-circuit secondary: } Z_{\text{SC}} = (R_1 + R_2') + j\omega(L_{l1} + L_{l2}')\end{gathered} \tag{D.1}$$

where ω is the angular frequency at which the measurement is obtained. Z_{OC} and Z_{SC} are the impedances measured with each test. Linear least-squares parameter estimation is applied to each dataset, and the corresponding equation is written as

$$\begin{bmatrix}\mathbf{Z}_x\end{bmatrix} = \begin{bmatrix}\mathbf{1} & \omega\end{bmatrix} \begin{bmatrix}\text{Re}(\hat{Z}_x) \\ \text{Im}(\hat{Z}_x)\end{bmatrix},\ x = \{\text{OC},\ \text{SC}\} \tag{D.2}$$

where $\mathbf{Z}_x$ is a vector of measurements obtained at the ω frequencies. $\hat{Z}_x$ is the estimated impedance and is a scalar quantity. Based on [47], it is assumed that the leakage inductance is small; therefore, $L_{l1} + L_{l2}' << L_{m1}$. Also, leakage inductance $L_{l1} = L_{l2}'$ is assumed. The turns ratio is determined by applying a fixed voltage sinusoid at the transducer's resonant frequency using a function generator at the transformer's primary and measuring the voltage at the transformer's secondary with an oscilloscope. Algebraic manipulation of $\hat{Z}_x$ determines the transformer parameters, and Table D.1 summarizes the estimates.

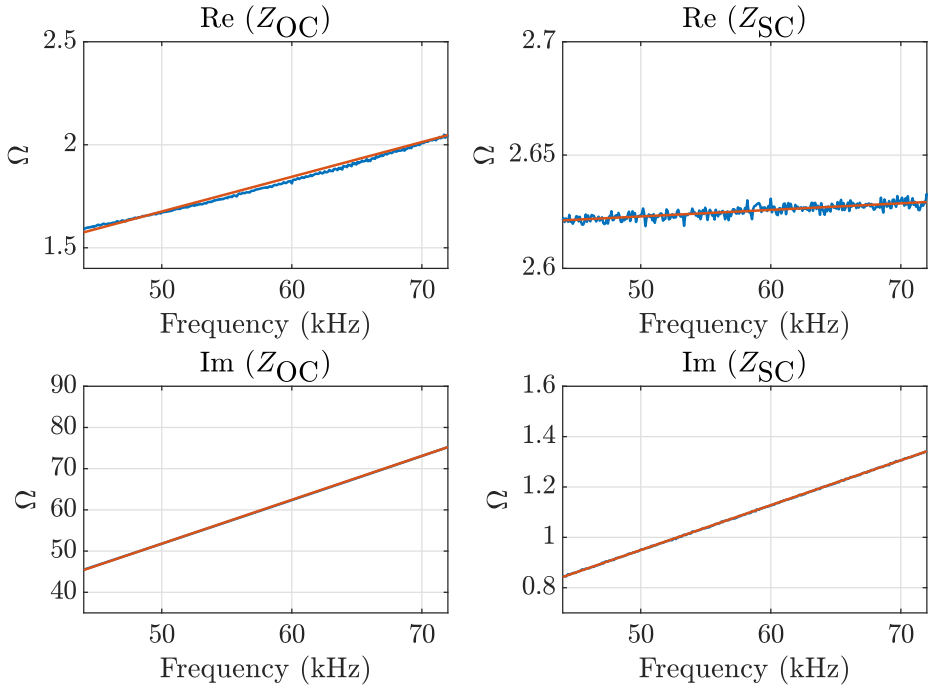

Figure D.1: Frequency response analyzer measurements for transformer parameter estimation (measured [—], linear least-squares fit [—]).

Note that the transformer used has center-taps in the primary side. Measurements obtained during parameter estimation consider the full primary coil and do not use the center tap. With a center-tap configuration, the primary coil inductance modifies to $L_{m1,\,ct} = \dfrac{L_{m1}}{2}$, the secondary:primary turns ratio modifies to $n_{ct} = 2n$, $R_{1,\,ct} = \dfrac{R_1}{2}$ and $R'_{2,\,ct} = \dfrac{R'_2}{2}$, where the subscript "*ct*" denotes the parameters in the center-tapped configuration.

Table D.1: Estimated Transformer Parameters

Parameter	Symbol	Estimate	Datasheet	Units
Primary Coil Resistance	R_1	1.81	–	Ω
Secondary Coil Resistance referred to Primary	R'_2	0.81	–	Ω
Primary Coil Inductance	L_{m1}	164.02	169.26	μH
Secondary Coil Inductance	L_{m2}	2.91	3	mH
Leakage Inductance	$L_{l1} = L'_{l2}$	1.49	–	μH
Turns Ratio	n	4.21		V/V

APPENDIX E

RANGE RESOLUTION

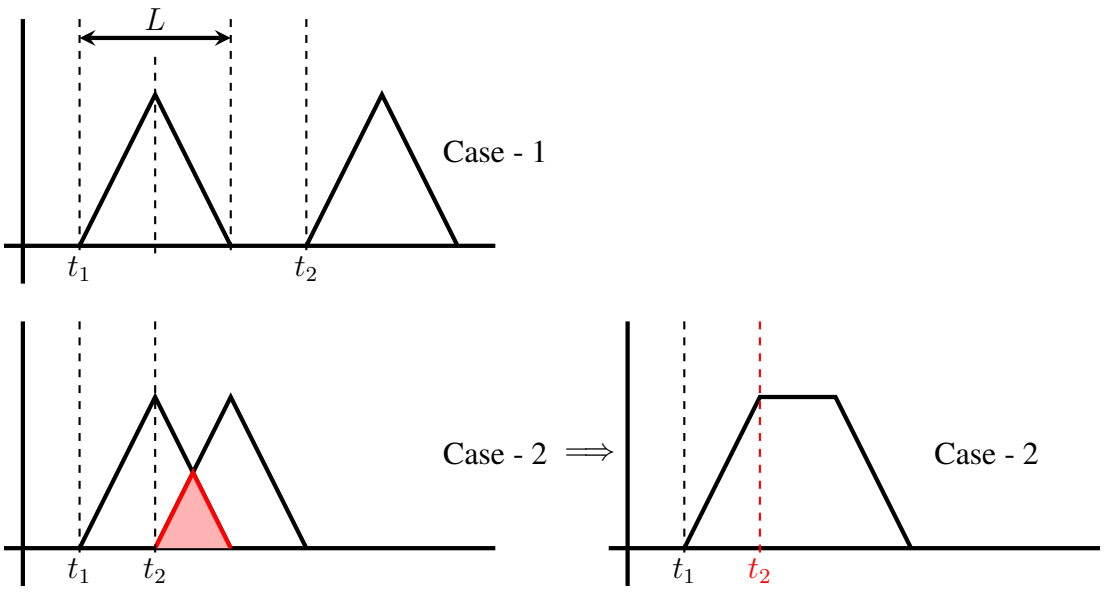

Figure E.1: Range resolution. Case-1 shows the detection of both echoes. In Case-2, the second echo overlaps with the first and is hidden.

The range resolution of an ultrasonic sensor is the ability to distinguish between two objects that have a small separation. Figure E.1 illustrates the issue, where the triangular envelope represents an echo and has an equal rise time and fall time. Let the temporal length of the wave packet be L. Two echoes from the scene are present, at t_1 and t_2, which are from two objects 1 and 2 in the scene. In Case-1, since both echoes are temporally separated, the echoes are easily detected, giving the range estimates:

$$r_i = \frac{t_i v_{sound}}{2}, \quad i = 1,\ 2 \tag{E.1}$$

On the other hand, Case-2 is obtained by moving object 2 closer towards object 1. Consequently, the time difference between t_1 and t_2 reduces, and t_2 starts getting closer to the echo at t_1. At some point, the echoes overlap as shown by the red region in Figure E.1, and

due to superposition, results in a flat top and occurs when $t_2 = t_1 + \frac{L}{2}$. For $t_2 < t_1 + \frac{L}{2}$, the echoes from object 2 and object 1 merge and appear as though a single object produced the echo. Therefore, for the objects to be detectable we need

$$t_2 > t_1 + \frac{L}{2} \tag{E.2}$$

Using Equation E.1, the range inequality may be determined by multiplying the term $\frac{v_{sound}}{2}$ giving

$$\begin{aligned} \frac{v_{sound}}{2} t_2 &> \frac{v_{sound}}{2}\left(t_1 + \frac{L}{2}\right) \\ r_2 - r_1 &> \frac{L v_{sound}}{4} \end{aligned} \tag{E.3}$$

The lower bound for range resolution Δr (the minimum separation between two objects) is given by

$$\Delta r > \frac{L v_{sound}}{4} \tag{E.4}$$

APPENDIX F

MICROPHONE ARRAY DESIGN

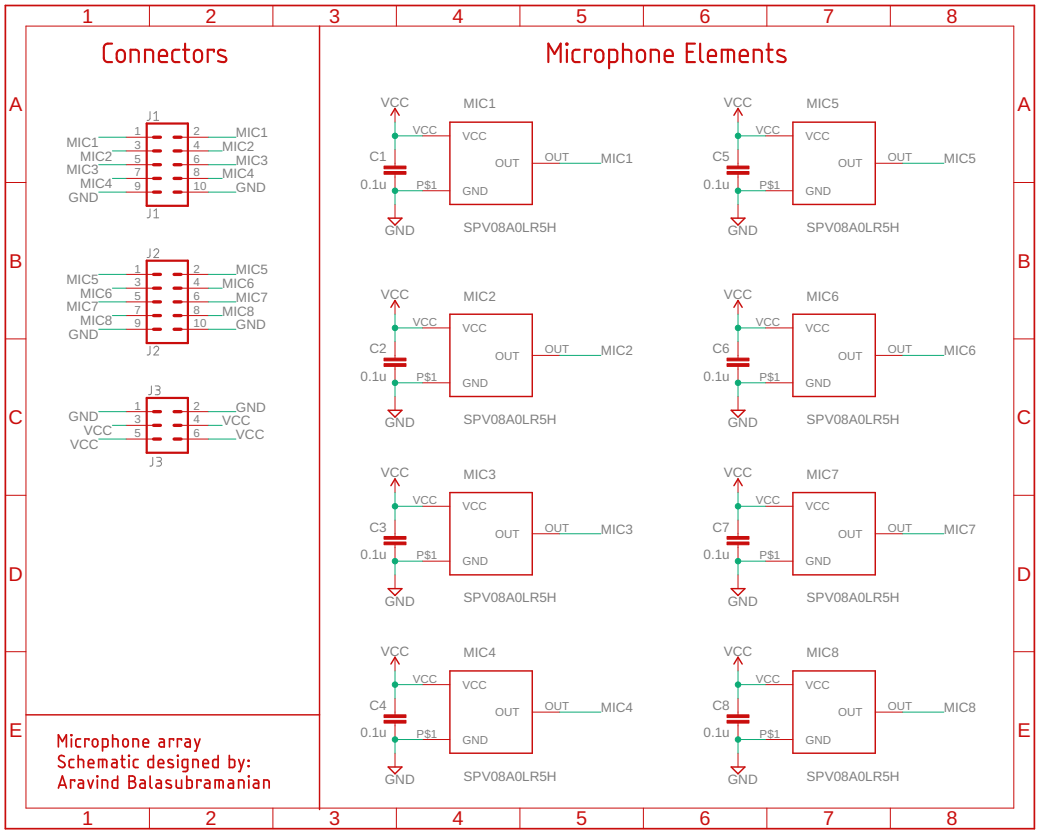

(a) Array schematic consisting of $M = 8$ microphone elements.

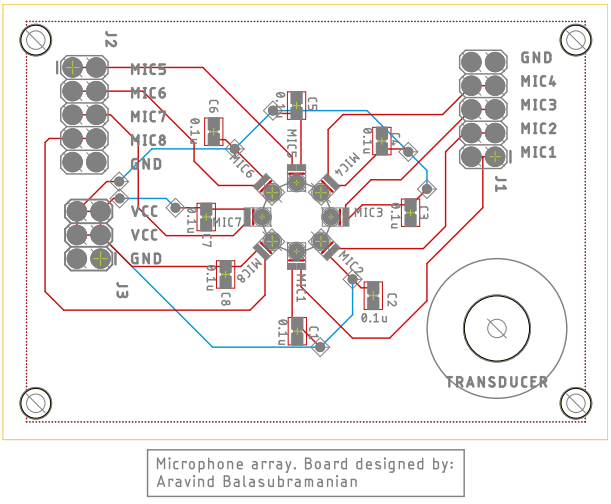

(b) Board layout. Microphone elements are on a ring of radius = 3.7 mm.

Figure F.1: Microphone array design.

APPENDIX G

PARAMETER ESTIMATION OF THE DYNAMIXEL SMART-SERVO MOTOR

This section discusses the parameter estimation procedure for the Dynamixel XM430-W210R smart-servo. The motor package includes a gearbox, position encoder, and a current sensor, all packed into a compact assembly. The smart-servo is designed to be used as a black-box actuator and consists of an onboard embedded processor that implements several control algorithms – position, speed, and current control. A user only needs to specify commands to the servo motor and is exchanged through a serial communication interface. Control loop gains can be programmed based on the application. The motor's parameters are used for generating simulation-based datasets in Chapter 8. The simulation plant model is given by Equation 8.6, which is equivalent to the two-stage position control formulation given by Equation 8.4. The motor's embedded software implements proprietary control algorithms for the various operating modes. Hence a sophisticated input signal is designed inspired by the work presented in [66]. The motor is operated without a load in the speed control mode to obtain reliable measurement data. A persistently exciting speed command signal is applied to the motor and is given by

$$\omega_{cmd} = \omega_1 \sin(2\pi f_1 t) + \omega_2 \sin(2\pi f_2 t) \tag{G.1}$$

where $\omega_1 = 9,\ \omega_2 = 3$ rad/s and $f_1 = 10,\ f_2 = 50$ Hz. Other command signals (position, current, and voltage) are affected by the motor's embedded controller, which implements several proprietary safety mechanisms. Figure G.1 shows the motor's sensor data, and the measured speed does not follow the commanded speed due to loop gains and motor inertia. However, the measured current and voltage show frequency components present in the designed commanded signal. Neglecting the disturbance terms present in Equation 8.4 we

get

$$\ddot{\theta} = -\alpha\dot{\theta} + \beta i \tag{G.2}$$

where $\alpha = \dfrac{b_m}{J}$ and $\beta = \dfrac{K_m}{J}$. After taking Laplace transform we get

$$s^2\Theta(s) = -\alpha s\Theta(s) + \beta I(s) \tag{G.3}$$

Note that for the stiffness estimation work in Chapter 8, α modifies when an object (spring) is introduced into the system. However, during the parameter extraction procedure, to obtain accurate estimates of β, the α term is retained. The linear least squares parameter identification from [59] is used. Equation G.3 is multiplied by the filter $H(s) = \dfrac{\lambda^3}{(s+\lambda)^3}$ with the design parameter λ, we get

$$\begin{bmatrix} H_2(s)\Theta(s) \end{bmatrix} = \begin{bmatrix} -H_1(s)\Theta(s) & H_0(s)I(s) \end{bmatrix} \begin{bmatrix} \alpha \\ \beta \end{bmatrix} \tag{G.4}$$

where $H_i(s) = \dfrac{\lambda^3 s^i}{(s+\lambda)^3}$, for $i = 0, 1, 2$. When $\theta(t)$ and $i(t)$ are passed through the filters defined by $H_i(s)$, we obtain

$$\Theta_i(s) = H_i(s)\Theta(s) \quad \text{and} \quad I_i(s) = H_i(s)I(s) \tag{G.5}$$

Equation G.5 gives the filtered components of the measured signals to obtain the unknown parameters α and β. The resulting parameters are listed in Table G.1 achieving a quality of fit of 94.9% with the linear least-squares method. For comparison, the greybox parameter identification tool built into MATLAB is used and results in a quality of fit of 95.8%.

Table G.1: Dynamixel Parameter Estimation

Symbol	Value	
	Least-Squares	Greybox
α	564.52	578.65
β	11.21	7.99
Fit %	94.9	95.8

Filter parameter $\lambda = 50$ rad/s.

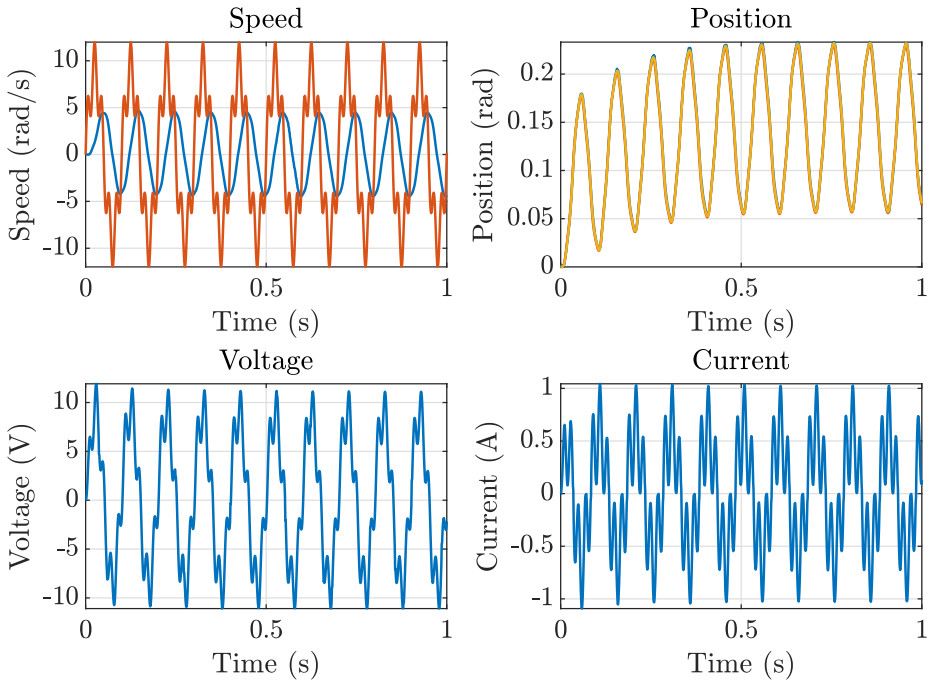

Figure G.1: Dynamixel data collection for stiffness estimation. Sampling frequency = 1 kHz. For speed plot: Measured speed [—] and commanded speed [—]. For the position plot: Measured position [—], linear least-squares [—] and greybox [—].

APPENDIX H

PARAMETER ESTIMATION OF THE LINEAR ACTUATOR

The linear actuator from Actuonix L12-P is used in the stiffness apparatus of Chapter 9. The actuator consists of a built-in potentiometer to provide position measurements. The single stage position control loop given by the plant design equations Equation 8.3 is implemented. Consequently, only two parameters α and β need to be identified by the parameter estimation procedure. Note that Equation 8.3 provides the plant design model for a rotary actuator. As a linear actuator is used, the linear analogues (mass, linear damping, linear position, linear velocity, etc.) are used in the model. The voltage input applied to the linear actuator is shown in Figure H.1 and the corresponding position measurement is shown in Figure H.2. Neglecting the disturbance term in Equation 8.3 and denoting the linear position by $x(t)$, we get

$$\ddot{x} = -\alpha\dot{x} + \beta u \tag{H.1}$$

with the Laplace transform given by

$$s^2X(s) = -\alpha sX(s) + \beta U(s) \tag{H.2}$$

Similar to Appendix G, the linear least-squares parameter identification from [59] is applied. A filter $H(s) = \dfrac{\lambda^3}{(s+\lambda)^3}$ is multiplied on both the sides of Equation H.2 with the filter design parameter λ, we get

$$\begin{bmatrix} H_2(s)X(s) \end{bmatrix} = \begin{bmatrix} -H_1(s)X(s) & H_0(s)U(s) \end{bmatrix} \begin{bmatrix} \alpha \\ \beta \end{bmatrix} \tag{H.3}$$

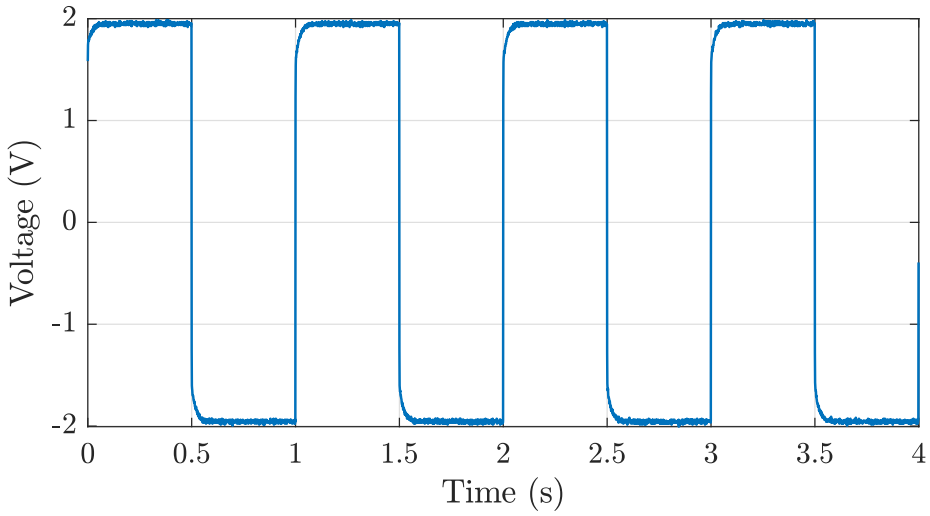

Figure H.1: Input voltage applied to the motor for parameter estimation collected at 1 kHz sampling frequency.

where $H_i(s) = \dfrac{\lambda^3 s^i}{(s+\lambda)^3}$, for $i = 0, 1, 2$.

When $x(t)$ and $u(t)$ are passed through the filters defined by $H_i(s)$, we obtain

$$X_i(s) = H_i(s)X(s) \quad \text{and} \quad U_i(s) = H_i(s)U(s) \tag{H.4}$$

They are the filtered components of the measured signals and are used in Equation H.3 to obtain the unknown parameters α and β. The resulting parameters are shown in Table H.1 and achieve a quality of fit of 95% using the linear least-squares estimation procedure. For comparison, the parameters are also determined using the greybox parameter identification tool built into MATLAB, which provides a quality of fit of 95.2%.

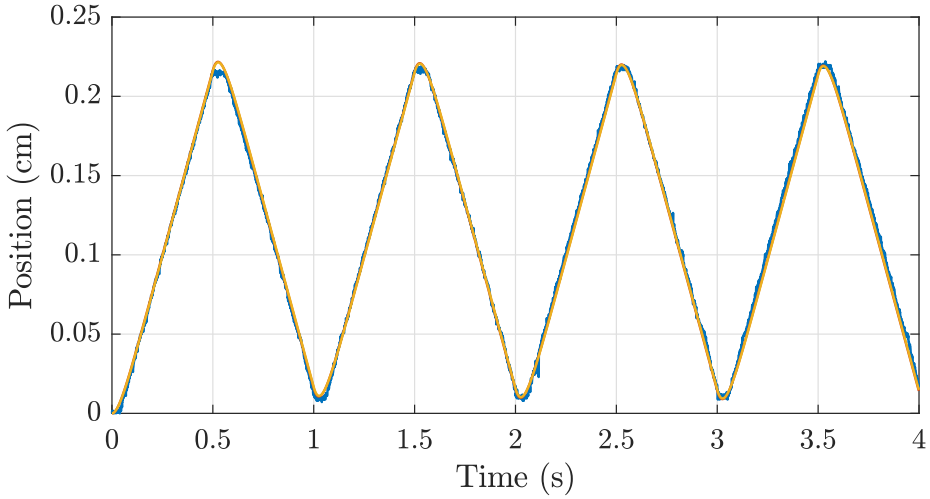

Figure H.2: Linear actuator position data collected at 1 kHz sampling frequency (measured [—], linear least squares [—], greybox [—]).

Table H.1: Linear Actuator Parameter Estimation

Symbol	Value	
	Least-Squares	Greybox
α	28.106	29.29
β	0.067	0.0701
Fit %	95	95.2

Filter parameter $\lambda = 50$ rad/s.

The formulas for $\alpha = \dfrac{K_m^2 + b_m R}{M_m R}$ and $\beta = \dfrac{K_m}{M_m R}$.

The units are skipped because α and β have multiple terms.

REFERENCES

[1] G. Miller, R. Boie, and M. Sibilia, "Active Damping of Ultrasonic Transducers for Robotic Applications," *IEEE International Conference on Robotics and Automation*, pp. 379–384, 1984.

[2] A. Ramos, J. Emeterio, and P. Sanz, "Improvement in Transient Piezoelectric Responses of NDE Transceivers Using Selective Damping and Tuning Networks," *IEEE Transactions on Ultrasonics, Ferroelectrics, and Frequency Control*, vol. 47, no. 4, pp. 826–835, 2000.

[3] O. Yurchenko, W. DuVall, and W. Johnson, "Methods for Reducing Ringing of Ultrasonic Transducers," *US Patent 6,731,569*, 2004.

[4] L. Cheng and C. Chen, "An Active Damping Control Method for a Bi-directional Flyback Converter Driving a Piezeoelectric Transducer," *IEEE Industrial Electronics Society Conference*, pp. 4160–4165, 2014.

[5] L. Ding and S. Ramaswamy, "Tuning for Ultrasonic Transducer," *US Patent 10,585,177*, 2020.

[6] B. Cheng and T. Chang, "Enhancing Ultrasonic Imaging with Low Transient Pulse Shaping," *IEEE Transactions on Ultrasonics, Ferroelectrics, and Frequency Control*, vol. 54, no. 3, pp. 627–635, 2007.

[7] X. Liu, X. Chen, X. Le, Y. Wang, C. Wu, and J. Xie, "Reducing Ring-down Time of pMUTs with Phase Shift of Driving Waveform," *Sensors and Actuators A: Physical*, vol. 281, pp. 100–107, 2018.

[8] S. Dixon, L. Kang, A. Feeney, and W. Somerset, "Active Damping of Ultrasonic Receiving Sensors through Engineered Pressure Waves," *Journal of Physics D: Applied Physics*, vol. 54, no. 13LT01, p. 5, 2021.

[9] S. Pala, Z. Shao, Y. Peng, and L. Lin, "Improved Ring-Down Time and Axial Resolution of pMUTs via a Phase-Shift Excitation Scheme," *IEEE MEMS Conference*, pp. 390–393, 2021.

[10] J. Huang, C. Lee, C. Yeh, W. Wu, and C. Lin, "High-Precision Ultrasonic Ranging System Platform Based on Peak-Detected Self-Interference Technique," *IEEE Transactions on Instrumentation and Measurement*, vol. 60, no. 12, pp. 3775–3780, 2011.

[11] K. Sasaki, H. Tsuritani, Y. Tsukamoto, and S. Iwatsubo, "Air-Coupled Ultrasonic Time-Of-Flight Measurement System Using Amplitude-Modulated and Phase Inverted Driving Signal for Accurate Distance Measurements," *IEICE Electronics Express*, vol. 6, no. 21, pp. 1516–1521, 2009.

[12] A. Raine, N. Aslam, C. Underwood, and S. Danaher, "Development of an Ultrasonic Airflow Measurement Device for Ducted Air," *Sensors*, vol. 15, pp. 10 705–10 722, 2015.

[13] M. Garg, D. Hernandez, and B. Beckham, "Haptic Actuator Controller," *US Patent 9,274,602*, 2016.

[14] L. Kleeman and R. Kuc, "Mobile Robot Sonar for Target Localization and Classification," *International Journal of Robotics Research*, vol. 14, no. 4, pp. 295–318, 1995.

[15] B. Barshan, "Location and Curvature Estimation of Spherical Targets Using Multiple Sonar Time-of-Flight Measurements," *IEEE Transactions on Instrumentation and Measurement*, vol. 48, no. 6, pp. 1212–1223, 1999.

[16] D. Browne and L. Kleeman, "An Advanced Sonar Ring Design with 48 Channels of Continuous Echo Processing Using Matched Filters," *IEEE International Conference on Intelligent Robots and Systems*, pp. 4040–4046, 2009.

[17] C. Walter and H. Schweinzer, "An Accurate Compact Ultrasonic 3D Sensor Using Broadband Impulses Requiring No Initial Calibration," *IEEE International Instrumentation and Measurement Technology Conference*, pp. 1571–1576, 2012.

[18] L. Chassagne, O. Bruneau, A. Bialek, C. Falguiere, E. Broussard, and O. Barrois, "Ultrasonic Sensor Triangulation for Accurate 3D Relative Positioning of Humanoid Robot Feet," *IEEE Sensors Journal*, vol. 15, no. 5, pp. 2856–2865, 2014.

[19] C. Walter and H. Schweinzer, "Locating of Objects with Discontinuities, Boundaries and Intersections Using a Compact Ultrasonic 3D Sensor," *IEEE International Conference on Indoor Positioning and Indoor Navigation*, pp. 591–600, 2014.

[20] S. Harput and A. Bozkurt, "Ultrasonic Phased Array Device for Acoustic Imaging in Air," *IEEE Sensors Journal*, vol. 8, no. 11, pp. 1755–1762, 2008.

[21] J. Steckel, A. Boen, and H. Peremans, "Broadband 3-D Sonar System Using a Sparse Array for Indoor Navigation," *IEEE Transactions on Robotics*, vol. 29, no. 1, pp. 161–171, 2012.

[22] I. Dokmanic and I. Tashev, "Hardware and Algorithms for Ultrasonic Depth Imaging," *IEEE International Conference on Acoustics, Speech and Signal Processing*, pp. 6702–6706, 2014.

[23] A. Das, I. Tashev, and S. Mohammed, "Ultrasound Based Gesture Recognition," *IEEE International Conference on Acoustics, Speech and Signal Processing*, pp. 406–410, 2017.

[24] R. Kerstens, D. Laurijssen, and J. Steckel, "ERTIS: A Fully Embedded Real Time 3D Imaging Sonar Sensor for Robotic Applications," *IEEE International Conference on Robotics and Automation*, pp. 1438–1443, 2019.

[25] T. Verellen, R. Kerstens, and J. Steckel, "High-Resolution Ultrasound Sensing for Robotics Using Dense Microphone Arrays," *IEEE Access*, vol. 8, pp. 190 083–190 093, 2020.

[26] G. Allevato, M. Rutsch, J. Hinrichs, M. Pesavento, and M. Kupnik, "Embedded Air-Coupled Ultrasonic 3D Sonar System with GPU Acceleration," *IEEE Sensors*, pp. 1–4, 2020.

[27] M. Rubsamen and A. Gershman, "Search-Free DOA Estimation Algorithms for Nonuniform Sensor Arrays," *Classical and Modern Direction-of-Arrival Estimation*, pp. 161–183, 2009.

[28] C. Balanis, "Antenna Theory: Analysis and Design," *John Wiley & Sons*, 2015.

[29] D. Johnson and D. Dudgeon, "Array Signal Processing: Concepts and Techniques," *Simon & Schuster Inc*, 1992.

[30] M. Richards, "Fundamentals of Radar Signal Processing," *McGraw-Hill Education*, 2014.

[31] G. Allevato *et al.*, "Real-Time 3-D Imaging Using an Air-Coupled Ultrasonic Phased-Array," *IEEE Transactions on Ultrasonics, Ferroelectrics, and Frequency Control*, vol. 68, no. 3, pp. 796–806, 2020.

[32] M. Liarokapis, B. Calli, A. Spiers, and A. Dollar, "Unplanned, Model-Free, Single Grasp Object Classification with Underactuated Hands and Force Sensors," *IEEE International Conference on Intelligent Robots and Systems*, pp. 5073–5080, 2015.

[33] A. Spiers, M. Liarokapis, B. Calli, and A. Dollar, "Single-Grasp Object Classification and Feature Extraction with Simple Robot Hands and Tactile Sensors," *IEEE Transactions on Haptics*, vol. 9, no. 2, pp. 207–220, 2016.

[34] Z. Kappassov, J. Corrales, and V. Perdereau, "Tactile Sensing in Dexterous Robot Hands," *Robotics and Autonomous Systems*, vol. 74, pp. 195–220, 2015.

[35] T. Bhattacharjee, J. Rehg, and C. Kemp, "Inferring Object Properties with a Tactile-Sensing Array Given Varying Joint Stiffness and Velocity," *International Journal of Humanoid Robotics*, vol. 15, no. 1, p. 1 750 024, 2018.

[36] L. Birglen, T. Laliberte, and C. Gosselin, "Underactuated Robotic Hands," *Springer*, vol. 40, 2007.

[37] A. Drimus, G. Kootstra, A. Bilberg, and D. Kragic, "Design of a Flexible Tactile Sensor for Classification of Rigid and Deformable Objects," *Robotics and Autonomous Systems*, vol. 62, no. 1, pp. 3–15, 2014.

[38] W. Yuan, M. Srinivasan, and E. Adelson, "Estimating Object Hardness with a Gelsight Touch Sensor," *IEEE International Conference on Intelligent Robots and Systems*, pp. 208–215, 2016.

[39] W. Yuan, C. Zhu, A. Owens, M. Srinivasan, and E. Adelson, "Shape-Independent Hardness Estimation Using Deep Learning and a Gelsight Tactile Sensor," *IEEE International Conference on Robotics and Automation*, pp. 951–958, 2017.

[40] S. Luo, J. Bimbo, R. Dahiya, and H. Liu, "Robotic Tactile Perception of Object Properties: A Review," *Mechatronics*, vol. 48, pp. 54–67, 2017.

[41] Y. Abu-Mostafa, M. Magdon-Ismail, and H. Lin, "Learning from Data," *AMLBook*, vol. 4, 2012.

[42] I. Goodfellow, Y. Bengio, and A. Courville, "Deep Learning," *MIT Press*, 2016.

[43] X. Peng, M. Andrychowicz, W. Zaremba, and P. Abbeel, "Sim-to-Real Transfer of Robotic Control with Dynamics Randomization," *IEEE International Conference on Robotics and Automation*, pp. 3803–3810, 2018.

[44] S. Rupitsch, "Piezoelectric Sensors and Actuators," *Springer*, 2019.

[45] L. Svilainis and V. Dumbrava, "Measurement of Complex Impedance of Ultrasonic Transducers," *Ultragarsas Ultrasound*, vol. 62, no. 1, pp. 26–29, 2007.

[46] J. Svoboda and R. Dorf, "Introduction to Electric Circuits," *John Wiley & Sons*, 2013.

[47] P. Krause, O. Wasynczuk, S. Sudhoff, and S. Pekarek, "Analysis of Electric Machinery and Drive Systems," *John Wiley & Sons*, vol. 75, 2013.

[48] R. Urick, "Principles of Underwater Sound for Engineers," *McGraw-Hill Inc*, 1975.

[49] K. Sastry, "M.S. Thesis: Minimum-Time Control of the Damped Harmonic Oscillator via Multi-Mode PWM," *Georgia Institute of Technology*, 2020.

[50] L. Biegler, "Nonlinear Programming: Concepts, Algorithms, and Applications to Chemical Processes," *SIAM*, 2010.

[51] J. Andersson, J. Gillis, G. H. G, J. Rawlings, and M. Diehl, "Casadi: A Software Framework for Nonlinear Optimization and Optimal Control," *Mathematical Programming Computation*, vol. 11, no. 1, pp. 1–36, 2019.

[52] M. Athans and P. Falb, "Optimal Control: An Introduction to the Theory and Its Applications," *Courier Corp*, 2013.

[53] A. Balasubramanian, K. Sastry, D. Magee, and D. Taylor, "Time Optimal Operation of Flexural Ultrasonic Transducers for Enhanced Ranging," *IEEE Industrial Electronics Society Conference*, pp. 1–6, 2021.

[54] I. Santamaria, C. Pantaleon, and J. Ibanez, "A Comparative Study of High-Accuracy Frequency Estimation Methods," *Mechanical Systems and Signal Processing*, vol. 14, no. 5, pp. 819–834, 2000.

[55] A. Balasubramanian, K. Sastry, D. Magee, and D. Taylor, "Transmitter and Receiver Enhancements for Ultrasonic Distance Sensing Systems," *IEEE Sensors Journal*, vol. 22, no. 11, pp. 10 692–10 698, 2022.

[56] V. Manohar and Y. Rahmat-Samii, "Revisiting the Appearance of Grating Lobes for Antennas with Circular Periodicity," *IEEE Transactions on Antennas and Propagation*, vol. 67, no. 8, pp. 5723–5728, 2019.

[57] S. Gleason, M. Hunt, and W. Jatko, "Subpixel Measurement of Image Features Based on Paraboloid Surface Fit," *SPIE Machine Vision Systems Integration in Industry*, vol. 1386, pp. 135–144, 1991.

[58] R. Lyons, "Digital Envelope Detection: The Good, the Bad, and the Ugly [Tips and Tricks]," *IEEE Signal Processing Magazine*, vol. 34, no. 4, pp. 183–187, 2017.

[59] D. Taylor, "Control System Design (ECE – 4550) Class Notes," *Georgia Institute of Technology*, 2022.

[60] E. Pennestri, V. Rossi, P. Salvini, and P. Valentini, "Review and Comparison of Dry Friction Force Models," *Nonlinear Dynamics*, vol. 83, no. 4, pp. 1785–1801, 2016.

[61] D. Karnopp, "Computer Simulation of Stick Slip Friction in Mechanical Dynamic Systems," *Transactions of the ASME*, 1985.

[62] G. Franklin, J. Powell, and M. Workman, "Digital Control of Dynamic Systems," *Addison-Wesley*, vol. 3, 1998.

[63] A. Balasubramanian, D. Magee, and D. Taylor, "Stiffness Estimation in Single Degree of Freedom Mechanisms using Regression," *IEEE Industrial Electronics Society Conference*, pp. 1–6, 2021.

[64] L. Tsai, "Robot Analysis: The Mechanics of Serial and Parallel Manipulators," *John Wiley & Sons*, 1999.

[65] "Ultrasonic Transducer Datasheet - Murata MA58MF14-7N,"

[66] W. Khan, "Ph.D. Dissertation: Nonlinear and Adaptive Control of Motor Drives with Compensation of Drive Electronics," *Georgia Institute of Technology*, 1999.